Global Climate [in “State of the Climate in 2024“]

R. Dunn, J. Blannin, K. Willett, N. Gobron, G. Morris, Melanie Ades, Robert Adler, Mihai Alexe, Richard Allan, John Anderson, et al.

STATE OF THE CLIMATE IN 2024

GLOBAL CLIMATE

R. J. H. Dunn, J. Blannin, K. M. Willett, N. Gobron, and G. A. Morris, Eds.

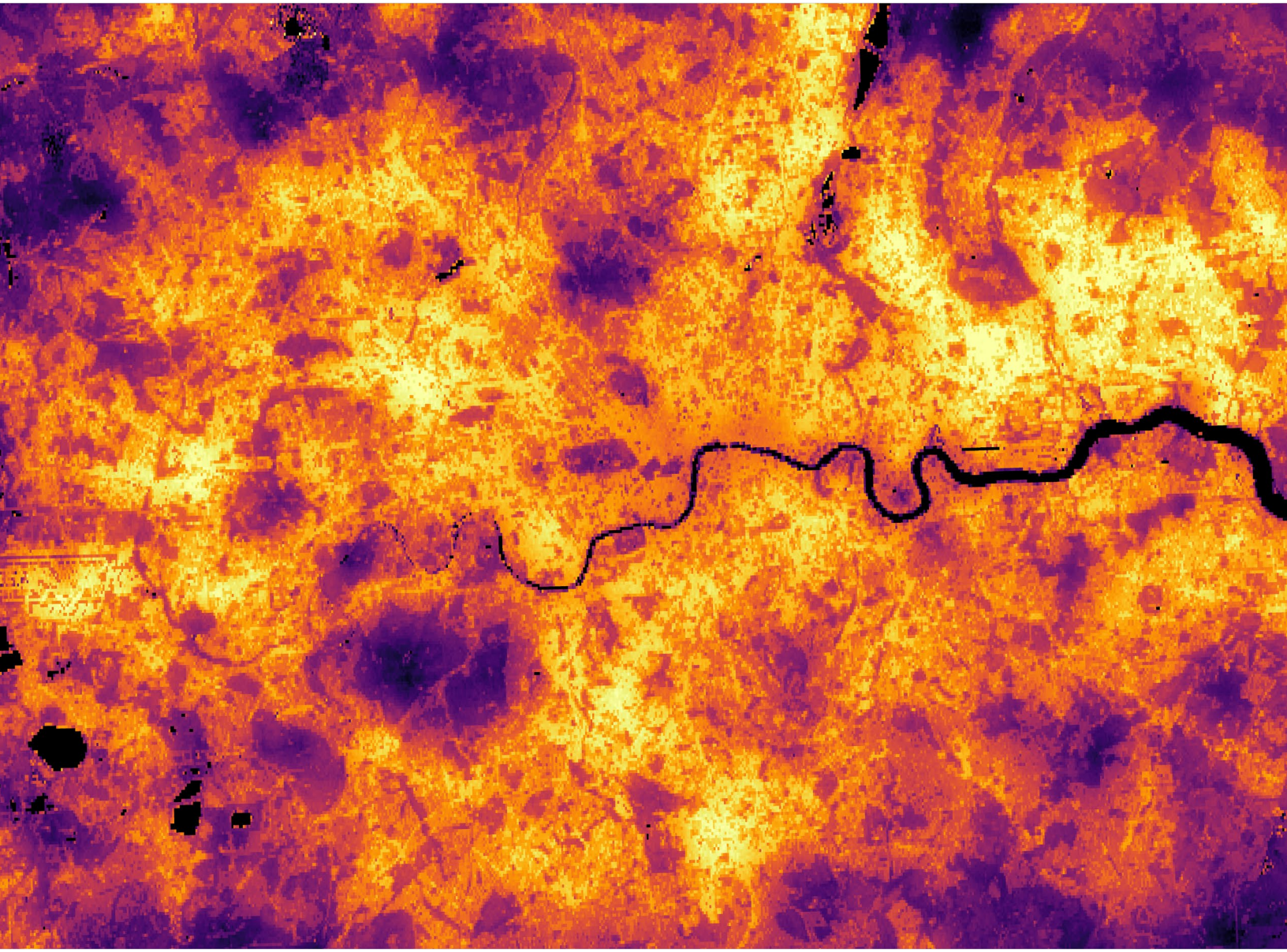

Special Online Supplement to the *Bulletin of the American Meteorological Society* Vol. 106, No. 8, August, 2025

https://doi.org/10.1175/BAMS-D-25-0102.1

Corresponding author: Robert Dunn / robert.dunn@metoffice.gov.uk

STATE OF THE CLIMATE IN 2024
Global Climate

Editors

Jessica Blunden
James Reagan

Chapter Editors

Anthony Arguez
Josh Blannin
Peter Bissolli
Kyle R. Clem
Howard J. Diamond
Matthew L. Druckenmiller
Robert J. H. Dunn
Catherine Ganter
Nadine Gobron
Gregory C. Johnson
Rick Lumpkin
Rodney Martinez
Ademe Mekonnen
Twila A. Moon
Gary A. Morris
Marilyn N. Raphael
Carl J. Schreck III
Laura Stevens
Richard L. Thoman
Kate M. Willett
Zhiwei Zhu

Technical Editor

Lukas Noguchi

BAMS Special Editor for Climate

Timothy DelSole

American Meteorological Society

Cover Credit:
Land Surface Temperature (LST) view of London, UK, on 30 July 2024 from Sentinel 3a. The LST data have been downscaled using Vis/SWIR inputs from Landsat 9 and Sentinel 2a and a bottom-of-atmosphere optimal estimation methodology to refine the estimates from 1 km data to 100 m.

Credit: M. Perry, C. Paton, B. Courtier, D, Ghent, NCEO, University of Leicester

How to cite this document:
Global Climate is one chapter from the *State of the Climate in 2024* annual report and is available from https://doi.org/10.1175/BAMS-D-25-0102.1. Compiled by NOAA's National Centers for Environmental Information, *State of the Climate in 2024* is based on contributions from scientists from around the world. It provides a detailed update on global climate indicators, notable weather events, and other data collected by environmental monitoring stations and instruments located on land, water, ice, and in space. The full report is available from https://doi.org/10.1175/2025BAMSStateoftheClimate.1.

Citing the complete report:
Blunden, J. and J. Reagan, Eds., 2025: "State of the Climate in 2024". Bull. Amer. Meteor. Soc., 106 (8), Si–S513 https://doi.org/10.1175/2025BAMSStateoftheClimate.1.

Citing this chapter:
Dunn, R. J. H., J. Blannin, K. M. Willett, N. Gobron, and G. A. Morris, Eds., 2025:
Global Climate [in "State of the Climate in 2024"]. Bull. Amer. Meteor. Soc., 106 (8), S11–S172, https://doi.org/10.1175/BAMS-D-25-0102.1.

Citing a section (example):
Fereday, D., D. Campos, and G. Macara, 2025: Mean sea level pressure and related modes of variabiity [in "State of the Climate in 2024"]. Bull. Amer. Meteor. Soc., 106 (8), S80–S81, https://doi.org/10.1175/BAMS-D-25-0102.1.

Editor and Author Affiliations (alphabetical by name)

Ades, Melanie, European Centre for Medium-Range Weather Forecasts, Reading, United Kingdom

Adler, Robert, Earth System Science Interdisciplinary Center, University of Maryland, College Park, Maryland

Alexe, Mihai, European Centre for Medium-Range Weather Forecasts, Bonn, Germany

Allan, Richard P., Department of Meteorology, University of Reading, Reading, United Kingdom; National Centre for Earth Observation (NCEO), University of Leicester, Leicester, United Kingdom

Anderson, John, Hampton University, Hampton, Virginia

Anneville, Orlane, National Research Institute for Agriculture, Food and Environment (INRAE), CARRTEL, Université Savoie Mont Blanc, Thonon les Bains, France

Aono, Yasuyuki, Graduate School of Agriculture, Osaka Metropolitan University, Sakai, Japan

Arguez, Anthony, NOAA/NESDIS National Centers for Environmental Information, Asheville, North Carolina

Armenteras-Pascual, Dolors, Science Faculty, Universidad Nacional de Colombia, Bogotá, Colombia

Arosio, Carlo, University of Bremen, Bremen, Germany

Asher, Elizabeth, Cooperative Institute for Research in Environmental Sciences, University of Colorado Boulder, Boulder, Colorado; NOAA Global Monitoring Laboratory, Boulder, Colorado

Augustine, John A., NOAA Global Monitoring Laboratory, Boulder, Colorado

Azorin-Molina, Cesar, Centro de Investigaciones sobre Desertificación – Spanish National Research Council (CSIC-UV-GVA), Valencia, Spain

Baez-Villanueva, Oscar M., Hydro-Climate Extremes Lab (H-CEL), Ghent University, Ghent, Belgium

Barichivich, Jonathan, Laboratoire des Sciences du Climat et de l'Environnement (LSCE), LSCE/IPSL, CEA-CNRS-UVSQ, Gif-sur-Yvette, France

Baron, Alexandre, Cooperative Institute for Research in Environmental Sciences, University of Colorado Boulder, Boulder, Colorado; NOAA Chemical Sciences Laboratory, Boulder, Colorado

Beck, Hylke E., Physical Science and Engineering Division, King Abdullah University of Science and Technology, Thuwal, Saudi Arabia

Bellouin, Nicolas, University of Reading, Reading, United Kingdom; Institute Pierre Simon Laplace (IPSL), Guyancourt, France

Benedetti, Angela, European Centre for Medium-Range Weather Forecasts, Reading, United Kingdom

Blannin, Josh, Met Office Hadley Centre, Exeter, United Kingdom

Blenkinsop, Stephen, School of Engineering, Newcastle University, Newcastle-upon-Tyne, United Kingdom; Tyndall Centre for Climate Change Research, Norwich, United Kingdom

Bock, Olivier, Université Paris Cité, Institut de physique du globe de Paris, CNRS, IGN, Paris, France; Univ Gustave Eiffel, ENSG, IGN, Marne-la-Vallée, France

Bodin, Xavier, Laboratoire EDYTEM, CNRS/Université Savoie Mont-Blanc, Le Bourget-du-Lac, France

Bonte, Olivier, Hydro-Climate Extremes Lab (H-CEL), Ghent University, Ghent, Belgium

Bosilovich, Michael G., Global Modeling and Assimilation Office, NASA Goddard Space Flight Center, Greenbelt, Maryland

Boucher, Olivier, Institute Pierre Simon Laplace (IPSL), Guyancourt, France

Bowman, Kevin, Jet Propulsion Laboratory, California Institute of Technology, Pasadena, California

Buehler, Sarah A., Universität Hamburg, Hamburg, Germany

Bunno, Ayaka, Japan Meteorological Agency, Tokyo, Japan

Byrne, Michael, P., School of Earth and Environmental Sciences, University of St Andrews, St Andrews, United Kingdom

Campos, Diego, Barcelona Supercomputing Centre, Barcelona, Spain

Cappucci, Fabrizio, Joint Research Centre, European Commission, Ispra, Italy

Carrea, Laura, University of Reading, Reading, United Kingdom

Casado-Rodríguez, Jesús, Joint Research Centre, European Commission, Ispra, Italy

Chang, Kai-Lan, Cooperative Institute for Research in Environmental Sciences, University of Colorado Boulder, Boulder, Colorado; NOAA Chemical Sciences Laboratory, Boulder, Colorado

Christiansen, Hanne H., Arctic Geophysics Department, University Centre in Svalbard, Longyearbyen, Norway

Christy, John R., University of Alabama in Huntsville, Huntsville, Alabama

Chung, Eui-Seok, Korea Polar Research Institute, Incheon, South Korea

Ciasto, Laura M., NOAA/NWS National Centers for Environmental Prediction, Climate Prediction Center, College Park, Maryland

Clingan, Scott, Cooperative Institute for Research in Environmental Sciences, University of Colorado Boulder, Boulder, Colorado; NOAA Global Monitoring Laboratory, Boulder, Colorado

Coldewey-Egbers, Melanie, German Aerospace Center (DLR), Oberpfaffenhofen, Germany

Cooley, Sarah, Duke University, Durham, North Carolina

Cooper, Owen R., NOAA Chemical Sciences Laboratory, Boulder, Colorado

Cornes, Richard C., National Oceanography Centre, Southampton, United Kingdom

Covey, Curt, Lawrence Livermore National Laboratory, Livermore, California

Crétaux, Jean-Francois, LEGOS (CNES/CNRS/IRD/UPS), Université de Toulouse, Toulouse, France

Crimmins, Theresa, USA National Phenology Network, School of Natural Resources and the Environment, University of Arizona, Tucson, Arizona

Crotwell, Molly, Cooperative Institute for Research in Earth Science, University of Colorado Boulder, Boulder, Colorado; NOAA Global Monitoring Laboratory, Boulder, Colorado

Culpepper, Joshua, Department of Biology, York University, Toronto, Canada

Cusicanqui, Diego, Institut de Géosciences de l'Environnement (IGE), Université Grenoble Alpes, INRAE, CNRS, IRD, Grenoble INP, ISTerre, Grenoble, France

Davis, Sean M., NOAA Chemical Sciences Laboratory, Boulder, Colorado

de Jeu, Richard A. M., Transmissivity B.V., Haarlem, The Netherlands

de Laat, Jos, Royal Netherlands Meteorological Institute (KNMI), DeBilt, The Netherlands

Degenstein, Doug, University of Saskatchewan, Saskatoon, Canada

Delaloye, Reynald, Department of Geosciences, University of Fribourg, Fribourg, Switzerland

Di Tomaso, Enza, European Centre for Medium-Range Weather Forecasts, Bonn, Germany

Dokulil, Martin T., Research Institute for Limnology, University of Innsbruck, Mondsee, Austria

Donat, Markus G., Barcelona Supercomputing Centre, Barcelona, Spain; Catalan Institution for Research and Advanced Studies (ICREA), Barcelona, Spain

Dorigo, Wouter A., Department of Geodesy and Geoinformation, TU Wien, Vienna, Austria

Dugan, Hilary, Center of Limnology, University of Wisconsin-Madison, Madison, Wisconsin

Dunn, Robert J. H., Met Office Hadley Centre, Exeter, United Kingdom

Durre, Imke, Climate Science and Services Division, NOAA/NESDIS National Centers for Environmental Information, Asheville, North Carolina

Dutton, Geoff, Cooperative Institute for Research in Earth Science, University of Colorado Boulder, Boulder, Colorado

Effertz, Peter, Cooperative Institute for Research in Environmental Sciences, University of Colorado Boulder, Boulder, Colorado; NOAA Global Monitoring Laboratory, Boulder, Colorado

Enno, Sven-Erik, EUMETSAT, Darmstadt, Germany

Estilow, Thomas W., Rutgers University, Piscataway, New Jersey

Estrella, Nicole, Ecoclimatology, Department of Life Science Systems, TUM School of Life Sciences, Technical University of Munich, Freising, Germany

Fereday, David, Met Office Hadley Centre, Exeter, United Kingdom

Fioletov, Vitali E., Environment and Climate Change Canada, Toronto, Canada
Flemming, Johannes, European Centre for Medium-Range Weather Forecasts, Bonn, Germany
Formanek, Maud, Department of Geodesy and Geoinformation, TU Wien, Vienna, Austria
Foster, Michael J., Cooperative Institute for Meteorological Satellite Studies, Space Science and Engineering Center, University of Wisconsin-Madison, Madison, Wisconsin
Frederikse, Thomas, Planet Labs, Haarlem, The Netherlands
Frith, Stacey M., Science Systems and Applications, Inc, Lanham, Maryland; NASA Goddard Space Flight Center, Greenbelt, Maryland
Froidevaux, Lucien, Jet Propulsion Laboratory, California Institute of Technology, Pasadena, California
Füllekrug, Martin, University of Bath, Bath, United Kingdom
Gallemann, Thomas, Bavarian Environment Agency, Augsburg, Germany
Garforth, Judith, Woodland Trust, Grantham, United Kingdom
Garg, Jay, ADNET Systems, Inc., Hampton, Virginia
Ghent, Darren, National Centre for Earth Observation (NCEO), University of Leicester, Leicester, United Kingdom; School of Physics and Astronomy, University of Leicester, Leicester, United Kingdom
Gobron, Nadine, Joint Research Centre, European Commission, Ispra, Italy
Gollop, Amee, Climatic Research Unit, School of Environmental Sciences, University of East Anglia, Norwich, United Kingdom
Good, Elizabeth, Met Office, Exeter, United Kingdom
Goodman, Steven, Thunderbolt Global Analytics, Huntsville, Alabama
Goto, Atsushi, Japan Meteorological Agency, Tokyo, Japan
Grimaldi, Stefania, Joint Research Centre, European Commission, Ispra, Italy
Gruber, Alexander, Department of Geodesy and Geoinformation, TU Wien, Vienna, Austria
Gu, Guojun, Earth System Science Interdisciplinary Center, University of Maryland, College Park, Maryland
Guglielmin, Mauro, Department of Theoretical and Applied Sciences, Insubria University, Varese, Italy
Haghdoost, Shekoofeh, Hydro-Climate Extremes Lab (H-CEL), Ghent University, Ghent, Belgium
Hahn, Sebastian, Department of Geodesy and Geoinformation, TU Wien, Vienna, Austria
Haimberger, Leopold, Department of Meteorology and Geophysics, University of Vienna, Austria
Hall, Brad D., NOAA Global Monitoring Laboratory, Boulder, Colorado
Harlan, Merritt E., U.S. Geological Survey, Denver, Colorado
Harris, Bethan L., National Centre for Earth Observation (NCEO), University of Leicester, Leicester, United Kingdom; United Kingdom Centre for Ecology & Hydrology, Wallingford, United Kingdom
Harris, Ian, National Centre for Atmospheric Science (NCAS), University of East Anglia, Norwich, United Kingdom; Climatic Research Unit, School of Environmental Sciences, University of East Anglia, Norwich, United Kingdom
Hemming, Deborah L., Met Office Hadley Centre, Exeter, United Kingdom; Birmingham Institute of Forest Research, Birmingham University, Birmingham, United Kingdom
Ho, Shu-peng (Ben), NOAA/NESDIS Center for Satellite Applications and Research, College Park, Maryland
Holliday, Rebecca, Met Office, Exeter, United Kingdom
Holzworth, Robert, University of Washington, Seattle, Washington
Horton, Radley M., Columbia Climate School, Columbia University, New York, New York
Hrbáček, Filip, Department of Geography, Masaryk University, Brno, Czech Republic
Hu, Guojie, Cryosphere Research Station on Qinghai-Tibet Plateau, Northwestern Institute of Eco-Environment and Resources, CAS, Lanzhou, China
Inness, Antje, European Centre for Medium-Range Weather Forecasts, Reading, United Kingdom
Isaksen, Ketil, Norwegian Meteorological Institute, Oslo, Norway
John, Viju O., EUMETSAT, Darmstadt, Germany
Jones, Philip D., Climatic Research Unit, School of Environmental Sciences, University of East Anglia, Norwich, United Kingdom
Junod, Robert, Earth System Science Center, University of Alabama in Huntsville, Huntsville, Alabama
Kääb, Andreas, Department of Geosciences, University of Oslo, Norway
Kaiser, Johannes W., Norwegian Institute for Air Research (NILU), Kjeller, Norway
Kaufmann, Viktor, Institute of Geodesy, Working Group Remote Sensing and Photogrammetry, Graz University of Technology, Graz, Austria
Kellerer-Pirklbauer, Andreas, Department of Geography and Regional Science, Cascade—The Mountain Processes and Mountain Hazards Group, University of Graz, Graz, Austria
Kent, Elizabeth C., National Oceanography Centre, Southampton, United Kingdom
Khaykin, Sergey, Laboratoire Atmosphères, Observations Spatiales (LATMOS), UVSQ, Sorbonne Université, CNRS, IPSL, Guyancourt, France
Kidd, Richard, EODC GmbH, Vienna, Austria
Kipling, Zak, European Centre for Medium-Range Weather Forecasts, Reading, United Kingdom
Kirkpatrick, Sarah, Fenner School of Environment and Society, Australian National University, Canberra, Australia
Kondragunta, Shobha, NOAA/NESDIS, College Park, Maryland
Kovács, Dávid D., Department of Geodesy and Geoinformation, TU Wien, Vienna, Austria
Kraemer, Benjamin M., University of Freiburg, Freiburg, Germany
Laas, Alo, Estonian University of Life Sciences, Tartumaa, Estonia
Lan, Xin, Cooperative Institute for Research in the Environmental Sciences, University of Colorado Boulder, Boulder, Colorado; NOAA Global Monitoring Laboratory, Boulder, Colorado
Lantz, Kathleen O., NOAA Global Monitoring Laboratory, Boulder, Colorado
Lavers, David A., European Centre for Medium-Range Weather Forecasts, Reading, United Kingdom
Leibensperger, Eric, Department of Physics and Astronomy, Ithaca College, Ithaca, New York
Lems, Johanna, Department of Geodesy and Geoinformation, TU Wien, Vienna, Austria
Lennard, Chris, Department of Environmental and Geographical Science, University of Cape Town, Cape Town, South Africa
Levenson, Eric S., University of Oregon, Eugene, Oregon
Liley, Ben, National Institute of Water and Atmospheric Research (NIWA), Lauder, New Zealand
Lo, Y. T. Eunice, Cabot Institute for the Environment; University of Bristol, Bristol, United Kingdom; Elizabeth Blackwell Institute for Health Research, University of Bristol, Bristol, United Kingdom
Loeb, Norman G., NASA Langley Research Center, Hampton, Virginia
Loyola, Diego, German Aerospace Center (DLR), Oberpfaffenhofen, Germany
Macara, Gregor, National Institute of Water and Atmospheric Research (NIWA), Lauder, New Zealand
Magnin, Florence, Laboratoire EDYTEM, CNRS/Université Savoie Mont-Blanc, Le Bourget-du-Lac, France
Matsuzaki, Shin-Ichiro, National Institute for Environmental Studies, Tsukuba, Japan
Matthews, Tom, Department of Geography, King's College London, London, United Kingdom
Mayer, Michael, Department of Meteorology and Geophysics, University of Vienna, Vienna, Austria; Research Department, European Centre for Medium-Range Weather Forecasts, Bonn, Germany

McVicar, Tim R., CSIRO Environment, Canberra, Australia; Australian Research Council Centre of Excellence for Climate Extremes, Sydney, Australia
Mears, Carl A., Remote Sensing Systems, Santa Rosa, California
Menzel, Annette, Ecoclimatology, Department of Life Science Systems, TUM School of Life Sciences, Technical University of Munich, Freising, Germany; Institute for Advanced Study, Technical University of Munich, Garching, Germany
Merchant, Christopher J., University of Reading, Reading, United Kingdom
Meyer, Michael F., U.S. Geological Survey, Madison, Wisconsin
Miralles, Diego G., Hydro-Climate Extremes Lab (H-CEL), Ghent University, Ghent, Belgium
Montzka, Stephan A., NOAA Global Monitoring Laboratory, Boulder, Colorado
Morice, Colin, Met Office Hadley Centre, Exeter, United Kingdom
Morino, Isamu, National Institute for Environmental Studies Tsukuba, Ibaraki, Japan
Morris, Gary A., NOAA Global Monitoring Laboratory, Boulder, Colorado
Mrekaj, Ivan, Technical University in Zvolen, Zvolen, Slovakia
Mühle, Jens, Scripps Institution of Oceanography, San Diego, California
Nance, D., Cooperative Institute for Research in Environmental Sciences, University of Colorado Boulder, Boulder, Colorado
Nicolas, Julien P., European Centre for Medium-Range Weather Forecasts, Bonn, Germany
Noetzli, Jeannette, WSL Institute for Snow and Avalanche Research SLF, Davos Dorf, Switzerland; Climate Change, Extremes and Natural Hazards in Alpine Regions Research Centre (CERC), Davos Dorf, Switzerland
O'Keefe, John, The Harvard Forest, Harvard University, Petersham, Massachusetts
Ollinik, Jessica Erin, Department of Chemistry and Biochemistry, University of Regina, Regina, Canada
Osborn, Timothy J., Climatic Research Unit, School of Environmental Sciences, University of East Anglia, Norwich, United Kingdom
Parrington, Mark, European Centre for Medium-Range Weather Forecasts, Bonn, Germany
Pellet, Cécile, Department of Geosciences, University of Fribourg, Fribourg, Switzerland
Pelto, Mauri, Nichols College, Dudley, Massachusetts
Pennington, Elyse, Jet Propulsion Laboratory, California Institute of Technology, Pasadena, California
Petersen, Kyle, Cooperative Institute for Research in Environmental Sciences, University of Colorado Boulder, Boulder, Colorado; NOAA Global Monitoring Laboratory, Boulder, Colorado
Phillips, Coda, Cooperative Institute for Meteorological Satellite Studies, Space Science and Engineering Center, University of Wisconsin-Madison, Madison, Wisconsin
Pierson, Don, Department of Ecology and Genetics, Uppsala University, Uppsala, Sweden
Pinto, Izidine, Royal Netherlands Meteorological Institute (KNMI), De Bilt, The Netherlands
Po-Chedley, Stephen, Lawrence Livermore National Laboratory, Livermore, California
Pogliotti, Paolo, Environmental Protection Agency of Valle d'Aosta, Saint Christophe, Italy
Polvani, Lorenzo, Columbia University, New York, New York
Preimesberger, Wolfgang, Department of Geodesy and Geoinformation, TU Wien, Vienna, Austria
Price, Colin, Tel Aviv University, Tel Aviv, Israel
Pulkkanen, Merja, Finnish Environment Institute (SYKE), Helsinki, Finland
Randel, William J., National Center for Atmospheric Research, Boulder, Colorado
Raymond, Colin, Joint Institute for Regional Earth System Science and Engineering, University of California, Los Angeles, Los Angeles, California
Remy, Samuel, HYGEOS, Lille, France
Ricciardulli, Lucrezia, Remote Sensing Systems, Santa Rosa, California
Richardson, Andrew D., School of Informatics, Computing, and Cyber Systems, Northern Arizona University, Flagstaff, Arizona; Center for Ecosystem Science and Society, Northern Arizona University, Flagstaff, Arizona
Robinson, David A., Rutgers University, Piscataway, New Jersey
Rodell, Matthew, Earth Sciences Division, NASA Goddard Space Flight Center, Greenbelt, Maryland
Rodriguez-Fernandez, Nemesio, CESBIO, Université de Toulouse, CNES/CNRS/INRAe/IRD/UPS, Toulouse, France
Rogers, Cassandra D.W., Bureau of Meteorology, Melbourne, Australia
Rohini, P., India Meteorological Department, Ministry of Earth Sciences, Pune, India
Rosenlof, Karen H., NOAA Chemical Sciences Laboratory, Boulder, Colorado
Rozanov, Alexei, University of Bremen, Bremen, Germany
Rozkošný, Jozef, Slovak Hydrometeorological Institute, Bratislava, Slovakia
Rusanovskaya, Olga O., Institute of Biology, Irkutsk State University, Irkutsk, Russia
Rutishauser, This, Swiss Academy of Sciences (SCNAT), Bern, Switzerland
Sabeerali, C. T., India Meteorological Department, Ministry of Earth Sciences, Pune, India
Sakai, Tetsu, Meteorological Research Institute, Japan Meteorological Agency, Tsukuba, Ibaraki, Japan
Salamon, Peter, Joint Research Centre, European Commission, Ispra, Italy
Sánchez-Lugo, Ahira, NOAA/NESDIS National Centers for Environmental Information, Asheville, North Carolina
Sawaengphokhai, Parnchai, ADNET Systems, Inc., Hampton, Virginia
Schenzinger, Verena, Medical University of Innsbruck, Innsbruck, Austria
Schmid, Martin, Eawag, Department Surface Waters—Research and Management, Kastanienbaum, Switzerland
Sezaki, Fumi, Japan Meteorological Agency, Tokyo, Japan
Shao, Xi, Earth System Science Interdisciplinary Center, University of Maryland, College Park, Maryland
Sharma, Sapna, Department of Biology, York University, Toronto, Ontario, Canada
Shi, Lei, NOAA/NESDIS National Centers for Environmental Information, Asheville, North Carolina
Shimaraeva, Svetlana V., Institute of Biology, Irkutsk State University, Irkutsk, Russia
Shinohara, Ryuichiro, Regional Environment Conservation Division, National Institute for Environmental Studies, Tsukuba, Ibaraki, Japan
Silow, Eugene A., Institute of Biology, Irkutsk State University, Irkutsk, Russia
Simmons, Adrian J., European Centre for Medium-Range Weather Forecasts, Reading, United Kingdom
Smith, Katie, Cooperative Institute for Research in Environmental Sciences, University of Colorado Boulder, Boulder, Colorado; NOAA Chemical Sciences Laboratory, Boulder, Colorado
Smith, Sharon L., Geological Survey of Canada, Natural Resources Canada, Ottawa, Canada
Soden, Brian J., University of Miami, Miami, Florida
Sofieva, Viktoria, Finnish Meteorological Institute, Helsinki, Finland
Soldo, Logan, Cooperative Institute for Research in Environmental Sciences, University of Colorado Boulder, Boulder, Colorado; NOAA Global Monitoring Laboratory, Boulder, Colorado
Sreejith, O. P., India Meteorological Department, Ministry of Earth Sciences, Pune, India
Stackhouse, Jr., Paul W., NASA Langley Research Center, Hampton, Virginia
Stauffer, Ryan M., Atmospheric Chemistry and Dynamics Laboratory, NASA Goddard Space Flight Center, Greenbelt, Maryland
Steinbrecht, Wolfgang, Deutscher Wetterdienst, Hohenpeissenberg, Germany
Steiner, Andrea K., Wegener Center for Climate and Global Change, University of Graz, Graz, Austria
Stevens, Thea, Department of Meteorology, University of Reading, Reading, United Kingdom

Editor and Author Affiliations (continued)

Stoy, Paul C., College of Agricultural and Life Sciences, University of Wisconsin-Madison, Madison, Wisconsin

Streletskiy, Dmitry A., George Washington University, Washington, DC

Taha, Ghassan, Morgan State University, Baltimore, Maryland; NASA Goddard Flight Center, Greenbelt, Maryland

Thackeray, Stephen J., United Kingdom Centre for Ecology & Hydrology, Lancaster, United Kingdom

Thibert, Emmanuel, Institut de Géosciences de l'Environnement (IGE), Université Grenoble Alpes, INRAE, CNRS, IRD, Grenoble INP, IGE, Grenoble, France

Timofeyev, Maxim A., Institute of Biology, Irkutsk State University, Irkutsk, Russia

Tourpali, Kleareti, Aristotle University, Thessaloniki, Greece

Tronquo, Emma, Hydro-Climate Extremes Lab (H-CEL), Ghent University, Ghent, Belgium; Department of Geoscience and Remote Sensing, TU Delft, Delft, The Netherlands

Tye, Mari R., National Center for Atmospheric Research, Boulder, Colorado

Urraca, Ruben, Joint Research Centre, European Commission, Ispra, Italy

van der A, Ronald, Royal Netherlands Meteorological Institute (KNMI), DeBilt, The Netherlands

van der Schrier, Gerard, Royal Netherlands Meteorological Institute (KNMI), DeBilt, The Netherlands

VanScoy, Greta, The Harvard Forest, Harvard University, Petersham, Massachusetts

van Vliet, Arnold J. H., Earth Systems and Global Change Group, Wageningen University & Research, The Netherlands

Veal, Karen, National Centre for Earth Observation (NCEO), University of Leicester, Leicester, United Kingdom; School of Physics and Astronomy, University of Leicester, Leicester, United Kingdom

Verburg, Piet, National Institute of Water and Atmospheric Research (NIWA), Hamilton, New Zealand

Vernier, Jean-Paul, NASA Langley Research Center, Hampton, Virginia

Vimont, Isaac J., NOAA Global Monitoring Laboratory, Boulder, Colorado

Viticchie, Bartolomeo, EUMETSAT, Darmstadt, Germany

Vivero, Sebastián, Department of Geosciences, University of Fribourg, Fribourg, Switzerland

Vömel, Holger, National Center for Atmospheric Research, Boulder, Colorado

Vose, Russell S., NOAA/NESDIS National Centers for Environmental Information, Asheville, North Carolina

Wang, Donqian, Climate Change Division, National Climate Center, China Meteorological Administration, Beijing, China

Wang, Ray H. J., Georgia Institute of Technology, Atlanta, Georgia

Waring, Abigail Marie, National Centre for Earth Observation (NCEO), University of Leicester, Leicester, United Kingdom; School of Physics and Astronomy, University of Leicester, Leicester, United Kingdom

Warnock, Taran, University of Saskatchewan, Saskatoon, Canada

Weber, Mark, University of Bremen, Bremen, Germany

Wei, Zigang, Science and Technology Corporation (STC), College Park, Maryland

Wiese, David N., Jet Propulsion Laboratory, California Institute of Technology, Pasadena, California

Wild, Jeannette D., Earth System Science Interdisciplinary Center, University of Maryland, College Park, Maryland; NOAA/NESDIS Center for Satellite Applications and Research, College Park, Maryland

Willett, Kate M., Met Office Hadley Centre, Exeter, United Kingdom

Williams, Earle, Massachusetts Institute of Technology, Cambridge, Massachusetts

Wong, Takmeng, NASA Langley Research Center, Hampton, Virginia

Wood, Tom, Department of Geography, King's College London, London, United Kingdom

Woolway, Richard Iestyn, School of Ocean Sciences, Bangor University, Bangor, United Kingdom

Worden, John, Jet Propulsion Laboratory, California Institute of Technology, Pasadena, California

Yang, Kai, Department of Atmospheric and Oceanic Sciences, University of Maryland, College Park, Maryland

Yin, Xungang, NOAA/NESDIS National Centers for Environmental Information, Asheville, North Carolina

Zeng, Zhenzhong, School of Environmental Science and Engineering, Southern University of Science and Technology, Shenzhen, China

Zhao, Lin, School of Geographical Sciences, Nanjing University of Information Science and Technology, Nanjing, China

Ziemke, Jerry R., Goddard Earth Sciences Technology and Research, Morgan State University, Baltimore, Maryland; NASA Goddard Space Flight Center, Greenbelt, Maryland

Ziese, Markus, Global Precipitation Climatology Centre, Deutscher Wetterdienst, Offenbach, Germany

Zotta, Ruxandra-Maria, TU Wien, Vienna, Austria

Zou, Cheng-Zhi, George Mason University, Fairfax, Virginia

Editorial and Production Team

Allen, Jessicca, Graphics Support, Cooperative Institute for Satellite Earth System Studies, North Carolina State University, Asheville, North Carolina

Camper, Amy V., Graphics Support, Innovative Consulting and Management Services, LLC, NOAA/NESDIS National Centers for Environmental Information, Asheville, North Carolina

Carroll, Lauren, Content Team Lead, Communications and Outreach, NOAA/NESDIS National Centers for Environmental Information, Asheville, North Carolina

Haley, Bridgette O., Graphics Support, NOAA/NESDIS National Centers for Environmental Information, Asheville, North Carolina

Love-Brotak, S. Elizabeth, Lead Graphics Production, NOAA/NESDIS National Centers for Environmental Information, Asheville, North Carolina

Ohlmann, Laura, Technical Editor, Innovative Consulting and Management Services, LLC, NOAA/NESDIS National Centers for Environmental Information, Asheville, North Carolina

Noguchi, Lukas, Technical Editor, Innovative Consulting and Management Services, LLC, NOAA/NESDIS National Centers for Environmental Information, Asheville, North Carolina

Riddle, Deborah B., Graphics Support, NOAA/NESDIS National Centers for Environmental Information, Asheville, North Carolina

Veasey, Sara W., Visual Communications Team Lead, Communications and Outreach, NOAA/NESDIS National Centers for Environmental Information, Asheville, North Carolina

2. Table of Contents

2. Table of Contents

2. GLOBAL CLIMATE

R. J. H. Dunn, J. Blannin, K. M. Willett, N. Gobron, and G. A. Morris, Eds.

a. Overview

—R. J. H. Dunn, J. Blannin, K. M. Willett, N. Gobron, and G. A. Morris

For the second year in a row, record-high global surface temperatures were set in 2024, according to all six global temperature datasets assessed in this report (Berkeley Earth, GISTEMP, HadCRUT5, the NOAA Merged Land Ocean Global Surface Temperature Analysis [NOAAGlobalTemp], ERA5, and the Japanese Reanalysis for Three Quarters of a Century [JRA-3Q]). The last time consecutive years set records was in 2015 and 2016 when a strong El Niño similarly boosted global temperatures. The last 10 years (2015–24) are now the warmest 10 in the instrumental record—warmer than the 2011–20 average—and hence "more likely than not warmer than any multi-century period after the last interglacial period, roughly 125,000 years ago" (Gulev et al. 2021). The increased energy within the climate system is detectable at the top of the atmosphere, with the outgoing longwave radiation anomaly continuing to be above the range of natural variability.

During 2024, El Niño conditions that had been present since the middle of 2023 faded to neutral by the end of the year. The warm conditions observed around the globe over the last two years had impacts across the climate system, as demonstrated by many of the metrics presented in this chapter. Other temperature metrics also reached record levels over the instrumental periods assessed in this chapter: over the oceans at night, on the surfaces of lakes, and in the lower troposphere as well as measures of equivalent temperature (which considers the moisture contribution to heat), and high and low temperature extremes.

The frozen parts of Earth responded with permafrost temperatures continuing to reach record-high levels in many locations, and the active-layer thickness (the portion that melts and refreezes annually) also increasing at most sites. Repeated high temperatures over the European Alps during recent summers has led to large increases in rock glacier velocities in that region. The Great Lakes had much-below-average ice cover over the 2023/24 winter, and there was below-average snow cover extent in the Northern Hemisphere. All 58 reference glaciers across five continents lost ice during 2024, resulting in the greatest average ice loss in the record, which began in 1970. One more glacier was also declared extinct during 2024.

Higher global temperatures impacted the water cycle. Although lower than 2023 values, water evaporation from land in the Northern Hemisphere reached one of the highest annual values on record, in line with the long-term increasing trend. Specific humidity reached record levels over land and ocean, and relative humidity over both domains was higher than 2023. There was little relief from high humid-heat conditions, with the frequency of high humid-heat days at a record level and intensity at the second-highest level in the record—only a fraction of a degree cooler than that of 2023. The global atmosphere contained the greatest amount of water vapor in the record, and over one-fifth of the globe recorded their highest values. This far exceeded 2023, where only one-tenth of the globe experienced record-high total column water vapor. Rainfall was globally high; 2024 was the third-wettest year since records began in 1983. However, rainfall over land was close to average, while over the ocean it was the fourth-wettest year on record (following 2015, 2016, and 1998). Extreme rainfall, as characterized by the annual maximum daily rainfall over land, was the wettest on record. Averaged globally (4190 lakes), lakes had a small increase in water storage, and regionally, over 40% of monitored lakes showed significant changes in storage and level.

The effects of ongoing droughts in southern Africa and in North and South America can be seen in the soil moisture and water storage patterns. They are also apparent in the river discharge and runoff levels, which are topics that will be covered in the chapter after a few years of absence. Globally, however, drought severity and extent decreased from the record set in 2023.

Atmospheric concentrations of the three main greenhouse gases (carbon dioxide [CO_2], methane [CH_4], nitrous oxide [N_2O]) again all reached record levels, with a record-equal annual increase in the annual change of CO_2 concentrations. However, concentrations of ozone-depleting substances continued to decline, corroborated by stratospheric ozone columns well above the 1998–2008 average, especially in the Northern Hemisphere. In contrast, stratospheric aerosols remained high because of the Ruang eruption in April 2024, affecting the atmospheric transmission of solar radiation over Hawaii later in the year, and the ongoing effects from the Hunga eruption in 2022. The latter eruption also caused the ongoing elevated stratospheric water vapor concentrations.

Our planet's surface albedo continued to darken with increased plant growth and decreased snow and ice cover. Plants responded to the warmer temperatures with some of the earliest starts to spring in the record over Europe—one to two weeks earlier than the 2000–20 baseline—and a warm autumn resulted in a much longer leaf-on season. Severe wildfire seasons occurred in South America (the worst since 2010), Canada (for the second consecutive year), and the Arctic, contributing to the second-highest atmospheric carbon monoxide concentrations since 2003 and the highest tropospheric aerosol optical depth since 2019, at 550 nm.

This year's iteration of the Global Climate chapter features two Sidebars, both of which present new topics that have not yet been explored in the report. The first covers the ability of satellite products to monitor changes in land surface temperature extremes and identify hotspots where regions of Earth are becoming uninhabitable. This Sidebar also discusses the importance of dataset stability for climate studies, as well as the correlation of land surface temperature and air temperature anomalies. The second Sidebar complements the section on greenhouse gas concentrations by examining short-lived climate forcers—compounds that have lifetimes ranging from a few hours to a few decades.

As usual in the Global Climate chapter, Plate 2.1 shows maps of global annual anomalies for many of the variables and metrics presented herein. Many of these variables are also presented as time series in Plate 1.1. Most sections now use the 1991–2020 climatological reference period, in line with the World Meteorological Organization's (WMO) recommendations, although this reference period is not possible for all datasets due to their length or legacy processing methods.

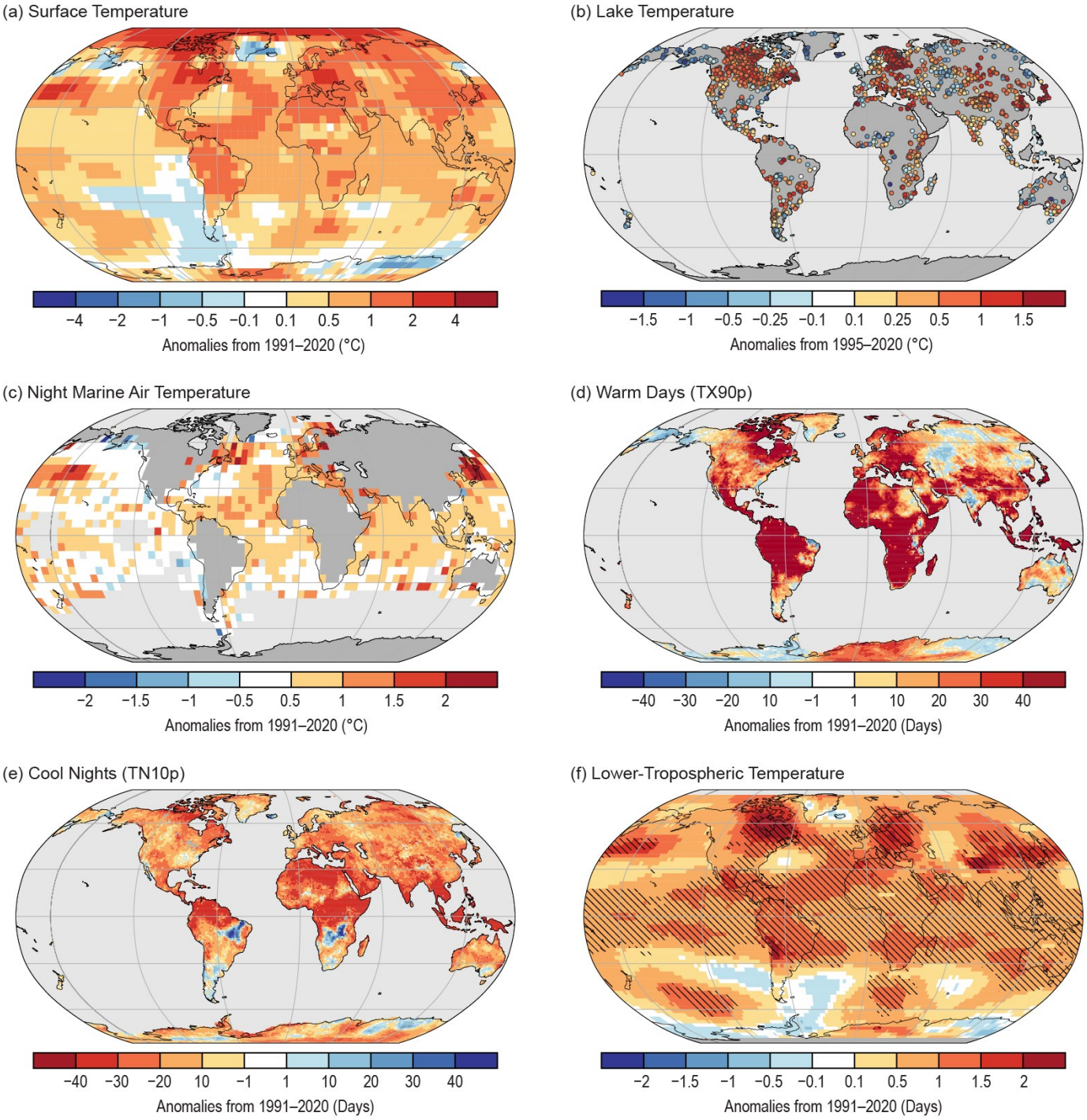

Plate 2.1. (a) NOAA NCEI Global land and ocean surface annual temperature anomalies (°C); (b) Satellite-derived lake surface water temperature annual anomalies, from European Space Agency (ESA) Climate Change Initiative (CCI) LAKES/Copernicus Climate Change Service (C3S) / Earth Observation Climate Information Service (EOCIS) (°C); (c) Climate Linked Atlantic Sector Science Night Marine Air Temperature (CLASSnmat) night marine air temperature annual average anomalies (°C); (d) ERA5 warm day threshold exceedance (TX90p); (e) ERA5 cool night threshold exceedance (TN10p); (f) Average of Remote Sensing Systems (RSS) and University of Alabama in Huntsville (UAH) lower-tropospheric annual temperature anomalies (°C). Hatching denotes regions in which 2024 was the warmest year on record; (g) ERA5 annual equivalent temperature anomalies (°C);

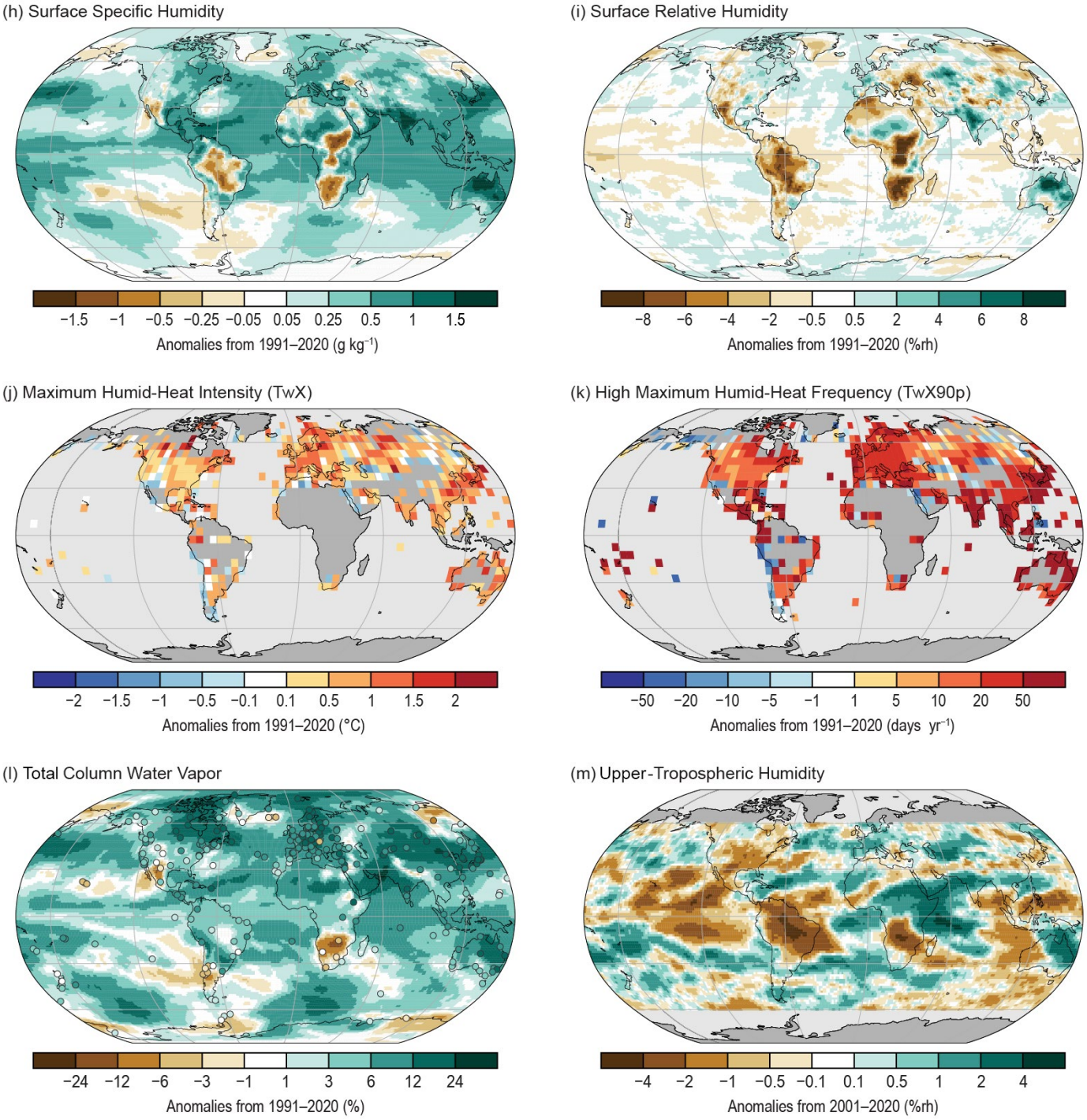

Plate 2.1 (cont.) (h) ERA5 surface specific humidity anomalies (g kg^{-1}); (i) ERA5 surface relative humidity anomalies (%rh); (j) Met Office Hadley Centre International Surface Dataset of Humidity extremes (HadISDH.extremes) humid heat intensity (T_wX), measured by the annual median anomaly of daily maximum wet-bulb temperature (°C). Gray background (over land) represent regions with insufficient data; (k) HadISDH.extremes humid heat frequency anomalies (T_wX90p), measured by the number of days where the daily maximum wet-bulb temperature exceeds the local daily 90th percentile (days yr^{-1}). Gray background (over land) represent regions with insufficient data; (l) JRA-3Q Total column water vapor (TCWV) anomalies (%). Data from Global Navigation Satellite System (GNSS) stations are plotted as filled circles; (m) Annual microwave-based upper-tropospheric humidity (UTH) anomalies (%rh); (n) Global Precipitation Climatology Centre (GPCC) annual mean precipitation anomalies (mm yr^{-1});

(o) Rx5day Anomalies

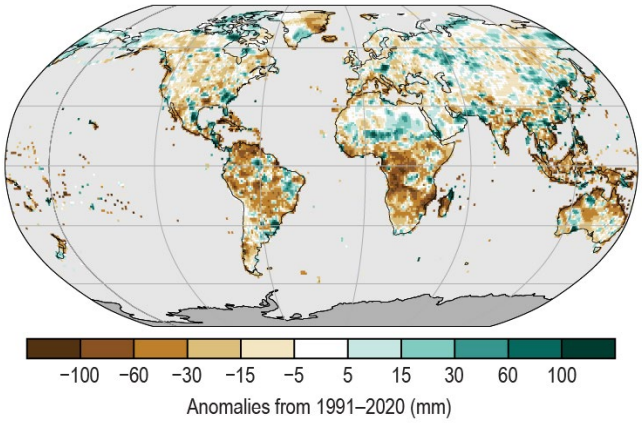

(p) Cloudiness

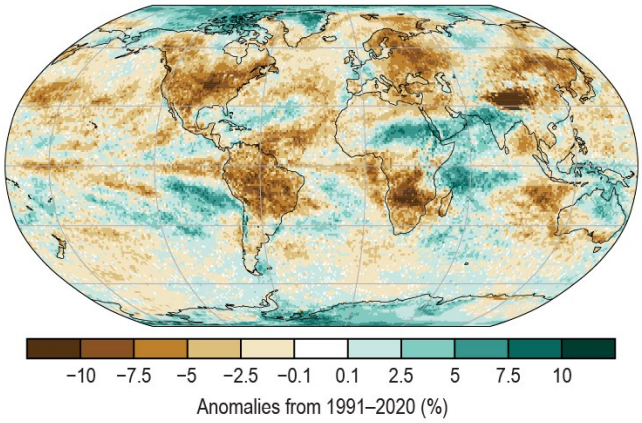

(q) Lake Water Storage

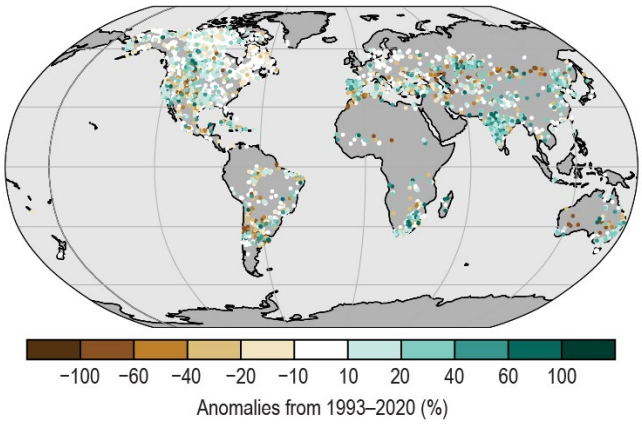

(r) Runoff

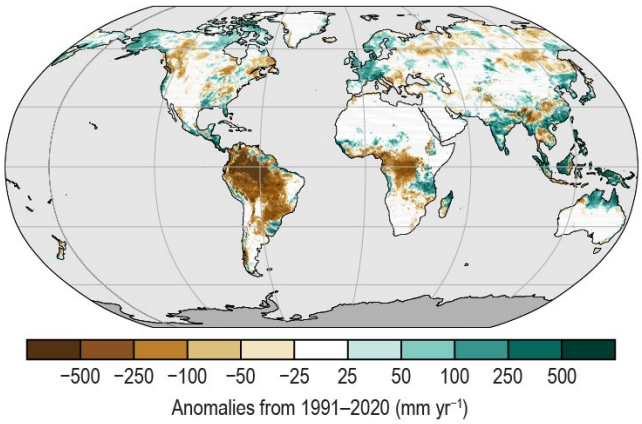

(s) River Discharge

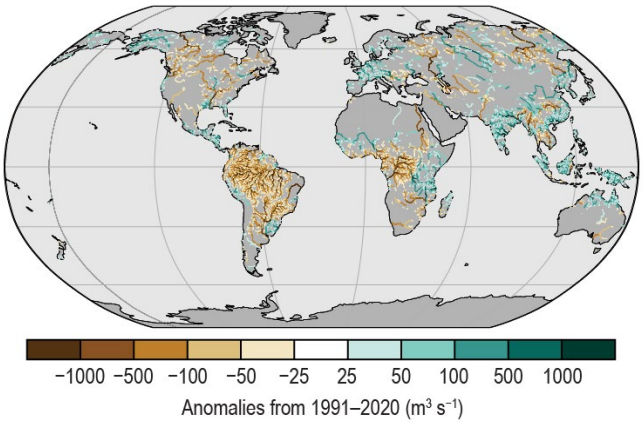

(t) Terrestrial Water Storage Difference

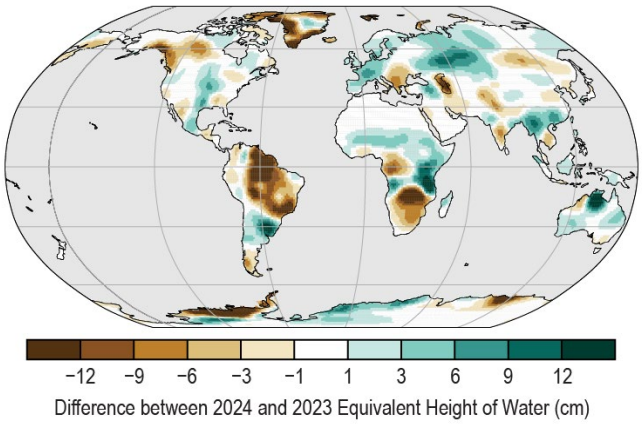

(u) Terrestrial Water Storage

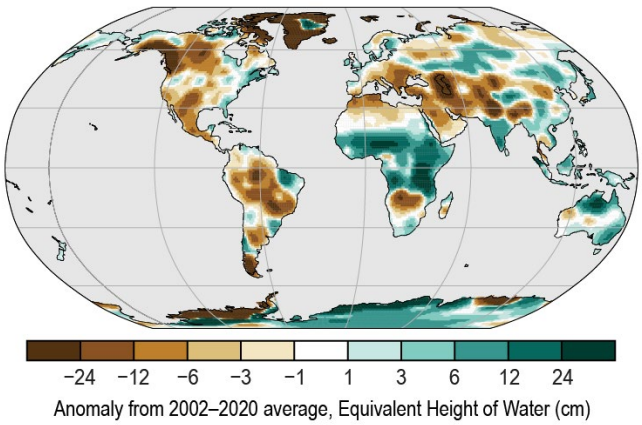

Plate 2.1 (cont.) (o) GPCC maximum five-day (Rx5day) annual precipitation anomalies (mm); (p) PATMOS-x 6.0 cloud fraction annual anomalies (%); (q) GloLakes lake water storage anomalies (%); (r) Global Flood Awareness System version 4 (GloFASv4) runoff anomalies (mm yr^{-1}); (s) GloFASv4 river discharge anomalies (m^3 s^{-1}); (t) Gravity Recovery and Climate Experiment Follow-On (GRACE-FO) difference in annual-mean terrestrial water storage between 2023 and 2024 (cm); (u) GRACE-FO terrestrial water storage anomalies (cm);

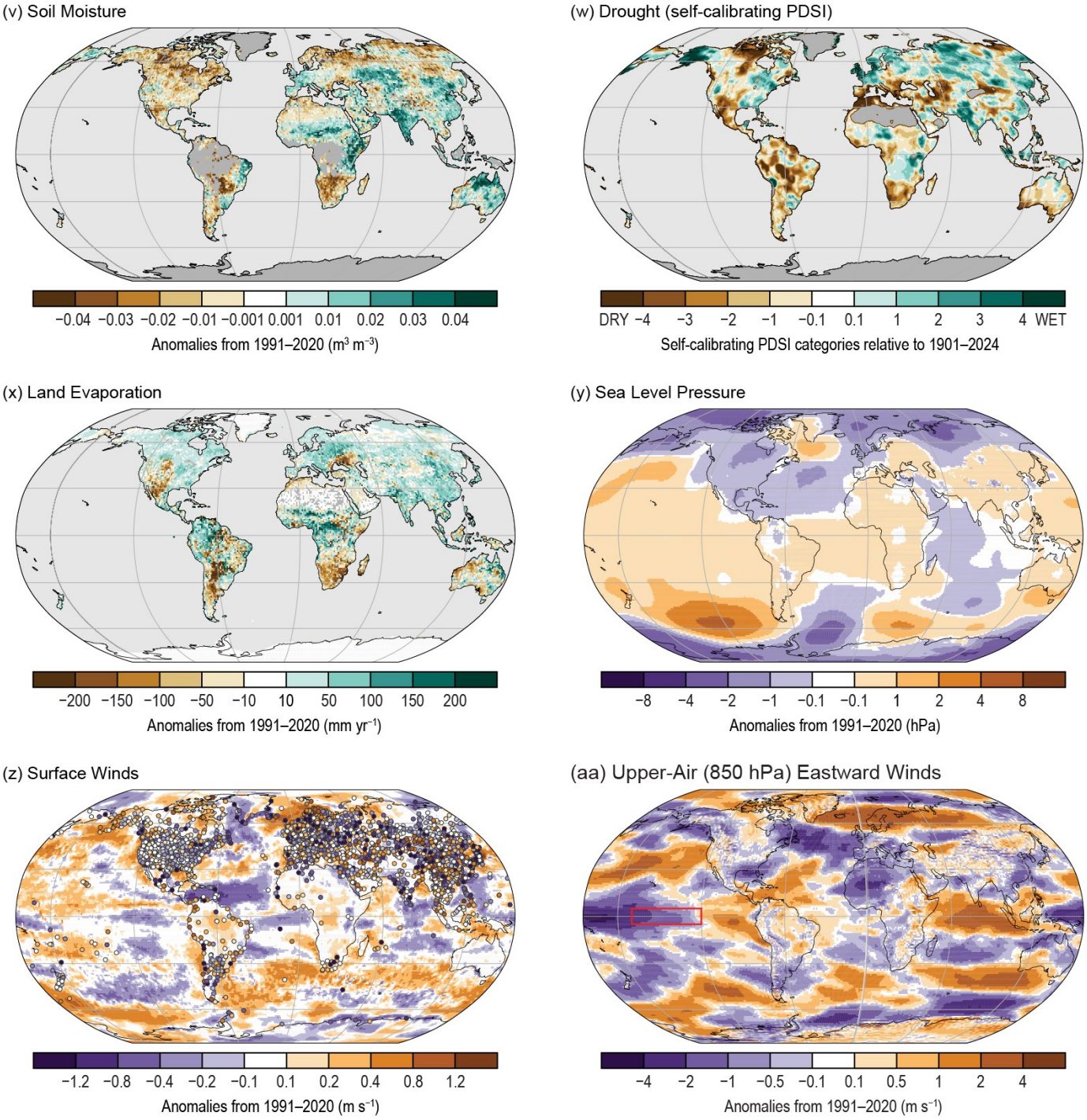

Plate 2.1 (cont.) (v) Copernicus Climate Change Service (C3S) average surface soil moisture anomalies ($m^3 m^{-3}$). Data are masked where no retrieval is possible or where the quality is not assured and flagged, for example due to dense vegetation, frozen soil, or radio frequency interference; (w) Mean self-calibrating Palmer Drought Severity Index (scPDSI). Droughts are indicated by negative values (brown), wet episodes by positive values (green). No calculation is made where a drought index is meaningless (gray areas: ice sheets or deserts with approximately zero mean precipitation); (x) Great Lakes Environmental Assessment and Mapping Project (GLEAM) land evaporation anomalies (mm yr^{-1}); (y) ERA5 mean sea level pressure anomalies (hPa); (z) Surface wind speed anomalies (m s^{-1}) from the observational HadISD3 dataset (land, circles), the ERA5 reanalysis output (land, shaded areas), and RSS satellite observations (ocean, shaded areas); (aa) ERA5 850-hPa eastward wind speed anomalies for Oct–Dec (m s^{-1}); (ab) Copernicus Atmosphere Monitoring Service (CAMS) reanalysis total aerosol optical depth (AOD) anomalies at 550 nm;

(ac) PM2.5

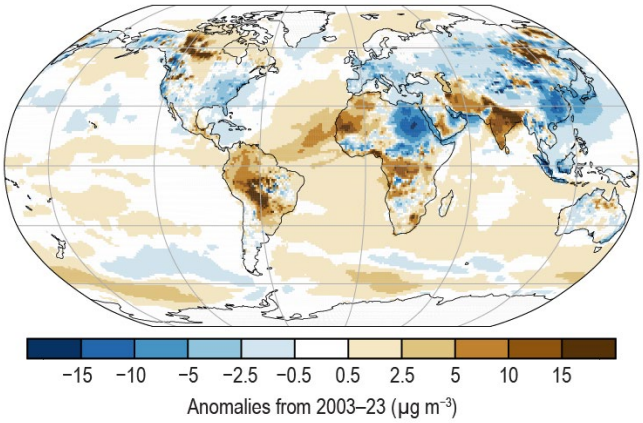

(ad) Extreme Aerosol Days

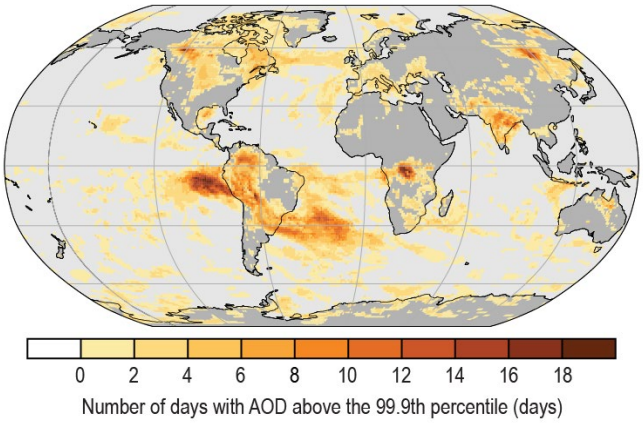

(ae) OMI/MLS Tropospheric Column Ozone

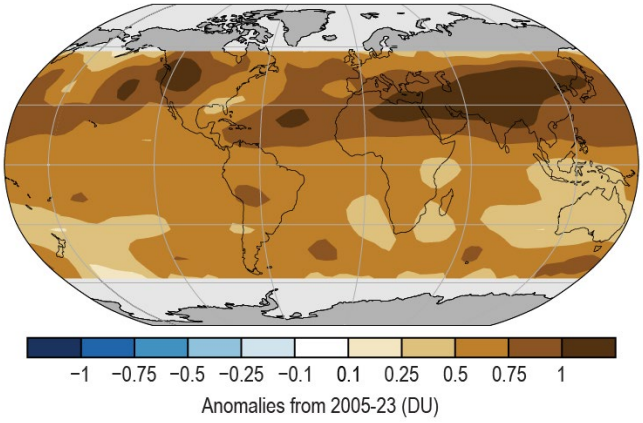

(af) Stratospheric (Total Column) Ozone

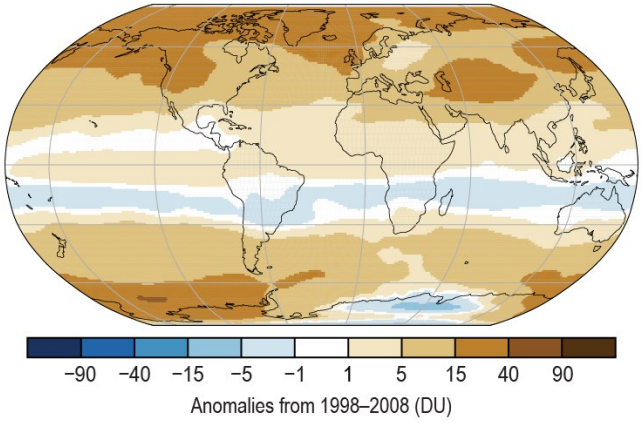

(ag) Carbon Monoxide

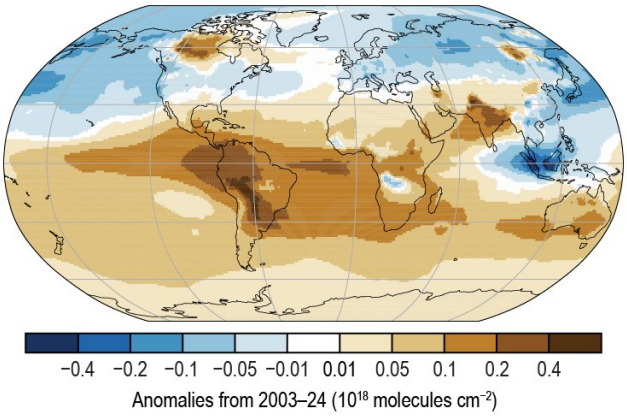

(ah) Visible Land Surface Albedo

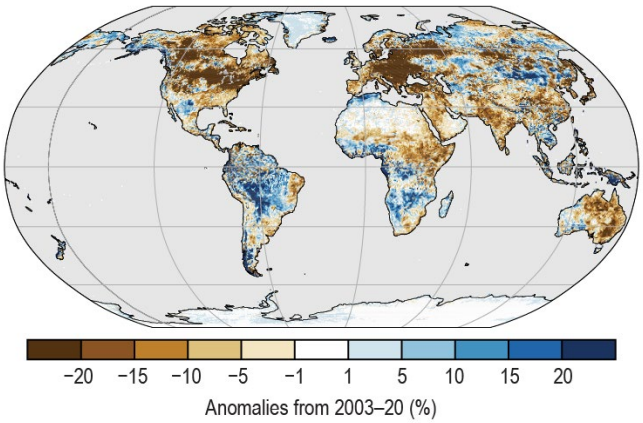

(ai) Near Infrared Land Surface Albedo

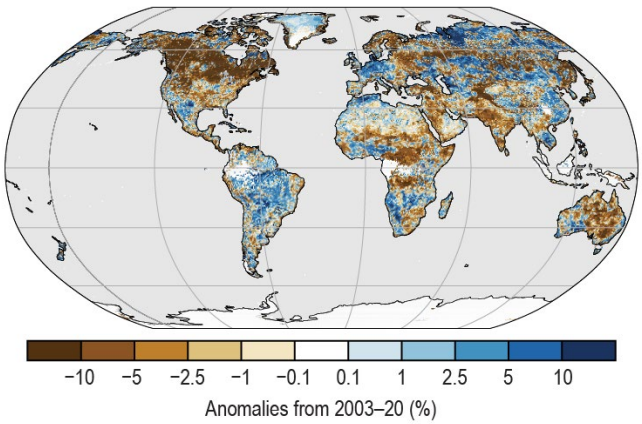

Plate 2.1 (cont.) (ac) CAMS reanalysis PM2.5 anomalies (μg m^{-3}); (ad) Number of days with AOD above the 99.9th percentile from CAMS reanalysis. Areas with zero days appear as the white/gray background; (ae) Ozone Monitoring Instrument (OMI)/Microwave Limb Sounder (MLS) tropospheric ozone column anomalies for 60°S–60°N (DU); (af) total column ozone anomalies determined from Tropospheric Monitoring Instrument (TROPOMI) aboard Sentinel-5 Precursor (S5P; DU); (ag) CAMS reanalysis total column carbon monoxide anomalies (× 10^{18} molecules cm^{-2}); (ah) Visible Infrared Imaging Radiometer Suite (VIIRS) land surface visible broadband albedo anomalies (%); (ai) VIIRS land surface near-infrared albedo anomalies (%);

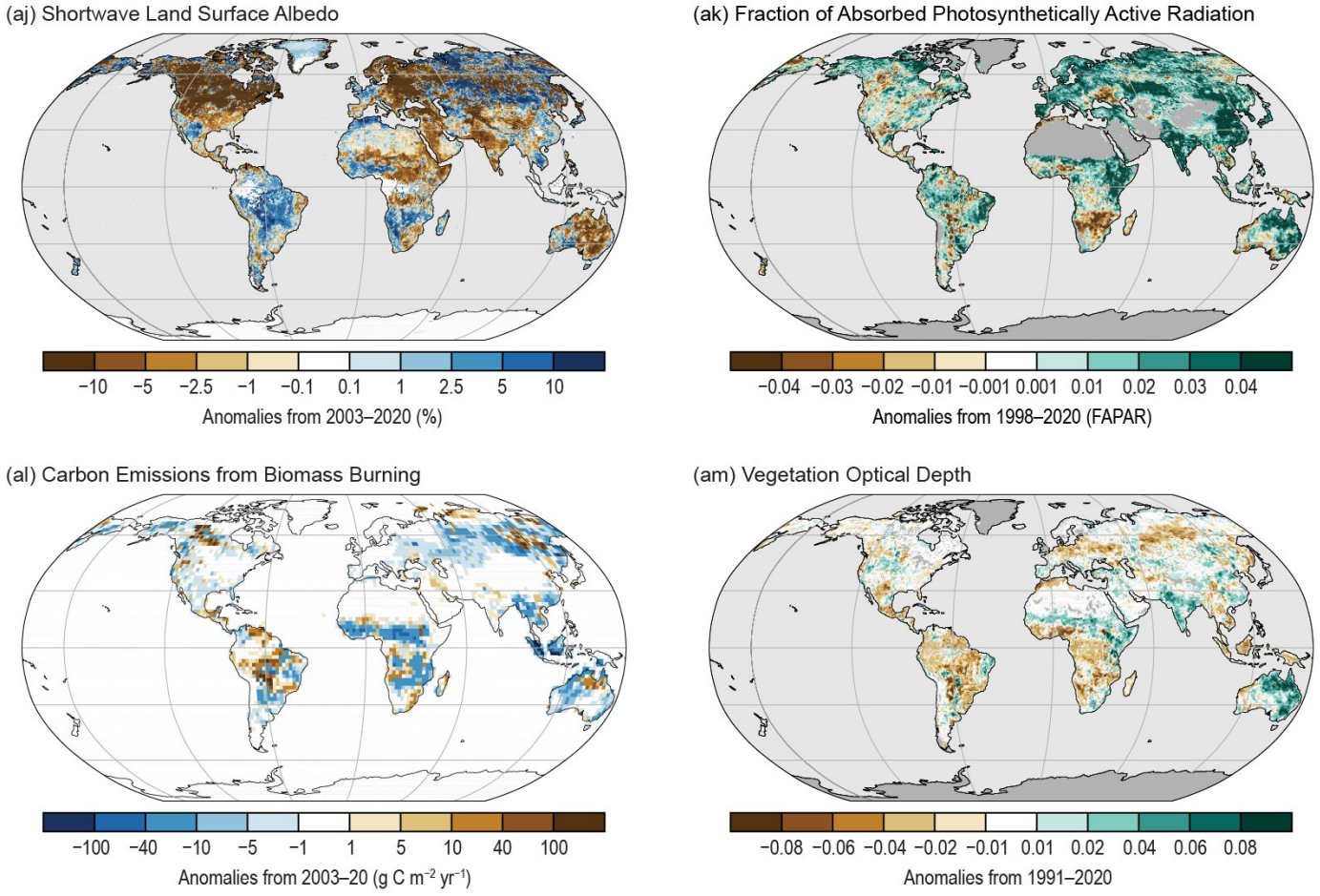

Plate 2.1 (cont.) (aj) VIIRS land surface shortwave broadband albedo anomalies (%); (ak) Fraction of absorbed photosynthetically active radiation (FAPAR) anomalies; (al) Global Fire Assimilation System version 1.4 (GFASv1.4) carbonaceous emission anomalies (g C m^{-2} yr^{-1}) from biomass burning; (am) Vegetation Optical Depth Climate Archive (VODCA) CXKu-band vegetation optical depth (VOD) anomalies.

b. Temperature

1. SURFACE TEMPERATURE

—A. Arguez, A. Bunno, A. Goto, C. Morice, J. P. Nicolas, A. Sánchez-Lugo, and F. Sezaki

For the second consecutive year, a new global surface temperature record was set. According to six global temperature datasets, the global surface temperature for 2024 was 0.63°C–0.72°C above the 1991–2020 average, (Table 2.1; Fig. 2.1). This was the highest value since global records began in the mid-1800s to mid-1900s, surpassing the previous warmest year on record set only last year (2023) by a margin of +0.08°C to +0.12°C.

According to all six global datasets, the last 10 years (2015–24) were the 10 warmest years on record. The datasets consist of four global in situ surface temperature analyses (GISTEMP, Lenssen et al. 2019; HadCRUT5, Morice et al. 2021; the NOAA Merged Land Ocean Global Surface Temperature Analysis [NOAAGlobalTemp], Vose et al. 2021; Berkeley Earth, Rhode and Hausfather 2020) and two global atmospheric reanalyses (ERA5, Hersbach et al. 2020, Soci et al. 2024; the Japanese Reanalysis for Three Quarters of a Century [JRA-3Q], Kosaka et al. 2024).

The global surface temperature for 2024 was also 1.46°C–1.62°C above the 1850–1900 average (a period commonly used to represent pre-industrial conditions). The pre-industrial temperature anomaly range was computed using the three datasets that extend back to 1850 (NOAAGlobalTemp, HadCRUT5, Berkeley Earth) using each dataset's own 1850–1900 baseline. Two of the three datasets indicated that the yearly temperature anomaly surpassed +1.5°C, the most ambitious limit set by the Paris Agreement (Paris Agreement 2015). Of note, exceeding +1.5°C in a single year does not represent a failure to achieve the Paris Agreement limit; this would require breaching +1.5°C over a longer period (WMO 2025a).

The global trends are within 0.20°C–0.22°C decade^{-1} for the short-term (1981–2024) and are within 0.08°C–0.09°C decade^{-1} for the long-term (1880–2024). Following the Arguez et al. (2020) approach, 2024 was 0.23°C–0.29°C above the value derived from the linear trend

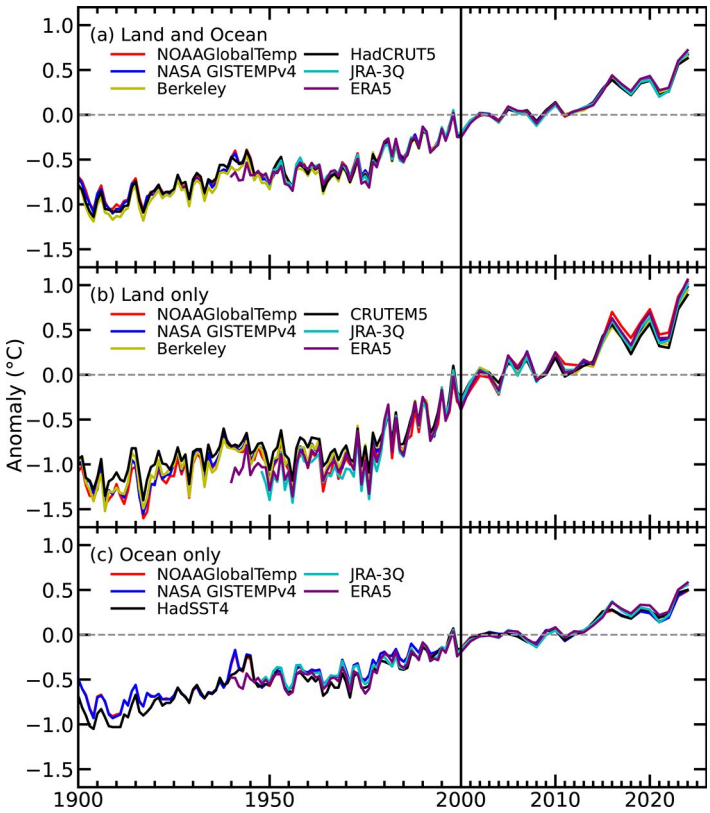

Fig. 2.1. Global average surface air temperature anomalies (°C; 1991–2020 base period). In situ estimates are shown from the NOAA Merged Land Ocean Global Surface Temperature Analysis (NOAAGlobalTemp; Vose et al. 2021), NASA Goddard Institute for Space Studies Surface Temperature Analysis version 4 (GISTEMPv4; Lenssen et al. 2019), Hadley Centre/Climatic Research Unit Temperature version 5 (HadCRUT5; Morice et al. 2021), Climatic Research Unit temperature version 5 (CRUTEM5; Osborn et al. 2021), Hadley Centre Sea Surface Temperature Dataset version 4 (HadSST4; Kennedy et al. 2019), and Berkeley Earth (Rhode and Hausfather 2020). Reanalysis estimates are shown from ERA5 (Hersbach et al. 2020; Bell et al. 2021) and the Japanese Reanalysis for Three Quarters of a Century (JRA-3Q; Kosaka et al. 2024).

Table 2.1. Global temperature anomalies (°C; 1991–2020 base period) for 2024. Note that for the HadCRUT5 column, land values were computed using the Climatic Research Unit Temperature version 5 (CRUTEM.5.0.2.0) dataset (Osborn et al. 2021), ocean values were computed using the Hadley Centre Sea Surface Temperature Dataset version 4 (HadSST.4.0.1.0) dataset (Kennedy et al. 2019), and global land and ocean values were computed using the HadCRUT.5.0.2.0 dataset (Morice et al. 2021).

Global	NASA-GISTEMPv4	HadCRUT5	NOAA GlobalTemp	Berkeley Earth	ERA5	JRA-3Q
Land	+0.98	+0.89	+1.04	+0.94	+1.06	+1.01
Ocean	+0.50	+0.50	+0.49	-	+0.58	+0.56
Land and Ocean	+0.67	+0.63	+0.67	+0.65	+0.72	+0.69

calculated over the last 50 years (1975–2024), registering the highest departures above the trend lines in all six global datasets.

The annual global land-only and ocean-only surface temperatures were also record high, at 0.89°C–1.06°C and 0.49°C–0.58°C above the 1991–2020 average, respectively (Table 2.1). The year was characterized by much-warmer-than-average conditions across most of the world's surface (Plate 2.1a; Appendix Figs. A2.1–A2.4), with record-high annual temperatures observed across parts of each continent and across large areas in the North and tropical Atlantic Ocean, North Indian Ocean, western Pacific Ocean, Arctic Ocean, and the Southern Ocean. In contrast, below-average annual temperatures were observed across Iceland, southern Greenland, the Bering Sea, the Okhotsk Sea, and parts of the eastern South Pacific, Southern Ocean, and Antarctica.

Monthly global surface temperatures were exceptionally high throughout the year, with each month ranking either as the warmest or the second-warmest on record. A strong El Niño event, which began during boreal summer 2023, continued into early 2024 before ending in boreal spring. The ensuing El Niño–Southern Oscillation (ENSO)-neutral conditions persisted through the remainder of the year until La Niña-like conditions emerged at the end of 2024. While several factors may have contributed to the record-high temperature in 2024, the influence of El Niño together with unusually warm oceans across many basins were key contributors to the high monthly global surface temperature records observed, especially during the first half of the year, adding warmth on top of the long-term warming caused by anthropogenic greenhouse gas emissions. The last time at least two consecutive years reached a new global surface temperature record was in 2015 and 2016, when a strong El Niño developed during the latter half of 2015 and dissipated by May 2016.

2. LAKE SURFACE TEMPERATURE

—L. Carrea, C. J. Merchant, R. I Woolway, J.-F. Creatux, T. M. Dokulil, H. Dugan, A. Laas, E. Leibensperger, S.-I. Matsuzaki, D. Pierson, M. Pulkkanen, O. O. Rusanovskaya, S. V. Shimaraeva, E. A. Silow, M. Schmid, M. A. Timofeyev, and P. Verburg

In 2024, the global average lake surface water temperature (LSWT) anomaly derived from satellite data during the warm season was +0.52°C with respect to the 1995–2020 baseline; the anomalies were positive for 79% and negative for 21% of the 1944 studied lakes. The 2024 anomaly is the largest since the record began in 1995. The mean LSWT trend during 1995 to 2024 was 0.22±0.01°C decade^{-1}, broadly consistent with previous analyses even though the number of lakes analyzed has doubled since 2022 (Woolway et al. 2017, 2018; Carrea et al. 2019, 2020, 2021, 2022a, 2023b, 2024; Fig. 2.2). The warm-season lake-mean LSWT anomalies for each lake are shown in Plate 2.1b.

In 2024, 56% of all observed lakes showed LSWT anomalies in excess of +0.5°C, and extensive regions with consistently large LSWT anomalies were detected. (Plate 2.1b). The largest positive anomalies were reported for lakes situated in Canada, China, Japan, the Tibetan area, eastern Europe, and the Middle East, while in Patagonia, Greenland, Alaska, and northeast Russia, lakes were found to be cooler than average.

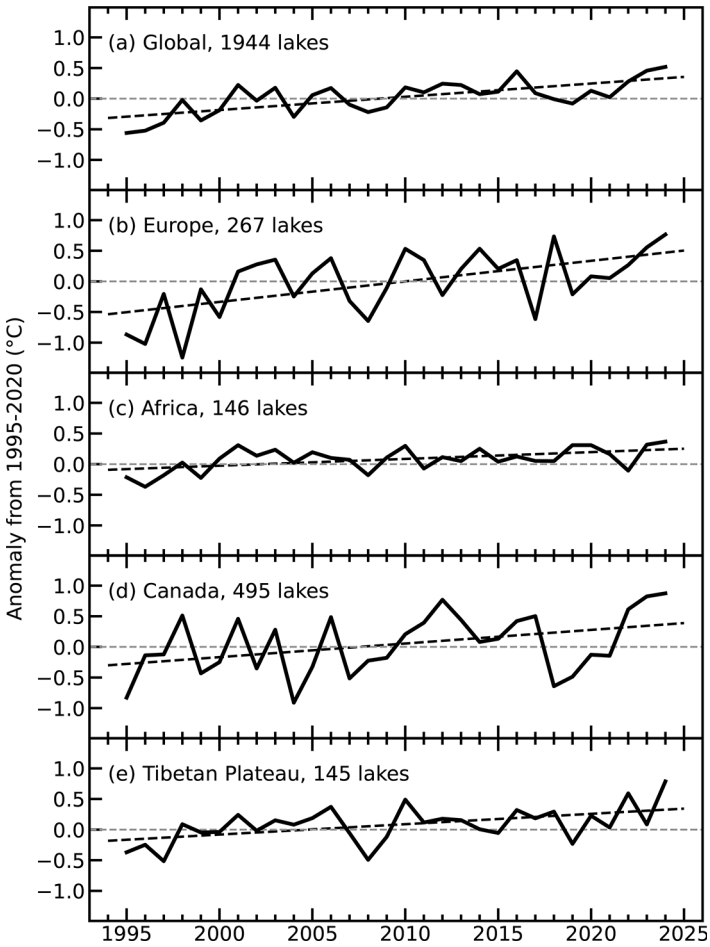

Fig. 2.2. Annual time series of satellite-derived warm-season lake surface water temperature anomalies (°C; 1995–2020 base period) from 1995 to 2024 for lakes distributed (a) globally, and regionally in (b) Europe, (c) Africa, (d) Canada, and (e) the Tibetan Plateau.

As in previous reports (see for example Carrea et al. 2023b, 2024), four regions were studied in more detail: Europe (number of lakes, n = 267, Figs. 2.2b, 2.3a), Africa (n =146, Figs. 2.2c, 2.3b), Tibet (n = 145, Figs. 2.2e, 2.3d), and Canada (n = 495, Figs. 2.2d, 2.3c). In these areas, the warm-season LSWT anomalies generally align with the air temperature anomalies extracted at the locations of the lakes from the dataset compiled by NASA's Goddard Institute for Space Studies (GISS; Hansen et al. 2010; GISTEMP Team 2025). The average LSWT trend was +0.34±0.03°C decade^{-1} in Europe (Fig. 2.2b) and +0.22±0.03°C decade^{-1} in Canada (Fig. 2.2d). In Canada, 96% of observed lakes were warmer than average, with only 4% being cooler than average, and the mean LSWT anomaly was +0.87°C in 2024. In Europe, the average anomaly was +0.77°C, and 86% of lakes presented positive anomalies. In Africa and Tibet, the long-term change in LSWT is comparatively smaller, at +0.11±0.01°C decade^{-1} and +0.17±0.02°C decade^{-1}, respectively (Figs. 2.2c,e). In Africa, 77% of the 146 lakes had positive LSWT anomalies, and the average anomaly in 2024 was +0.37°C. In Tibet, the average anomaly was +0.79°C, and the LSWT anomaly was positive for 143 lakes and negative for 2. In all these regions, the 2024 mean anomaly was the largest since the record began in 1995.

In situ single-point observations from 38 lakes were used to compute the warm-season temperature anomalies depicted in Fig. 2.4. Among these lakes, 27 have measurements for 2024, with an average anomaly of +1.25°C. Only three lakes experienced negative anomalies (average −0.59°C) and 24 lakes had positive anomalies (average +1.48°C) in 2024; Fig. 2.4 clearly shows that lakes are warming, especially after the year 2000. It is important to note that anomalies based on in situ measurements, which are point measurements, generally differ from those derived from satellite data, which instead represent lake-wide averages, and therefore are more representative of the lake response than single point. On the other hand, in situ measurements can offer high coverage in time while satellite data are sparser in time.

The period 1995–2020 is used as a baseline to compute the anomalies for both in situ (unless data were not available for the full period) and satellite temperature. The warm-season averages for midlatitude lakes were calculated

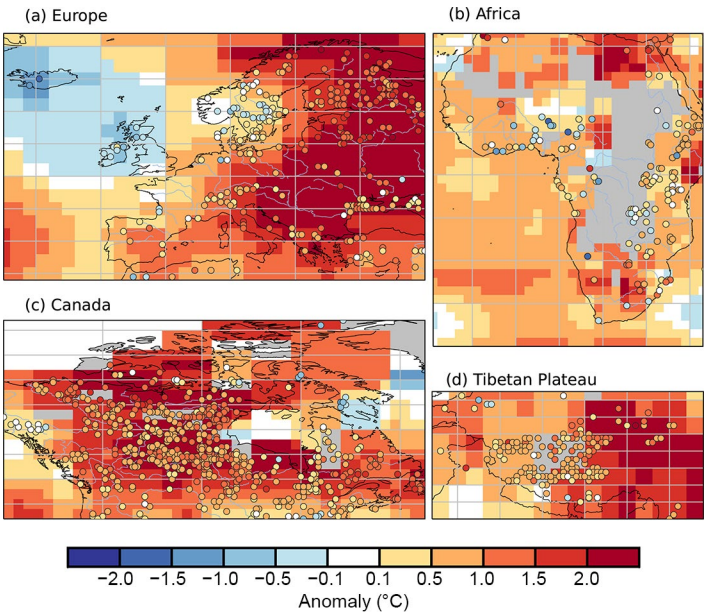

Fig. 2.3. Lake temperature anomalies (°C, colored dots) and 2-m air temperature anomalies (°C; NASA Goddard Institute for Space Studies [GISS]; Hansen et al. 2010, GISS Surface Temperature Analysis [GISTEMP] Team 2025) in 2024 for lakes in (a) Europe, (b) Africa, (c) Canada, and (d) the Tibetan Plateau. These values were calculated for the warm season (Jul–Sep in the extratropical Northern Hemisphere; Jan–Mar in the extratropical Southern Hemisphere; Jan–Dec in the tropics) with reference to the 1995–2020 base period.

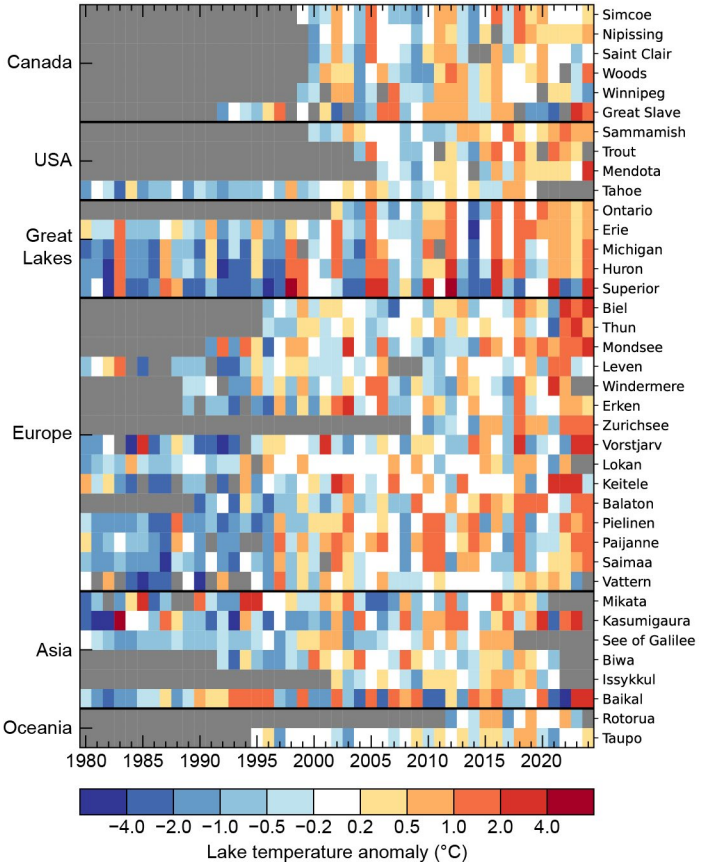

Fig. 2.4. In situ lake surface water temperature (LSWT) observations from 38 globally distributed lakes, showing the annually averaged warm season (Jul–Sep in the Northern Hemisphere; Jan–Mar in the Southern Hemisphere) anomalies (°C; 1995–2020 base period).

for the summer months (July–September in the Northern Hemisphere and January–March in the Southern Hemisphere), while annual averages are used for tropical lakes located within 23.5° of the equator. For global averages, an unweighted mean of all the lake LSWT anomalies was computed. LSWT time series were derived from the Copernicus Climate Change Service (until 2022) and the Earth Observation Climate Information Service climate data record (Carrea et al. 2022b, 2023a), which was based on the European Space Agency Climate Change Initiative LAKES v2.1 dataset and subsequently extended. For 2024, LSWT was retrieved from satellite observations from Sea and Land Surface Temperature Radiometers (SLSTR) onboard Sentinel3A and 3B. The retrieval method of MacCallum and Merchant (2012) was applied on image pixels filled with water according to both the inland water dataset of Carrea et al. (2015) and a reflectance-based water detection scheme (Carrea et al. 2023a).

The satellite-derived LSWT data were validated with in situ measurements with an average satellite minus in situ temperature difference of less than 0.5°C (Carrea et al. 2023a). The satellite-derived LSWT data were averaged spatially for each of a total of 1944 lakes, and lake-wide average surface temperatures have been shown to give a more representative picture of LSWT responses to climate change than single-point measurements (Woolway and Merchant 2018).

The averaged surface air temperature was calculated from the Global Historical Climatology Network version 4 (GHCNv4; 250-km smoothing radius) data of the NASA GISS surface temperature analysis (Hansen et al. 2010; GISTEMP Team 2025).

3. NIGHT MARINE AIR TEMPERATURE

—R. C. Cornes, R. Junod, and E. C. Kent

The global annual average night marine air temperature (NMAT) for 2024 was 0.44°C above the 1991–2020 baseline in the University of Alabama in Huntsville Night Marine Air Temperature (UAHNMAT; Junod and Christy 2020) dataset and 0.54°C in the Climate Linked Atlantic Sector Science Night Marine Air Temperature (CLASSnmat; Cornes et al. 2020) dataset. These values represent the highest in the record dating to 1900 and are 0.04°C higher than those of 2023 in both datasets.

Between 1900 and 2024, annual global average NMAT increased at a rate of 0.07°C decade^{-1} in UAHNMAT and 0.08°C decade^{-1} in CLASSnmat. As noted in previous *State of the Climate* reports (e.g., Cornes et al. 2023), sea surface temperatures (SSTs) have been increasing faster than NMAT for reasons that are not fully understood. For example, over the same 1900–2024 period, global annual averages in the Hadley Centre Sea Surface Temperature Dataset version 4 (HadSST4; Kennedy et al. 2019) increased at a rate of 0.09°C decade^{-1}. As a result, SST anomalies have consistently been higher than NMAT anomalies over the past decade (Fig. 2.5). The differences between SST and NMAT for individual years over that period have generally not been statistically significant due to the size

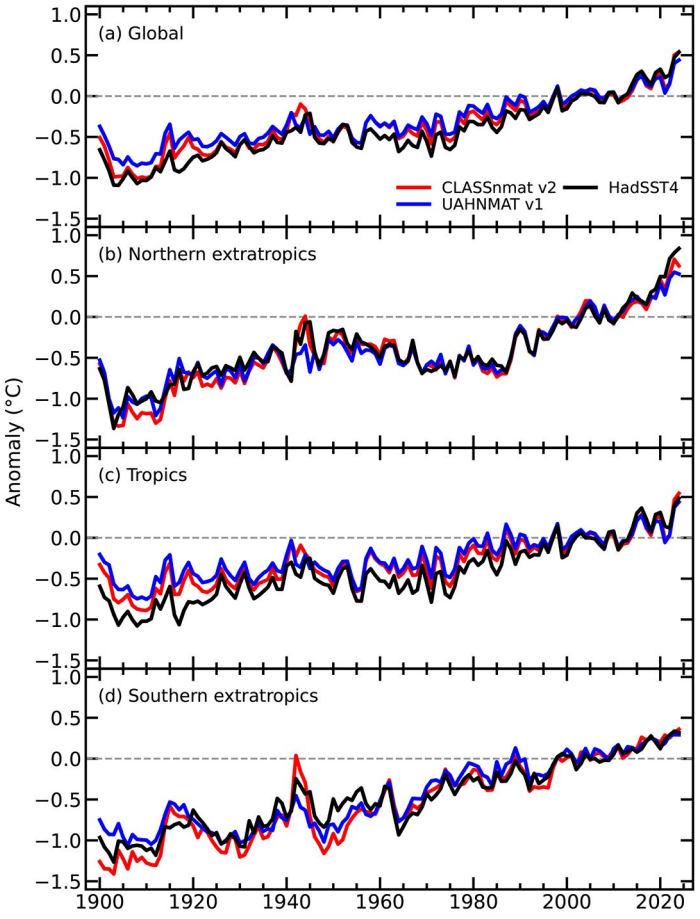

Fig. 2.5. Annual average night marine air temperature anomalies (°C; 1991–2020 base period) calculated from the Climate Linked Atlantic Sector Science Night Marine Air Temperature (CLASSnmat), University of Alabama in Huntsville Night Marine Air Temperature (UAHNMAT), and Hadley Centre Sea Surface Temperature Dataset version 4 (HadSST4) datasets averaged over the (a) globe, (b) northern extratropics, (c) tropics, and (d) southern extratropics. The tropics is defined as the latitude range 30°S–30°N and the northern (southern) extratropics as >30°N (<30°S). The averages only include values that are common to all three datasets for a given year; since UAHNMAT starts in 1900, only values for the period 1900–2024 are plotted.

of uncertainty estimates in the datasets (with 2-σ uncertainty around 0.1°C), although the large differences seen in 2021/22 have not been observed over the last two years.

Record temperatures were observed across the tropics in 2024, with anomalies of +0.54°C in CLASSnmat and +0.44°C in UAHNMAT. In the northern extratropics, however, NMAT values in 2024 were slightly lower than in 2023 (c.f. +0.71 in 2023 and +0.63°C in 2024 in CLASSnmat and +0.55 versus +0.53°C in UAHNMAT), making 2024 the second-warmest year in the record. In contrast, HadSST4 recorded 2024 as the warmest year in the northern extratropics, with an anomaly of +0.84°C. To prevent unequal spatial sampling affecting these results, all three datasets have been masked to ensure common coverage.

Regional differences in NMAT anomalies are further illustrated in Plate 2.1c. Temperature anomalies above +0.5°C were widespread across the globe in 2024, with especially large anomalies of up to +1.5°C relative to the 1991–2020 baseline observed across certain areas and notably across the northwestern Pacific. Negative temperature anomalies were present in the southeastern Pacific—and to a lesser extent, the northeastern Pacific—linked to the weakening El Niño conditions throughout 2024 and the switch to La Nina-like conditions at the end of the year (see section 4b for details). This change is reflected in the global monthly averages for NMAT and SST (Fig. 2.6). Starting in June 2023, exceptional temperature anomalies were recorded in these data (Cornes and Junod 2024) and continued into early 2024, with the highest anomalies peaking in January. While temperature anomalies slightly reduced in the second half of 2024 compared to 2023, they remained notably higher than previous years, with anomalies still 0.4°C above 1991–2020 levels.

The causes of these anomalously high temperatures in 2023 and 2024 have been variously discussed in the literature (see also section 2b1). Cattiaux et al. (2024) suggest that a combination of long-term anthropogenic warming and a significant peak in internal variability accounts for the observed conditions. Gettelman et al. (2024) propose that the anomalies in 2022/23 are due to an increase in net radiative forcing, driven by mandated reductions in ship-based sulfur emissions that came into effect in 2020. Further analysis is needed to understand the relative contributions of these factors to NMAT versus SST. However, based on the results presented here, no distinct difference is observed between NMAT and SST in terms of large-scale averages over the past two years. The fact that global and tropical average anomalies from CLASSnmat are now comparable to those from HadSST4 for the first time in 10 years may suggest an external forcing mechanism. However, the differences between UAHNMAT and CLASSnmat—despite using essentially the same input data, but undergoing different quality control and bias adjustment processes—are of the same magnitude as the differences between SST and NMAT. This suggests that structural uncertainties in dataset preparation may obscure any potential external forcing mechanisms.

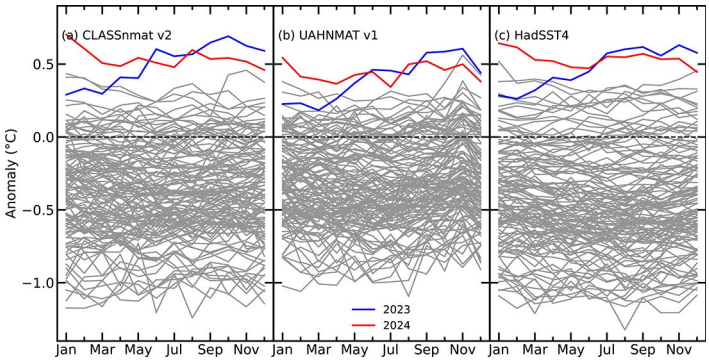

Fig. 2.6. Global monthly average night marine air temperature anomalies (°C; 1991–2020 base period) in the (a) Climate Linked Atlantic Sector Science Night Marine Air Temperature (CLASSnmat), (b) University of Alabama in Huntsville Night Marine Air Temperature (UAHNMAT), and (c) Hadley Centre Sea Surface Temperature Dataset version 4 (HadSST4) datasets. Each line represents a year of data, and the results for 2023 and 2024 are shown in blue and red, respectively.

4. SURFACE TEMPERATURE EXTREMES

—R. J. H. Dunn, M. G. Donat, S. Kirkpatrick, and M. G. Bosilovich

Ongoing record-breaking average global surface temperatures in 2024 (section 2b1) again was accompanied by further record-high numbers of warm days (TX90p; Table 2.2) and record-low numbers of cool nights (TN10p; Table 2.2) across all datasets assessed herein.

The globally averaged number of warm days indicated by the Global Historical Climatology Network Daily Extremes (GHCNDEX) dataset of gridded in situ observations (Donat et al. 2013) was 75±7 days, four days more than the value for 2023 (Fig. 2.7a; Table 2.2). At the other end of

the scale, there were only 13±8 cool nights, the lowest in this dataset (starting 1951; Fig. 2.7b) and substantially less than half the expected number (36.5 days by definition). As outlined in previous reports (e.g., Dunn et al. 2024a), GHCNDEX has severely limited spatial coverage for recent years (Appendix Fig. A2.5); thus three reanalysis products (ERA5, Hersbach et al. 2020, Bell et al. 2021, Soci et al. 2024; JRA-3Q, Kosada et al. 2024; MERRA-2, Gelaro et al. 2017) were used to give a globally complete (including Antarctica) assessment of the land surface extreme temperatures following Dunn et al. (2022b). As shown in Fig. 2.7c and Table 2.2, all these products show record-high and record-low values in 2024 for the number of warm days and cool nights, respectively, in the global average over land. The large differences between the GHCNDEX values in Table 2.2 and those from ERA5 and JRA-3Q using a 1961–90 reference period are likely due to the low spatial coverage of GHCNDEX (Appendix Fig. A2.5).

Especially high numbers of warm days were experienced across almost all of Africa and Central and South America as well as in northeastern Canada, eastern and southern Europe, and parts of the Middle East, China, and Southeast Asia. Some of these areas experienced twice as many warm days as would be expected on average within a year during the baseline period (Plate 2.1d). During 2024, many of these areas had the regionally highest number of warm days on record (Fig. 2.8a), often associated also with the highest absolute temperatures, particularly in parts of Central and South America and Africa (Fig. 2.8e). Moreover, areas in South America broke records in numbers of warm days (TX90p), which were only set last year (Fig. 2.8 in Dunn et al. 2024a).

Figure 2.8b shows the time series from calculating the land fraction setting record-high numbers of warm days sequentially in each year, i.e., the land area fraction in Fig. 2.8a categorized as “highest” but working through each year in turn to determine the area setting new records of TX90p per year. The first year will by default set a record value across the entire globe, but in a stable climate, records should become rarer over time. Therefore, the values from the first 20 years of each reanalysis are not shown. JRA-3Q has the largest land area experiencing record numbers of warm days in 2024, but a lower fraction than ERA5 which, along with MERRA-2, has the second largest (ERA5 has most in 2010 and MERRA-2 in 2002). For TN10p, in 2024 MERRA-2 has the largest area with new record-fewest numbers of cool nights, with JRA-3Q and ERA5 tied for second in 1998. The fraction of land with the highest annual maximum temperature (TXx; Fig. 2.8f; Table 2.2) is greatest in MERRA-2 and a close second to 1983 in JRA-3Q.

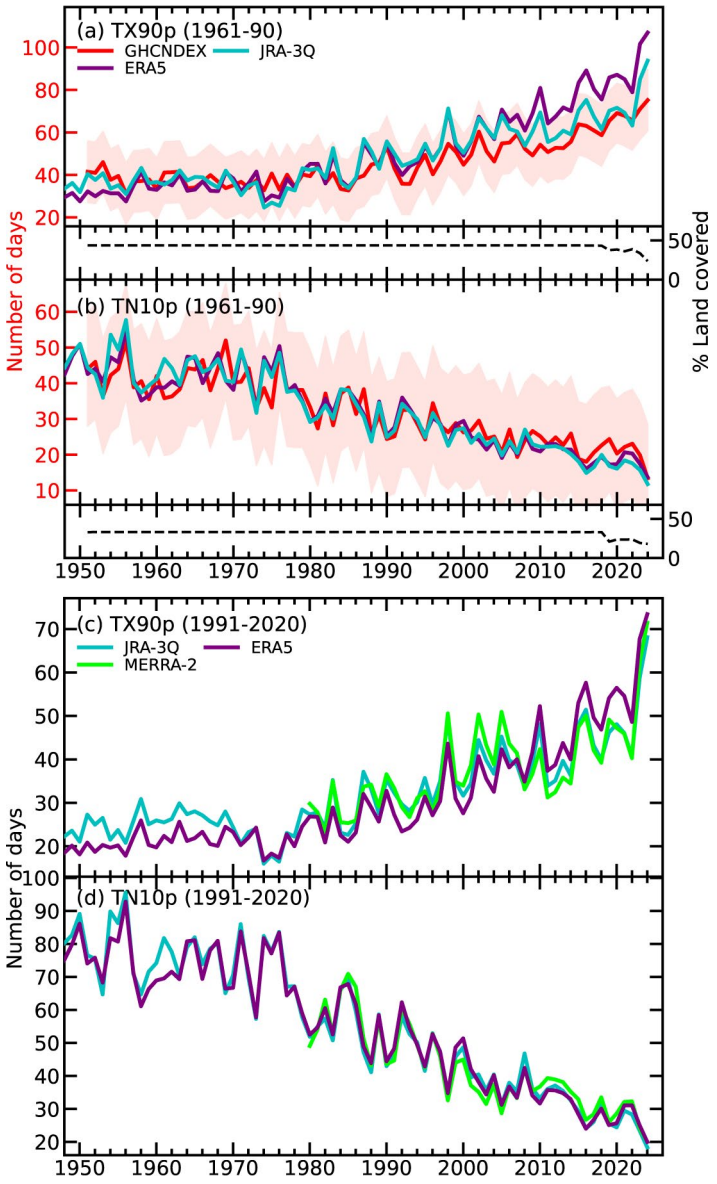

Fig. 2.7. (a),(b) Time series of the (a) annual number of warm days (TX90p) and (b) cool nights (TN10p) averaged over global land regions based on gridded station data from Global Historical Climatology Network Daily Extremes dataset (GHCNDEX), ERA5, and the Japanese Reanalysis for Three Quarters of a Century (JRA-3Q) reanalyses using 1961–90 as the reference period. The spatial coverage in GHCNDEX is limited; the black dashed lines show the percentage of land area covered (right y-axis). The 2-σ coverage uncertainty (following Brohan et al. 2006; Dunn et al. 2020) is shown by the light red bands in (a),(b). (c),(d) As in (a),(b), for three atmospheric reanalyses (ERA5, MERRA-2, and JRA-3Q) using 1991–2020 as the reference period.

Lower-than-expected numbers (36.5) of cool nights (TN10p) were found almost globally, with only parts of the Amazon basin and central-southern Africa experiencing higher-than-expected numbers (Plate 2.1e). This index is zero bounded (there cannot be fewer than zero cool nights, an anomaly of –36.5 days), in contrast to TX90p, which is bounded to zero for cold anomalies but asymmetrically bounded to 100% of days (i.e., 365 per year) for warm anomalies; with our choice of reference period in the current climate, we are far from this upper bound. Therefore, the magnitude of the anomalies in TN10p appear smaller as this index asymptotically reduces to zero as the temperature distribution moves farther from the 10% threshold (Dunn and Morice 2022).

Regionally, the record-lowest numbers of cool nights (TN10p) were found across much of tropical and northern Africa, Southeast Asia, eastern Europe, and northern South America (Fig. 2.8c), and the global area with record-low values is largest (in MERRA-2) or second largest (in ERA5 and JRA-3Q, both record in 1998) within the periods of the respective datasets (Fig. 2.8d).

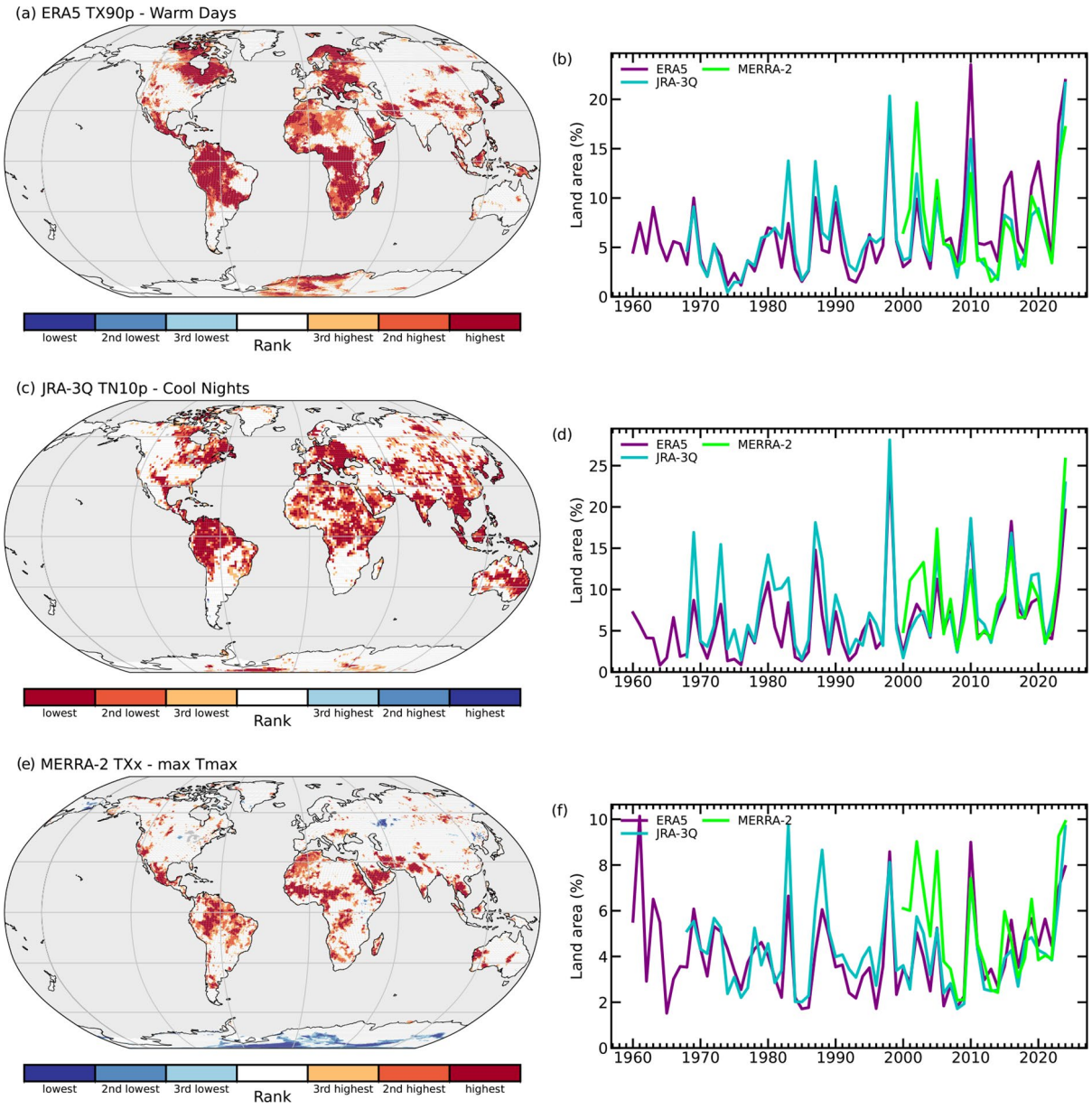

Fig. 2.8. Maps indicating grid cells where (a) the warm day index (TX90p) from ERA5 (since 1940), (c) the cool night index (TN10p) from the Japanese Reanalysis for Three Quarters of a Century (JRA-3Q; since 1948), and (e) the annual maximum temperature (TXx) from MERRA-2 (since 1980) for 2024 ranked in the three highest (orange to red) or three lowest (blue) values. Time series of the percent of land area ranked as the highest value for (b) TX90p, (d) TN10p, and (f) TXx sequentially in each year for ERA5 (from 1960), JRA-3Q (from 1968), and MERRA-2 (from 2000). The ranks from the first 20 years of each reanalysis are not calculated.

A number of indices have been recommended by the World Meteorological Organization to characterize temperature and precipitation extremes (Zhang et al. 2011; Dunn et al. 2024b), of which we present three here (Table 2.2). Dunn et al. (2022b) show there is good agreement between the observation-based and reanalysis products, especially for the two percentile-based indices used in this section. See Donat et al. (2013) and Dunn et al. (2022b) for details of indices from the observation-based and reanalyses datasets, respectively.

The indices shown here use fixed reference periods, and an intercomparison between these is not trivial (Dunn et al. 2020; Yosef et al. 2021; Dunn and Morice 2022); we show versions using both 1961–90 (for GHCNDEX, ERA5, and JRA-3Q) and 1991–2020 (for ERA5, MERRA-2, and JRA-3Q).

Table 2.2. Definitions of indices used for land surface temperature extremes, their globally averaged values (days) for 2024, and ranks from the four datasets. Coverage uncertainties are shown for GHCNDEX.

Index	Name	Definition	GHCNDEX (1951–2024) Value, [rank] Ref. Period 1961–90	ERA5 (1940–2024) Value, [rank] Ref. Period 1961–90	JRA-3Q (1948–2024) Value, [rank] Ref. Period 1961–90	ERA5 (1940–2024) Value, [rank] Ref. Period 1991–2020	JRA-3Q (1948–2024) Value, [rank] Ref. Period 1991–2020	MERRA-2 (1980–2024) Value, [rank] Ref. Period 1991–2020
TX90p	Warm days	Annual count of days when the daily maximum temperature exceeds the 90th percentile	75±7 [highest]	107 [highest]	94 [highest]	73 [highest]	68 [highest]	72 [highest]
TN10p	Cool nights	Annual count of nights when the daily minimum temperature falls below the 10th percentile	13±8 [lowest]	13 [lowest]	12 [lowest]	20 [lowest]	18 [lowest]	20 [lowest]
TXx	Warmest T-max	Annual maximum of the maximum temperature	36.5±0.3 [highest]	-	-	31.1 [highest]	30.6 [highest]	31.7 [highest]

Sidebar 2.1: **Super extreme land surface temperature hotspots**

—E. GOOD, J. BLANNIN, A. WARING, K. VEAL, AND D. GHENT

It is well documented that as Earth's climate warms, the frequency of extreme heat events is increasing (IPCC 2021; Dunn 2024a; Willett 2023b). Evidence suggests that the fraction of land becoming uninhabitable due to extreme heat will also increase with global warming (Matthews et al. 2025). Surface temperatures are traditionally monitored using data from weather stations measuring near-surface air temperature at ~1.5m–2m above the surface (T2m). However, station density and location limit spatial coverage and, therefore, knowledge of how extreme temperature frequency and intensity are evolving in many regions of the world (section 2b4; Dunn et al. 2024).

An alternative, independent source of information can be obtained from satellite observations of land surface temperature (LST) derived from sensors operating in the infrared (IR) and microwave regions of the electromagnetic spectrum. An advantage of using LST from satellites over ground-based T2m is in the global provision of data. However, a disadvantage is that the LST cannot be measured directly, as it relies on modeling of the impact of the atmosphere between the satellite and the surface to estimate it; furthermore, in the case of IR LSTs, only cloud-free observations are available. Additionally, although strongly correlated, LST and T2m are different variables. Over bare surfaces, LST represents how hot Earth's surface is to the touch, whereas over dense vegetation, it more closely represents the canopy surface temperature. Therefore, simultaneous LST–T2m differences often reach several °C and may exceed 20°C in some conditions (Good 2016). However, studies have shown that the long-term signal of change observed in LST and T2m datasets is similar

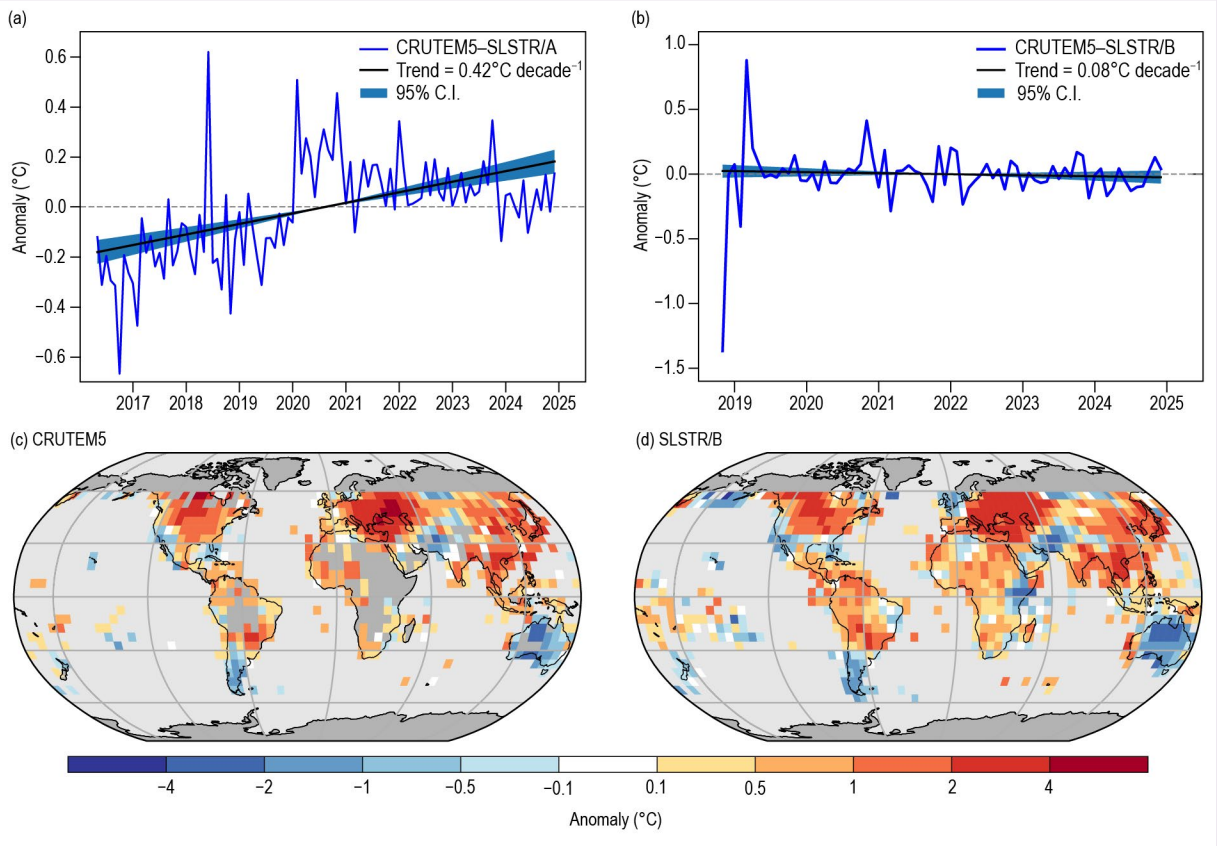

Fig. SB2.1. Time series for spatially matched 5° latitude–longitude data between ±60° latitude for (a) Sea and Land Surface Temperature Radiometer onboard the Sentinel-3A platform (SLSTR/A) land surface temperature (LST)-Climatic Research Unit temperature version 5 (CRUTEM5) anomalies of near-surface air temperature at ~1.5m–2m above the surface (T2m; reference baseline period is May 2016 to Dec 2024; the CRUTEM5 anomalies have been adjusted from the 1961–90 baseline period following Good et al. [2017]) and (b) Sea and Land Surface Temperature Radiometer onboard the Sentinel-3B platform (SLSTR/B) LST-CRUTEM5 T2m anomalies (baseline period Nov 2018 to Dec 2024). Trends have been calculated using the Theil-Sen/median of pairwise slopes method (Sen 1968). The Mar 2019 outlier in the SLSTR/B time series is due to 19 days of missing SLSTR/B data. The Nov 2018 outlier is outside the super extreme hotspot analysis period. Example 5° latitude–longitude anomaly maps for April 2024 for (c) SLSTR/B LST and (d) CRUTEM5 are also shown. All units are °C.

(Good et al. 2017, 2022). The objective of this analysis is to demonstrate how LST may be used to map and monitor super extreme hotspots (SEHs)—where Earth may already be, or is becoming, uninhabitable under climate change. Using LST is advantageous as many of these SEHs occur in regions with few T2m observations.

The data used are from the Sea and Land Surface Temperature Radiometer onboard the Sentinel-3B platform (SLSTR/B), which has been in polar orbit since April 2018. LST data for November 2018 to December 2024 have been obtained from the European Space Agency (ESA) Climate Change Initiative for LST (LST_cci; https://climate.esa.int/en/projects/land-surface-temperature/; version 4.00) and, for recent months in 2024, from the U.K. Earth Observation Climate Information Service (https://eocis.org/). The data from both sources are consistent and have been processed using the same approach (Ghent et al. 2024). The SLSTR/B instrument images Earth at ~1-km spatial resolution, providing a near-global view each day. However, as the SLSTR/B operates in the IR, only cloud-free LSTs are available. This dataset was selected as it is the only climate-quality LST dataset currently available for 2024. The widely-used LSTs from the Moderate Resolution Imaging Spectroradiometer (MODIS) sensors (2000–present) cannot be used, as these data are temporally unstable from around 2021 due to a changing observation time (https://modis-land.gsfc.nasa.gov/news.html). Similarly, data from the SLSTR onboard Sentinel-3A (SLSTR/A: 2016–24) cannot be used, as this dataset is unstable due to a variation in the processing by the ESA of the raw satellite data time series. Establishing temporal stability of LST datasets is crucial due to its often strong diurnal variation (Good 2016); a changing overpass time or any other non-climatic discontinuity in the dataset can have a critical effect on time series analysis.

Following the approach used by Good et al. (2017, 2022), the stability of SLSTR/A and /B between ±60° latitude is assessed using Climatic Research Unit temperature version 5 (CRUTEM5; Osborn et al. 2021). CRUTEM5 is a monthly 5° latitude–longitude T2m dataset based on homogenized global station data and provides a stable reference for assessing LST stability. There is a statistically significant slope in the mean daily SLSTR/A-minus-CRUTEM5 anomaly time series (Fig. SB2.1a, 0.42°C decade^{-1}; 95% confidence interval [CI] 0.31°C decade^{-1} to 0.54°C decade^{-1}) as well as a non-climatic discontinuity. By contrast, the SLSTR/B dataset (Fig. SB2.1b) appears stable (–0.08°C decade^{-1}; 95% CI –0.24°C decade^{-1} to 0.09°C decade^{-1}) and the monthly SLSTR/B and CRUTEM5 anomalies are similar and well correlated (Pearson correlation coefficient r = 0.81). Also shown in Figs. SB2.1c,d are examples of the SLSTR/B and CRUTEM5 anomaly maps for April 2024. The spatial pattern of the anomalies shows a high degree of spatial consistency (r = 0.84), confirming the overall similarity between the clear-sky LST and all-sky T2m signals and the more complete spatial coverage of the LST data.

With the stability of the SLSTR/B LSTs assured, the occurrence and temporal evolution of SEHs can be characterized. For context, Fig. SB2.2 shows the maximum SLSTR/B LST observed during 2024. The hottest regions occur in western North America, North Africa, the Arabian Peninsula, parts of South and Central Asia, and Australia, where LSTs of >60°C can occur. Using only full-year daytime data between 2019 and 2024, thresholds of 50°C and 55°C are used to identify SEHs; for context, 55°C is above the 99th percentile for the 2019–24 SLSTR-B data (53.2°C), thus these are globally extreme LSTs. Fig. SB2.3a shows the locations of SEHs in 2024; together with exceedances of other LST thresholds, SEHs are prevalent in the Arabian peninsula, Iran (Lut desert), across central Asia, parts of North Africa, western North America, and Australia, which is generally consistent with Mildrexler et al. (2006) and Zhao et al. (2021), who used MODIS to map global LST hotspots. Figure SB2.3b shows the annual time series of the number of SEH locations. Figure SB2.3c shows the fraction of valid observations across all grid cells exceeding each threshold, essentially representing the accumulated global frequency of SEHs each year. Both time series have small negative trends, although the p values indicate these are statistically insignificant. This is not surprising given the relatively short six-year period of data compared to the 30+ year record often used for climate applications. For all SEH metrics, 2019 is ranked as the most extreme year, followed by 2023, while

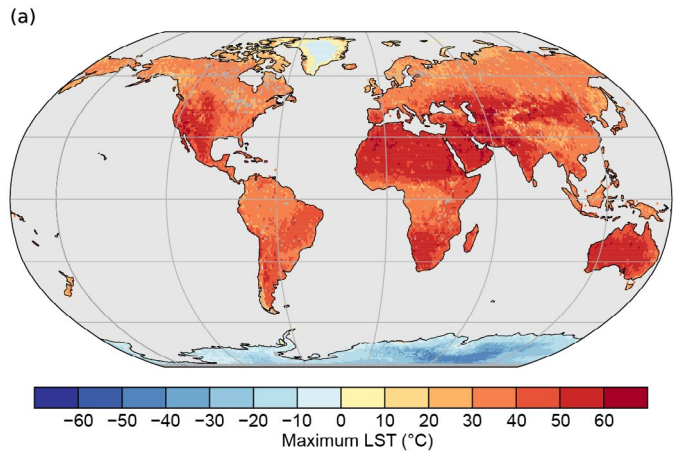

Fig. SB2.2. Maximum land surface temperature (LST; °C) observed during 2024 by the Sea and Land Surface Temperature Radiometer onboard the Sentinel-3B platform (SLSTR/B) at 0.1° latitude–longitude. The percentiles from the 2024 distribution of maximum LSTs at the native 0.01° spatial resolution are: 50.5°C (95th), 57.7°C (99th), and 62.3°C (99.9th). The hottest LSTs above ~62°C often occur in isolated grid cells and are associated with lava flows or wildfires.

2024 is third for both 50°C metrics and fourth for both 55°C metrics (i.e., both for the number of locations and total fraction per year). With a longer stable LST time series, this analysis demonstrates how LST could be used to monitor global heat extremes and the occurrence of SEHs, which may not be observable using T2m data.

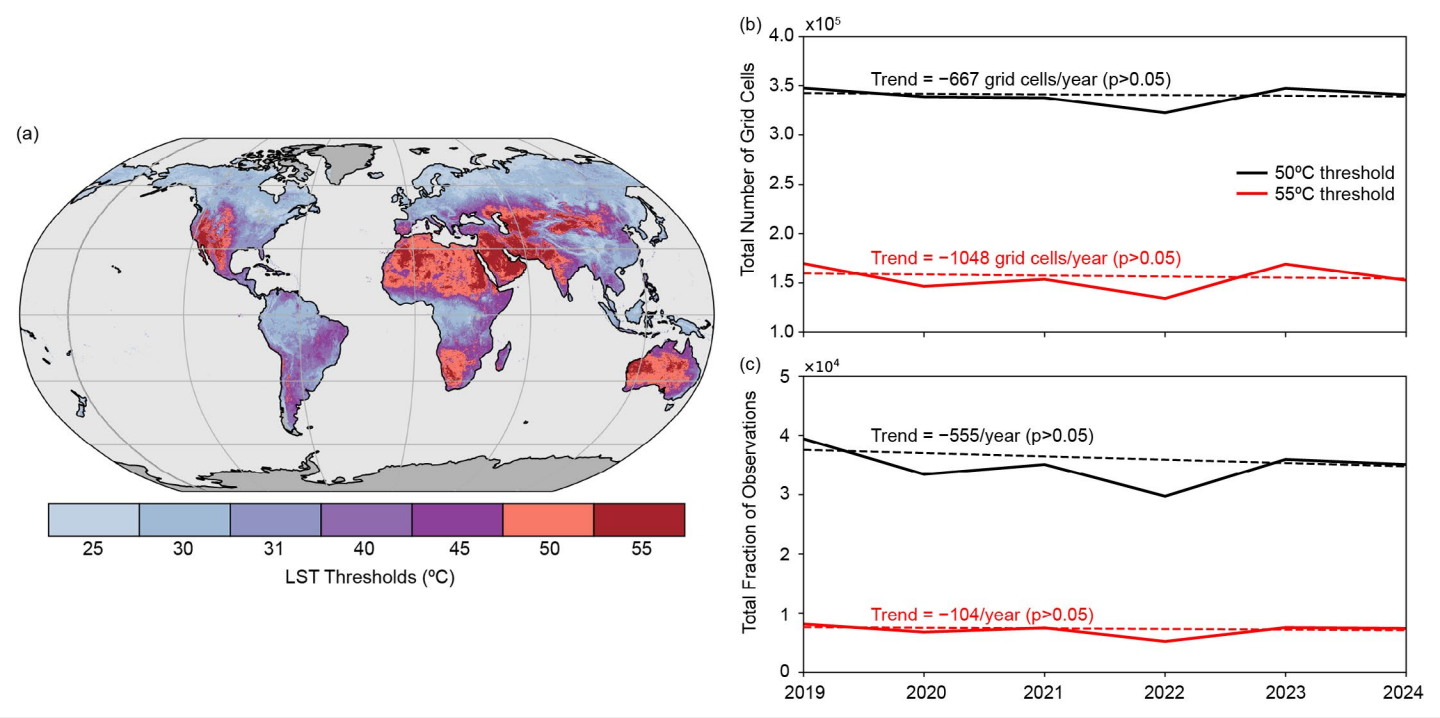

Fig. SB2.3. (a) Map showing where two or more valid Sea and Land Surface Temperature Radiometer onboard the Sentinel-3B platform (SLSTR/B) land surface temperature (LST) observations in 2024 exceed selected LST thresholds (25°C, 30°C, 35°C, 40°C, 45°C, 50°C, and 55°C); the SLSTR/B data have been resampled to 0.1° latitude–longitude. The time series of the number of (b) 0.1° grid cells for each year that exceed the 50°C (black) and 55°C (red) thresholds and (c) sum of the annual fraction of valid observations in each year that exceed these thresholds across all grid cells. The linear trends and p values are shown for information.

5. TROPOSPHERIC TEMPERATURE

—S. Po-Chedley, J. R. Christy, C.-Z. Zou, C. Mears, and L. Haimberger

Record-high global lower tropospheric temperature (LTT) values in the second half of 2023 persisted through boreal summer in 2024 (Fig. 2.9), producing a 2024 global-mean LTT that was 0.84°C (0.77°C–0.92°C depending on dataset) above the 1991–2020 climatological mean (Fig. 2.10). All nine tropospheric temperature datasets considered here (Table 2.3) ranked 2024 as the warmest year for global LTT, making 2023 the second-warmest year in most datasets.

Some of the recent tropospheric warmth is attributable to the strong El Niño event that peaked in the boreal winter of 2023/24. During El Niño events, tropical and global tropospheric temperatures lag behind warm central and eastern Pacific sea surface temperatures by three to five months, which helps to explain the exceptional warmth in the first half of 2024 (Fig. 2.10). Although the ENSO relaxed to neutral conditions by April–June and approached La Niña conditions by the end of the year (see section 4b for details), global LTT remained close to the record-breaking warmth in the final months of 2024 (Fig. 2.9). Most of the tropics and roughly half of Earth overall experienced record-warm LTT conditions in 2024 (Plate 2.1f).

Although the warmth seen over 2023/24 was above normal, it is consistent with long-term, greenhouse gas-driven warming that is evident in both global LTT and tropical tropospheric temperatures (TTTs) across a variety of tropospheric temperature datasets (Table 2.3); this is the fourth time in the last 10 years that record-warm global tropospheric temperatures have been reported in the *State of the Climate* (Po-Chedley et al. 2024, 2021; Christy 2017). Tropospheric temperature time series are derived from sparse weather balloon-based radiosonde records that measure temperatures as a function of height, satellite-borne microwave measurements that provide near-global observations over broad atmospheric layers, and reanalysis models that ingest and combine many observations to produce horizontally and vertically resolved estimates and forecasts of numerous

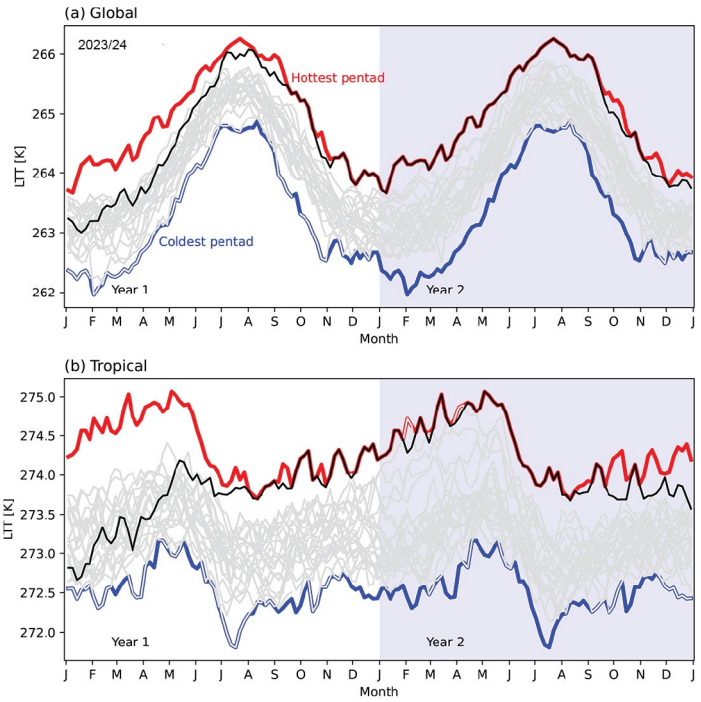

Fig. 2.9. (a) Global and (b) tropical (20°S–20°N) lower-tropospheric temperature (LTT) pentad averages over two-year segments (gray lines) from the University of Alabama in Huntsville (UAH) dataset. Each year is shown only once: odd (even) years are on the left (right) side of the figure. The most recent segment (2023/24) is shown in black and the hottest and coldest pentad values (of all years) are shown in red and blue, respectively.

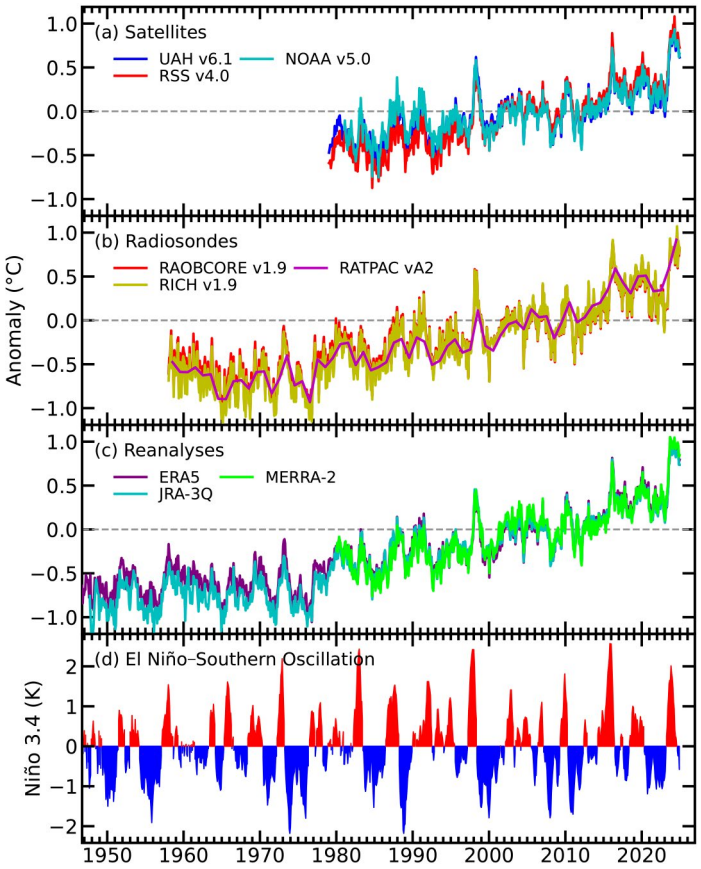

Fig. 2.10. Monthly average global lower-tropospheric temperature (LTT) anomalies for (a) satellite, (b) radiosonde, and (c) reanalysis datasets. In panel (d), red (blue) denotes positive (negative) values in the Niño-3.4 index. Annual averages are displayed for the Radiosonde Atmospheric Temperature Products for Assessing Climate (RATPAC)-A dataset. Anomalies are with respect to a 1991–2020 base period.

geophysical variables, including atmospheric temperature. In this report, the vertically resolved atmospheric temperature data from radiosondes and reanalyses are converted into a satellite-equivalent LTT time series, which represents the average temperature over a layer from the surface to ~10 km, and a TTT time series, which spans the surface to the tropical tropopause. Despite diversity in measurement methods and calibration procedures, all of the datasets exhibit similar variability and long-term trends (Fig. 2.10; Table 2.3).

The annual-mean tropospheric temperature was above the 1991–2020 climatological mean over more than 90% of Earth's surface (Plate 2.1f). Record-setting values covered about half of Earth's surface, including the deep tropics (20°S–20°N), Europe, eastern Canada, East Asia, and parts of the Southern Ocean. Below-average tropospheric temperatures were observed over less than 5% of Earth's surface (Plate 2.1f).

The recent surge in global temperatures in the past two years deserves continued scrutiny. While the contributions of internal variability and greenhouse gas-driven warming are key components of the record LTT values over 2023 and 2024, other factors including the solar cycle, reductions in ship-based aerosol emissions, and multi-year trends in planetary albedo have also likely played a role (e.g., Raghuraman et al. 2024; Goessling et al. 2025; Gettelman et al. 2024). The evolution of the global climate beyond 2024 will be of significant scientific interest as we strive to better understand the factors that contributed to the recent exceptional tropospheric warmth.

Table 2.3. Temperature trends (°C decade^{-1}) for global lower-tropospheric temperature (LTT) and tropical (20°S–20°N) tropospheric temperature (TTT) over the periods 1958–2024 and 1979–2024. NASA MERRA-2 data begin in 1980 and NOAA v5.0 LTT begins in 1981. Cells marked with a dash signify that the data do not extend back to 1958.

Method	Dataset	LTT (90°S–90°N) 1958	LTT (90°S–90°N) 1979	TTT (20°S–20°N) 1958	TTT (20°S–20°N) 1979
Radiosonde	NOAA RATPAC vA2 (Free et al. 2005)	0.19	0.24	0.18	0.20
Radiosonde	RAOBCORE v1.9 (Haimberger et al. 2012)	0.17	0.19	0.15	0.17
Radiosonde	RICH v1.9 (Haimberger et al. 2012)	0.19	0.21	0.19	0.21
Satellite	UAH v6.1 (Spencer et al. 2017)	-	0.15[1]	-	0.15
Satellite	RSS v4.0 (Mears and Wentz, 2016)	-	0.23	-	0.19
Satellite	NOAA v5.0 (Zou et al. 2023)	-	0.15[1]	-	0.13
Reanalysis	ERA5 (Hersbach et al. 2020)	0.17	0.20	0.17	0.19
Reanalysis	JRA-3Q (Kosaka et al. 2024)	0.19	0.20	0.19	0.18
Reanalysis	NASA MERRA-2 (Gelaro et al. 2017)	-	0.21	-	0.21
Median	N/A	0.19	0.20	0.18	0.19

[1] The vertical sampling in UAH and NOAA LTT is slightly different from other datasets and results in temperature trends that are approximately 0.01°C decade^{-1} smaller than in other datasets.

6. STRATOSPHERIC TEMPERATURE

—W. J. Randel, C. Covey, L. Polvani, and A. K. Steiner

Global-mean temperatures in the lower, middle, and upper stratosphere increased slightly during 2024, mainly reflecting a recovery from anomalous cooling due to the Hunga volcanic eruption in early 2022. The long-term trends during the satellite era of 1979–2024, however, show multi-decadal cooling of the stratosphere due to ozone depletion in the first two decades as well as anthropogenic CO_2 increases over the whole period. The Arctic stratospheric polar vortex was disturbed by two major stratospheric warming events during early 2024, while the Antarctic polar vortex was strong and persistent during the year. The stratospheric quasi-biennial oscillation (QBO) progressed normally in 2024, with equatorial westerly zonal wind shears and positive temperature anomalies descending from the middle to lower stratosphere during the year.

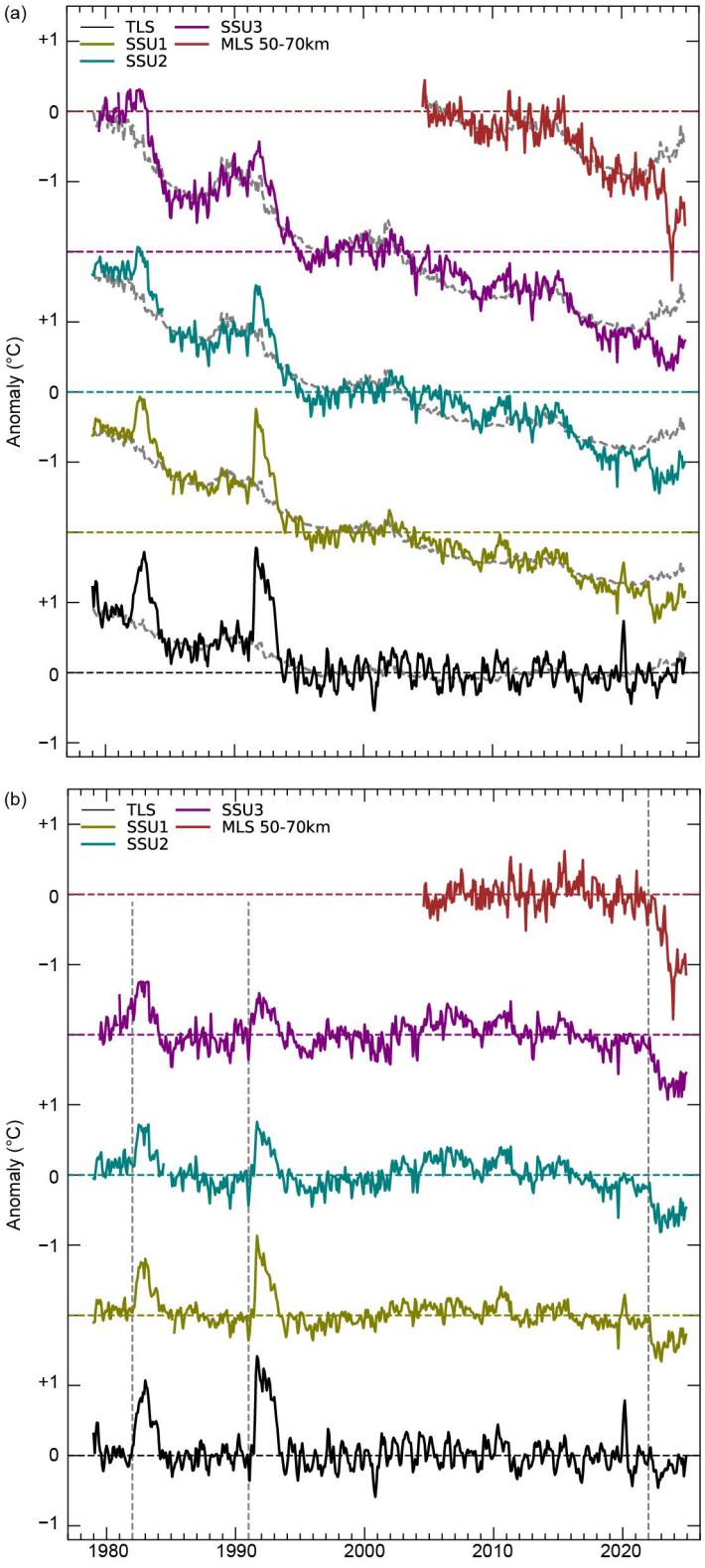

Global stratospheric temperatures have been monitored from satellite observations for over 40 years, and Fig. 2.11a shows time series of global monthly temperature anomalies spanning the lower to upper stratosphere and mesosphere from merged satellite data. In addition to long-term stratospheric cooling (due to CO_2 increases and stratospheric ozone changes), transient variations arise from the 11-year solar cycle and effects of large volcanic eruptions: El Chichón (1982), Pinatubo (1991), and Hunga (2022). Transient warming of the lower stratosphere is also evident following the Australian wildfires in early 2020 (Yu et al. 2021; Stocker et al. 2021). Effects of the volcanic eruptions and wildfires are more easily seen in Fig. 2.11b, which shows global temperature anomalies after removing the decadal-scale trends and solar cycle effects. The time series show anomalous cooling of the middle to upper stratosphere by 0.5°C–1.0°C in 2022/23, caused by radiative impacts of the unusually large quantities of water vapor (H_2O) injected directly to the stratosphere by the January 2022 Hunga volcanic eruption (Millan et al. 2022; Stocker et al. 2024; Randel et al. 2024).

Fig. 2.11. (a) Time series of monthly global average temperature anomalies (°C) for thick-layer averages spanning the lower to upper stratosphere and mesosphere (bottom to top). Middle and upper stratosphere data are from the Stratospheric Sounding Unit (SSU) updated with Microwave Limb Sounder (MLS) measurements, representing thick-layer averages centered near 30 km, 38 km, and 45 km (SSU1, SSU2 and SSU3, respectively). Lower-stratosphere temperatures (TLS) are ~13 km–22 km layer averages from satellite microwave measurements. These datasets are discussed in Steiner et al (2020). Mesosphere temperatures are 50-km–70-km averages from MLS data. (b) Global average temperature anomalies (°C) for each level, derived by subtracting linear trend and solar cycle fits to the time series in (a). These fits for each level are shown as dashed lines in panel (a). The vertical lines in (b) denote the El Chichón (1982), Pinatubo (1991), and Hunga (2022) volcanic eruptions. Figure updated from Randel et al (2024).

The Hunga water vapor anomalies have been diffusing globally and decreasing over time (e.g., Zhou et al. 2024), resulting in smaller stratospheric radiative impacts and a partial recovery from the anomalous cooling during 2024. The 11-year solar cycle was also near a maximum during 2024 (https://www.swpc.noaa.gov/products/solar-cycle-progression), contributing to slightly higher temperatures in the middle and upper stratosphere.

We note that the observed Hunga cooling over 2022–24 in the middle stratosphere is comparable in magnitude, but opposite in sign, to warm anomalies tied to the El Chichón (1982) and Pinatubo (1991) volcanic eruptions. The difference in sign is due to the stratospheric cooling effects of large water vapor anomalies from Hunga, whereas the El Chichón and Pinatubo warmings arise from sulfate aerosol-dominated warming effects. While the magnitude of the cooling anomalies due to Hunga increases with altitude, the magnitude of warming anomalies due to El Chichón and Pinatubo decreases with altitude. In the mesosphere, the Hunga cooling is a result of H_2O-induced ozone depletion (Randel et al. 2024).

Variations in polar vortex temperatures contribute little to global temperature anomalies but provide context for regional variability. Time series of Arctic and Antarctic polar vortex temperatures in 2024 are shown in Fig. 2.12, highlighting strong variability in the Arctic, with two separate stratospheric warming events in early 2024 (Lee et al. 2025). These events were caused by enhanced planetary wave forcing from the troposphere; the occurrence of two major warming events in the same year is unusual but has been observed several times in the past and has little to do with long-term climate change. In contrast, the Antarctic polar vortex shows a larger annual cycle with relatively little variability, although a series of weak wave-induced warming events were observed during austral mid-winter 2024.

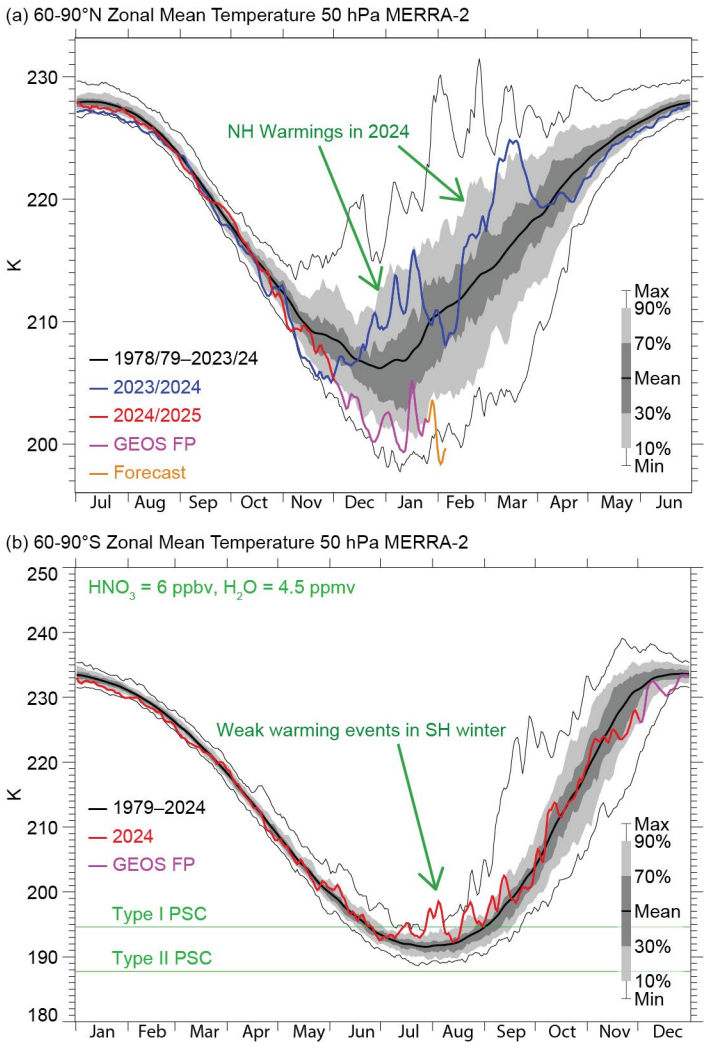

Fig. 2.12. (a) Time series of Arctic polar cap (60°N–90°N) temperatures in the lower stratosphere (50 hPa) during 2024, compared with the historical distribution of temperatures since 1978/79. Green arrows denote two stratospheric major warming events in early 2024. (b) Similar time series over the Antarctic (60°S–90°S) at 50 hPa. Note the different vertical axes between (a) and (b), and that the time axes are shifted by six months. (Data are from https://acd-ext.gsfc.nasa.gov/Data_services/met/ann_data.html.)

7. EQUIVALENT TEMPERATURE

—T. Matthews, T. Wood, P. Stoy, and M. Byrne

Global-mean equivalent temperature (*Teq*) reached its highest level in 2024 since at least 1979 according to reanalyses data, breaking its previous record (set in 2023) by 0.35°C–0.38°C.

Teq was introduced last year in the *State of the Climate in 2023* (Matthews et al. 2024). It is a more complete metric than air temperature (T) for tracking heat accumulation in the atmosphere:

$$Teq = T + qL/C_p$$

where T is the (dry-bulb) air temperature, q is the specific humidity (kg kg^{-1}), L is the latent heat of vaporization, and C_p is the specific heat capacity of the air. Note that Teq/C_p thus yields the 'moist static energy' that has also the subject of trend assessments (e.g., Peterson et al. 2011). *Teq* is therefore also closely related to wet-bulb temperature (T_w; section 2d2), but it has the advantage

of being linearly related to atmospheric heat accumulation; by comparison successive 1°C increments in T_w require progressively more heat accumulation.

The second term comprising *Teq* (the 'latent temperature', *Tq*) grows exponentially with *T* if relative humidity (*RH*) remains constant (due to the non-linearity in saturation vapor pressure as described by the Clausius Clapeyron equation). Hence, using *T* alone increasingly downplays the magnitude of changes in *Tq* and, accordingly, total heat content as the climate warms. This problem is not spatially uniform and is greater in regions with higher baseline *Tq* (such as within the tropics), where in some regions *Tq* is already rising faster than *T* (Matthews et al. 2022). Not only is *Teq* therefore more theoretically appropriate to track atmospheric heat accumulation as the climate changes, it is also more closely related to some key societal impacts. For example, extreme precipitation and human heat stress should be expected to scale more with *Teq* than *T* (Matthews et al. 2022; Song et al. 2022; Stoy et al. 2022). Note, however, that the closely related T_w remains much more widely used in the study of heat extremes (section 2d2).

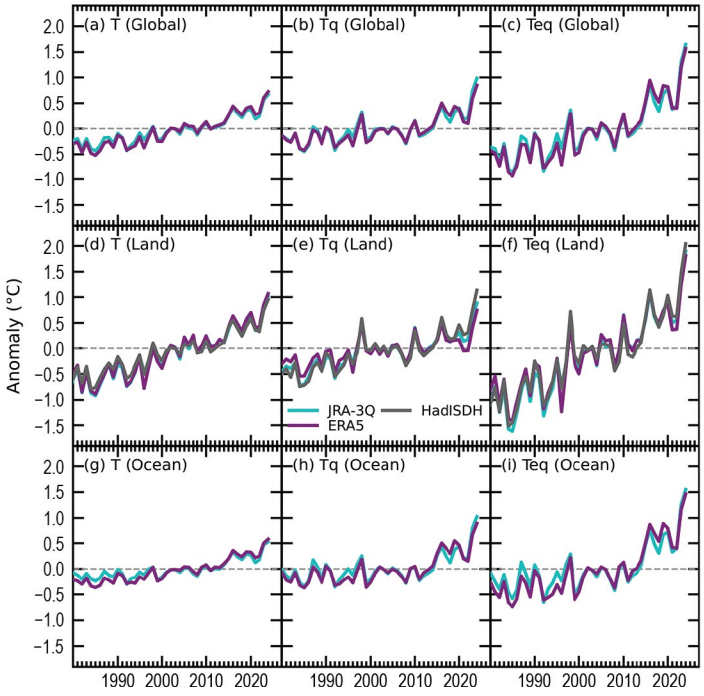

Fig. 2.13. (a),(d),(g) 2-m air temperature (*T*), (c),(f),(i) equivalent temperature (*Teq*), and (b),(e),(h) latent temperature (*Tq*) for (a),(b),(c) ocean + land, (d),(e),(f) land-only, and (g),(h),(i) ocean-only spatial mean anomalies versus the 1991–2020 baseline (°C). Each dataset is shown by colored lines: ERA5 (purple) and the Japanese Reanalysis for Three Quarters of a Century (JRA-3Q; cyan). Land-only sub-figures (d),(e),(f) also show Met Office Hadley Centre Integrated Surface Dataset of Humidity (HadISDH) anomalies (dark gray).

Teq anomalies for 2024 are assessed here using ERA5 (Hersbach et al. 2020) and JRA-3Q (Kosaka et al. 2024) reanalyses, along with the land-only station-based Met Office Hadley Centre Integrated Surface Dataset of Humidity over land (HadISDH.land; Willett et al. 2013, 2014). Globally (over land and ocean), *Teq* in 2024 was the highest on record according to both reanalyses datasets (Fig. 2.13), exceeding the previous records set in 2023 with departures of +1.57°C and +1.65°C above the 1991–2020 baseline for ERA5 and JRA-3Q, respectively (Table 2.4). Both datasets also rank the constituent parts of *Teq* (T and *Tq*) in the global series highest in 2024 (Appendix Tables A2.1–A2.3).

Across ERA5 and JRA-3Q, the mean 2024 global *Teq* anomaly (1.61±0.06°C, where uncertainty is one standard deviation across datasets) is much larger than that of *T* (0.70±0.04°C).

Table 2.4. Global equivalent temperature (*Teq*) anomalies and their constituent parts (*T*, *Tq*) in °C (1991–2020 base period) for 2024 and [rank] since 1979 (the earliest year common to all datasets). The uncertainty in the ensemble mean column represents one standard deviation.

Dataset	ERA5 *Teq*	ERA5 *T*	ERA5 *Tq*	JRA-3Q *Teq*	JRA-3Q *T*	JRA-3Q *Tq*	HadISDH *Teq*	HadISDH *T*	HadISDH *Tq*	Ensemble Mean *Teq*	Ensemble Mean *T*	Ensemble Mean *Tq*
Land + Ocean	1.57 [1]	0.72 [1]	0.85 [1]	1.65 [1]	0.67 [1]	0.98 [1]	-	-	-	1.61±0.06	0.70±0.04	0.92±0.09
Land only	1.80 [1]	1.06 [1]	0.73 [1]	1.90 [1]	1.01 [1]	0.89 [1]	2.04 [1]	0.96 [1]	1.13 [1]	1.91±0.12	1.01±0.05	0.92±0.20
Ocean only	1.46 [1]	0.58 [1]	0.88 [1]	1.55 [1]	0.52 [1]	1.02 [1]	-	-	-	1.51±0.06	0.55±0.04	0.95±0.10

This amplification is consistent with expectations of global-mean *RH* remaining approximately constant: the (exponential) increase in saturation vapor pressure with warming means that *Teq* must increase by more than *T* unless *RH* decreases sufficiently to leave *Tq* unchanged.

Considering spatial variation, both reanalyses agree that 2024 was the highest on record for *Teq*, *Tq*, and *T* over the oceans and over land (Table 2.4). For these datasets, the 2024 *T* anomaly was larger over land (1.01±0.05°C) than the ocean (0.55±0.04°C), whereas the *Tq* anomaly was more similar between land and ocean (0.92±0.20°C versus 0.95±0.10°C). As *Teq* is a combination of *T* and *Tq*, the land–ocean contrast for the 2024 anomaly (1.91±0.12°C versus 1.51±0.06°C) was also muted compared to *T*. Latitudinally, *Teq* anomalies in 2024 exhibited a more complex pattern than *T* (characterized by strong amplification in the Arctic; Figs. 2.14i–l). *Teq* had anomalies in the tropics and northern subtropics almost equal to those in the Arctic due to the much larger *Tq* anomalies at lower latitudes.

In general, 2024 *Tq* anomalies were therefore more likely to exceed *T* over the oceans and towards the equator (Figs. 2.14g,h,l). This pattern is consistent with theoretical expectations of *Tq* increasing by greater amounts relative to *T* in regions of higher baseline specific humidity

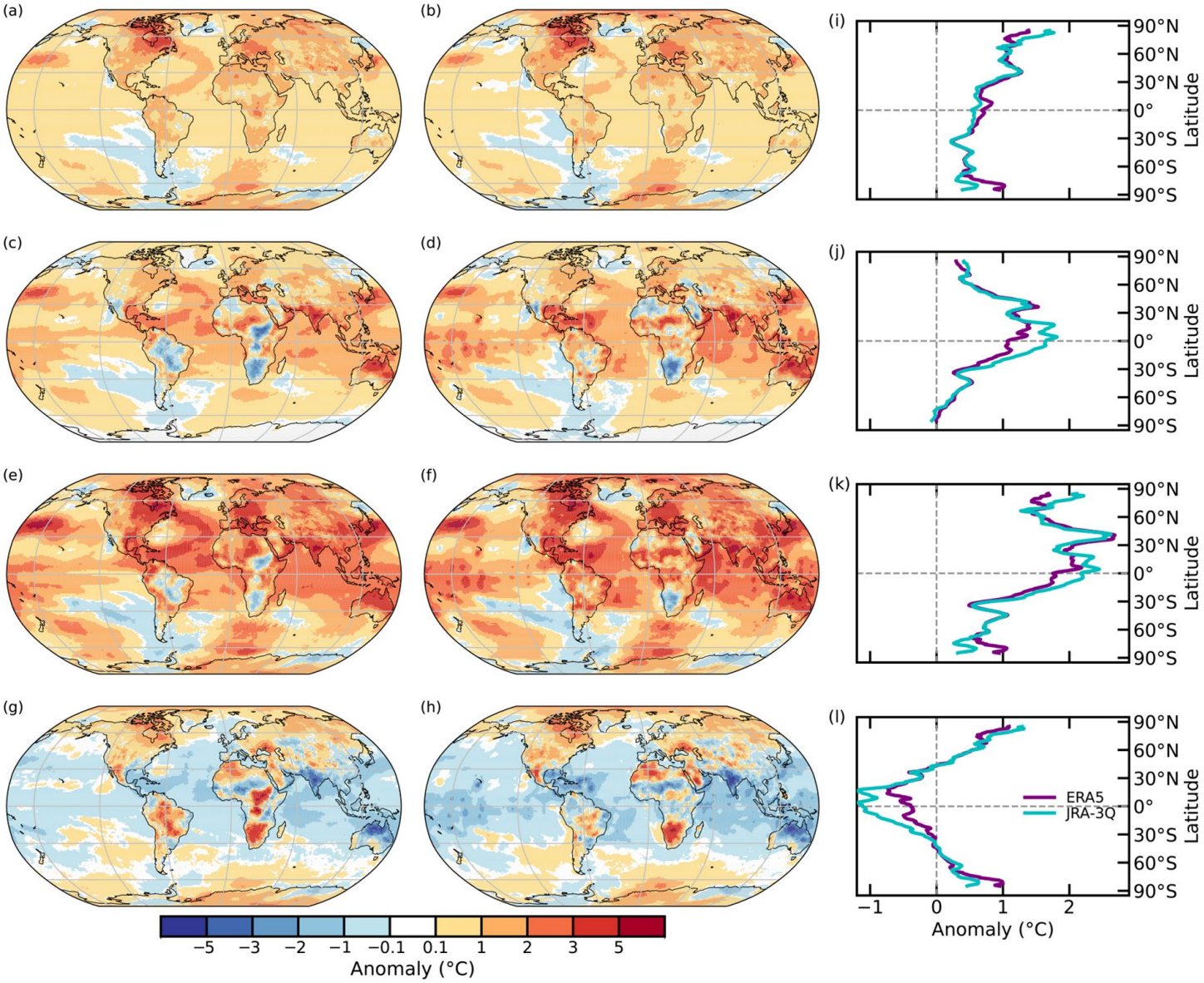

Fig. 2.14. Anomalies for (top to bottom): 2-m air temperature (*T*), latent temperature (*Tq*), equivalent temperature (*Teq*), and *T*–*Tq* according to ERA5 (left; [a],[c],[e],[g]) and the Japanese Reanalysis for Three Quarters of a Century (JRA-3Q) (right; [b],[d],[f],[h]) global (land and ocean). Zonal means for each variable are shown in the rightmost column (i)–(l) restricted to 85°S–85°N. Blue regions in the bottom row (*T*–*Tq*) experienced a larger 2024 anomaly in the latent heat term (*Tq*); red regions had a larger *T* anomaly.

(Matthews et al. 2022). It also highlights the importance of using *Teq* alongside *T* if hotspots in total atmospheric heat accumulation are to be correctly identified.

There were, however, exceptions in 2024 to the patterns of change in *T* and *Tq* expected from the baseline climates, with perhaps the most notable in Amazonia and North Africa (Figs. 2.14g,h). Under the assumption of constant *RH*, Amazonia (with relatively high baseline *Tq*) is one of the regions anticipated to experience larger changes in *Tq* than *T* under warming; the expectation is reversed for the relatively dry climate of North Africa (Matthews et al. 2022). The larger 2024 *T* anomalies in Amazonia and greater *Tq* anomalies in parts of North Africa are therefore consistent with reported drought conditions in Amazonia in 2024 (Maciel et al. 2024) and the extreme wet season rainfall in the Sahel (Pinto et al. 2024).

In summary, 2024 was a record-breaking year for *Teq*, with all datasets unanimous in their agreement that it was easily the highest over land and ocean since at least 1979.

c. Cryosphere

1. PERMAFROST TEMPERATURE AND ACTIVE-LAYER THICKNESS

—J. Noetzli, H. H. Christiansen, T. Gallemann, M. Gugliemin, F. Hrbáček, G. Hu, K. Isaksen, F. Magnin, P. Pogliotti, S. L. Smith, L. Zhao, and D. A. Streletskiy

Ground remaining at or below 0°C for two or more years—known as permafrost—occurs in polar and high mountain regions. Its warming and degradation can have important impacts on the landscape, ecosystems, infrastructure, and natural hazards. Widespread permafrost warming, thickening of the active layer (i.e., the seasonally thawed layer above the permafrost), and ground ice loss continued to be observed in 2024. Globally, permafrost warming rates at 10-m–20-m depth in cold permafrost (<–2°C) reach up to 1°C decade^{-1}. Warming rates are significantly reduced (<0.3°C decade^{-1}) in warm ice-bearing permafrost due to latent heat effects (Noetzli et al. 2024a; Smith et al. 2022; Zhao et al. 2024). Therefore, ground temperatures close to 0°C in ice-rich permafrost can remain nearly stable for years as ground ice is melting. Ground ice loss was observed in the Arctic (O'Neill et al. 2023; Streletskiy et al. 2025), European mountains (Etzelmüller et al. 2020; Mollaret et al. 2019), and the Qinghai–Tibet Plateau (QTP; Wang et al. 2023; Zou et al. 2024). Decadal active-layer thickening ranges from centimeters in continuous permafrost in Arctic sediments, to tens of centimeters in discontinuous bedrock permafrost in polar regions (Smith et al. 2024), southern Scandinavia (Etzelmüller et al. 2023), and the QTP (Zhao 2024; Hu 2024), to meters in bedrock or talus (scree) slopes in the European Alps (PERMOS 2024; Magnin et al. 2023).

Arctic permafrost has warmed by <0.3°C decade^{-1} in warmer permafrost to 0.8°C decade^{-1} in cold permafrost (Smith et al. 2024; see section 5j). Permafrost temperatures in 2024 were generally higher than in 2023. They were the highest on record at 8 of 25 sites reporting (7 in North America and 1 on Svalbard). In the Beaufort–Chukchi region (northern Alaska and Canadian Mackenzie Valley), higher permafrost temperatures in 2024 reflect higher surface air temperature (SAT) in 2023 that followed a short cooling period. Permafrost temperatures in high Arctic Svalbard increased again in 2024 following a cooling period after 2019 (Isaksen et al. 2022) and were close to previous values. Arctic permafrost is described in detail in section 5j.

On the Antarctic Peninsula, the annual shallow ground temperature in 2024 was 0.3°C below the 2011–20 mean on James Ross Island (Hrbáček et al. 2023) and within 0.1°C in the South Shetlands (de Pablo et al. 2024).

Permafrost in European mountains changed at rates between −0.01°C decade^{-1} and +1.77°C decade^{-1} (mean 0.41°C decade^{-1}) at 10-m depth during 2013–22 based on 50 time series, where permafrost was present at this depth for at least part of the decade (Noetzli et al. 2024b). Warming was >0.7°C decade^{-1} at 20% of these sites, which are in cold polar or high-elevation locations or where permafrost has recently disappeared. At 20-m depth, rates are generally lower (up to 0.7°C decade^{-1}) due to the delayed warming with increasing depth. In 2024, permafrost temperatures in the European Alps reached record highs at 10-m depth for most of the sites reporting (Fig. 2.15). This resulted from three consecutive exceptionally warm years and an early snow cover in winter 2024 following a warm autumn (MeteoSwiss 2025; PERMOS 2025). In northern Scandinavia, a record-warm summer 2024 led to strong permafrost warming at 10-m depth.

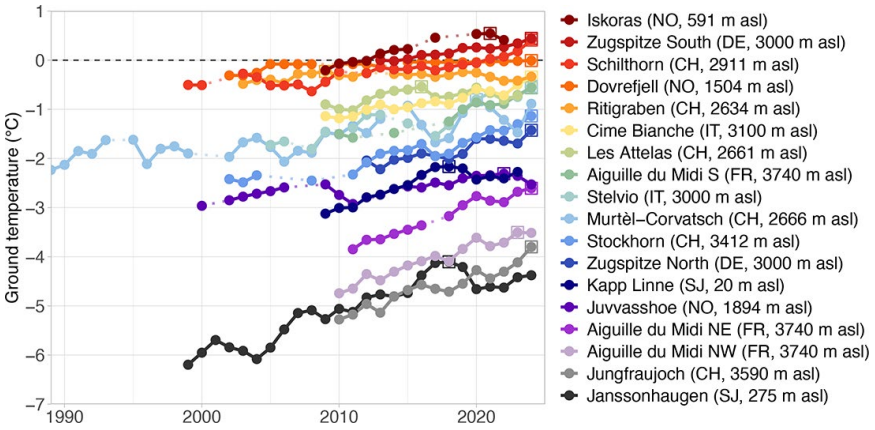

Fig. 2.15. Mean annual ground temperature (°C) measured in European permafrost boreholes in the Alps, Scandinavia, and Svalbard at a depth of ~10 m. Maximum values for each time series are highlighted by a square. (Data sources: Norway [NO] and Svalbard [SJ]: Norwegian Meteorological Institute and the University Centre in Svalbard [UNIS]; Switzerland [CH]: Swiss Permafrost Monitoring Network [PERMOS]; France [FR]: Updated from Magnin et al. 2023; Italy [IT]: Updated from Pogliotti et al. 2023 and Guglielmin, M. unpublished data. Germany [DE]: Bavarian Environment Agency.)

At Iskoras in northern Norway, permafrost thawed to a depth of 24 m, with >15 m of permafrost lost since 2008 (Etzelmüller et al. 2023).

In the central Asian QTP, significant permafrost warming for 2005–23 is reported for six sites at rates between 0.04°C decade^{-1} and 0.4°C decade^{-1} at 10-m depth (Fig. 2.16) and between 0.02°C decade^{-1} and 0.25°C decade^{-1} at 20-m depth.

Active-layer thickness (ALT) increase in the Arctic continued in 2024 and was more pronounced in areas of discontinuous permafrost than in areas of continuous permafrost (Fig. 2.17; section 5j). In Interior Alaska and Mackenzie Valley, ALT was larger in 2023 and 2024 than in 2022. In Greenland, it was larger than average in 2024. In Svalbard, ALT reached an all-time high, following the third summer in a row with unprecedented high summer SAT. ALT in the European North and West Siberia was lower in 2024 than in 2023, but substantially above the 2000–20 mean. For the limited sites reporting in East Siberia and Chukotka, the ALT decrease over the past five years continued, with values that were lower in 2024 than in 2023 and below the 2000–24 mean.

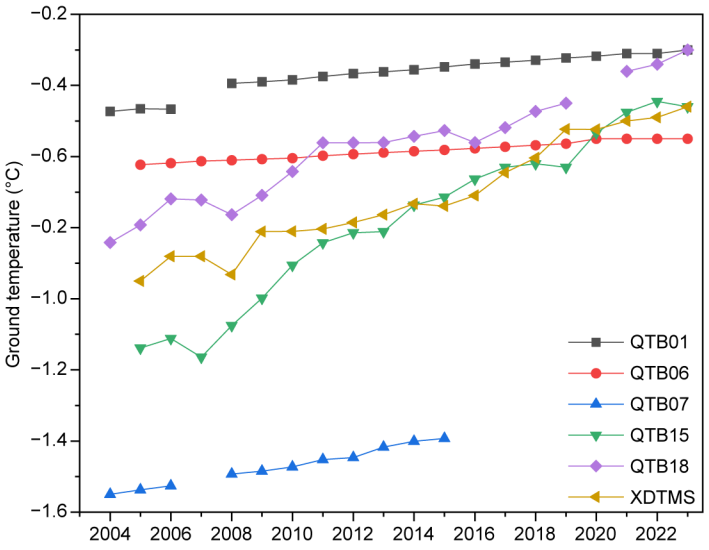

Fig. 2.16. Ground temperature (°C) measured at 10-m depth in the Qinghai–Tibet Plateau (QTP) in the period 2005–23. (Data source: Cryosphere Research Station on Qinghai-Xizang Plateau, Chinese Academy of Sciences [CAS].)

On the Antarctic Peninsula, the maximum ALT since the start of measurements in 2014 was registered in 2023. In 2024, ALT was only slightly above the long-term mean and the lowest observed since 2020.

In Europe's mountains, ALT reached or exceeded the 2022/23 record values and continued the marked thickening of the past three years. During the period 2000–20, ALT increased by meters at several sites, reaching values beyond the climatic variability (Fig. 2.17b). At Schilthorn, Swiss Alps, ALT tripled to >13 m during 1998–2022, and the ground did not re-freeze in winter 2024 (PERMOS 2025).

ALT near Kunlun mountain pass (QTP) increased by 20.2 cm decade^{-1} during 1981–2023 at 10 sites, following a significant SAT increase during that period.

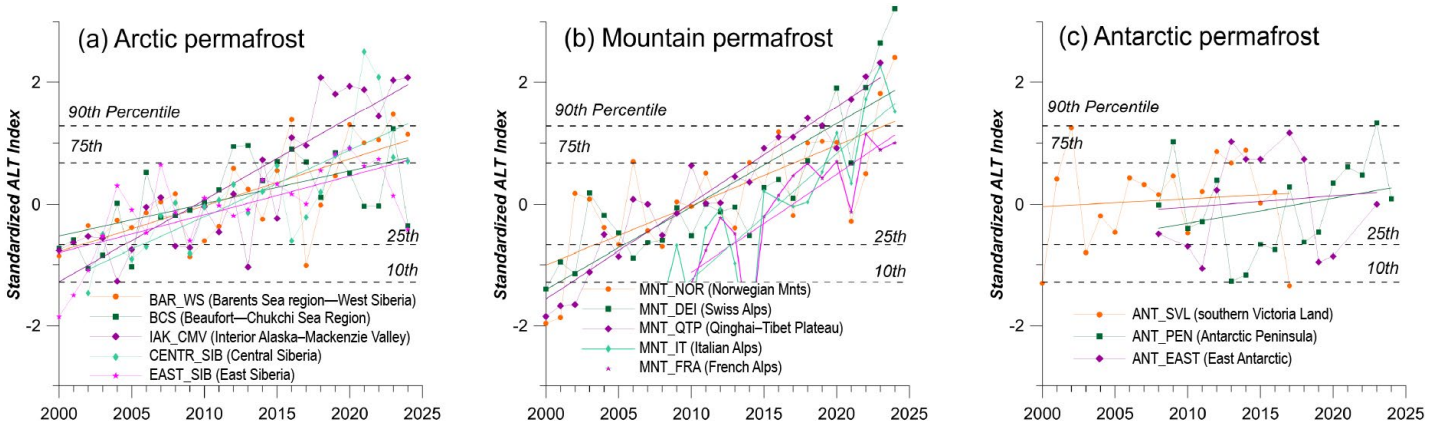

Fig. 2.17. Standardized index of active-layer thickness (ALT) relative to 2000–20. (a) Arctic regions: Beaufort–Chukchi Sea–Arctic Alaska and Mackenzie Delta region (BCS), Interior Alaska and central Mackenzie Valley, Northwest Territories (IAK_CMV), Barents Sea region–West Siberia (BAR_WS), Central Siberia (CENT_SIB), East Siberia (EAST_SIB); (b) Mountain regions: Norwegian mountains (MNT_NOR), Swiss Alps (MNT_SWI), Italian Alps (MNT_IT), French Alps (MNT_FRA), Qinghai-Tibet Plateau (MNT_QTP); and (c) Antarctic: southern Victoria Land (ANT_SVL), Antarctic Peninsula (ANT_PEN), East Antarctic (ANT_EAST). Note that only data from 30% of the Russian sites are reported. (Data source: Circumpolar Active Layer Monitoring [CALM].)

2. ROCK GLACIER VELOCITY

—C. Pellet, X. Bodin, D. Cusicanqui, R. Delaloye, A. Kääb, V. Kaufmann, E. Thibert, S. Vivero, and A. Kellerer-Pirklbauer

Rock glaciers are debris landforms generated by the creep of perennially frozen ground (permafrost). Their velocity evolutions are indicative of changes in the thermal state of permafrost and associated ground hydrological characteristics (RGIK 2023a). An overall increasing trend of rock glacier velocity (RGV) has been observed in mountain ranges worldwide since the 1950s (Pellet et al. 2024). In 2024, RGVs consistently increased in the European Alps compared to 2023, and in the Dry Andes, RGVs remained at a high level, with values similar to 2020. RGVs recently compiled in the United States further confirm this general trend of RGV increase (Kääb and Røste 2024), which is consistent with the increase of permafrost temperatures (section 2c1) to which RGV respond more or less synchronously (e.g., Staub et al. 2016).

In the European Alps, 2024 was the second-warmest hydrological year on record based on the average of five high-elevation stations (+1.52°C; Fig. 2.18a) yielding a general increase of RGVs. Compared to 2023, the highest RGV increase occurred in the Swiss Alps (+80.8% at Gemmi/Furggentälti and +80.7% at Grosses Gufer), whereas a +16.9% increase was observed in the French Alps at Laurichard as well as +3.4% and +5.1% increases in the Austrian Alps at Dösen and Hinteres Langtalkar, respectively (Fig. 2.18b). These observations are consistent with the permafrost temperature observations (section 2c1) as confirmed by the increasing temperatures measured in 2024 at 10-m depth on the rock glacier Murtèl in eastern Switzerland (Fig. 2.18a). The regional differences in magnitude of velocity increase is related to landform-specific characteristics combined with the spatial variability of snow conditions, namely early onset and well-above-average snow height throughout the winter in Switzerland and France (preventing any cooling of the ground; PERMOS 2025) as well as early onset followed by below-average snow heights in Austria (enabling limited cooling). The reported RGV observations in 2024 in the European Alps are consistent with the general acceleration trend observed at all sites since the 1950s (Kellerer-Pirklbauer et al. 2024).

In the Dry Andes, RGVs observed during 2023/24 show increases of +13.7% and +1.3% on El Cachito and Las Tolas, respectively, whereas a –15.9% decrease is observed on Tapado compared to 2019/20 (Fig. 2.18c). Velocities reached maximum values at El Cachito and remained at a high level compared to the entire time series on Las Tolas and Tapado. The overall increase observed since the 2000s is further confirmed by a recent study on Largo rock glacier (Fig. 2.18c; Cusicanqui et al. 2024) and is consistent with the slight air temperature increase observed in the region since 1976 (Vivero et al. 2021).

In Central Asia, RGVs observed on four landforms since the 1950s exhibit a general increase, with a marked acceleration in the period 2010–20 (Fig. 2.18d). This evolution is consistent with increasing air temperatures in the region (Azisov et al. 2022; Sorg et al. 2015).

In the United States, RGVs compiled on six rock glaciers show an overall increase since the first available measurements in the 1950s (Fig. 2.18e; Kääb and Røste 2024). This trend is consistent with the strongly increasing air temperature observed in that region (Kääb and Røste 2024).

RGV refers to velocities related to permafrost creep, which has to be understood as a combination of internal deformation of the frozen ground (creep stricto sensu) and shearing in one or more layers at depth (shear horizon; RGIK 2023b). RGVs are mostly related to the evolution of ground temperature and liquid water content between the upper surface of permafrost and the shear horizon (Cicoira et al. 2019; Staub et al. 2016). RGV increase and decrease positively correlates with temperature change. Despite differences in size, morphology, topographical, climatic, and geological settings, as well as velocity ranges, consistent regional RGV evolutions have been highlighted in several studies (see Hu et al. 2025). RGV time series are produced using both in situ and optical remote sensing (airborne and spaceborne) measurements. Surface displacements are computed based on matching between images or digital elevation models taken at different times, with the resulting accuracy strongly depending on the characteristics of the input data (Kääb et al. 2021; Vivero et al. 2021). Surface displacements are averaged for a cluster of points/pixels selected within areas considered as representative of the downslope movement

of the rock glacier (RGIK 2023b). The in situ measurements consist of annually repeated terrestrial geodetic surveys of the positions of selected boulders (10–100 per landform), yielding displacement observation with an average accuracy of mm to cm (Lambiel and Delaloye 2004; Thibert and Bodin 2022).

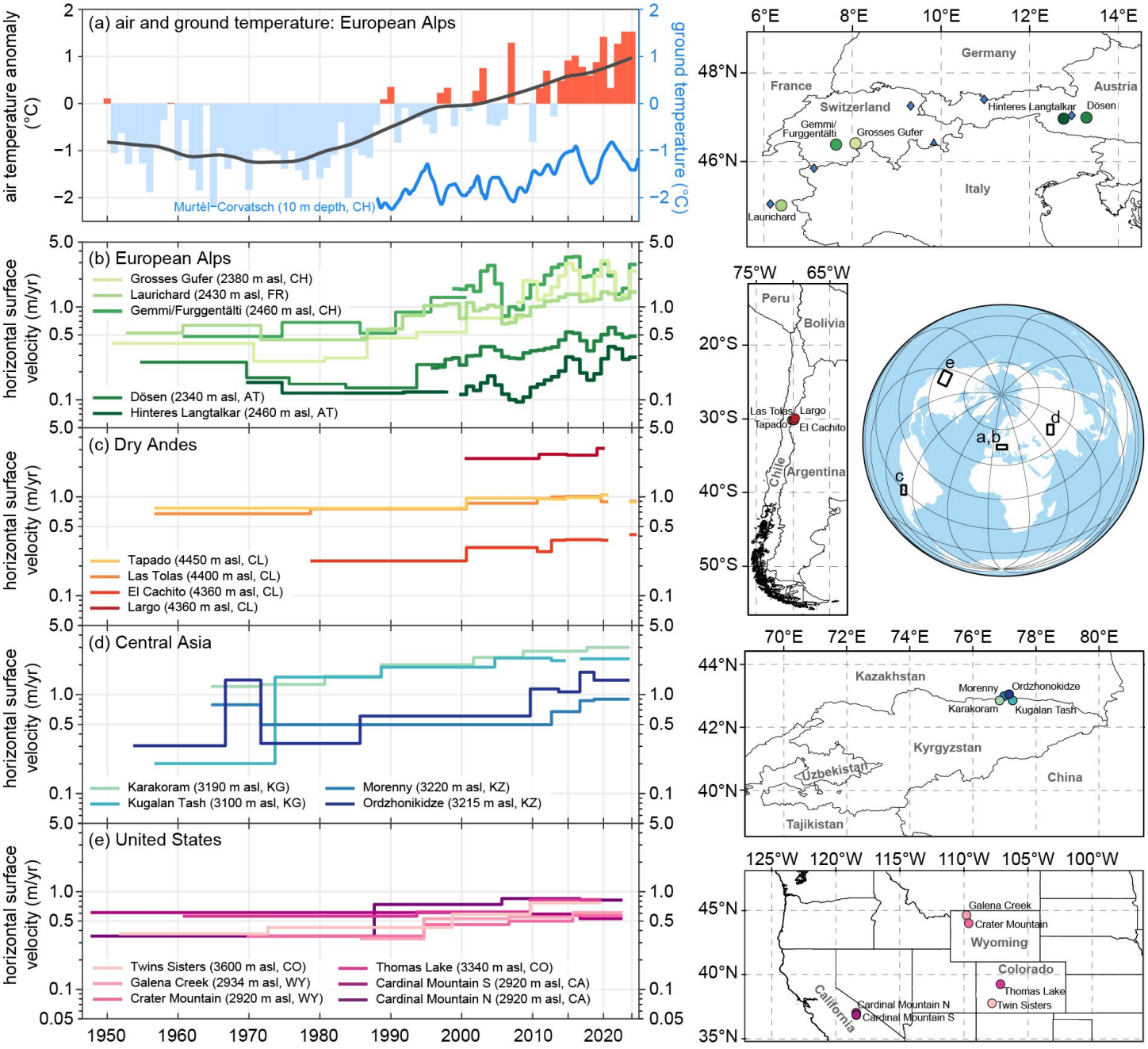

Fig. 2.18. Rock glacier velocity and climate: (a) air temperature in the European Alps and ground temperature in the Swiss Alps (°C), (b)–(e) rock glacier velocities (m yr^{-1}) at selected sites in the (b) European Alps, (c) Dry Andes (updated from Vivero et al. 2021 and Cusicanqui et al. 2024), (d) Central Asia (updated from Kääb et al. 2021), and (e) United States (adapted from Kääb and Røste 2024). Rock glacier velocities are based on in situ geodetic surveys ([b], since 2000s) or photogrammetry ([b]–[e]) in the context of long-term monitoring. In situ hydrological mean annual permafrost temperature measured at 10-m depth (blue line) at Murtèl Corvatsch (blue triangle on Europe map) and air temperature: composite anomaly to the 1991–2020 base period (bars) and composite 20-year running mean (solid line) at Besse (France [FR]), Grand Saint-Bernard (Switzerland [CH]), Saentis (CH), Sonnblick (Austria [AT]), and Zugspitze (Germany [D], blue diamonds on Europe map). (Sources: Météo-France, Deutscher Wetterdienst [DWD], MeteoSwiss, GeoSphere Austria, Swiss Permafrost Monitoring Network [PERMOS], University of Fribourg, University of Graz, Graz University of Technology, Université Grenoble Alpes National Institute of Agricultural Research [INRAE], University of Oslo).

3. ALPINE GLACIERS

—M. Pelto

In 2024, all 58 global reference glaciers reported a negative annual mass balance. This is only the second year in the 1970–2024 period with all negative annual balances, following 2023. The global average annual mass balance based on equal weighting of 19 regions is –1.30 m water equivalent (w.e.), the most negative value in the record (Fig. 2.19).

The 2024 dataset of submitted glaciological observations includes 142 glaciers from six continents and 27 nations, with 140 reporting a negative balance and 2 a positive balance. In 2024, the mean annual mass balance of the 58 global reference glaciers was –1.44 m w.e. and –1.36 m w.e. for all 142 reporting glaciers. This is a similar result to 2023, which saw a mean reference glacier balance of –1.62 m w.e. and –1.35 m w.e. for all 116 reporting glaciers.

The 2024 regionalized global average of –1.30 m w.e. exceeds the previous most negative year in 2023, which saw a regionalized global average of –1.25 m w.e. This makes 2024 the 37th consecutive year with a global alpine mass balance loss and the 15th consecutive year with a regionalized global mass balance below –0.5 m w.e. The acceleration of mass balance loss indicates that alpine glaciers are not approaching equilibrium. The acceleration of mass balance loss is apparent regardless of datasets used to determine it, including glaciological, geodetic, altimetry, and gravimetric observations (The GlaMBIE Team 2025). The intercomparison assessment identified that global glaciers annually lost 273±26 gigatons (Gt) in mass from 2000 to 2023, with loss having been 36% greater in the second half than in the first half of this period (The GlaMBIE Team 2025).

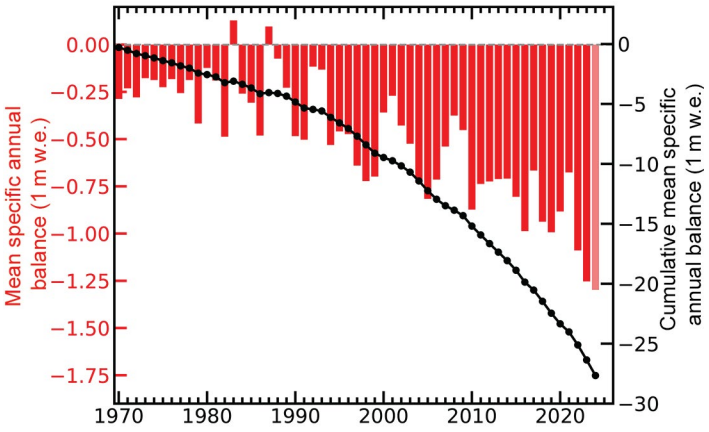

Fig. 2.19. Time series of regionalized average global mean annual glacier mass balance of alpine glaciers from 1970–2024 in m w.e., as determined by the World Glacier Monitoring Service. Annual mass balance is shown in red bars and annual cumulative mass balance is indicated by black dots.

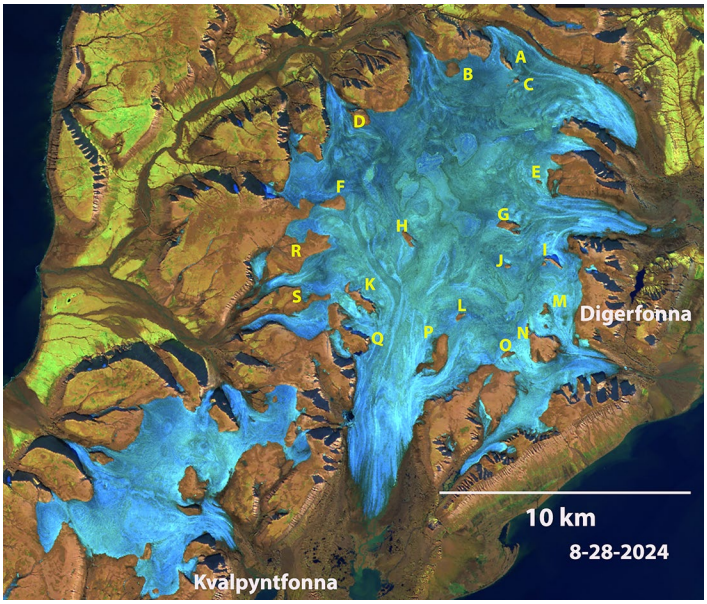

Fig. 2.20. Snow-free ice caps on Edgeoya Island, Svalbard, in Sentinel-2 Short-Wave Infrared RGB Composite imagery from 28 August 2024. Green represents vegetation, brown represents rock and soil, black represents water, white to very light blue represents snow, and darker grays and blues represent ice and firn. Glaciers across Svalbard were largely snow-free, leading to consistent mass balance losses exceeding –1.25 m w.e.

In the European Alps, all 49 glaciers reported negative mass balances, with 45 losing over 1 m w.e. All 10 Icelandic glaciers had negative balances. In Svalbard, all seven had negative balances exceeding an exceptional loss of 1.25 m w.e. This was the result of near complete snow cover loss across most glaciers (Fig. 2.20) following record temperatures in August (see section 7f5 for details). Twelve of the 13 glaciers from Norway and Sweden had mass losses of more than 1.0 m w.e.

Across High Mountain Asia, 20 of 21 glaciers, reporting from seven nations, had negative balances. The highest average losses were in the Himalayas of Nepal and the lowest in the Pamir Range of Tajikistan.

In the Andes Mountains of South America, all 14 glaciers, reporting from five nations, had negative balances. Conejeras Glacier (Colombia), following a 5.04 m w.e. loss in 2023, was declared extinct in 2024. The daily hydrograph below this glacier changed from a predominance

of days with a purely melt-driven hydrograph from 2006 to 2016 to an increase in the frequency of days with flows less influenced by melt after 2016 (Morán-Tejeda et al. 2018).

All 16 glaciers in North America had negative balances. All four glaciers in Arctic Canada had mass balance losses under 1 m w.e. In western Canada and Washington and Montana (United States), all 16 glaciers reporting had losses exceeding 1 m w.e. The Ice Worm Glacier (Washington) was listed as extinct in 2023 after 40 years of continuous observations (Pelto 2024). In 2024, loss from the relict ice (ice that is no longer moving or part of a glacier) was 2.4 m and melt runoff below the glacier had decreased similar to Conejeras Glacier (Pelto and Pelto 2025). In Alaska, all three glaciers had mass balance losses. Davies et al. (2024) examined the Juneau Icefield, the most observed icefield in Alaska in terms of mass balance, and found an acceleration of mass loss with a doubling after 2010 compared to 1979–2010.

Alpine annual mass balance glaciological observations are reported to the World Glacier Monitoring Service (WGMS) by national representatives with a 1 December annual submission deadline. WGMS reference glaciers have at least 30 continuous years of mass balance observation. Benchmark glaciers have at least a 10-year mass balance record and are in regions that lack sufficient reference glaciers. The combination of benchmark and reference glaciers is used to generate regional averages (WGMS 2023). Global values are calculated using a single averaged value for each of 19 mountain regions, limiting bias from observed regions (WGMS 2023). As this dataset expands, the annual values are reanalyzed and updated.

4. LAKE ICE COVER

—J. Culpepper, S. Sharma, R. I. Woolway, and J. E. Ollinik

Northern Hemisphere (NH) lakes tended toward later ice formation, earlier ice breakup, and shorter duration during the winter of 2023/24, similar to long-standing trends (Sharma et al. 2021). However, there was regional variability in ice patterns between North America and Europe, likely resulting from stronger warm anomalies in winter air temperatures in North America (see section 7b).

On average, NH lakes froze 3.6 days later, broke up 6.1 days earlier, and ice duration was 10 days shorter, based on ERA5 reanalysis data and compared to the 1991–2020 base period (Figs. 2.21a–c). Most regions experienced shorter ice duration, with the exception of Scandinavia, which saw longer duration owing partially to colder winter air temperature anomalies, particularly in the late autumn and early winter (October–January; Figs. 2.21c,d).

On average, during the 2023/24 winter, in situ lake ice observations (n = 123) revealed that ice-on was 7.6 days later, ice-off was 17.5 days earlier, and ice duration was 24 days shorter relative to the 1991–2020 base period (Figs. 2.22a–c). The lakes in North America had on average 42.4 fewer days of ice cover, whereas lakes in Finland and Sweden experienced 13.5 more days

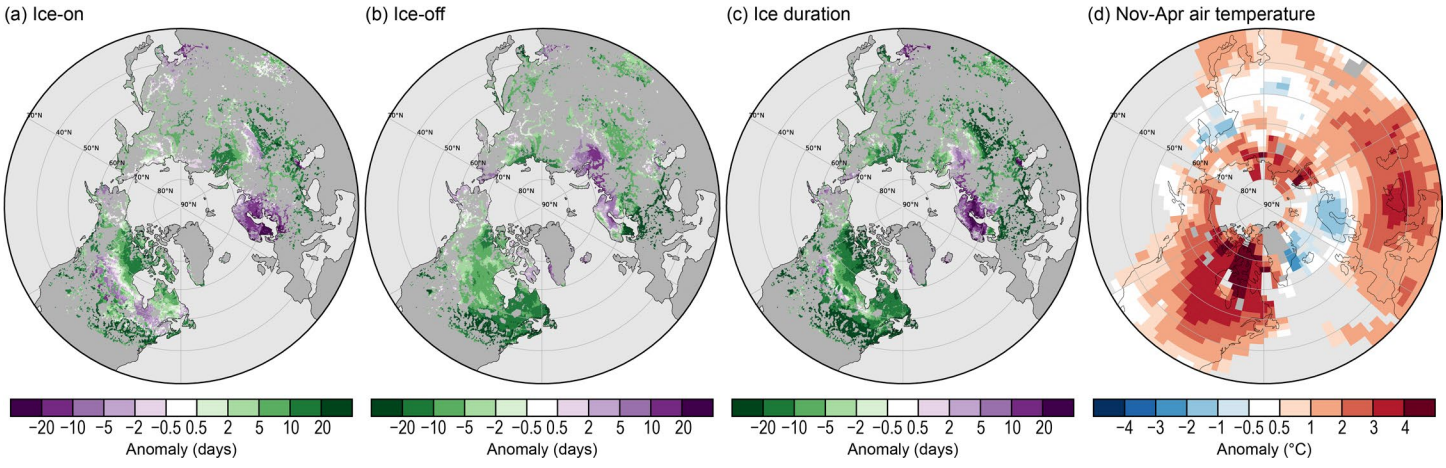

Fig. 2.21. Anomalies (days) compared to 1991–2020 base period in lake ice cover across the Northern Hemisphere during the winter of 2023/24 for the (a) ice formation period (negative [positive] values indicate earlier [later] ice formation), (b) ice breakup period (negative [positive] values indicate earlier [later] ice breakup), and (c) ice duration period. For duration (c), negative (positive) values indicate shorter (longer) ice cover. (d) The surface temperature anomalies (°C) for average temperatures between Nov 2023 and Apr 2024, where negative (positive) values are colder (warmer) temperatures.

of ice cover. El Niño-related temperature pattern conditions (Fig. 2.21d) strongly decreased ice coverage in North American lakes. Furthermore, Lake Suwa in Japan (36.0499°N, 138.0857°E) did not freeze, continuing a pattern of intermittent freezing. Lake Suwa has frozen in only 17 of the last 30 years, but has frozen every year between 2021 and 2023. Notably, Lake Suwa froze in 87 years in the twentieth century, although the majority of the ice-free years occurred after the 1970s.

Mountain lakes in North America and Europe experienced an average of 6.8 fewer days of ice cover (n = 13), resulting from ice formation (n = 14) that was 0.8 days earlier and ice breakup (n = 13) that was 6.9 days earlier (Fig. 2.22). Mountain lakes are a separate subset of in situ lakes identified using digital elevation models, which have an elevation of at least 300 m a.s.l. Ice loss can be more extreme in these lakes. For example, Lake Lunz only experienced 2 days of ice cover in 2024, compared to an average of 62 days between 1990 and 2019 (Kainz et al. 2017). Despite warmer temperatures during November through April, ice breakup was later in North American mountain lakes. Anomalously high snow cover (section 2c5) in the western United States likely drove delayed ice breakup in the California (Chandra et al. 2023) and Colorado (Caine et al. 2024) lakes included in this dataset.

The Laurentian Great Lakes had 31.8% less maximal ice coverage during the 2023/24 winter relative to the winters of 1991–2020. Lake Superior had 42.5% less ice coverage, followed by Lakes Erie (40.3%), Huron (37.3%), Ontario (20.9%), and Michigan (18.1%; Fig. 2.23). The Great Lakes reached their maximal ice coverage of 16% on 22 January, 31 days earlier than average. Notably, there was only 2.7% ice coverage across all of the Great Lakes on 11 February, the lowest ice coverage measured in mid-February since 1973. The Great Lakes region was characterized by generally warm winter air temperatures in 2023/24, with only a brief period of cold air temperatures in January 2024 (NOAA 2024). After the year 2000, an oscillatory pattern figures prominently in the time series (Fig. 2.23). Research suggests that a combination of the El Niño–Southern Oscillation (ENSO) and North Atlantic Oscillation (NAO) contribute to the variability in ice cover conditions in the Laurentian Great Lakes. For example, the Great Lakes have lower ice cover during strong La Niña events and the positive phase of the NAO (Bai et al. 2012). Moreover, NAO and ENSO can also interact to influence ice cover in a winter (Bai et al. 2012).

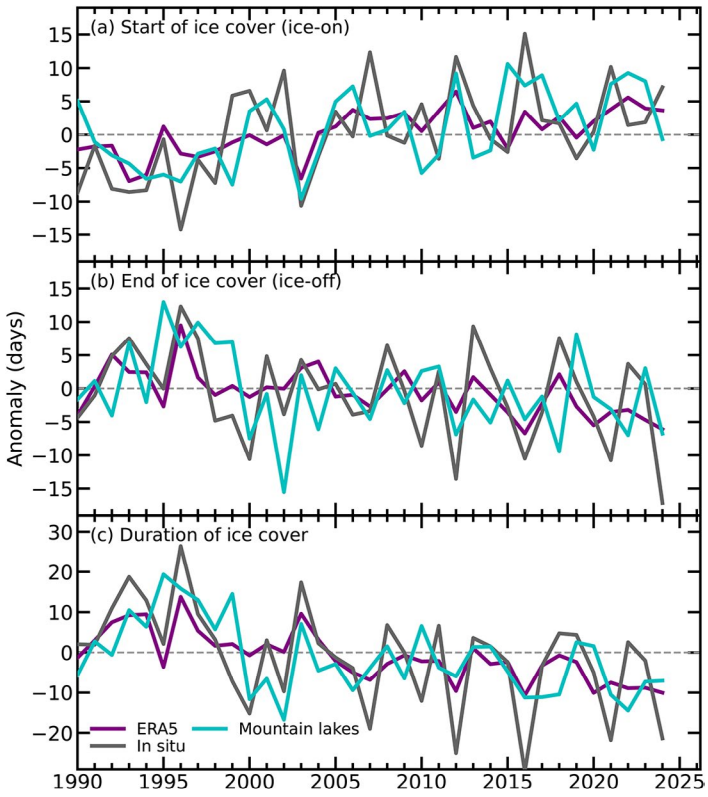

Fig. 2.22. The (a) ice-on, (b) ice-off, and (c) ice duration anomalies (days) for Northern Hemisphere lakes from 1990 to 2024 compared to the 1991–2020 base period for in situ observations (gray), mountain lake observations (blue), and ERA5 (black). Negative (positive) values indicate earlier (later) ice-on, earlier (later) ice-off, and shorter (longer) ice duration.

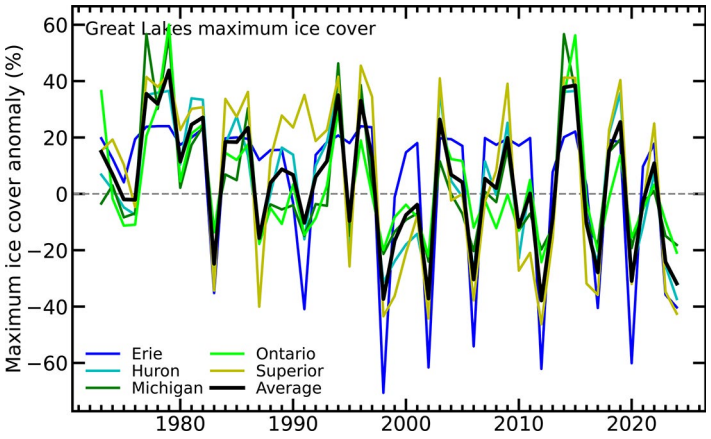

Fig. 2.23. Anomalies of the maximum ice cover extent (%) of the Laurentian Great Lakes for the period of 1973 to 2024 in relation to the 1991–2020 base period. The colored lines indicate individual lake anomalies (e.g., Erie anomaly in blue), while the black line shows the average anomaly. Negative (positive) values indicate less (more) maximum ice cover extent.

Established monitoring networks and citizen scientists contributed in situ observations for 123 lakes across Canada (n = 5 lakes), the United States (n = 88), Finland (n = 27), Sweden (n = 1), and Japan (n = 1) (Sharma et al. 2022). Mountain lake ice cover was derived from a similar network of scientists through the NH in North America (n = 8 lakes) and Europe (n = 10; Caine et al. 2024; Chandra et al. 2023; Kainz et al. 2017). Anomalies for each in situ lake were calculated as the difference between the 2023/24 ice value (i.e., ice-on, ice-off, duration) and the average of the 1991–2020 base period. Information on lake ice phenology was downloaded from ERA5 (Hersbach et al. 2020). Annual maximum ice coverage (%) data for each of the Laurentian Great Lakes were acquired for 1973–2024 from the NOAA Great Lakes Environmental Research Laboratory. Notably, the definitions of ice-on and ice-off varied by lake (e.g., complete ice cover, the date most of the lake is frozen [90%] or when most of the lake is ice-free [10%], the first or last time a boat could travel through two points), but did not vary over time for each lake (Sharma et al. 2022).

5. NORTHERN HEMISPHERE CONTINENTAL SNOW COVER EXTENT

—D. A. Robinson and T. W. Estilow

Annual snow cover extent (SCE) over Northern Hemisphere (NH) land averaged 23.9 million km² in 2024. This was 1.0 million km² less than the 1991–2020 mean and 1.2 million km² below the mean of the full period of record (1967–2024; Table 2.5). Overall, 2024 had the third-least-extensive cover on record. Twelve-month running mean SCE departures over all NH lands have not been as low as they were at the end of 2024 since June 2007, and before then July 1990 (Fig. 2.24a). Monthly SCE in 2024 ranged from a maximum of 46.9 million km² in January to a minimum of 2.6 million km² in August. Annual-mean SCE in North America (NA) was the least extensive on record in 2024, 0.1 million km² less than that of 1990; 2024 is now the second-least-extensive year on record. In terms of 12-month running means, the June 2024 value was the lowest since May 1968. Weekly NH SCE in 2024 was below long-term means for all but a few weeks from a winter maximum SCE in early January through the melt season. Autumn SCE was close to normal to begin the season, later becoming more erratic week to week from November into December (Fig. 2.24b).

In January, the NH SCE was in the middle tercile of the 58-year record. From February onward through spring, NH ranked in the lower tercile, from 1st to 19th least-extensive, with April having been record low. NA SCE in January was the 16th most extensive in January, while Eurasia was 18th least extensive. Both continents ranked from 3rd to 20th least extensive in each month from February to June. NA SCE was the third least extensive in both February and April. The 2024 snow season began in autumn with the 17th-most-extensive SCE over Europe in September and 18th in October. Meanwhile, snow was slow to appear over NA, with the 5th- and 13th-least-extensive SCE in September and October, respectively.

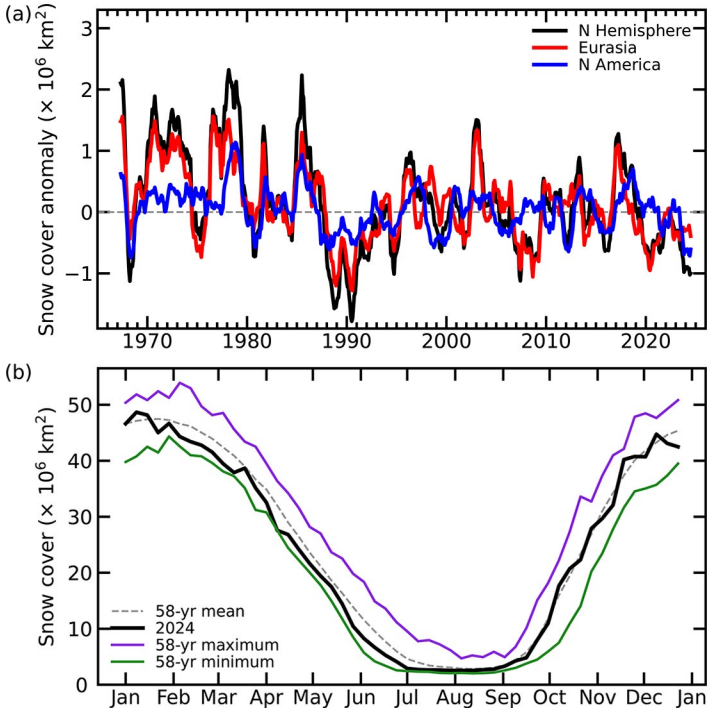

Fig. 2.24. (a) Twelve-month running anomalies of monthly snow cover extent (SCE) over Northern Hemisphere (NH) lands as a whole and Europe (EUR) and North America (NA) separately plotted on the seventh month using values from Nov 1966 to Dec 2024. Anomalies are calculated from NOAA snow maps. Mean NH SCE is 25.1 million km² for the full period of record. Monthly means for the period of record are used for nine missing months during 1968, 1969, and 1971 to create a continuous series of running means. Missing months fall between Jun and Oct. (b) Weekly NH SCE for 2024 (black) plotted with the mean (gray dashed line), maximum (purple), and minimum (green) SCE for each week. Mean weekly SCE and extremes are calculated using the 58-year record from Jan 1967 to Dec 2024. Weekly means for the period of record are used for 4, 21, and 12 missing weeks during 1968, 1969, and 1971 respectively. Weekly data granules represent SCE for each seven-day period ending on Monday.

NH SCE was the 19th least extensive in September and 25th most extensive in October. November and December SCE was 27th and 12th least extensive, respectively.

The contiguous United States' (U.S.) SCE was above normal, 16th most extensive, to start 2024, then rapidly fell to the 2nd least extensive in February. March through May ranged from 26th to 14th least extensive. Across Canada (CAN), the highest ranking for the winter and spring was 22nd least extensive in January, with each month from February through June ranging from 4th to 10th least extensive. In September, CAN ranked fourth least extensive and the U.S. was almost snow free. The U.S. and CAN SCE ranked, respectively, as the 17th and 16th least extensive in October. CAN also observed the 16th-least-extensive SCE in November, while the U.S. SCE increased to 24th most extensive. Snow conditions for the two nations reversed in December, with the U.S. seeing its 8th-least-extensive ranking and CAN its 15th most extensive.

SCE is calculated at the Rutgers Global Snow Lab (GSL) from daily SCE maps produced by meteorologists at the U.S. National Ice Center, who rely primarily on visible satellite imagery to construct the maps (Estilow et al. 2015). Maps depicting daily, weekly, and monthly conditions, anomalies, and climatologies may be viewed at the GSL website (https://snowcover.org).

Table 2.5. Monthly and annual climatological information for Northern Hemisphere (NH), Eurasia (EUR), and North America (NA) snow cover extent (SCE) between Nov 1966 and Dec 2024. Included are the numbers of years with data used in the calculations, NH anomalies, NH means, NH standard deviations (Std. Dev.), and ranks. Areas are in millions of square kilometers. 1968, 1969, and 1971 have one, five, and three missing months, respectively, and thus are not included in the annual (Ann) calculations. NA includes Greenland. Ranks are from most to least extensive (least to most in parentheses).

Time Period	Yrs	NH Anomaly	NH Mean	NH Std. Dev.	2024 NH Rank	2024 EUR Rank	2024 NA Rank
Jan	58	–0.2	47.1	1.5	32 (27)	41 (18)	16 (43)
Feb	58	–2.1	45.9	1.8	50 (9)	39 (20)	56 (3)
Mar	58	–2.0	40.4	1.8	51 (8)	46 (13)	45 (14)
Apr	58	–2.6	30.4	1.7	58 (1)	49 (10)	56 (3)
May	58	–1.9	19.0	2.0	45 (14)	40 (19)	53 (6)
Jun	57	–2.6	9.2	2.5	46 (12)	44 (14)	48 (10)
Jul	55	–1.1	3.8	1.2	45 (11)	45 (11)	44 (12)
Aug	56	–0.3	2.9	0.7	33 (24)	51 (6)	23 (34)
Sep	56	–0.5	5.4	0.9	40 (17)	17 (40)	54 (3)
Oct	57	+0.3	18.6	2.6	25 (33)	18 (40)	47 (11)
Nov	59	0.0	34.4	2.1	32 (28)	30 (30)	33 (27)
Dec	59	–1.0	43.7	1.8	47 (13)	39 (21)	44 (16)
Ann	55	–1.2	25.1	0.8	53 (3)	47 (9)	55 (1)

d. Hydrological cycle (atmosphere)

1. SURFACE HUMIDITY

—K. M. Willett, A. J. Simmons, M. Bosilovich, and D. A. Lavers

Global near-surface humidity remained exceptionally high in 2024, with a record-wet annual-mean specific humidity (q) anomaly over both land and ocean (Fig. 2.25; Table 2.6). This was the case for all data products, with record anomalies ranging from 0.32 g kg^{-1} (ERA5) to 0.58 g kg^{-1} (MERRA-2 masked to Met Office Hadley Centre Integrated Surface Dataset of Humidity [HadISDH] coverage) over land and 0.35 g kg^{-1} (ERA5) to 0.56 g kg^{-1} (HadISDH) over ocean. In all cases, 2024 land and ocean q was at least 0.1 g kg^{-1} wetter than in 2023. Global-mean relative humidity (*RH*), excluding MERRA-2, remained below the 1991–2020 baseline over land, between −0.13%rh to −0.71%rh (note that %rh is the unit for relative humidity, which is a percentage of how saturated the air is), meaning that air saturation is still low. However, land *RH* was not as dry as recent years in ERA5 and HadISDH, including 2023. Ocean near-surface *RH* was at or above the long-term mean in 2024. It showed a greater level of saturation than in 2023 in all data products, continuing a moistening tendency from 2020/21 and becoming a record-humid year for HadISDH and the Japanese Reanalysis for Three Quarters of a Century (JRA-3Q). Unlike land and ocean q, as well as land *RH*, there is little temporal agreement between any of the data products. Hence, uncertainty in ocean *RH* is large.

The recent ocean *RH* increase was consistent with the large increase in ocean near-surface water vapor, as inferred by q. This was related to the presence of El Niño from June 2023 to May 2024, which pumped extra moisture into the air in response to the warmer air and sea temperatures. Additional potential drivers of the extraordinarily warm near-surface air temperature in 2023/24 are still being explored (Goessling et al. 2025), including ongoing greenhouse gas emissions, reduced aerosol emissions, unusual heat in the North Atlantic Ocean, reduced low-cloud cover (Goessling et al. 2025), approach to solar maximum (NASA 2024), and additional stratospheric water vapor from the Hunga eruption. If these factors have been sufficient to contribute to global mean temperature, then they will likely also be contributing to the large amount of water vapor (q) and greater saturation (*RH*) compared to recent years.

Notably, previous El Niño events of 1972/73, 1977/78, 1982/83, 1986/87, 1991/92, 1997/98, 2009/10, 2015/16, and even the weak 2020 event are detectable in the global mean land and ocean q records (Figs. 2.25a–d, 2.26a). Associated peaks in *RH* are present but less clear, especially for ocean *RH*, with some events apparent in some data products but not others (Figs. 2.25e–h, 2.26c). Other sources of variability, including observational errors and biases, also contribute to *RH* variability. The 2023/24 El Niño was weaker and shorter (in terms of Niño-3.4 region temperatures) than the 1982/83, 1997/98, and 2015/16 events, making the q and *RH* anomalies even more noteworthy. The 1977/78, 1986/87, 2009/10, and 2023/24 El Niños were preceded by protracted periods of La Niña, which likely suppressed humidity somewhat, resulting in apparently larger increases thereafter. This was evident

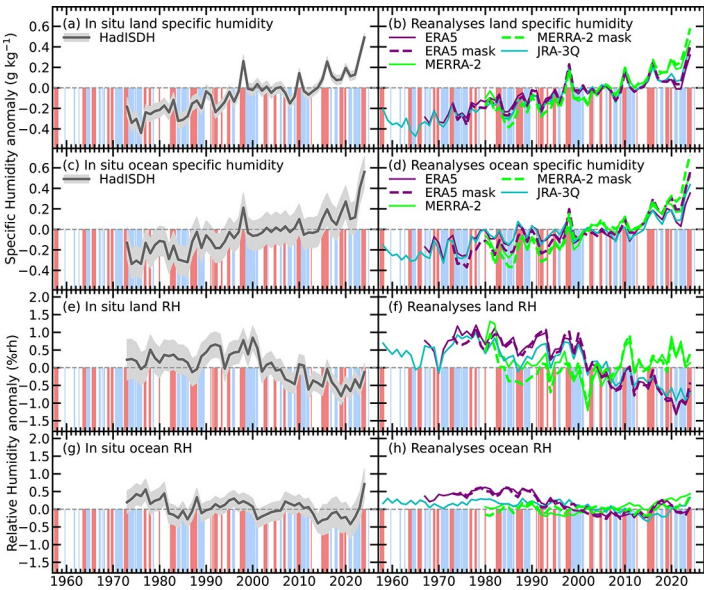

Fig. 2.25. Global average surface humidity annual anomalies (g kg^{-1} for [a]–[d] and %rh for [e]–[h]; 1991–2020 base period). For the in situ datasets, 2-m surface humidity is used over land, and ~10-m surface humidity over the oceans. For the reanalysis, 2-m humidity is used over the whole globe. For ERA5, ocean-series-only points over open sea are selected. ERA5 mask is a version of ERA5 limited to the spatial coverage of the Met Office Hadley Centre Integrated Surface Dataset of Humidity (HadISDH). 2-sigma uncertainty is shown for HadISDH capturing the observation, gridbox sampling, and spatial coverage uncertainty. Pink and blue shading highlights El Niño and La Niña years respectively, as identified by the NOAA Physical Sciences Laboratory Nino-3.4 index using the ±0.5°C threshold. (Sources: HadISDH [Willett et al. 2013, 2014, 2020]; ERA5 [Hersbach et al. 2020]; the Japanese Reanalysis for Three Quarters of a Century [JRA-3Q; Kosaka et al. 2024]; MERRA-2 [Gelaro et al. 2017].)

for *q* land and ocean but inconsistent for *RH* land and ocean, with differences between data products. Masked versions of MERRA-2 and ERA5, matching HadISDH coverage, show consistently higher *q* anomalies for recent years than their full-coverage equivalents (Table 2.6). This suggests that HadISDH is undersampling regions with lower *q* anomalies, which tend to be the drier regions (Simpson et al. 2024). Note that MERRA-2 land *RH* is quite different from that of the other estimates; the reasons for this are an active area of investigation.

Gaps over the drier land regions in HadISDH are clear in Appendix Figs. A2.6 and A2.8, as is the limited ocean coverage, leaving the Southern Ocean and central and eastern tropical Pacific barely sampled. Widespread wet anomalies in *q* exceeded 1 g kg^{-1} over northern Australia, South and North Korea, Japan, and their surrounding seas, as well as over India, the Caribbean and Central America, part of the North Pacific, and parts of northern tropical Africa. These were common to all data products (Plate 2.1h; Appendix Fig. A2.7) but with slight divergence over the North Pacific region. Anomalously large water vapor amounts were more widespread than

Table 2.6. Global mean surface-specific (*q*) and relative humidity (RH) anomalies (g kg^{-1} and %rh, respectively) for 2024 and 2023. Note that no previous record is reported for ocean RH because a long-term trend has not been robustly established. Values with a thermometer icon (🌡) identify new record-high values and year of previous highest.

Dataset	*q* (g kg^{-1}) 2024 Global Mean Anomaly	*q* (g kg^{-1}) 2023 Global Mean Anomaly	RH (%rh) 2024 Global Mean Anomaly	RH (%rh) 2023 Global Mean Anomaly	RH (%rh) Record low (Year of Record Low)
HadISDH.land	0.49 (2023) 🌡	0.31	–0.13	–0.56	–0.79 (2019)
ERA5 Over Land	0.32 (2016) 🌡	0.17	–0.67	–1.05	–1.32 (2021)
ERA5 Over Land Masked	0.40 (2023) 🌡	0.22	–0.43	–1.02	–1.26 (2021)
MERRA-2 Over Land	0.46 (2023) 🌡	0.33	0.14	0.01	–1.21 (2002)
MERRA-2 Over Land Masked	0.58 (2023) 🌡	0.40	0.40	0.04	–1.10 (2002)
JRA-3Q Over Land	0.38 (2023) 🌡	0.26	–0.71	–0.91	–0.93 (2021)
HadISDH.marine	0.56 (2023) 🌡	0.4	0.71 (1977) 🌡	0.06	-
ERA5 Over Ocean	0.35 (2023) 🌡	0.24	0.03	–0.08	-
ERA5 Over Ocean Masked	0.56 (2023) 🌡	0.39	0.07	–0.18	-
MERRA-2 Over Ocean	0.52 (2023) 🌡	0.42	0.44	0.37	-
MERRA-2 Over Ocean Masked	0.73 (2023) 🌡	0.55	0.39	0.14	-
JRA-3Q Over Ocean	0.44 (2023) 🌡	0.34	0.33 (1959) 🌡	0.10	-

in 2023. Then, the El Niño warm tongue pattern, strong positive Indian Ocean dipole, and high North Atlantic sea surface temperature (SST) patterns were clear. This spreading of positive *q* anomalies is common to many El Niño years. However, the 2023/24 *q* anomalies, in the context of the historical record, were unusually widespread and large (Fig. 2.26a). Despite this, some dry anomalies persisted from 2023 over the Amazon, central and southern Africa, and Mexico, and were actually more widespread and intense.

Positive, more-saturated-than-normal *RH* anomalies were more widespread and stronger than in recent years (Fig. 2.26; Plate 2.1i; Appendix Figs. A2.7, A2.9). Northern and eastern Australia, India, eastern Mongolia and northeastern China, Kazakhstan, and northeastern North America over land were more humid than normal. The positive anomalies over the eastern tropical Pacific, northeast Atlantic, and North Pacific were also notable. As for *q*, more-arid-than-normal anomalies strengthened relative to 2023 over the Amazon, central and southern Africa, and Mexico. HadISDH differs from ERA5 and MERRA-2 by showing less intense negative *RH* anomalies.

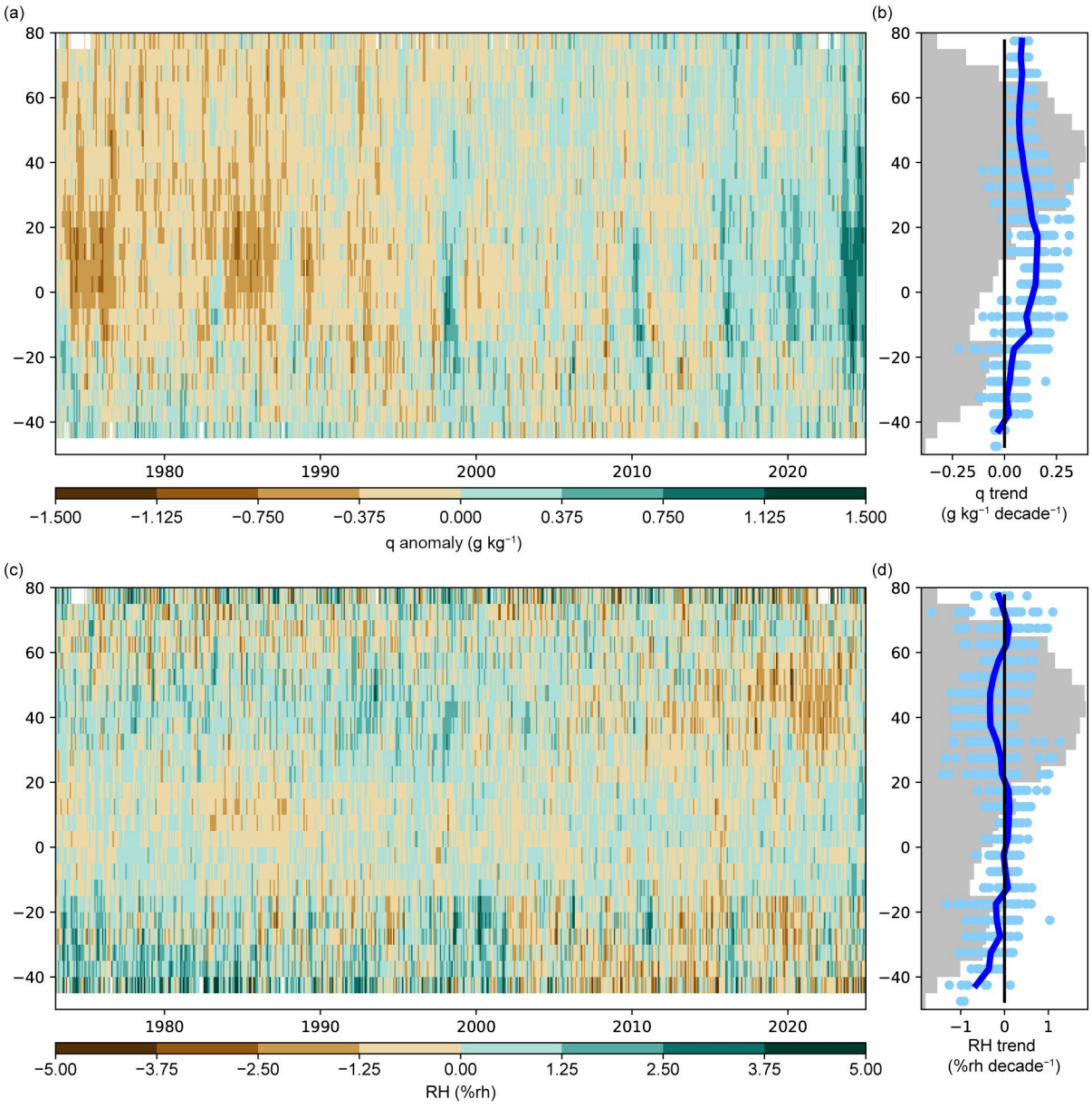

Fig. 2.26. Latitudinal monthly mean anomalies of (a) specific humidity (g kg⁻¹) and (c) relative humidity (%rh) by month from Met Office Hadley Centre Integrated Surface Dataset of Humidity over Land and Ocean (HadISDH.blend). (b),(d) Decadal trends for each gridbox (dots) and latitude band mean (line) are fitted using an ordinary least-squares (OLS) linear regression with an autoregressive (1) correction following Santer et al. (2008), with gray shading representing the percentage of globe covered by observations (in gridboxes) at each latitude band. Latitude band means are only calculated where there are at least five gridboxes (5° × 5°).

2. HUMID-HEAT EXTREMES OVER LAND

—K. M. Willett, R. M. Horton, Y. T. E. Lo, C. Raymond, C. D. W. Rogers, and D. Wang

Following an exceptional increase in the intensity and frequency of high humid heat in 2023, 2024 continued the upward trajectory (Fig. 2.27; Table 2.7). Maximum humid-heat intensity (T_wX; Table 2.7) was 0.5°C higher than the 1991–2020 average and only slightly lower than that of 2023 (0.6°C); where maximum humid-heat intensity is the annual median of the global land median monthly maximum wet-bulb temperature. Remarkably, high daily maximum humid-heat frequency (T_wX90p; Table 2.7) far exceeded the previous record, at 35.6 days above average versus 26.1 days in 2023; where high daily maximum humid-heat frequency is the annual sum of global-mean days per month with daily maximum wet-bulb temperature exceeding the local 90th percentile. These values are based on the gridded HadISDH Extremes (HadISDH.extremes.1.2.0.2024f; Willett 2023a,b,c; Willett et al. 2024) dataset, where monthly indices of daily maximum and minimum wet-bulb temperature are used as a measure of humid heat. Note that for the purposes of this review, "humid heat" is used as an energetic term that includes the contribution of temperature and moisture over the entire globe and annual cycle, rather than a term that focuses exclusively on regions and seasons where temperature and moisture are high.

For all specific thresholds of T_wX exceedance (Fig. 2.27d; Table 2.7), 2024 had record-high frequencies for the second consecutive year. For T_wX25, T_wX27, and T_wX29, these anomalies (with respect to the 1991–2020 base period) were 11.0 days, 13.8 days, and 1.7 days, respectively. T_wX31 anomalies were tied for record most frequent with both 2023 and 1998, at 0.2 days. In much of the tropics, almost every day of the year exceeds the T_w = 25°C threshold. Hence, the maximum possible globally averaged anomaly for T_wX25 is constrained and, therefore, can be less than the anomalies for T_wX27.

In 2024, most global land regions experienced more intense (T_wX) and more frequent (T_wX90p) high daily maximum humid-heat days than the 1991–2020 average (Plates 2.1j,k). High daily maximum humid heat was particularly frequent over India, Southeast Asia, East Asia, Australia, the Caribbean, Central America, and Europe (Plate 2.1k). There were several small regions of negative anomalies, which are mostly consistent between T_wX and T_wX90p; these occurred notably east of the Caspian Sea, in Mongolia, around the Red Sea,

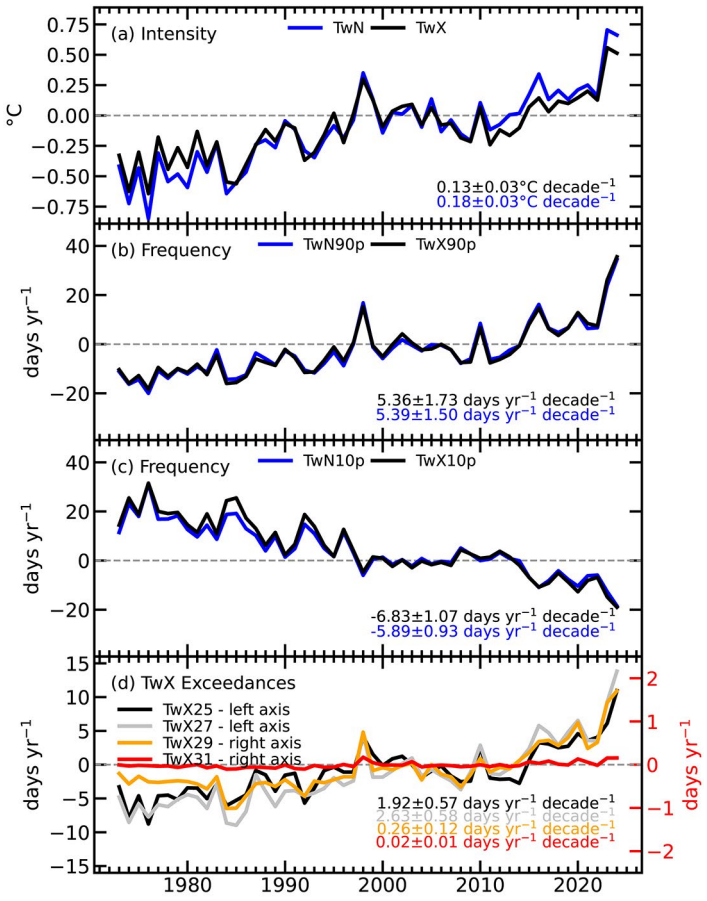

Fig. 2.27. Global land annual anomaly time series of various daily maximum and minimum humid-heat indices from Met Office Hadley Centre Integrated Surface Dataset of Humidity Extremes (HadISDH.extremes), relative to a 1991–2020 base period. Decadal trends (significant at p<0.01) are also shown. Trends were fitted using an ordinary least-squares linear regression with an autoregressive (1) correction following Santer et al. (2008). (a) Anomaly of the annual median of the global median monthly maximum (black) and minimum (blue) wet-bulb temperature (°C). (b) Anomaly of the annual sum of days where maximum (black) and minimum (blue) wet-bulb temperature exceeds the locally defined daily 90th percentile. (c) Anomaly of the annual sum of days where maximum (black) and minimum (blue) wet-bulb temperature is lower than the locally defined daily 10th percentile. (d) Anomalies of the annual sums of days where the maximum wet-bulb temperature ≥25°C, 27°C, 29°C, and 31°C thresholds. Note that coverage is skewed towards the northern extratropical latitudes with large data gaps over Africa, as well as considerable gaps over South America, Australia, and parts of Central Asia (see Plates 2.1j,k for spatial coverage).

in western portions of South America, and in the Sonoran Desert of northwestern Mexico and the southwestern United States.

Figure 2.28 presents 2024 indices by their decile relative to the historical record. Southeast Asia, eastern China, southern Japan, India, and northern Australia stood out as regions where T_wX25 and T_wX27 exceedances were "very unusually frequent" (top decile; Figs. 2.28a,b). This was similar to 2023, but 2024 also had more widespread "very unusually frequent" exceedances for the threshold of T_wX29 (Fig. 2.28c)—notably over eastern China and southern Japan, reflecting a record-setting high-humid-heat event in July and early August. Counting only gridboxes where exceedances of the respective thresholds occurred climatologically (≥15 years within the 1991–2020 period), 24%–37% of the 2024 gridbox-level high-humid-heat frequency fell in the "very unusually frequent" category and just 0%–4% in the "very unusually infrequent" category (not shown).

High humid heat is of particular concern to human health (Xu et al. 2025), including its daily maximum values (Matthews et al. 2025) and nighttime values (Okamoto-Mizuno et al. 1999). This year, four new indices are introduced (Table 2.7). The minimum humid-heat intensity (T_wN) and high daily minimum humid-heat frequency (T_wN90p) are presented. Low humid-heat (i.e., fresh-cool) day frequencies (T_wX10p, T_wN10p) are also introduced, defined in Table 2.7 (Figs. 2.27a–c). Daily minimum wet-bulb temperatures are not always representative of nighttime wet-bulb temperatures, and so that distinction is avoided here.

The time series of T_wN indices closely follow the T_wX equivalents. T_wN in 2024 was well above average (+0.7°C) and only a fraction of a degree cooler than in 2023. T_wN90p was 34.4 days above average in 2024, breaking the record set in 2023 (23.8 days). Overall, 1973–2024 trends in maximum and minimum humid-heat intensity (T_wX = 0.13±0.03 decade^{-1}; T_wN = 0.18±0.03°C decade^{-1}) and

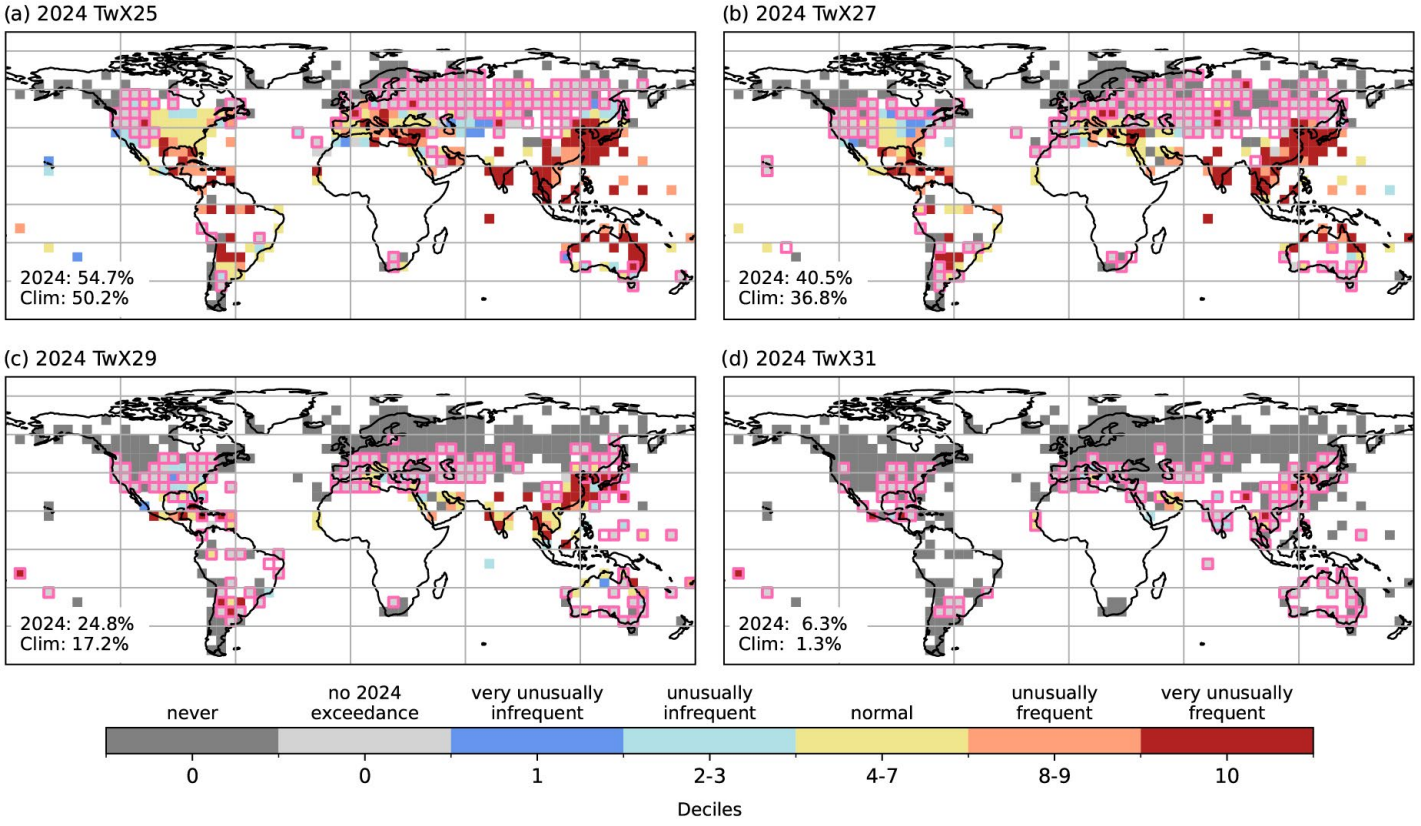

Fig. 2.28. High humid-heat extremes of 2024 as deciles over the period 1973–2024, ranking the number of days with maximum wet-bulb temperature (T_w)≥(a) 25°C (T_wX25), (b) 27°C (T_wX27), (c) 29°C (T_wX29), and (d) 31°C (T_wX31). Gridboxes bounded in pink indicate <15 years within the 1991–2020 period when exceedances occur. These panels are annotated with the percentage of observed gridbox area where an exceedance occurred in 2024 and climatologically (including only gridboxes with ≥15 years of at least one exceedance between 1991 and 2020). Data have been screened to remove gridboxes where temporal completeness is less than 70% (<36 years in 52), with whole years removed if one or more months are missing. White gridboxes (over land) represent regions with insufficient data.

high humid-heat frequency (T_wX90p = 5.36±1.73 days year^{-1} decade^{-1}; T_wN90p = 5.39±1.50 days year^{-1} decade^{-1}) were similar, robustly portraying increasing humid heat. Positive trends for daily minimum humid-heat anomalies for T_wN and T_wN90p (Appendix Figs. A2.10, A2.11) were marginally more ubiquitous than for T_wX and T_wX90p (Plates 2.1j,k).

As for the equivalent dry-bulb temperature extremes (section 2b4; Figs 2.7b,d), frequencies of low humid-heat days (Fig. 2.27c) have decreased substantially, with the rate being slightly stronger than for high humid-heat days, but with the opposite sign. T_wX10p and T_wN10p were 19 days and 18.4 days below the 1991–2020 average in 2024, respectively, both of which were new record lows.

Table 2.7. Definitions of 10 humid-heat indices and their respective recent global land annual anomalies (1991–2020 base period). The global annual anomalies for the exceedance indices (not T_wX or T_wN) are the sum of the monthly spatial means over the globe. For T_wX and T_wN, the median is used as a more robust measure in the presence of outliers, finding the median first over space for each month and then over time.

Index	Description	Meaning	2021 Global Anomaly	2022 Global Anomaly	2023 Global Anomaly	2024 Global Anomaly
T_wX	Annual median of monthly maximum of the daily-maximum wet-bulb temperature	Intensity of maximum humid heat	0.2°C	0.1°C	0.6°C	0.5°C
T_wN	Annual median of monthly minimum of the daily-minimum wet-bulb temperature	Intensity of minimum humid heat	0.3°C	0.2°C	0.7°C	0.7°C
T_wX90p	Days per year exceeding the 90th percentile of the climatological daily-maximum wet-bulb temperature (seasonally varying)	Frequency of high daily-maximum humid-heat days relative to local climatology	8.4 days	7.5 days	26.1 days	35.6 days
T_wX10p	Days per year below the 10th percentile of the climatological daily-maximum wet-bulb temperature (seasonally varying)	Frequency of low daily-maximum humid-heat days relative to local climatology	–8.1 days	–6.8 days	–14.8 days	–19 days
T_wN90p	Days per year exceeding the 90th percentile of the climatological daily-minimum wet-bulb temperature (seasonally varying)	Frequency of high daily-minimum humid-heat days relative to local climatology	6.4 days	6.7 days	23.8 days	34.4 days
T_wN10p	Days per year below the 10th percentile of the climatological daily-minimum wet-bulb temperature (seasonally varying)	Frequency of low daily-minimum humid-heat days relative to local climatology	–6.2 days	–5.9 days	–12.6 days	–18.4 days
T_wX25	Days per year where the daily-maximum wet-bulb temperature was ≥25°C	Frequency of moderately high humid-heat days	3.6 days	4.1 days	6.1 days	11.0 days
T_wX27	Days per year where the daily-maximum wet-bulb temperature was ≥27°C	Frequency of high humid-heat days	3.6 days	3.5 days	9.3 days	13.8 days
T_wX29	Days per year where the daily-maximum wet-bulb temperature was ≥29°C	Frequency of very high humid-heat days	0.4 days	0.5 days	1.4 days	1.7 days
T_wX31	Days per year where the daily-maximum wet-bulb temperature was ≥31°C	Frequency of severe humid-heat days	0.1 days	–0.0 days	0.2 days	0.2 days

3. TOTAL COLUMN WATER VAPOR

—O. Bock, C. A. Mears, S. P. Ho, and X. Shao

In 2024, the global (60°S–60°N) mean total column water vapor (TCWV) was approximately 5% above the 1991–2020 climatological average (Table 2.8), with little difference between ocean and land, according to three global reanalyses (ERA5, MERRA-2, and JRA-3Q) and three observational datasets (Microwave Radiometer [MWR], satellite Global Navigation Satellite System Radio Occultation [GNSS-RO], and ground-based GNSS). It was the wettest year on record across all six datasets and for all three domains (global, ocean, and land), surpassing 2023, which had already set records in some datasets (Fig. 2.29). This remarkable positive anomaly is associated with the unprecedented high global-mean surface temperature (GMST; section 2b1), making 2024 the warmest year in a multi-dataset record dating back to the mid-1800s. The strong correlation between temperature and TCWV anomalies again highlights how tightly the Clausius–Clapeyron relation constrains the global climate system (O'Gorman and Muller 2010). The relation predicts that a GMST anomaly of 0.7°C (actual range was 0.63°C–0.72°C; section 2b1) corresponds to a TCWV anomaly of 4.9%, assuming a scaling factor of 7% per °C. Interestingly, there was a contrast between land and ocean GMST anomalies in 2024, with land slightly warmer than the ocean. This is also reflected in units of kg m^{-2} of TCWV, with ocean TCWV anomalies greater than for land, but not in percentage (Table 2.8). This result suggests a substantial moisture transport from ocean to land on interannual timescales (Trenberth and Fasullo 2013).

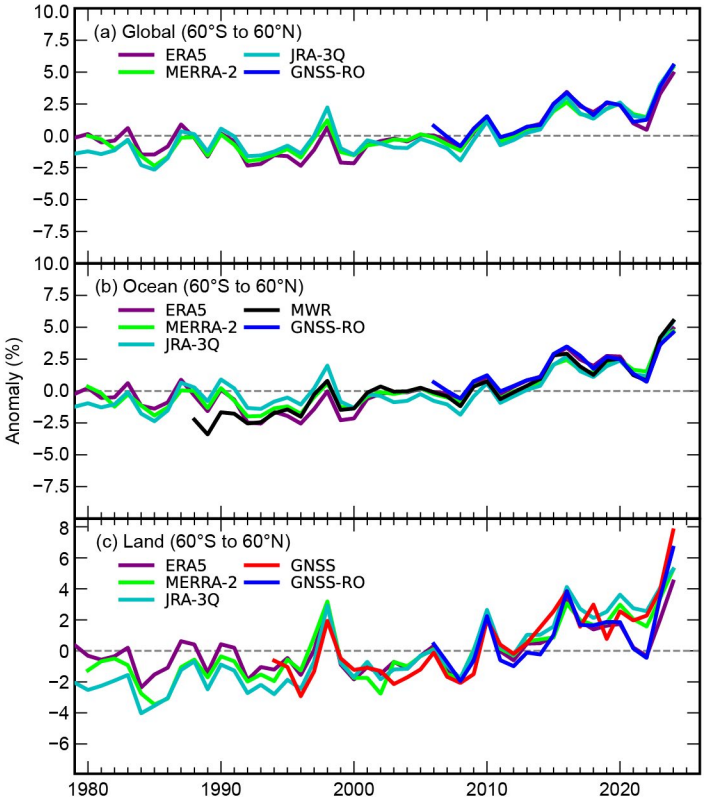

Fig. 2.29. Global mean (60°S–60°N) total column water vapor annual anomalies (%; 1991–2020 base period) over (a) land and ocean, (b) ocean-only, and (c) land-only from observations and reanalyses. The shorter time series from the observations have been adjusted, so there is zero mean difference relative to the ERA5 results during their respective periods of record.

The spatial distribution of TCWV anomalies in 2024 differs markedly from that of 2023, which exhibited a strong El Niño pattern, as well as from the La Niña years of 2021 and 2022 (Bock et al. 2024; Mears et al. 2023). In 2024, the moisture excess was nearly ubiquitous (Plate 2.1l). Almost 90% of the global atmosphere was wetter than the 1991–2020 climatological mean, with approximately 65% of the increase occurring over the oceans and 25% over land. Some regions experienced extreme positive TCWV anomalies reaching 15%–20%, including northeastern Canada, Europe, the Middle East, eastern Asia, and northeastern Australia. Most of these regions are adjacent to oceans that recorded exceptionally high temperature anomalies in 2024, notably the Indian and Atlantic Oceans, polar seas, and the extratropical Pacific.

Figure 2.30a shows the year of record-high TCWV anomaly across the globe from 1988 to 2024 for the JRA-3Q reanalysis, which is consistent with other datasets. Strong moistening (and warming) has particularly been observed in recent years, especially in 2023 and 2024, over the Indian and Atlantic Oceans and most land areas in the Northern Hemisphere. In contrast, the central-eastern Pacific experienced its strongest moist anomaly in 1998 during the exceptional 1997/98 El Niño event. The lower tropospheric temperature set a record in 2024 across most of the tropics, including the tropical Pacific as a whole (Plate 2.1f). Figure 2.30b shows that more than 20% of the globe recorded its highest TCWV anomaly in 2024—far exceeding 2023 (which ranks

Table 2.8. Global mean (60°S–60°N) total column water vapor (TCWV) anomalies (kg m^{-2} (%); 1991–2020 base period) for 2024 and linear trends (kg m^{-2} decade^{-1}) over the period 1991–2024 for reanalyses and Microwave Radiometer (MWR), (*) 2006–24 for Global Navigation Satellite System Radio Occultation (GNSS-RO), (**) 1995–2024 for ground-based GNSS (including 166 stations over land). Note that the inconsistency (ocean anomaly smaller than land) between GNSS-RO anomalies and those from reanalyses and satellites is likely due to the shorter base period.

TCWV Anomalies in 2024, Units in kg m^{-2} (%)						
Dataset	ERA5	MERRA-2	JRA-3Q	MWR	GNSS-RO*	GNSS**
Global	1.32 (4.9%)	1.50 (5.4%)	1.50 (5.5%)		1.45 (5.5%)	
Ocean	1.40 (4.9%)	1.38 (4.7%)	1.59 (5.5%)	1.63 (5.5%)	1.28 (4.6%)	
Land	1.04 (4.5%)	1.26 (5.2%)	1.19 (5.4%)		1.49 (6.6%)	1.48 (7.8%)
Trends over 1991–2024, Units in kg m^{-2} (% decade^{-1})						
Dataset	ERA5	MERRA-2	JRA-3Q	MWR	GNSS-RO*	GNSS**
Global	0.42 ± 0.06 (1.55 ± 0.23)	0.41 ± 0.07 (1.48 ± 0.25)	0.37 ± 0.10 (1.37 ± 0.35)		0.57 ± 0.17 (2.15 ± 0.63)	
Ocean	0.49 ± 0.06 (1.71 ± 0.22)	0.44 ± 0.07 (1.49 ± 0.24)	0.36 ± 0.12 (1.25 ± 0.40)	0.48 ± 0.07 (1.64 ± 0.25)	0.53 ± 0.16 (1.89 ± 0.58)	
Land	0.23 ± 0.07 (0.98 ± 0.29)	0.34 ± 0.08 (1.45 ± 0.35)	0.43 ± 0.06 (1.90 ± 0.28)		0.53 ± 0.20 (2.38 ± 0.90)	0.39 ± 0.08 (2.03 ± 0.47)

second at ~10%) and all previous years, including the three strongest El Niño years within the period (1997/98, 2009/10, and 2015/16).

The pronounced wet anomaly in 2024 significantly impacts the linear trend estimated from 1991 onward. The global-mean linear trend in ERA5 increases from 0.38 kg m^{-2} to 0.42 kg m^{-2} decade^{-1} (1.40% decade^{-1} to 1.55% decade^{-1}) between 2023 (Bock et al. 2024) and 2024 (Table 2.8). This increase is observed over ocean and land and is consistent across all datasets. Over the 34-year period, the total atmospheric water vapor content has increased by nearly 1.4 kg m^{-2} (or 5.1%), assuming an average trend value of 0.4 kg m^{-2} decade^{-1} (1.5% decade^{-1}).

This assessment is based on observations from satellite-borne MWRs over the oceans (Remote Sensing Systems [RSS] satellite; Mears et al. 2018), GNSS-RO data from the Constellation Observing System for Meteorology, Ionosphere, and Climate (COSMIC), Meteorological Operational satellite (MetOp)-A, -B, -C, COSMIC-2, PlanetIQ, Korea Multi-Purpose Satellite-5 (KOMPSAT-5), PAZ, TerraSAR-X (TSX), TerraSAR-X add-on for Digital Elevation Measurement (TDX), and Spire missions (Ho et al. 2020; Shao et al.

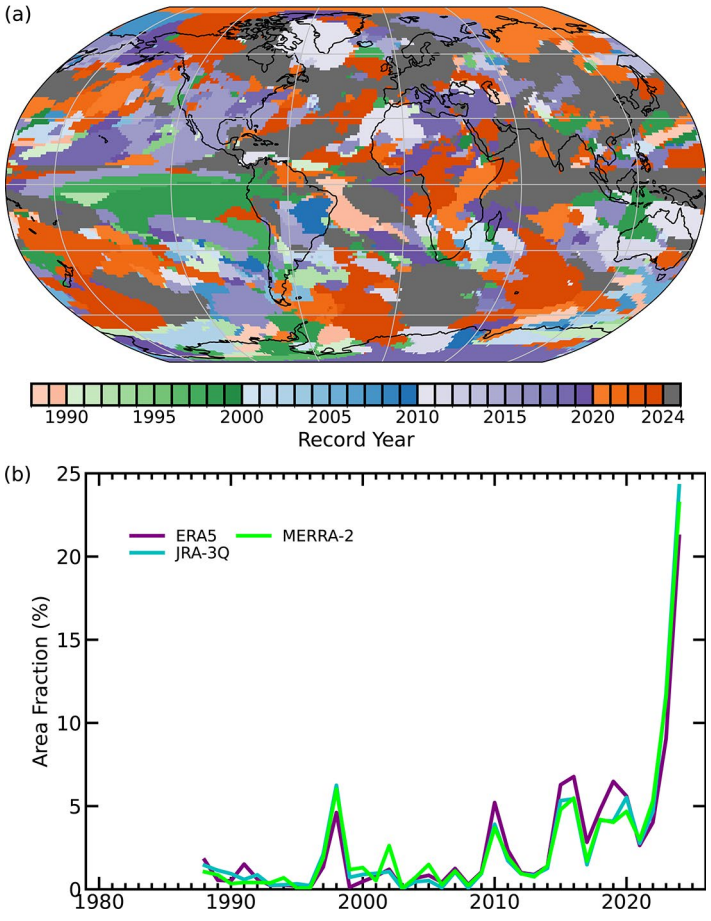

Fig. 2.30. (a) Record years in annual total column water vapor anomalies for the Japanese Reanalysis for Three Quarters of a Century (JRA-3Q) from 1988 to 2024. (b) Fraction of the globe for each year in (a).

2023), covering both land and ocean, as well as ground-based GNSS observations over land and islands (Bock 2025). Three global reanalysis products were used: ERA5 (Hersbach et al. 2020), MERRA-2 (Gelaro et al. 2017), and JRA-3Q (Kosaka et al. 2024). All three reanalyses assimilate satellite microwave radiometer data (as radiances) and GNSS-RO data (as bending angles) but not ground-based GNSS measurements, which serve as an independent validation dataset.

4. UPPER-TROPOSPHERIC HUMIDITY

—V. O. John, L. Shi, E.-S. Chung, T. Stevens, R. P. Allan, S. A. Buehler, and B. J. Soden

The global-mean upper-tropospheric humidity (UTH; %rh) anomalies, shown using relative humidity in Plate 2.1m (based on microwave data) and Fig. 2.31a, were slightly below normal in 2024, especially during the first half of the year (note that %rh is the unit for relative humidity, which is a percentage of how saturated the air is). This is expected during El Niño, which ended in boreal spring 2024, associated with large drier-than-average relative humidity anomalies at tropical and subtropical latitudes over the Pacific Ocean (McCarthy and Toumi 2004). As shown in Plate 2.1m, an annual average anomaly map of UTH in 2024, these drier areas are almost balanced by more humid-than-average anomalies in other areas of the tropics, unlike in 2023 (John et al. 2024). In 2023, there were slightly more areas in the tropics that were more humid than average (central and eastern Pacific, tropical Atlantic, and central Africa), but in 2024 the only substantial areas with above-average humidity were east Africa, the Arabian Sea, central India, northeast Australia, and adjacent areas of the western Pacific.

UTH anomalies, in general, reflect the large-scale circulation patterns. A strong positive phase of the Indian Ocean dipole (IOD) can be seen. Here, the cooler-than-normal eastern Indian Ocean and warmer-than-normal western Indian Ocean led to reduced convection in the east and enhanced convection in the west. There were generally dry conditions over northern South America and moist signatures over central India and the Horn of Africa. Very dry patches over southern Africa indicate ongoing drought in those regions, which began in late 2023. Despite 2023 and 2024 both being dominated by El Niño and a positive IOD, the spatial patterns are different. There were more widespread negative anomalies over North and South America and the western tropical Pacific in 2024 compared to 2023, as well as over eastern Asia and western Australia.

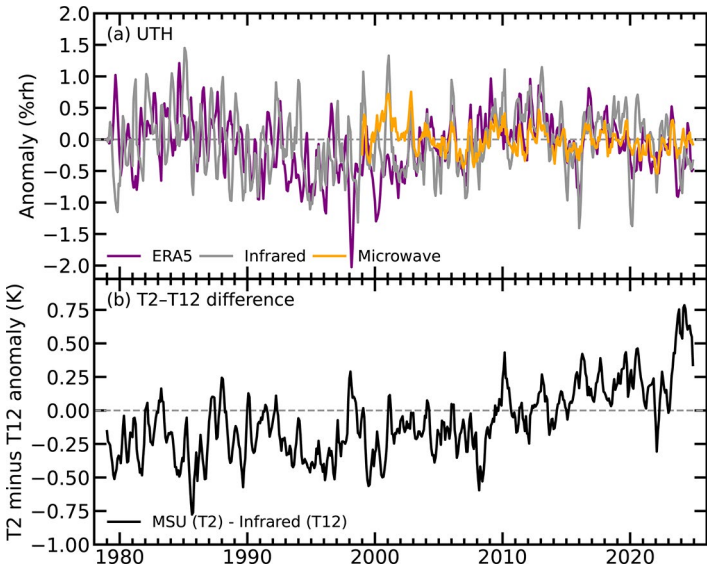

Fig. 2.31. Time series of (a) global monthly-mean anomaly upper-tropospheric humidity (UTH) for the three datasets (%rh; see text for details) and (b) the difference between upper-tropospheric temperature (T2) and water vapor channel (T12) brightness temperatures (K). Anomalies are with respect to the 2001–20 base period.

The mean and standard deviation (1-sigma) of the global monthly anomaly time series (Fig. 2.31) in 2024 were −0.10±0.22 %rh for the microwave based data (Chung et al. 2013), −0.47±0.44 %rh for the infrared based data (Shi and Bates 2011), and −0.31±0.44 %rh for ERA5 data (Hersbach et al. 2020). There is no significant long-term trend in any of the datasets. This is in line with the theoretical consideration that the large-scale relative humidity in the upper troposphere remains roughly unchanged (Ingram 2010). However, the absolute humidity (amount of water vapor) in the upper troposphere has increased. This is illustrated in Fig. 2.31b, which shows the difference between mid-to-upper-tropospheric mean layer temperature (Microwave Sounding Unit [MSU] T2; Zou et al. 2023) and the measured brightness temperature of the 6-μm water vapor channel (High-resolution Infrared Radiation Sounder [HIRS] T12), which is sensitive to the upper-tropospheric relative humidity. As the amount of water vapor in the upper troposphere (UT) increased, the emission level of the water vapor channel shifted higher in the troposphere. This resulted in water vapor emissions being associated with a lower temperature. Therefore, the positive trend in the difference (T2 – T12) time

series indicates moistening of the upper troposphere (Chung et al. 2014; Simmons 2022; John et al. 2024). The differences (T2 – T12) in 2024 were the largest in the series, implying record-high UT absolute humidity in 2024. These strikingly large anomalies are consistent with the presence of El Niño (for a portion of the year) as well as the record-high surface and lower tropospheric temperatures, near-surface specific humidity, and TCWV. The monthly anomalies became substantially less extreme late in 2024 as El Niño dissipated.

5. PRECIPITATION

—M. Ziese, R. S. Vose, R. Adler, G. Gu, and X. Yin

Precipitation is the primary source of fresh water needed for drinking, agriculture, hydropower, human wellbeing, and many other purposes. Both a lack (drought) and excess (e.g., flood) of water can have a large impact on human activities. The analyses presented here are based on data from two datasets: in situ from the Global Precipitation Climatology Centre (GPCC; Becker et al. 2013) and gauge-adjusted (including GPCC) satellite data from GPCP Version 3.2 (Huffman et al. 2023).

In 2024, excess precipitation (relative to the 1991–2020 baseline) was observed across much of the tropics (land and ocean; Fig. 2.32), Asia, and the northwestern Pacific, as well as the northern and southern subtropical Atlantic. A precipitation deficit occurred over southern Africa, the southeast Indian Ocean, the subtropical Pacific, South America, and the North Atlantic.

Globally, 2024 was the third-wettest year since 1983 (Fig. 2.33c; GPCP dataset only). While global land precipitation was around normal, precipitation over the oceans was far above normal, only exceeded by that of 1998, 2015, and 2016. The unusual high precipitation totals over the oceans (shown across the seasons in Fig. 2.32 but not in the land-only Plate 2.1n), were likely associated with above-normal sea surface temperatures (Plate 2.1a), which produced more regional evaporation (Plates 2.1h,l) and water for rainfall. This can be seen, for example, over the Gulf of America/Gulf of Mexico, Caribbean, and adjacent western Atlantic (Fig. 2.32) as well as over the Indian Ocean, western Pacific and South Pacific Convergence Zone, and northwestern Pacific. High ocean precipitation could be associated with the 2023/24 El Niño event; previous large El Niño events of 1997/98 and 2015/16 also preceded precipitation excess over the oceans.

Spatial variability of precipitation is higher compared to other atmospheric parameters such as air temperature. Therefore, precipitation totals as well as anomalies show a patchy pattern, where

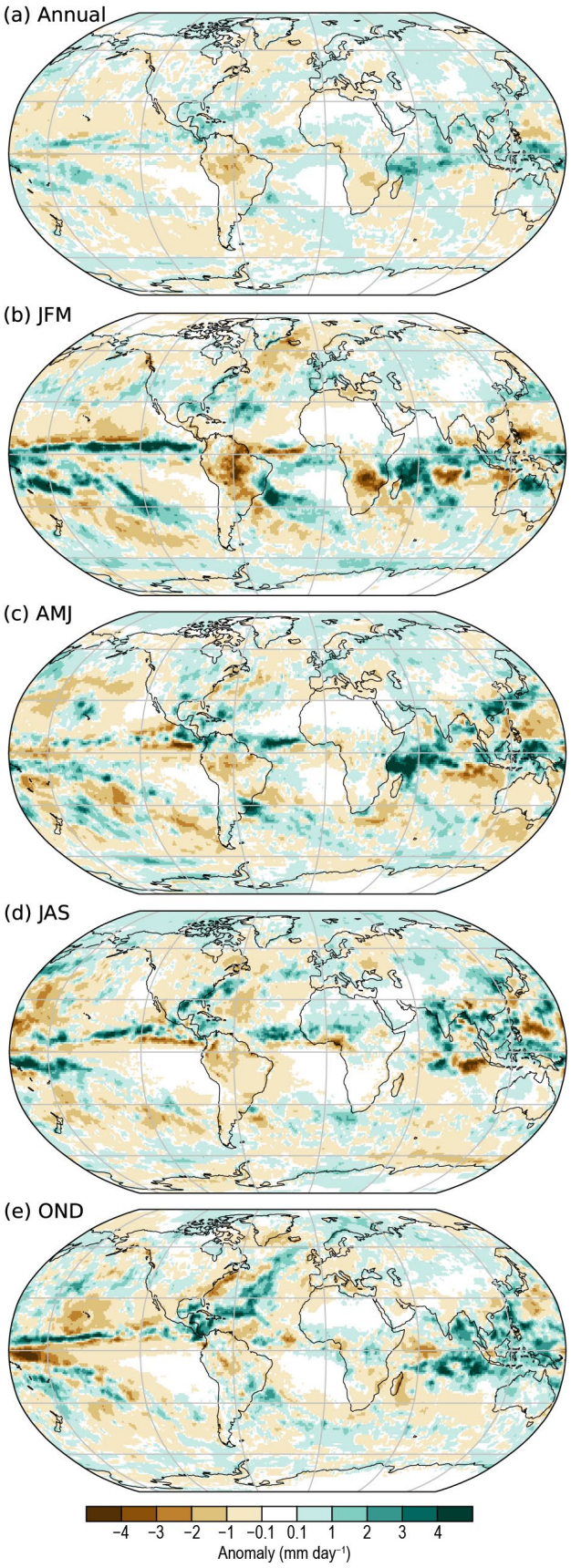

Fig. 2.32. 2024 annual and seasonal precipitation anomalies (mm day^{-1}; 1991–2020 base period) for (a) annual, (b) Jan–Mar (JFM), (c) Apr–Jun (AMJ), (d) Jul–Sep (JAS), and (e) Oct–Dec (OND). (Data source: Global Precipitation Climatology Project [GPCP].)

regions with excess precipitation (above the long-term mean) can be close to those with a precipitation deficit (below the long-term mean).

Focusing on land regions (Plate 2.1n), excess rainfall was observed in many parts of central and eastern Africa as well as in the Sahel region. Lower-than-usual rainfall was measured in southern Africa and western central Africa, reflecting drier-than-usual wet seasons. Madagascar and northwest Africa were also drier, having experienced multi-year drought (since 2020 and 2019, respectively; Fig. 2.32). These correspond with negative soil moisture anomalies (section 2d11).

Conditions were drier than usual in the Hindu Kush, parts of Southeast Asia, the Philippines, around the Laptev Sea in the Arctic, and also around the Himalayas. The latter was associated with a dry early monsoon season. Above-normal annual precipitation was mainly observed in the east, southeast, southwest, and northwest of Asia. All seasons were wetter than usual in northwestern and eastern Asia. Southern Asia exhibited strong wet anomalies in July, August, and September, but was otherwise mostly drier than usual.

In the Amazon basin, the drought that began in 2023 continued in 2024; all seasons were drier than usual (Fig. 2.33). While the majority of South America was drier than usual, some spots in the north, southeast, and south, such as western Patagonia, received excess precipitation (see section 7d for details).

Excess precipitation occurred across North America from the central Rocky Mountains to Florida (Plate 2.1n). Also, southern Central America and parts of the Caribbean, as well as some spots in north and northwest North America, were wetter than normal. Northern Central America, the northern Caribbean, and northeast and northern central North America were drier than usual.

The coastal regions in southern (including Tasmania), northwestern, and northeastern Australia had below-normal precipitation, as did smaller islands in the Pacific Ocean. The Maritime Continent, parts of northern, eastern, and western Australia, and some spots in New Zealand were wetter than normal.

Western and Central Europe as well as Scandinavia received more precipitation than the long-term mean. Eastern and southeastern Europe, the Middle East, and the region northward of the Black Sea were drier than normal.

The state of ENSO (El Niño–Southern Oscillation) influences regional precipitation patterns. El Niño conditions were present at the beginning of the year, then decreased and reached neutral conditions by April–June, which prevailed until the end of the year when weak La Niña-like conditions emerged. Associated with the El Niño conditions in the first months of the year are the below-normal precipitation totals in southern Africa and above-normal totals in eastern Africa, along with the wet conditions in East Asia, in southwestern North America, and northward of the Gulf of America/Gulf of Mexico (Fig. 2.32). These conditions dissipated by the latter half of 2024. Due to the ENSO-neutral conditions later in the year, corresponding seasonal anomalies were attributed to regional circulation and year-to-year variability.

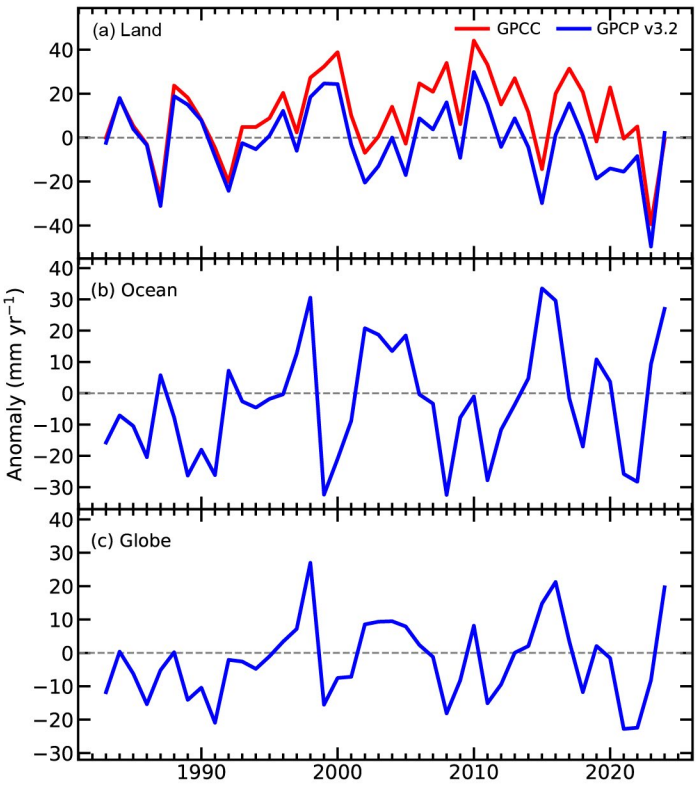

Fig. 2.33. 2024 globally averaged annual precipitation anomalies (mm yr^{-1}) relative to the 1991–2020 baseline period for (a) land areas, (b) ocean areas, and (c) globally (land and ocean).

6. LAND SURFACE PRECIPITATION EXTREMES

—M. R. Tye, S. Blenkinsop, M. G. Bosilovich, I. Durre, C. Lennard, I. Pinto, A. J. Simmons, and M. Ziese

Globally, 2024 was the wettest year on record with respect to extreme precipitation. The global-mean annual maximum daily precipitation total (Rx1day) from station and reanalysis records surpassed the previous record years of 2010 and 2020 (Fig. 2.34a).

More than two-thirds of the globe experienced unusually high precipitation (section 2d5), with attendant record-breaking extremes mostly occurring within the tropical belt. Many extremes occurred anomalously within extended droughts (sections 2d11, 2d12) or were seasonally unusual (e.g., during a dry season or during winter).

The strong El Niño in the first quarter, as well as the La Niña-like pattern that it transitioned to in the last quarter, both supported intensified precipitation extremes due to the accumulated atmospheric moisture associated with higher temperatures. Coupled with record ocean temperatures (see sections 2b1, 3b; Cheng et al. 2025), these conditions drove abnormally intense and clustered typhoons in the western Pacific (Cassidy 2024) and increased the distance of inland moisture transport into China (WWA 2024a). Cut-off lows across the North Atlantic spurred increased convective activity, which resulted in several record short-duration (sub-daily) rainfall totals. This activity included Storm Boris, which affected a large area in central Europe in September (see Sidebar 7.2; Magnusson et al. 2025), and intense rainfall that resulted in catastrophic flooding in Valencia, Spain, in October (see section 7f4; Pucik 2024). ENSO-associated shifts in the Intertropical Convergence Zone also impacted the locations of monsoonal systems and contributed to longer-duration precipitation extremes. A more-intense-than-normal hydrological cycle was apparent through connected mechanisms: above-normal air temperatures (section 2b1) and SSTs (sections 2b1, 3b), above-average seasonal precipitation (section 2d5), high soil moisture anomalies (section 2d11), high evaporation over land (section 2d13), high water vapor content (sections 2d1, 2d3), and the resultant precipitation maxima.

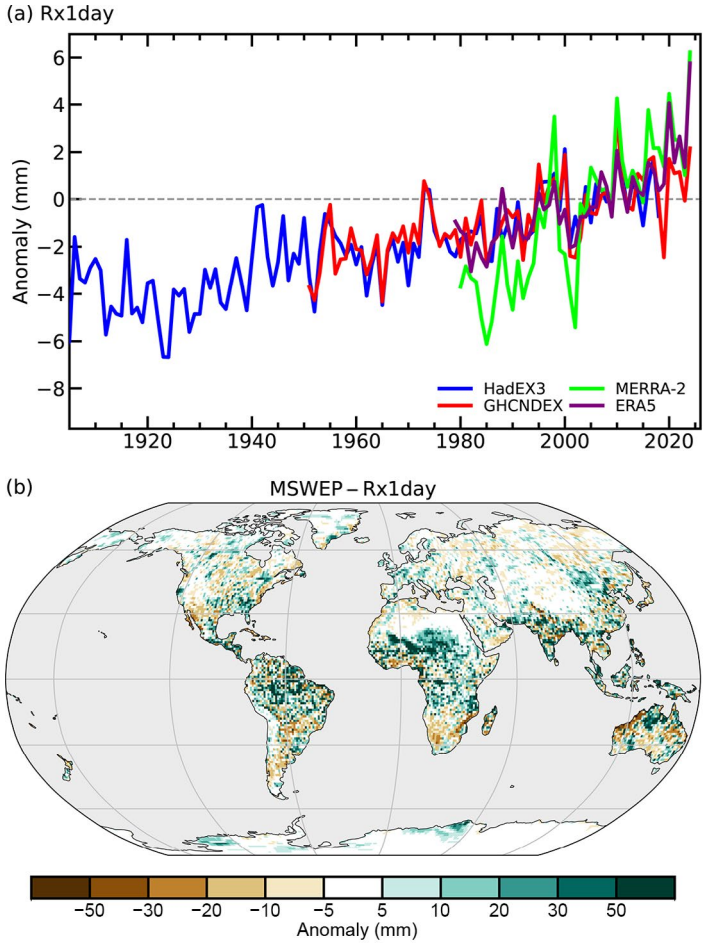

Fig. 2.34. (a) Global mean anomaly (with respect to 1991–2020) of one-day maxima (Rx1day) over land from the Met Office Hadley Centre Extremes dataset version 3 (HadEX3; Dunn et al. 2020), Global Historical Climatology Network Daily Extremes dataset (GHCNDEX; Donat et al. 2013), ERA5 (Hersbach et al. 2020), and MERRA-2 (Gelaro et al. 2017). (b) Global Rx1day anomalies in 2024 with respect to the 1991–2020 mean from Multi-Source Weighted-Ensemble Precipitation (MSWEP; Beck et al. 2019) highlighting a band of wet anomalies across the tropics.

Plate 2.1o and Figs. 2.34b, 2.35 show similar regions of wetter-than-normal one-day/accumulated five-day maxima (Rx1day, Rx5day) in a band between 30°S and 30°N. Higher latitudes experienced pockets of abnormal extreme precipitation within larger areas of drought conditions. Record-breaking accumulations, where noted, are limited by the availability of reliable long-duration observations.

At the continental scale, Australia experienced one of its wettest years on record (see section 7h4) with accompanying wetter-than-average precipitation maxima over the Northern Territory. Following record-breaking Rx1day/Rx5day in January, the transition to La Niña-like conditions

later in the year resulted in less severe precipitation extremes over Australasia compared with the rest of the globe (WMO 2024).

Despite fewer-than-normal typhoons in the western North Pacific (see section 4g4 for details), the season brought exceptionally heavy Rx1day/Rx5day and induced extensive flooding across the Philippines and surrounding countries in Southeast Asia in July and September (Tandon 2024). An exceptional clustering of six active typhoons occurred in the basin in less than a month in late October and November, further compounding the impacts of previous extreme precipitation (Cassidy 2024). As part of an active North Atlantic hurricane season (see section 4g2), a series of tropical cyclones developed in September and October. Notably, Hurricanes Helene and Milton each rapidly intensified, with Rx5day totals doubling previous records over parts of the eastern United States.

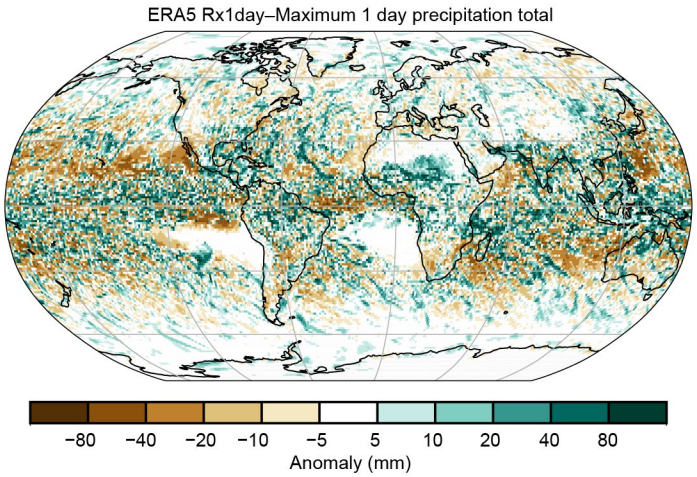

Fig. 2.35. 2024 accumulated one-day maxima (Rx1day; mm) anomalies from 1991–2020 from ERA5.

Precipitation extremes in southwestern Asia arose from the wetter-than-average monsoon and pre-monsoon (April–June), as the Indian Ocean experienced a below-average year for cyclones (see sections 4f, 4g5). Widespread heavy precipitation and flash floods over Pakistan and Afghanistan in April (Pakistan Meteorological Department 2025) were succeeded by record-breaking sub-daily precipitation in Lahore, Pakistan, in August (DW 2024). The highest multi-day precipitation in over 50 years occurred over northeast India and Bangladesh in August (Pandey and Sengupta 2024; Kamal et al. 2024), and Nepal in September (WWA 2024b).

A series of unusual Rx1day/Rx5day values occurred in otherwise arid or drought-affected countries surrounding the Mediterranean, the Persian Gulf, northeastern Africa, and the Sahel (section 2d5), all connected to active convection systems from cut-off lows. These included: the heaviest Rx1day in 75 years over northern Oman and the United Arab Emirates in April (Zhang et al. 2025); a series of heavy events that together generated the highest July rainfall total (since records began in 1956) at Cape Town International Airport in South Africa, triple its monthly climatology (South African Weather Service 2024); Rx1day and Rx5day each exceeding the monthly climatology in Morocco, Niger, and Nigeria in September; and historic hourly precipitation in southeastern Spain in late October (Kothari 2024). Torrential rain also occurred over Kenya and Tanzania in April, South Africa in June, and central Africa throughout July and August (NOAA NCEI 2025a).

Europe was affected by heavy precipitation throughout the year (ECMWF 2025). Geographic clusters of record-breaking Rx1day and Rx5day include France in April, Germany and the Netherlands in May and June, Poland and Czechia in September, and the United Kingdom and Ireland in November (see section 7f for details).

While much of Central and South America were in extended drought, isolated intense precipitation occurred across southwestern Brazil, Uruguay, and Argentina in March. Rio Grande do Sul experienced record-breaking Rx1day in April and May (see Sidebar 7.1; Zhang et al. 2025). Near-record precipitation also fell over Colombia and Bolivia during November (NOAA NCEI 2024; see section 7d).

7. CLOUDINESS

—C. Phillips and M. Foster

Cloud area fraction increased in 2024 compared to the record low observed in 2023. According to PATMOS-x observations (Foster et al. 2023; Fig. 2.36), global-mean cloud area fraction was significantly higher (0.4%) than in 2023. This is consistent with the Clouds and the Earth's Radiant Energy System (CERES) EBAF-TOA Ed4.2.1 cloud radiative effect data (Loeb et al. 2018). Compared to 2023, the global-mean shortwave cloud radiative effect (SWCRE) was 0.66 W m^{-2} more

"reflective", and in the longwave, global-mean cloud radiative effect (LWCRE) was 0.07 W m^{-2} more "insulating" in 2024. Combining shortwave and longwave changes (–0.59 W m^{-2}), the global-mean net cloud radiative effect corrected from the large 2023 anomaly such that 2024 was only 0.02 W m^{-2} above the 2000–20 average (–17.81 W m^{-2}).

Plate 2.1p shows the annual anomalies of cloud area fraction in 2024 compared to the 1991–2020 average. In 2023, the tropical Indian Ocean had an extremely low cloud area fraction, but it returned to normal levels in 2024. Southern Africa and South America saw below-average cloud area fraction, which aligns with observations of below-average water vapor and precipitation in these regions (Plates 2.1l,n).

Although cloud area fraction increased from 2023 to 2024, it remained well below the long-term average (–1.49% relative to 1991–2020) and was the second lowest since records began in 1980 (Fig. 2.36). Similarly, although greater than 2023, the CERES shortwave cloud radiative effect was both less reflective (SWCRE: –0.57 W m^{-2}) and less insulating (LWCRE: –0.55 W m^{-2}) than the long-term 2000–20 average. These findings of below-average cloud area fraction are consistent with the theory of a long-term trend of decreasing cloud cover discussed in previous reports (Phillips and Foster 2024). For example, global-mean shortwave cloud radiative effect has been trending towards less "reflective" (–0.44 W m^{-2} $decade^{-1}$), and the global-mean longwave cloud radiative effect has been trending towards less "insulating" since 2000 (–0.39 W m^{-2} $decade^{-1}$).

As an experiment, a GEO-Ring composite of Geostationary Operational Environmental Satellites (GOES)—namely GOES-16 and GOES-18—along with Himawari-9, Meteosat-9, and Meteosat-10, was processed for every six hours in 2024. Figure 2.37a shows the diurnal range of annual average cloud area fraction for 2024, in other words the difference in cloud between the peak and the trough time of day. The diurnal range of cloud area fraction for any given location is low, with an average value of 7.8%. Figure 2.37b shows the diurnal cycle of global-mean cloud area fraction for 2024. This is even smaller because some regions cancel each other out when the global mean is calculated. However, there are some regions with much higher diurnal variability. Most salient are the regions of stratocumulus clouds off the west coasts of continents. These

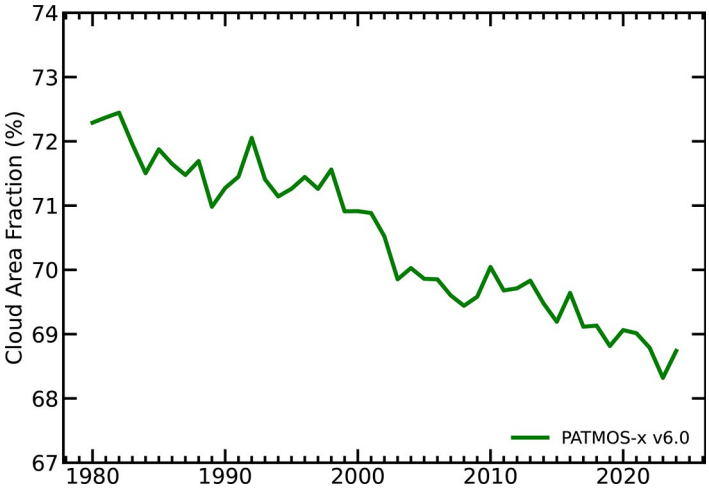

Fig. 2.36. Global annual mean cloud area fraction (%) from PATMOS-x v6.0.

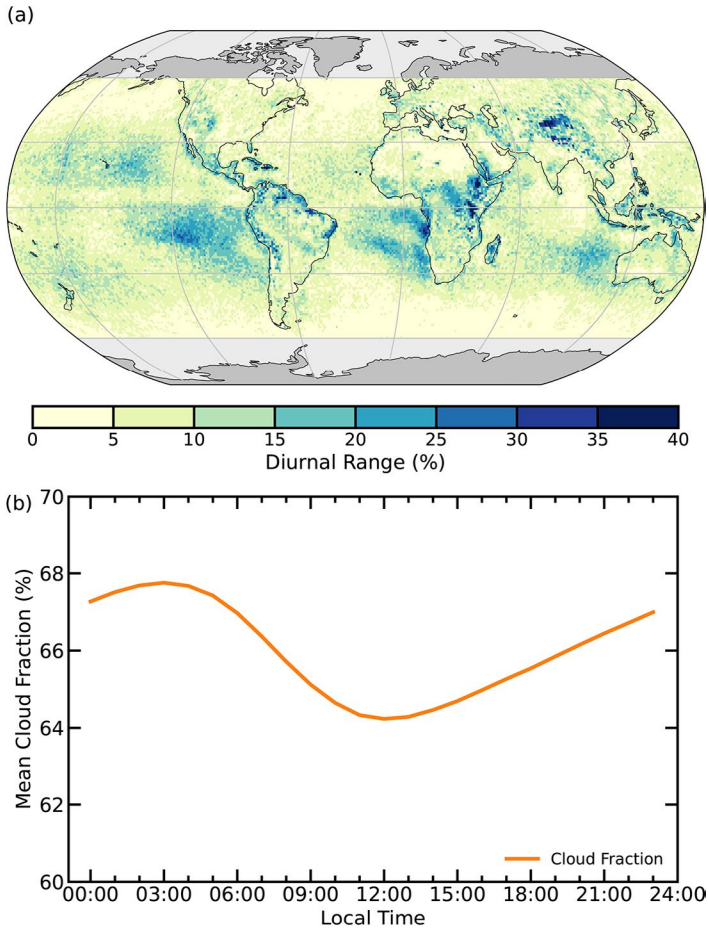

Fig. 2.37. The annual mean (a) diurnal range over the globe and (b) annual global mean diurnal cycle of average cloud area fraction (%) for 2024, as observed by the GEO-Ring composite of Geostationary Operational Environmental Satellite (GOES)-16, GOES-18, Himawari-9, Meteosat-9, and Meteosat-10.

regions should be considered carefully when performing cloud climatological studies, as the timing of observation can have a large impact on the results. The PATMOS-x observations used here (Plate 2.1p; Fig. 2.36) come from satellites with drifting observation times and must be corrected for such diurnal effects, though corrections to the 2024 global mean are negligible. Between 2023 and 2024, the NOAA-18 satellite drifted from 10:31 to 10:41 local time for morning equatorial crossing, NOAA-19 drifted from 08:37 to 09:17, and NOAA-15 drifted from 07:28 to 07:21 local time. Drift in the morning overpass is mostly cancelled by drift in the afternoon overpass such that the expected ensemble-mean effect is −0.03%, much smaller than the observed increase in cloud area fraction (0.4%).

d. Hydrological cycle (land)

8. LAKE WATER STORAGE AND LEVEL

—M. E. Harlan, M. F. Meyer, E. S. Levenson, S. Cooley, and B. M. Kraemer

In 2024, water storage and levels across 4487 lakes exhibited slight overall increases compared to a 1993–2020 baseline period based on two global datasets. Lake storage analysis was based on the GloLakes dataset (Hou et al. 2024; 4190 lakes, median area 5.52 km^2), and lake level was analyzed using the Global Reservoirs and Lakes Monitor (GREALM) dataset (Birkett et al. 2011; 297 lakes, median area 449.2 km^2). Relative to the 1993–2020 baseline, median storage increased by 1.61% in 2024, representing a median rise of 0.295 million cubic meters (MCM). The median lake level increased by 0.12 m, with anomalies ranging between −53 m and +28.9 m. However, marginal global changes obscured more substantial regional changes. After combining both datasets, level or storage increased in 57.8% and decreased in 42.2% of lakes relative to the baseline. A Welch's t-test comparing level and storage observations in 2024 relative to the baseline identified some of these trends as statistically robust (25.6% increased and 16.5% decreased; p<0.05). Long-term trends from these two datasets sometimes diverged (Fig. 2.38) and may not be representative of all lakes globally.

Regional patterns in lake storage were observed. Countries with the largest mean increases relative to the baseline included Syria, Senegal, Belize, Cambodia, Angola, Bangladesh, Sudan, and Libya (+23.4% to +84%), while decreases were most prominent in Niger, Chad, Mongolia, Algeria, Namibia, Argentina, Botswana, and Bosnia and Herzegovina (–20% to –74.8%). For lakes with substantial storage anomalies (>±20%), a weak positive correlation (r^2 = 0.11) between increased storage and higher ERA5 precipitation in 2024 was found, suggesting partial climatic influence (Hersbach et al. 2020). However, it is not advisable to overinterpret these country-level trends given the limited and uneven sampling of lakes, which may not capture broader hydrologic dynamics.

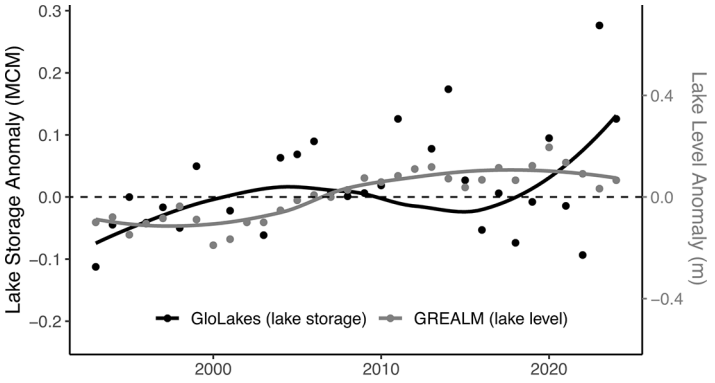

Fig. 2.38. Lake water storage and level anomalies relative to a baseline averaged period of 1993–2020 across each year from 1993 to 2024. Yearly median water storage (black) and level (gray) anomalies averaged across each water body are shown on dual y axes, expressed in million cubic meters (MCM) for lake water storage anomalies and meters (m) for lake water level anomalies. Local regression (loess) smoothing is applied to the annual median anomalies represented by the two curves.

Storage anomaly variance across binned lake sizes and between lakes classified as 'natural' or 'reservoir' was also analyzed using the Global Reservoir and Dam Database (Lehner et al. 2011). Statistically robust differences in storage variance were found across area bins and classifications (p<0.05; Levene's test for homogeneity of variance; Levene 1960), with smaller lakes and reservoirs showing higher anomaly variability (Fig. 2.39). The prevalence of both increasing and decreasing lake trends aligns with previous studies (Kraemer et al. 2020; Y. Feng et al. 2022). Discrepancies in global storage trends compared to more recent work (Yao et al. 2023) are likely a reflection of dataset differences. Continual monitoring of lake anomalies is critical for more accurately predicting dynamics in water availability, ecosystem resilience, and flood and drought risk (e.g., Weyhenmeyer et al. 2024; Han et al. 2024).

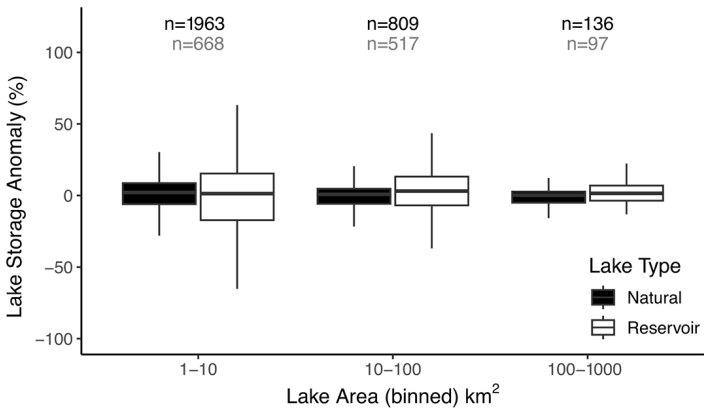

Fig. 2.39. Annual lake storage anomalies (%) for 2024 relative to 1993–2020 binned by lake size, and categorized as "natural" or "reservoir" based on inclusion in the Global Reservoir and Dam Database (Lehner et al. 2011). Lake bin counts (n) are displayed on top (black font) and reservoir counts are shown on bottom (gray font).

Both lake datasets incorporate remote sensing data to estimate storage (GloLakes) or level (GREALM). GloLakes combines Ice, Cloud, and land Elevation Satellite 2 (ICESat-2)

laser altimetry (Jasinski et al. 2023), GREALM radar altimetry data, and optical imagery from Landsat and Sentinel-2. The GloLakes dataset was refined by selecting lakes with at least 20 years of data, no data gaps longer than three years, and at least three observations in 2024. These 4190 lakes represent just 0.89% of global lake volume (HydroLAKES; Messager et al. 2016). To improve volume coverage, GREALM lake level data (Birkett et al. 2011) is also incorporated, adding an additional 297 lakes covering 88.7% of HydroLAKES volume. Anomalies are reported relative to a 1993–2020 baseline, consistent with GREALM availability. Both datasets are limited in spatiotemporal coverage globally, with overrepresentation in North America (Plate 2.1q) and underrepresentation in small (<1 km^2) lakes (Fig. 2.39), which dominate global lake area and storage variability (Pi et al. 2022; Xu et al. 2024). Further, satellite-based estimates of storage may not fully capture fine-scale temporal dynamics. Among the 85 lakes shared between GloLakes and GREALM, the median correlation coefficient (r^2) across each lake between storage and level anomalies was 0.361, yet 82.3% of lakes agree on 2024 anomaly direction. For the lakes present in both datasets, only anomalies for GREALM are provided, given the denser interannual record. Future integration of data from the recently launched Surface Water and Ocean Topography (SWOT) satellite mission or data from longer missions such as the Moderate Resolution Imaging Spectroradiometer (MODIS) may help increase spatiotemporal coverage.

9. RIVER DISCHARGE AND RUNOFF

—J. Casado-Rodríguez, S. Grimaldi, and P. Salamon

From the perspective of river discharge and runoff, 2024 was another dry year, continuing a trend of four consecutive years of below-normal global runoff (Fig. 2.40) and six years with below-normal global river discharge (Fig. 2.41).

Globally, runoff in 2024 exhibited drier-than-usual conditions compared with the reference period 1991–2020 (Fig. 2.40). However, this anomaly was not as pronounced as in 2023, which remains the driest year in the time series. A shift towards normal conditions was observed, likely associated with the transition from El Niño at the beginning of the year to a neutral phase (Oceanic Niño Index in Fig. 2.40; see section 4b for details). Additionally, 2024 was characterized by an intense negative phase of the Pacific Decadal Oscillation (PDO), which was the most negative since 1980. Despite this overarching pattern, significant regional differences were observed (Plate 2.1r). The Amazon, La Plata, and Congo basins experienced an extremely dry year (Toreti et al. 2024c). The anomaly in the Congo is partially attributed to an erroneous negative trend in the ERA5 precipitation over this region (section 2d5; Lavers et al. 2022; Liu et al. 2024). Drought conditions also affected the Atlantic and Pacific coasts of North America,

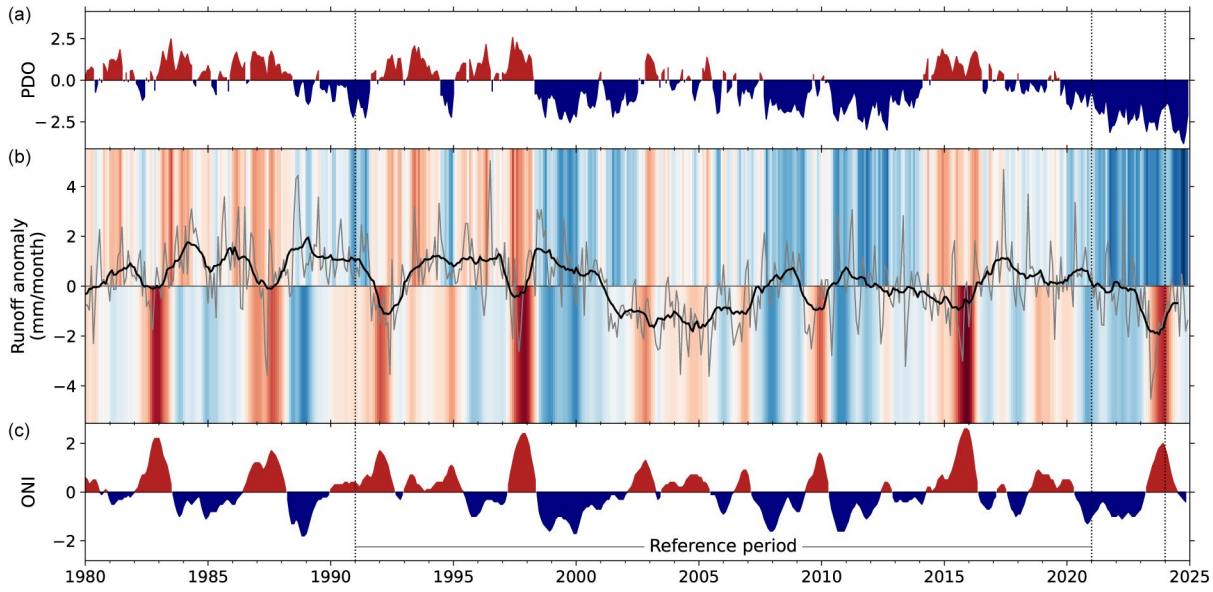

Fig. 2.40. Interannual variability of global runoff (b) and its connections with the (a) Pacific Decadal Oscillation (PDO) and (c) Oceanic Niño index (ONI). In panel (b), the gray line represents the monthly time series of anomalies compared with the base period 1991–2020, the black line represents the 12-month moving average, and the shading indicates the phase of the two indices (PDO in the upper part and ONI in the lower part).

southeastern Europe (Toreti et al. 2024b), Southeast Asia, and parts of Siberia. Conversely, Central America, Central and Northern Europe, the Indian subcontinent, the Pacific coast of Asia, and insular Southeast Asia experienced wetter-than-usual conditions.

A similar pattern was observed in freshwater discharge into the oceans, which remained below normal overall, though with notable regional variations (Fig. 2.41; Plate 2.1s). Discharge

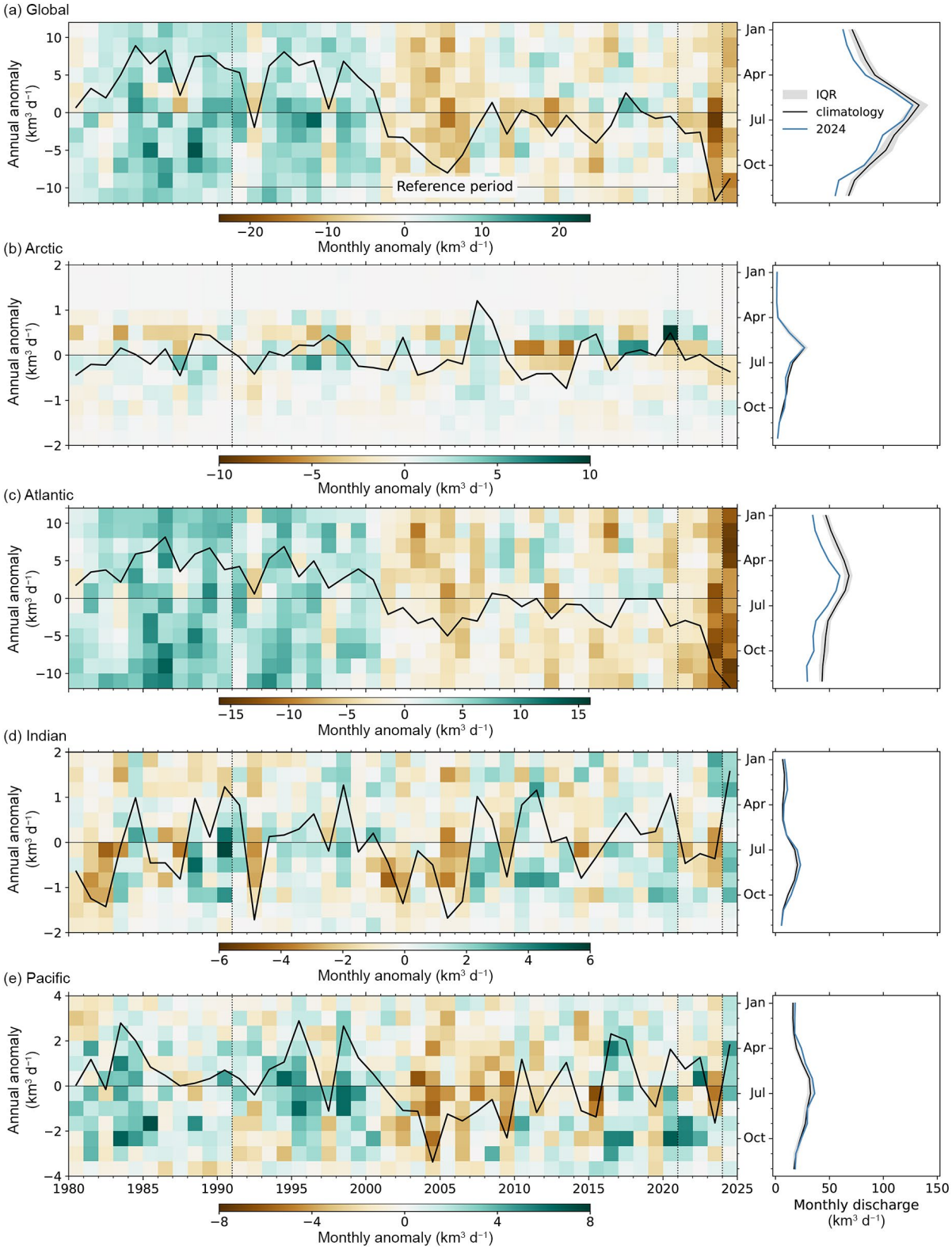

Fig. 2.41. Interannual variability and seasonality of freshwater discharge to the (a) global, (b) Arctic, (c) Atlantic, (d) Indian, and (e) Pacific Ocean basins (km³ day⁻¹). In the left panels, the black line represents the annual discharge anomaly, and the background heat map shows the monthly anomalies with respect to the reference seasonality in the base period 1991–2020. The right panels exhibit the seasonality, where the black line represents the climatological mean, the gray shading indicates the interquartile range in the climatology, and the blue line shows the seasonal variation in 2024.

into the Arctic Ocean was slightly below normal, particularly in summer. The Mackenzie and Nelson Rivers (North America) and the Lena River (Asia) experienced low discharge, whereas the Ob River (Asia) exhibited above-normal discharge (see section 5h for more details). The Atlantic basin faced severe drought conditions, receiving the lowest discharge in the series. Below-normal discharge persisted throughout the year, intensifying during the beginning of 2024 when El Niño was present. Major rivers, including the Amazon, Paraná, and Mississippi (America) as well as the Congo and Nile (Africa) had below-normal discharge. Exceptions to this pattern were the flooding that affected Rio Grande Do Sul (Brazil) in late April (see Sidebar 7.1; Dijk et al. 2025) and the Congo basin in January (WMO 2025b), the latter of which was the worst in six decades. Unlike the Atlantic basin, the Indian Ocean experienced its highest discharge from rivers in the time series, with above-average discharge spanning both wet seasons, while values remained normal during dry seasons. Severe flooding impacted Bangladesh in August (Dijk et al. 2025). The Pacific Ocean also received above-normal discharge, with the largest positive anomalies occurring between April and July.

The river discharge and runoff data used in this analysis are derived from the historical simulation of the Global Flood Awareness System version 4 (GloFASv4) of the Copernicus Emergency Management Service (Joint Research Centre - European Commission 2025). GloFASv4 employs the LISFLOOD-OS hydrological model (Burek et al. 2013), incorporating surface fields that represent land characteristics (Choulga et al. 2024) and parameters calibrated against discharge records from nearly 2000 stations, or regionalized where necessary. The historical simulation spans from 1979 to the present, utilizing a 0.05-degree grid and a daily temporal resolution. ERA5 (Hersbach et al. 2020) serves as the meteorological forcing input.

10. GROUNDWATER AND TERRESTRIAL WATER STORAGE

—M. Rodell and D. N. Wiese

In addition to the continued diminishment of polar ice sheets and glaciers, five regions around the world experienced major (>15 cm) changes in terrestrial water storage (TWS) from 2023 to 2024 (Plate 2.1t). By far the largest of these changes resulted from drought that encompassed most of Brazil and its neighbors to the north. For the equatorial portion of this region, it was a continuation of drought from 2023 (see Plate 2.1u), dropping TWS to record lows. A second major TWS change was a wet event that straddled Uruguay, northwestern Argentina, and southern Brazil, a reversal from the prior year (see section 7d). Changes in the rest of South America were small, though eastern Brazil remained wetter than normal. In contrast, TWS changes in North America were relatively unsubstantial, with some recovery from drought in the central plains of the United States and eastern Mexico, and continued TWS declines in north-central Canada and in the southwestern United States and northern Mexico, with record-low TWS and subsequent wildfires in some parts of these regions.

Remarkably large changes occurred in two regions of Africa. Zambia was at the center of a widespread TWS decline, extending a drought that has been its worst in at least two decades, while Tanzania, already experiencing pluvial conditions in prior years, accumulated even more TWS. Except for the Zambian drought region and another region in western equatorial Africa, a majority of sub-Saharan Africa gained water as the most intense (in terms of extent, duration, and TWS anomalies) wet event in the 23-year TWS record continued (Rodell and Li 2023), associated with unusually heavy rainfall. This led to all-time high TWS and flooding in several African drainage basins including those of the Niger, Congo, Nile, and Senegal Rivers, as well as Lake Chad and eastern lake basins.

The fifth region to experience a major change in TWS was the northern half of Australia's Northern Territory, which was pounded by rain from tropical cyclones in February and March (see section 4g7 for details), continuing northern Australia's wetting trend from the previous year. Much of Australia gained water, except for small declines along the northwestern and southeastern coasts. TWS remained elevated in much of New South Wales and Victoria.

Despite high temperatures, rainfall alleviated drought conditions in western Europe and even caused flooding in southern Spain; however, drought worsened in the Balkan Peninsula. A large area of western Russia and Kazakhstan experienced wetter-than-normal conditions

in 2024 as did parts of Southeast Asia, excluding southern India and Cambodia. TWS changes were mixed in the rest of Asia, with TWS remaining depleted in the Arabian Peninsula, the Middle East, and eastward into south central Asia, due to a combination of drought and overexploitation of water resources (Rodell et al. 2018).

Figures 2.42 and 2.43 display deseasonalized time series of monthly zonal-mean and global-mean TWS anomalies. Gaps indicate intervals when satellite observations were unavailable. We excluded regions from the averages where TWS declines are dominated by ice sheet and glacier ablation: Antarctica, Greenland, the Gulf Coast of Alaska, polar islands, High Mountain Asia, alpine western Canada, and the southern Andes. A 20°-wide zone of drying in the northern midlatitudes remained stable in 2024. Except for the northern portion, a 23°-wide equatorial zone of wetting diminished as the massive drought in South America counteracted the pluvial in Africa. South of that zone, TWS declines in South America and southern Africa overpowered the increase in northern Australia. A gradual decline in the boreal latitudes reflects ongoing drought in Canada and lingering depressed levels of TWS in much of northern Eurasia. Consistent with the end of El Niño, global-mean non-ice TWS (Fig. 2.43) recovered somewhat in 2024 from a near-record low a few months prior, but it remained in a lower range that was established after an abrupt decline during 2014–16 (Rodell et al. 2024).

TWS anomalies are derived from Gravity Recovery and Climate Experiment (GRACE) and GRACE Follow-On (GRACE-FO) satellite observations of Earth's time-varying gravity field (Tapley et al. 2004; Landerer et al. 2020). Uncertainty in these estimates is about 1 cm–2 cm equivalent height of water over a 500,000 km^2 region at midlatitudes (Wiese et al. 2016). Satellite observations are used because in situ measurements of groundwater, soil moisture, surface waters, snow, and ice (the components of TWS) do not provide the spatial density and vertical completeness required to monitor TWS at continental scales. On multi-year timescales, groundwater is typically the primary contributor of variations in TWS, except in the humid tropics and cold regions where surface water and ice/snow, respectively, are dominant (Getirana et al. 2017).

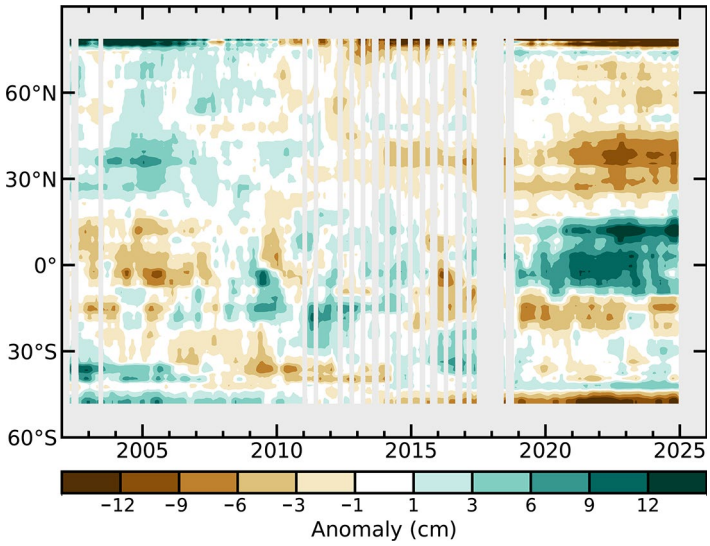

Fig. 2.42. Zonal means of monthly terrestrial water storage anomalies—excluding those in Antarctica, Greenland, the Gulf Coast of Alaska, polar islands, High Mountain Asia, alpine western Canada, and the southern Andes—in cm equivalent height of water, based on gravity observations from the Gravity Recovery and Climate Experiment (GRACE) and GRACE Follow-On (GRACE-FO). The anomalies are relative to a 2002–20 base period.

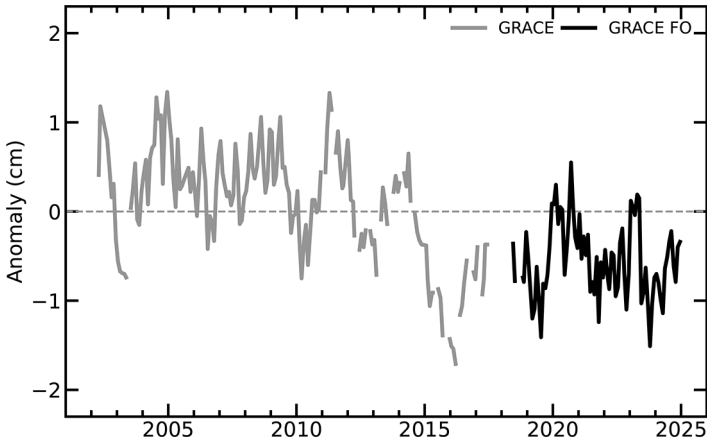

Fig. 2.43. Global average terrestrial water storage anomalies from Gravity Recovery and Climate Experiment (GRACE; gray) and GRACE Follow-On (GRACE-FO; black)—excluding those in Antarctica, Greenland, the gulf coast of Alaska, polar islands, High Mountain Asia, alpine western Canada, and the southern Andes—in cm equivalent height of water, relative to a 2002–20 base period.

11. SOIL MOISTURE

—J. Lems, W. Preimesberger, A. Gruber, D. D. Kovács, S. Hahn, M. Formanek, B. L. Harris, N. Rodriguez-Fernandez, T. Frederikse, R. Kidd, R. A. M. de Jeu, and W. A. Dorigo

Soil moisture is a crucial factor in land–atmosphere interactions, influencing surface air temperature, precipitation generation, and extreme weather events, including heatwaves and wildfires (Seneviratne et al. 2010).

In 2024, global soil moisture conditions were wetter than the 1991–2020 average (Fig. 2.44), with notable regional contrasts (Plate 2.1v). America, southern Africa, northern Europe, and Asia experienced drier-than-average conditions, while eastern South America, East Africa (including the Sahel), India, East Asia, and northern Australia saw above-average soil moisture levels. The Northern Hemisphere experienced wetter-than-normal conditions, while the Southern Hemisphere remained drier than average (Fig. 2.44). This contrast closely resembled that of 2023 (Hirschi 2024); however, the Northern Hemisphere saw a notable increase in soil moisture compared to the previous year. Consistent with the trend of the past five years, the most pronounced wet anomalies in the Northern Hemisphere were concentrated between the equator and 30°N (Fig. 2.45).

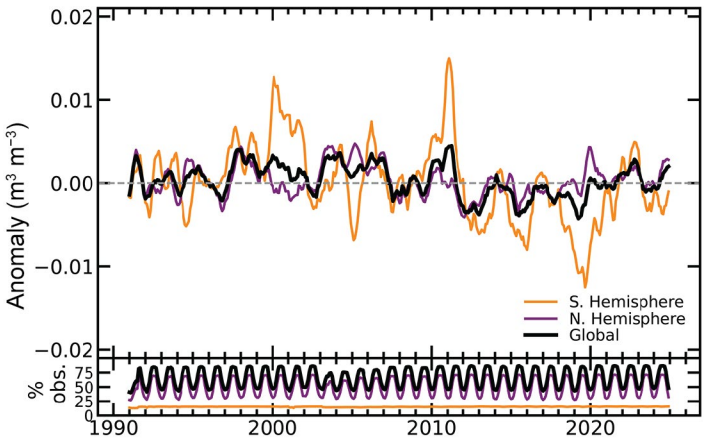

Fig. 2.44. (top) Time series of global (black), Northern Hemisphere (purple), and Southern Hemisphere (orange) monthly surface soil moisture anomalies (m³ m⁻³) for the period 1991–2024 (1991–2020 base period), and (bottom) the valid observations as a percentage (%) of total global land surface. Data are masked where no retrieval is possible or where the quality is not assured and flagged, for example due to dense vegetation, frozen soil, permanent ice cover, or radio frequency interference. (Source: Copernicus Climate Change Service [C3S] Soil Moisture.)

A strong El Niño in the first quarter of the year contributed to drier and warmer conditions in North America, Southeast Asia, Australia, and southern Africa (Song 2018; Hoell et al. 2017; Figs. 2.32, 2.46). In April, the El Niño transitioned to a neutral phase, which aligned with a return to normal soil moisture conditions in the Southern Hemisphere towards the end of 2024 (Fig. 2.44).

Wetter-than-normal conditions were present throughout most of the year in northern Australia, with wet anomalies that were particularly widespread in March (Fig. 2.46). Similarly, strong wet anomalies were also observed in India, starting in May and lasting through to the end of the year. In August and September, anomalously high soil moisture in Afghanistan and Pakistan was associated with heavy rain and flash floods. Also, parts of East Asia experienced noticeable wetter-than-normal conditions in 2024, similar to the last couple of years.

The Sahel experienced prolonged wet anomalies from August to November, with soil moisture amounts twice as high as normal in some areas. Meanwhile, northern and southern Africa faced extreme drought conditions, particularly southern Africa, which remained dry even after El Niño subsided.

Widespread drier-than-normal soil moisture conditions persisted across North and South America throughout 2024, with the

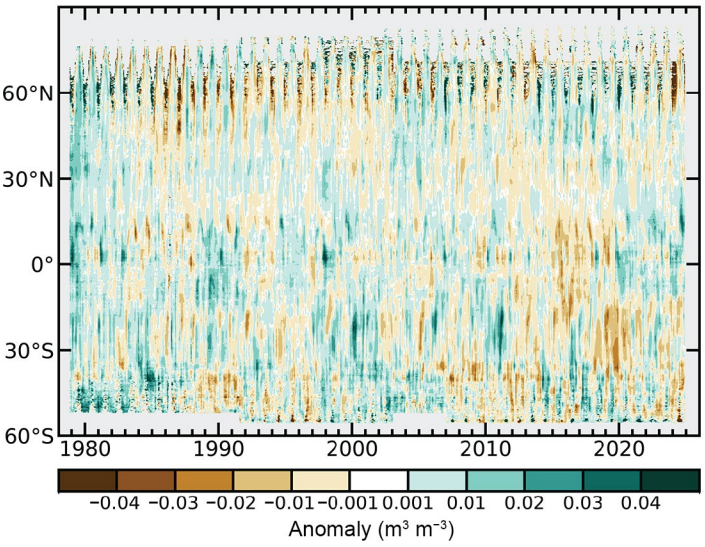

Fig. 2.45. Time–latitude diagram of monthly surface soil moisture anomalies (m³ m⁻³; 1991–2020 base period). Data are masked where no retrieval is possible or where the quality is not assured and flagged, for example due to dense vegetation, frozen soil, permanent ice cover, or radio frequency interference. (Source: Copernicus Climate Change Service [C3S] Soil Moisture).

continent experiencing the most significant negative soil moisture anomaly globally. Following a record-breaking warm and dry October (NCEI 2024), the drought footprint reached a nationwide record in the United States (Fig. 2.46), with 47% of the nation under moderate to extreme drought (section 2d12). September was exceptionally dry in inland South America and in Eastern Europe, primarily affecting Ukraine. Generally, Europe exhibited a distinct east–west contrast, with Western Europe experiencing a wetter-than-average summer, while Eastern and Southern Europe remained dry for most of the year.

Soil moisture was observed by microwave satellite remote sensing of the upper few centimeters of the soil layer, as provided by the COMBINED product of the Copernicus Climate Change Service (C3S) version 202312 (Dorigo et al. 2025). C3S combines multi-sensor data in the 1978–2024 period through statistical merging (Gruber et al. 2017, 2019). Wet and dry anomalies here refer to the deviation from the 1991–2020 average. Note that changes in spatiotemporal coverage (both between seasons and periods, e.g., resulting from the inclusion of additional sensors) can introduce uncertainties in the domain-averaged soil moisture time series (e.g., Bessenbacher et al. 2023).

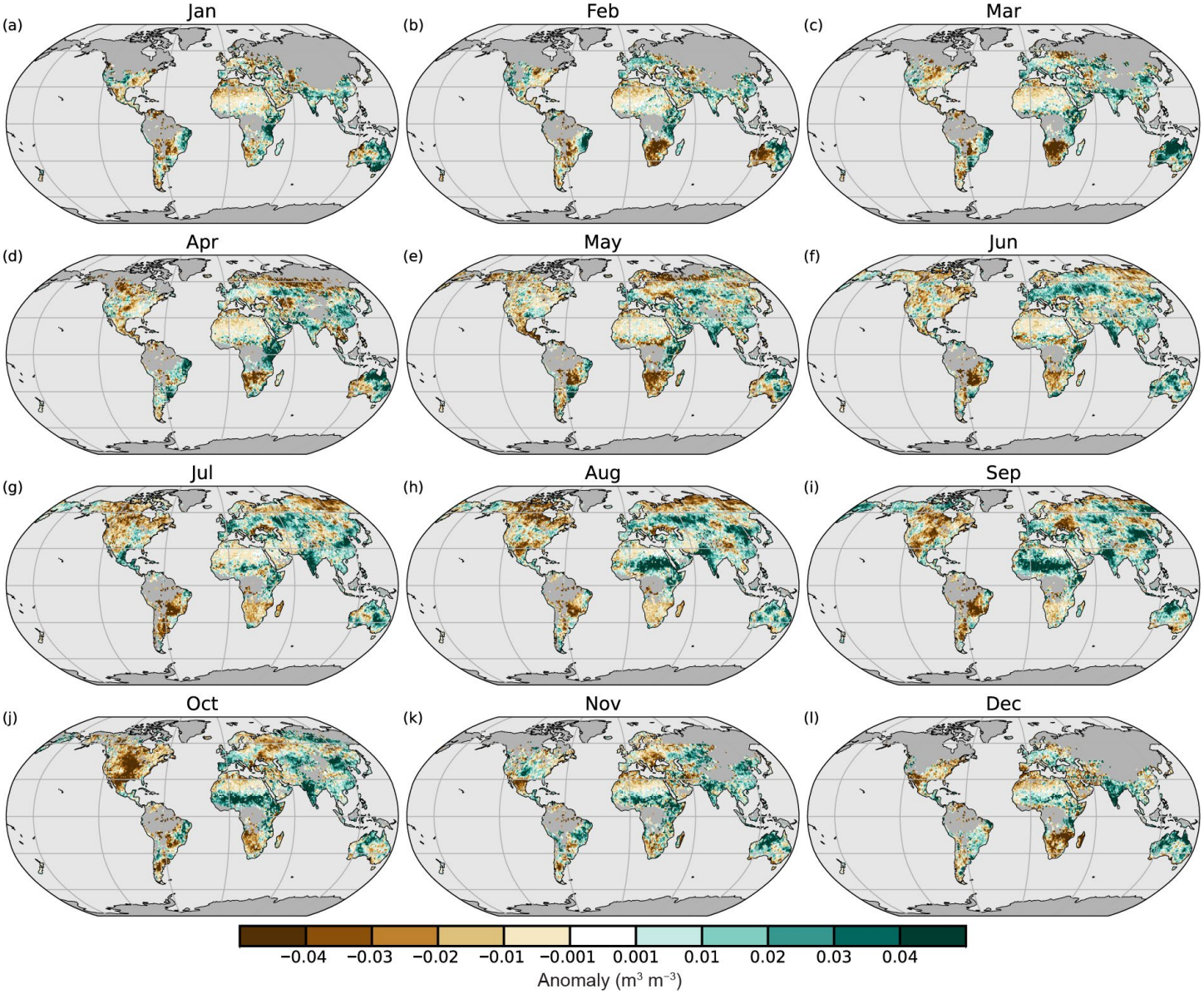

Fig. 2.46. Monthly average soil moisture anomalies for 2024 ($m^3\ m^{-3}$; 1991–2020 average). Data are masked where no retrieval is possible or where the quality is not assured and flagged, for example due to dense vegetation, frozen soil, permanent ice cover, or radio frequency interference. (Source: Copernicus Climate Change Service [C3S] Soil Moisture.)

12. MONITORING DROUGHT USING THE SELF-CALIBRATING PALMER DROUGHT SEVERITY INDEX

—J. Barichivich, T. J. Osborn, I. Harris, A. Gollop, G. van der Schrier, and P. D. Jones

The self-calibrating Palmer Drought Severity Index (scPDSI) for 1950–2024 indicates a decline in global drought severity and extent in 2024, following the record-high peak in late 2023 (Barichivich et al. 2024; Fig. 2.47). Extreme drought (scPDSI ≤–4) affected around 5% of the global land throughout 2024, down from over 7% in July–August 2023. Severe and extreme drought combined (scPDSI ≤–3) stabilized near 12% of the global land area after reaching a record 17% in July 2023. Similarly, moderate or worse drought (scPDSI ≤–2) affected about 23% of global land in 2024 compared to 28% in mid-2023. Most of this decline occurred in regions where drought conditions of 2023 transitioned to normal or wetter conditions, particularly in the La Plata Basin, much of non-Mediterranean Europe, and the midlatitudes of Central Asia (Fig. 2.48). Meanwhile, severe drought persisted in southwestern and northern North America, parts of tropical South America, the Mediterranean and northwest Africa, southern Africa, parts of the Middle East, southern Australia, and Mongolia (Plate 2.1w).

In Canada, 2024 ranked as the driest year on the nationally averaged yearly scPDSI for the 1950–2024 period. In the United States, severe-to-extreme drought conditions persisted through much of Arizona and New Mexico. Mexico and most countries across Central and South America experienced a mix of moderate drought and normal conditions (Plate 2.1w). On a country-averaged basis, 2024 was the third-driest year in both Peru and Brazil, with vast areas of the Amazon basin enduring extreme drought. By mid-October, the Rio Negro at Manaus, a major tributary of the Amazon River, recorded its lowest water levels since records began in 1902 (updated from Barichivich et al. 2018). In contrast, Chile experienced a moisture recovery in 2024 following a prolonged megadrought (Garreaud et al. 2025). In terms of average drought severity, 2024 ranked as the 18th-driest year since 1950, following the driest years on record in 2021 and 2022.

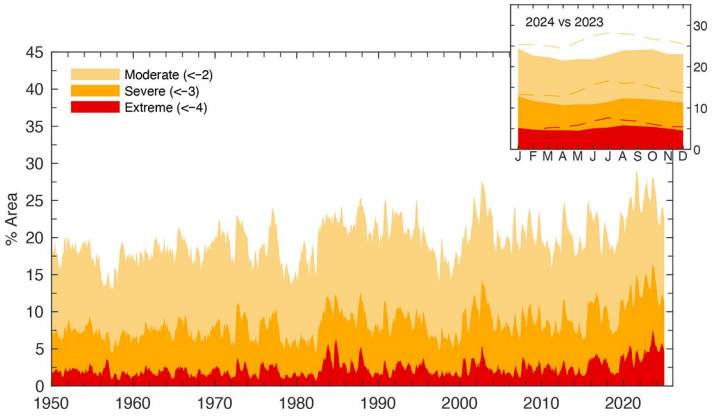

Fig. 2.47. Percentage of global land area (excluding ice sheets and deserts) with self-calibrating Palmer Drought Severity Index (scPDSI) indicating moderate (<–2), severe (<–3), and extreme (<–4) drought for each month of 1950–2024. Inset: each month of 2024 (shading) compared with 2023 (dashed lines).

Northwest Africa experienced record or near-record drought levels (Plate 2.1w), with 2024 being the driest year in the Canary Islands and Morocco, second driest in Algeria, and third driest in Tunisia. In southeastern Europe, it was the driest year in Greece and third driest in Bulgaria and Romania. In Italy, 2024 was ranked sixth driest for country-average drought severity, with the top six drought years all occurring in the last eight years.

Although uncertain due to sparser observations, moisture patterns in tropical Africa did not change much in 2024 with respect to 2023 (Fig. 2.48). Southern Africa experienced a continuation of drought conditions seen since 2018, and its severity continued mostly as moderate (Plate 2.1w). In Australia, the moisture pattern in 2024 also remained similar to that in 2023, with the coastal parts of the

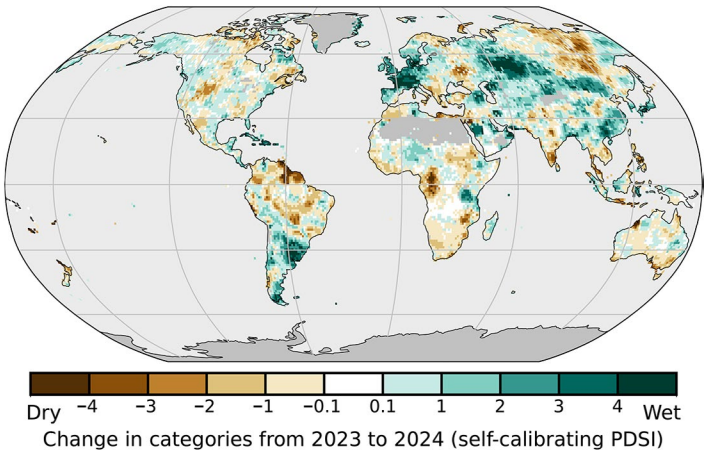

Fig. 2.48. Change in drought categories from 2023 to 2024 (mean self-calibrating Palmer Drought Severity Index [scPDSI] for 2024 minus mean scPDSI for 2023). Increases in drought severity are indicated by negative values (brown), and decreases by positive values (green). No calculation is made where a drought index is meaningless (gray areas: ice sheets or deserts with approximately zero mean precipitation).

country continuing under moderate drought (Plate 2.1w). Wet conditions seen through most of India and Southeast Asia since 2022 continued during 2024. Most of the previous severe-to-extreme drought conditions through China and Kazakhstan shifted to normal or wet conditions, but Mongolia saw continued drought.

Hydrological drought results from a period of abnormally low precipitation, sometimes exacerbated by a concurrent increase in evapotranspiration (ET). Its occurrence can be apparent in reduced river discharge (section 2d9), groundwater storage, (section 2d10), and/or soil moisture (section 2d11), depending on season and duration of the event. Here, the scPDSI (Wells et al. 2004; van der Schrier et al. 2013) is presented, using global precipitation and Penman–Monteith Potential ET from the Climatic Research Unit terrestrial series (CRU TS 4.09) dataset (Harris et al. 2020). A simple water balance at the core of the scPDSI estimates actual evapotranspiration, soil moisture content, and runoff based on the input precipitation and potential loss of moisture to the atmosphere. Estimated soil moisture categories are calibrated over the complete 1901–2024 period to ensure that "extreme" droughts and pluvials (wet periods) relate to events that do not occur more frequently than in approximately 2% of the months. This calibration affects direct comparison with other hydrological cycle variables in Plate 2.1w that use a different baseline period. All country rankings mentioned above are based on the ranking of spatial averages of annual scPDSI for each country for the 1950–2024 period; pre-1950 data are not used for rankings because observational coverage is poor in some countries.

13. LAND EVAPORATION

—D. G. Miralles, O. M. Baez-Villanueva, O. Bonte, E. Tronquo, S. Haghdoost, and H. E. Beck

A clear understanding of the spatial and temporal dynamics of terrestrial evaporation is fundamental for evaluating the impacts of natural and anthropogenic forcing on hydrological systems, since evaporation serves as a direct nexus between the energy and water balances. The global-mean land evaporation in 2024 aligned well with the multidecadal trend of approximately +0.4 mm year^{-1} (Fig. 2.49), a trend that has been attributed to an increase in atmospheric evaporative demand with global warming (Brutsaert 2017) and global greening (Yang et al. 2023). Despite 2024 being overall an El Niño year, which usually implies negative global evaporation anomalies due to the proliferation of drought conditions in the Southern Hemisphere (Martens et al. 2018; Miralles et al. 2014), it was also the warmest year on record (section 2b1). The latter explains the high mean evaporation in the Northern Hemisphere and the subsequent positive global anomaly, which is not an isolated event but contributes to the long-term increase witnessed since the early 1980s (Fig. 2.49).

The latitudinal anomaly profiles in Fig. 2.50 reveal the overall positive anomalies in Northern Hemisphere regions, which are consistent with warm temperatures in Europe, Asia, and North

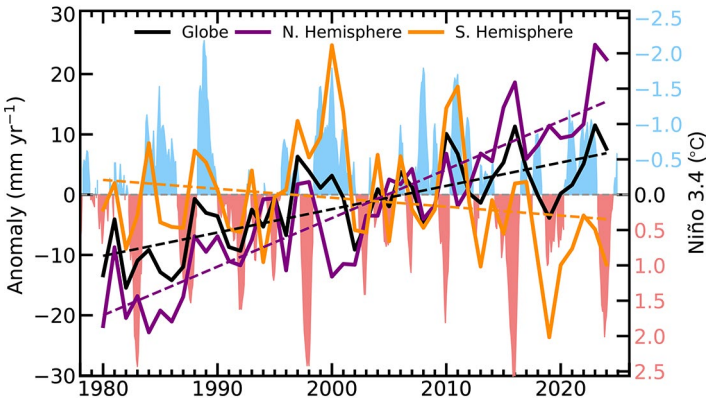

Fig. 2.49. Land evaporation anomaly (mm yr^{-1}; 1991–2020 base period) for the Northern Hemisphere, Southern Hemisphere, and the entire globe (purple, orange, and black solid lines, respectively). Linear trends in evaporation (dashed lines) and the Niño-3.4 index (right axis, shaded area) are also shown. (Source: Global Land Evaporation Amsterdam Model version 4 [GLEAM4] and NOAA Physical Sciences Laboratory [PSL].)

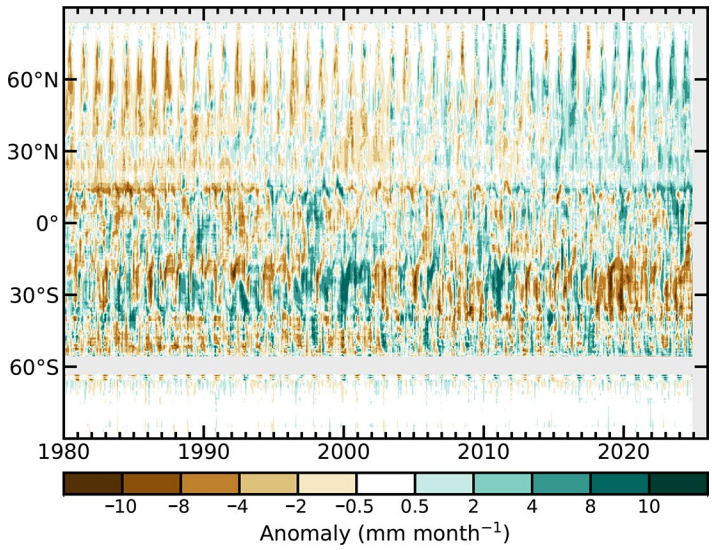

Fig. 2.50. Zonal mean terrestrial evaporation anomalies (mm month^{-1}; relative to 1991–2020). (Source: Global Land Evaporation Amsterdam Model version 4 [GLEAM4].)

America (section 2b1). The largest negative anomalies occurred in the latitudinal band from 0° to 30°S, and they reflect the extraordinary drought conditions experienced in South America and southern Africa in 2024 (sections 2d11, 2d12). Drought conditions tend to be associated with high atmospheric water demand, which initially enhances evaporation and accelerates soil desiccation. However, as soil moisture decreases, evaporation rates decline, leading to negative evaporation anomalies in later stages of the drought event (Miralles et al. 2019). This pattern is reflected in the positive evaporation anomalies at those latitudes during the first half of 2024, which then transitioned into negative anomalies in the second half (Fig. 2.50).

In terms of global patterns, there was a mix of positive and negative evaporation anomalies across different regions in 2024, reflecting a complex interplay of meteorological variables and land surface processes (Plate 2.1x). As expected during El Niño years, lower-than-usual evaporation occurred as a result of soil moisture limitations in southern Africa and most of South America; as mentioned above, those soil moisture limitations were caused by persistent drought events (Marengo et al. 2024). On the other hand, the lower-than-usual evaporation in western North America is less typical of El Niño conditions, and was also triggered by precipitation scarcity (section 2d5). Most of the world was, however, dominated by positive evaporation anomalies, as expected given the high temperatures in 2024 (Plate 2.1x). Major tropical forested regions experienced higher evaporation than normal, as the high atmospheric demand for water increased transpiration despite the negative anomalies in precipitation leading to lower-than-usual interception loss (i.e., water evaporating directly from wet canopies during and after precipitation events).

The evaporation estimates used in this analysis were obtained from the Global Land Evaporation Amsterdam Model version 4 (GLEAM4; Miralles et al. 2025), which integrates satellite observations and reanalysis data. GLEAM4 separately estimates the main components of terrestrial evaporation, including soil evaporation, transpiration, interception loss, and sublimation, and its estimates are routinely validated against in situ measurements from eddy-covariance flux towers and other ground-based observations. Despite recent advancements, uncertainties remain high, particularly in regions with sparse observational data. Ongoing efforts aim to refine different evaporation components by leveraging new satellite missions and improved reanalysis products. Future developments are expected to leverage emerging technologies from thermal missions—such as Ecosystem Spaceborne Thermal Radiometer Experiment on Space Station (ECOSTRESS; Fisher et al. 2020) and Thermal Infrared Imaging Satellite for High-resolution Natural Resource Assessment (TRISHNA; Lagouarde et al. 2018), along with hyper-resolution optical remote sensing from CubeSats (McCabe et al. 2017)—to improve global evaporation monitoring and understanding of its response to climate change.

e. Atmospheric circulation

1. MEAN SEA LEVEL PRESSURE AND RELATED MODES OF VARIABILITY

—D. Fereday, D. Campos, and G. Macara

Mean sea level pressure (MSLP) variability is characterized by large-scale modes that drive weather and climate anomalies and extremes. These modes include the Arctic Oscillation, the North Atlantic Oscillation (NAO), and the Pacific–North American (PNA) pattern in the Northern Hemisphere (NH) as well as the Southern Annular Mode (SAM; also known as the Antarctic Oscillation) in the Southern Hemisphere (SH; Kaplan 2011). Because of its direct tropical impact and important extratropical teleconnections to both hemispheres (Capotondi et al. 2015; Yeh et al. 2018), the El Niño–Southern Oscillation (ENSO) is one of the most significant global climate drivers (see section 4b for details).

In the NH, the NAO index fluctuated through the winter into early spring (December–March), remaining overall fairly neutral (Figs. 2.51a,e). An important driver of winter circulation variability in the NH is the stratospheric polar vortex. The vortex was unusually variable in winter 2023/24, with two major sudden stratospheric warmings (SSWs) occurring in January and March (Fig. 2.51e). Such events tend to favor a negative NAO (Baldwin and Dunkerton 2001), leaving northern Europe colder and drier, and southern Europe milder and wetter. However, this does not always occur (Kodera et al. 2016), and neither SSW in 2024 produced a strong negative NAO response (Lee at al. 2025). Nevertheless, the NH temperature anomalies for January–March 2024 resembled those seen in other El Niño winters that experienced an SSW (Ciasto and Butler 2024), with northeast North America having been warmer and southwest North America and northern Eurasia having been cooler. In NH spring, low-pressure anomalies over western Europe (Fig. 2.51b) were consistent with increased precipitation (see section 7f2). In NH summer, MSLP anomalies in North America remained weak (Fig. 2.51c). The summer NAO, an important driver of summer European climate (Folland et al. 2009), was also near-neutral. In December 2024, the PNA was positive, as was the winter NAO, consistent with warmer conditions in the eastern United States and drier conditions in the western United States (see section 7b2).

The Southern Oscillation Index (SOI), calculated by the MSLP difference between Tahiti and Darwin, highlights the atmospheric component of ENSO (Allan et al. 1996; Kaplan 2011). During 2024, the SOI transitioned slowly from negative to positive values through the year, associated with the decay of El Niño and neutral conditions in the second half of the year that gave way to La Niña-like conditions in the tropical Pacific Ocean by the end of 2024 (see section 4b for details). During the austral winter, with neutral SOI conditions, a pattern similar to the Pacific–South American (PSA) pattern (O'Kane and Franzke 2025) developed in the South Pacific, allowing the presence of an area of above-normal MSLP centered over the Bellingshausen Sea (Fig. 2.52c). This atmospheric blocking pattern was associated with wetter-than-normal conditions in south-central Chile during the winter (e.g., Rutllant and Fuenzalida 1991; Campos and Rondanelli 2023; see also Fig. 2.46; see section 7d3) despite the

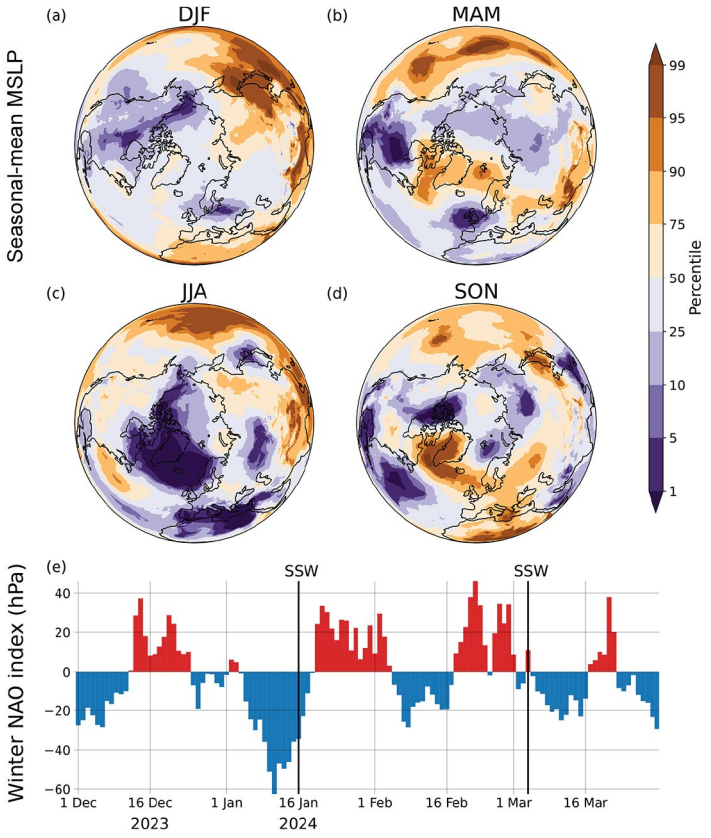

Fig. 2.51. Northern Hemisphere mean sea level pressure (MSLP) for 2024. Panels (a)–(d): seasonal mean MSLP for Dec 2023 to Nov 2024. Fields are anomalies with respect to a 1991–2020 climatology, expressed as percentiles. (Source: ERA5.) Panel (e): daily North Atlantic Oscillation (NAO) index for Dec 2023 to Mar 2024 defined as Azores minus Iceland MSLP. Black lines show the dates of the two major sudden stratospheric warmings. (Source: National Centers for Environmental Prediction reanalysis version 1 [NCEPv1].)

midterm megadrought (Garreaud et al. 2020). MSLP was also above-normal over and to the east of New Zealand during austral winter, associated with drier-than-normal conditions over the country during June and July and the country's third-warmest winter on record.

The annual MSLP anomalies in the SH (Plate 2.1y) resemble the positive phase of the SAM, which is the leading mode of extratropical variability in the SH (Fogt and Marshall 2020), explaining up to 34% of the variance of the extratropical atmospheric circulation. Two prominent centers of positive anomalies were observed in the extratropics: one in the southern Pacific Ocean and one in the southern Indian Ocean. At a seasonal scale, positive SAM conditions prevailed during the first months of the year where El Niño conditions were present (74% of the days between January and April; Figs. 2.52a,e). In the austral autumn, MSLP was higher than normal south of Australia, with below-average rainfall across southern parts of the country. In contrast, significant flooding affected large parts of central and northern parts of Australia, associated mostly with a monsoon trough (see section 4f) and Severe Tropical Cyclone Megan in March (see section 4g7). More frequent southwesterly winds than normal contributed to New Zealand observing its coolest autumn since 2012. During the austral winter (June–August), a period of nearly 45 consecutive days with the SAM in the negative phase was registered around August (Fig. 2.52e), associated with the positioning of the blocking high in the Bellingshausen Sea and an increase of the subtropical jet stream. From September to December, the SAM was variable, spending approximately half of the time in each phase (Fig. 2.52e).

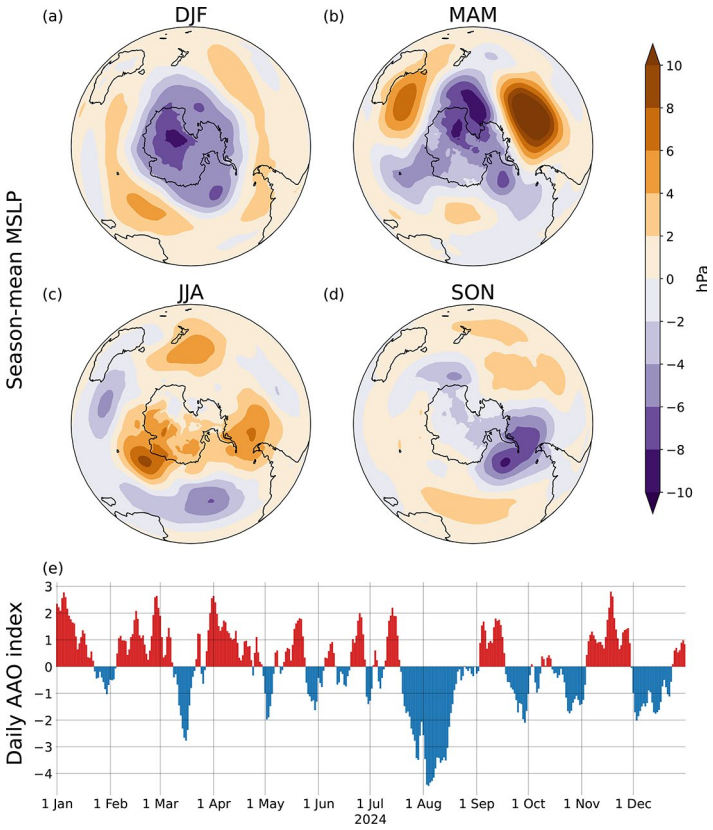

Fig. 2.52. Southern Hemisphere mean sea level pressure (MSLP) for 2023/24. Panels (a)–(d): seasonal-mean MSLP for Dec 2023 to Nov 2024. Fields are anomalies with respect to a 1991–2020 climatology. (Source: ERA5.) Panel (e): daily Antarctic Oscillation (AAO) index for Jan–Dec 2024. (Source: NOAA National Center for Environmental Prediction).

2. LAND AND OCEAN SURFACE WINDS

—C. Azorin-Molina, R. J. H. Dunn, L. Ricciardulli, T. R. McVicar, J. P. Nicolas, C. A. Mears, Z. Zeng, and M. G. Bosilovich

Northern Hemisphere land surface wind speeds at ~10 m above ground in 2024 were generally lower with respect to the 1991–2020 climatology (Plate 2.1z), with an anomaly (−0.034 m s^{-1}) similar to that reported for 2023 (Azorin-Molina et al. 2024; Table 2.9). The most notable spatial feature in the wind speed anomalies is an interhemispheric asymmetry, characterized by negative values in all northern regions (except for Central Asia) and positive values in South America. The "reversal" observed around the 2010s (Zeng et al. 2019), following decades of "stilling" (McVicar et al. 2012), is weakening as shown in Fig. 2.53a. In recent years, weak variations have been observed in the frequency of moderate (>3 m s^{-1}, Fig. 2.53c) and strong (>10 m s^{-1}, Fig. 2.53d) winds, although a declining trend persists for both categories over the period 1973–2024.

Land surface winds are assessed by comparing observations with reanalyses: 1) the Met Office Hadley Centre Integrated Surface Dataset 3 (HadISD3) observational dataset (1973–2024; Dunn et al. 2012, 2016; Dunn 2019); 2) the Global Historical Climatology Network hourly (GHCNh) observational dataset (1974–2023; Menne et al. 2025); 3) ERA5 (1979–2024; Hersbach et al. 2020; Bell et al. 2021); and 4) MERRA-2 (1980–2024; Gelaro et al. 2017). Atmospheric reanalyses can generally reproduce the climatology of station-based wind observations; however, they tend to underestimate the magnitude of observed anomalies and fail to accurately capture the multidecadal variability, even though their performance has consistently improved since the

mid-1990s (Fig. 2.53b; e.g., Torralba et al. 2017; Wohland et al. 2019).

Over the period 1979–2024, terrestrial wind speed declined (–0.052 m s^{-1} $decade^{-1}$) across all regions in the NH (Table 2.9), with the strongest decline observed in North America (–0.069 m s^{-1} $decade^{-1}$) and the weakest in East Asia (–0.027 m s^{-1} $decade^{-1}$). The interhemispheric asymmetry in the long-term changes of wind speeds persists (Zha et al. 2021): despite limited SH land observations, positive trends are reported in South America (+0.054 m s^{-1} $decade^{-1}$). This dipole in trend direction between hemispheres is partly captured by ERA5 (Fig. 2.54a).

In 2024, globally averaged ocean wind speed anomalies (relative to the 1991–2020 base period) were opposite in sign compared to land surfaces, with slightly positive values for radiometers (Remote Sensing Systems [RSS], +0.051 m s^{-1}) and close to zero for scatterometers (Advanced Scatterometer [ASCAT], –0.003 m s^{-1}) and reanalysis (ERA5, +0.006 m s^{-1}); see Fig. 2.55. Satellite wind datasets from RSS include the merged radiometers (Special Sensor Microwave/Imager [SSM/I] series, Special Sensor Microwave Imager/Sounder [SSMIS] series, Advanced Microwave Scanning Radiometer 2 [AMSR2] and AMSR for the Earth Observing System [AMSR-E], Tropical Rainfall Measuring Mission Microwave Imager [TMI], WindSat, and Global Precipitation Measurement Microwave Imager [GMI]), and the Quick Scatterometer (QuickSCAT) and ASCAT scatterometers (Wentz 1997, 2015; Wentz et al. 2007, 2024;

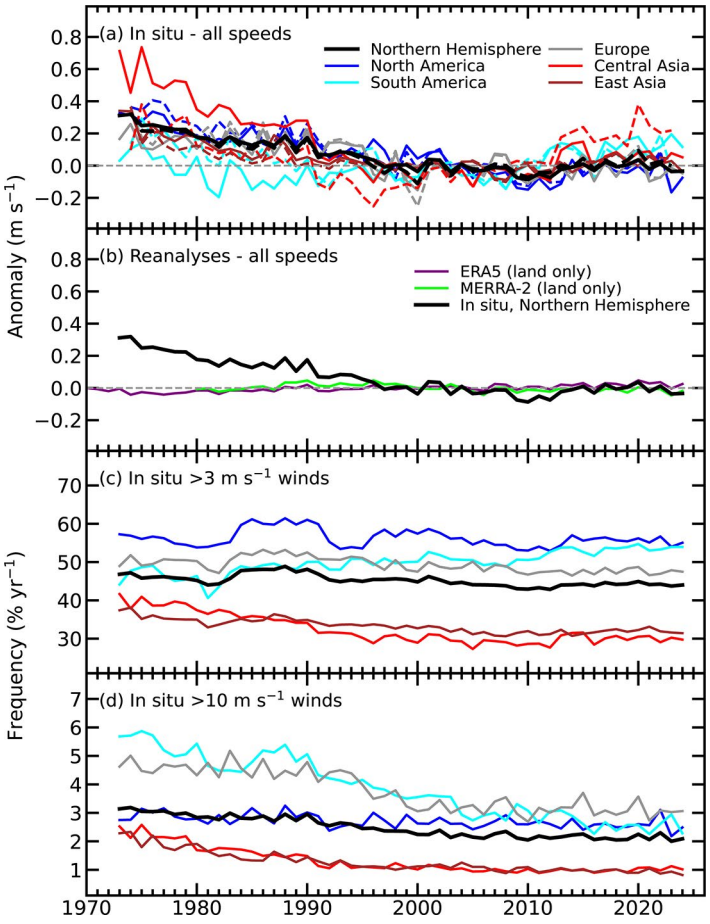

Fig. 2.53. Land surface Northern Hemisphere (20°N–70°N) and regional surface wind speed anomaly time series (m s^{-1}; 1991–2020 reference period). Panel (a) shows the Met Office Hadley Centre Integrated Surface Dataset 3 (HadISD3) observational dataset (1973–2024) in solid lines and Global Historical Climatology Network hourly (GHCNh; 1974–2023) in dashed lines, and (b) ERA5 (1970–2024) and MERRA-2 (1980–2024). The lower panels show HadISD3 occurrence frequencies (% yr^{-1}) for wind speeds (c) >3 m s^{-1} and (d) >10 m s^{-1}, with the same legend as in (a).

Table 2.9. Northern Hemisphere (20°N–70°N) and regional statistics for land surface wind speed (m s^{-1}) using the observational HadISD3 dataset for 1979–2024.

Region	Mean Wind Speed 1991–2020 (m s^{-1})	Wind Speed Anomaly 2024 (m s^{-1})	Wind Speed Trend 1979–2024 (m s^{-1} $decade^{-1}$)	Confidence Interval 5% (m s^{-1} $decade^{-1}$)	Confidence Interval 95% (m s^{-1} $decade^{-1}$)	Number of Stations
Northern Hemisphere	3.297	–0.034	–0.052	–0.066	–0.040	2811
North America	3.645	–0.075	–0.069	–0.084	–0.052	845
Europe	3.640	–0.048	–0.049	–0.067	–0.035	866
Central Asia	2.741	+0.052	–0.065	–0.098	–0.039	303
East Asia	2.720	–0.036	–0.027	–0.041	–0.014	538
South America	3.451	+0.116	+0.054	+0.039	+0.072	101

Ricciardulli and Wentz 2015; Ricciardulli and Manaster 2021). The ocean wind anomaly map for 2024 (Plate 2.1z) shows notable regional features, including: 1) a large negative anomaly in the tropical Atlantic, similar to 2023 but slightly reduced in both extent and magnitude; 2) a positive anomaly in the tropical Pacific, indicating the transition from El Niño to La Niña-like conditions; 3) slightly negative anomalies over the Indian Ocean; and 4) a dominance of moderate positive anomalies over the Southern Ocean, Greenland Sea, and North Pacific Ocean. The comparison between the RSS ASCAT anomaly time series and maps and ERA5 shows they are consistent both temporally and spatially. In the long term (1988–2024), ocean winds exhibit slightly positive trends (Fig. 2.55) for both RSS (+0.030 m s^{-1} $decade^{-1}$) and ERA5 (+0.030 m s^{-1} $decade^{-1}$) averaged over 60°S–60°N, and display similar spatial patterns (Fig. 2.54a) as those shown for the anomalies. Spatially, the trend map reveals a positive trend in the central Pacific and Southern Ocean, consistently observed in many of the past years.

The causes behind the opposite land (negative) and ocean (positive) anomalies are not yet attributable (see discussion in McVicar et al. 2012, for example). Long-term trends and multidecadal variability (stilling versus reversal) of land and ocean surface winds have primarily been attributed to decadal ocean–atmosphere oscillations (Zeng et al. 2019). Anthropogenic global warming is also driving the opposite trends between the Northern (negative) and Southern (positive) Hemisphere (Zha et al. 2021) due to changes in the pressure gradient (Zhang et al. 2021). Changes in land cover (Minola et al. 2022), data encoding issues (Dunn et al. 2022a), and biases in anemometer readings (Azorin-Molina et al. 2023; Liu et al. 2024) are likely secondary drivers of the observed trends and variability.

3. UPPER-AIR WINDS

—L. Haimberger, M. Mayer, C. T. Sabeerali, P. Rohini, O. P. Sreejith, and V. Schenzinger

Global atmospheric circulation patterns from the surface to stratospheric levels can be strongly impacted by oceanic temperatures and ENSO state. During October–December (OND; Plate 2.1aa) in 2024, a weakly negative Indian Ocean dipole (IOD) and La Niña conditions were indicated by the positive–negative 850-hPa zonal wind dipole over the equatorial

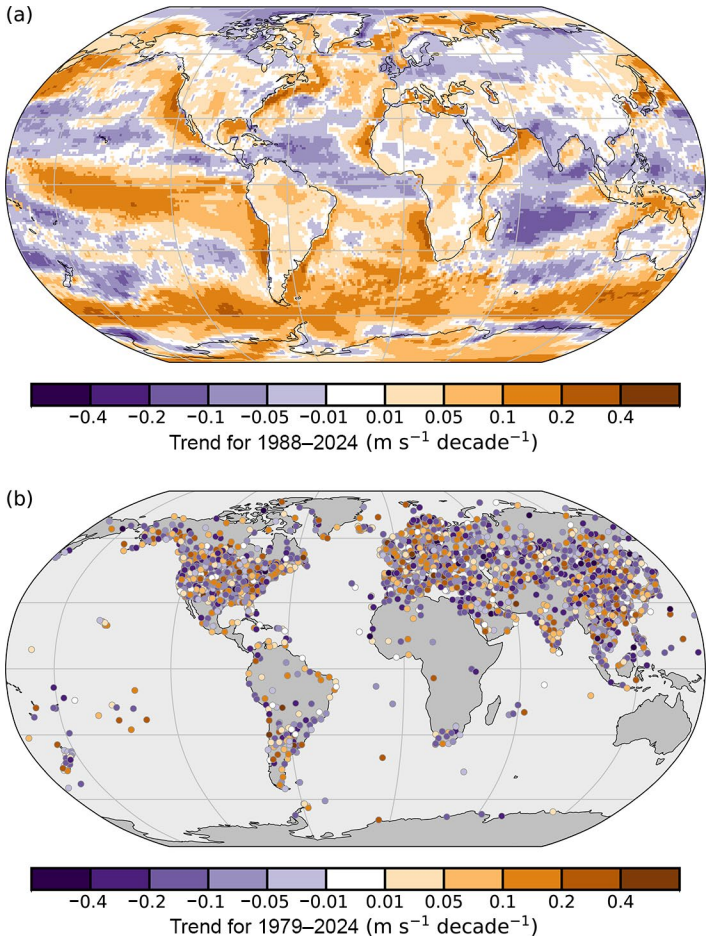

Fig. 2.54. Wind speed trends (m s^{-1} $decade^{-1}$) from the (a) ERA5 output over land/ice and Remote Sensing System (RSS) satellite radiometers (Special Sensor Microwave/Imager [SSM/I], Special Sensor Microwave Imager/Sounder [SSMIS], Tropical Rainfall Measuring Mission Microwave Imager [TMI], AMSR2 [Advanced Microwave Scanning Radiometer 2], ASMR-E [Advanced Microwave Scanning Radiometer for the Earth Observing System], WindSat, and Global Precipitation Measurement Microwave Imager [GMI]) over ocean for 1988–2024 (shaded areas), and (b) the observational Met Office Hadley Centre Integrated Surface Dataset 3 [HadISD3] dataset over land (circles) for 1979–2024.

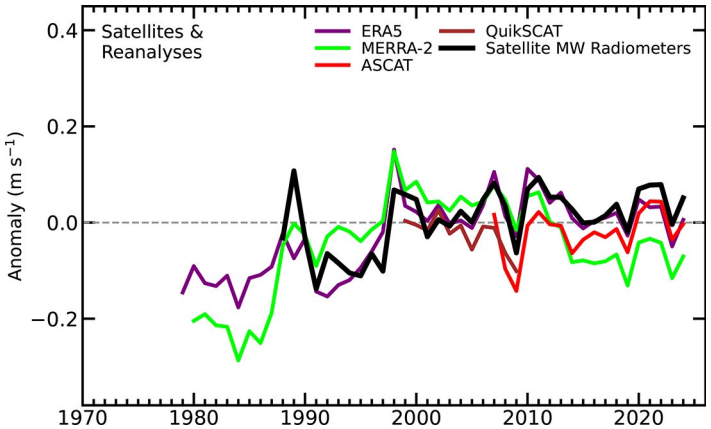

Fig. 2.55. Annual global anomalies of global mean wind speed (m s^{-1}; 1991–2020 base period) over the ocean from merged satellite radiometers, the Quick Scatterometer (QuickSCAT) and Advanced Scatterometer (ASCAT), and ERA5 and MERRA-2 reanalyses.

Indian and western Pacific Ocean basins, feeding the convective maximum over the Indonesian region with moisture. However, eastward wind anomalies covered the Niño-3.4 region of the eastern Pacific, along with westward wind anomalies near the South American coast, converging on positive sea surface temperature (SST) anomalies in the far eastern Pacific.

The year 2024 as a whole was relatively normal; the global wind anomaly was slightly positive (Fig. 2.53a). Trends for the period 1991–2024 were negative, with MERRA-2 having been the only outlier. In the Southern Ocean, the Antarctic Oscillation (AAO) anomaly turned from positive to moderately negative in the second half of 2024, leaving the significantly positive trends of the past three decades practically unchanged also for 1991–2024 (from 0.21 [MERRA, JRA55] to 0.23 [JRA-3Q] and 0.32 [ERA5] m s^{-1} $decade^{-1}$, not shown).

The imprint of ENSO in eastward wind anomalies of the Niño-3.4 region (5°S–5°N, 170°W–120°W), where El Niño events lead to significant reduction of the predominant easterlies (e.g., Trenberth 1997), is considered. Since the 1982/83 El Niño, the eastward anomalies appear to have weakened, even during strong El Niño events, in terms of temperature. This has led to a significant negative trend of ~0.4±0.2 m s^{-1} $decade^{-1}$ (across reanalyses) over the period 1991–2024 (Fig. 2.56). The 2023/24 El Niño, which coincided with a negative Pacific Decadal Oscillation (PDO) index, had a relatively weak westerly wind anomaly despite simultaneous global record temperatures. Generally, the westerly wind anomaly maxima appear stronger if the PDO and ENSO are in phase, in accord with Yoon and Yeh (2010).

Looking further back, it is noteworthy that the apparent "quiet" period from the strong 1940–42 El Niño until 1982, in terms of Niño-3.4 westerly wind anomalies, was associated with a mostly negative PDO. This is considered a robust result in terms of data quality, at least at the 850-hPa level, since there are enough surface wind data assimilated, and there are also long radiosonde station records nearby (e.g., Marshall Islands back to 1948).

Figure 2.57b depicts anomalies in pressure vertical velocity and zonal/vertical velocities averaged over the region spanning from 10°S to 10°N for the OND season. Although the conventional Oceanic Niño Index (ONI) indicated neutral ENSO conditions until November 2024 (see section 4b), other indices, such as the relative ONI (L'Heureux et al. 2024) and the Multivariate ENSO Index (https://psl.noaa.gov/enso/mei/), signaled La Niña conditions beginning in mid-2024. Indeed, the 2024 OND season displayed a pronounced descending motion over the central/eastern Pacific, similar to a classical La Niña pattern (see Fig. 2.49 in Mayer et al. 2023). At the same time, a strong ascending motion was observed over the Indo-Pacific Warm Pool, while descending motion prevailed over the tropical western Indian Ocean.

Anomalies of upper-tropospheric circulation in boreal autumn 2024, as reflected by 200-hPa velocity potential and divergent wind anomalies (Fig. 2.57a), were also consistent with La Niña conditions. Anomalously strong divergence prevailed in the Indo-Pacific Warm Pool, indicating enhanced convection, while anomalously strong convergence was seen in the central to eastern tropical Pacific, indicating anomalously strong sinking. Anomalous upper-air divergence extending well into the eastern Indian Ocean was consistent with a weakly positive IOD. The magnitude of 200-hPa divergent wind anomalies over the equatorial Pacific was weaker than during the protracted La Niña of 2020–22, consistent with the only

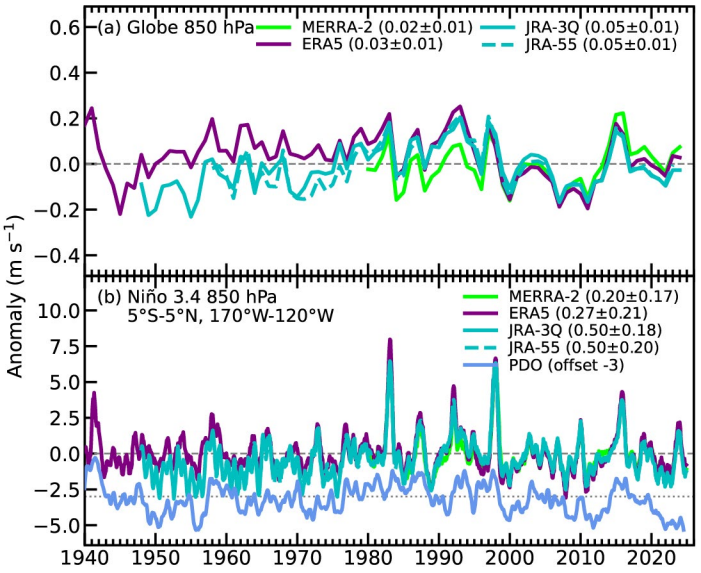

Fig. 2.56. Eastward wind speed anomalies (m s^{-1}; 1991–2020 climatology) averaged (a) globally and (b) over the Nino-3.4 region (5°S–5°N, 170°W–120°W), as depicted from two fourth-generation (MERRA-2 [Gelaro et al. 2017] and JRA-55 [Kobayashi et al. 2015]) and two fifth-generation (the Japanese Reanalysis for Three Quarters of a Century [JRA-3Q; Kosaka et al. 2024] and ERA5 [Hersbach et al. 2020] reanalyses). The Pacific Decadal Oscillation (PDO) index from the NOAA Physical Sciences Laboratory (PSL) Ensemble SST product is shown in panel (b) with the zero shifted for better visibility.

weak negative SST anomalies in OND 2024. The enhanced upper-tropospheric divergence in the Caribbean and central North Atlantic was consistent with the active 2024 hurricane season from mid-September to mid-November (see section 4g2 for details). The weak anomalous convergence over the east central tropical Pacific region was in line with the below-average Pacific hurricane activity (see section 4g3).

The quasi-biennial oscillation in 2024 was near-normal. The stratospheric zonal-mean zonal wind was dominated by a westerly shear zone, which descended from the 12-hPa level down to 80 hPa at about 1.37±0.87 km month^{-1}, which is faster than average, but not unusual. The maximum easterly amplitude occurred in February at 20hPa (–31.6 m s^{-1}) and the maximum westerly amplitude at 40 hPa in October (13.8 m s^{-1}). This amplitude is on the weaker end for a westerly shear zone, but still not an outlier in the historical record. The new easterly formed in October and started descending from the 10-hPa level.

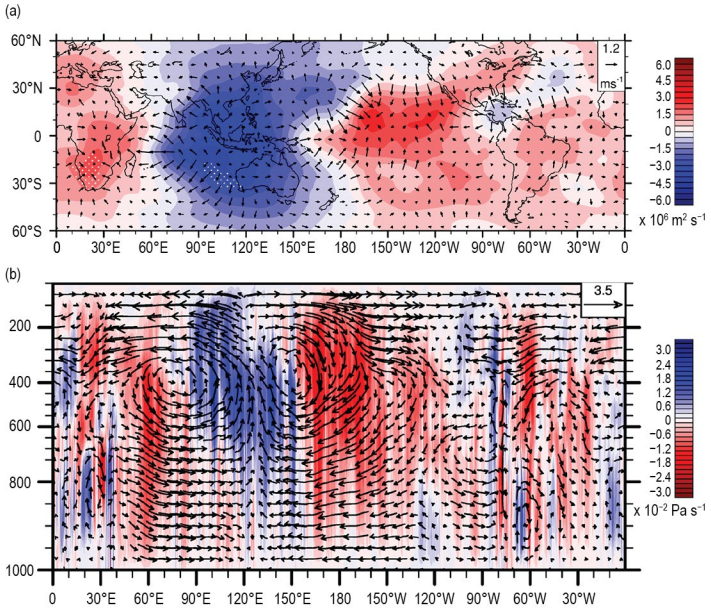

Fig. 2.57. (a) 200-hPa (colors) velocity potential (× 10^6 m^2 s^{-1}) and (arrows) divergent wind anomalies (m s^{-1}) with respect to the 1991–2020 climatology for Oct–Dec 2024; stippling indicates regions with anomalies exceeding 1.65 standard deviations of the seasonal anomalies. Based on ERA5 data. (b) Anomalies of pressure vertical velocity (shaded; units: × 10^{-2} Pa s^{-1}) and u/w anomalies (arrows) averaged over the region 10°S–10°N (zonal [divergent + rotational] wind anomaly [u] unit: m s^{-1}, pressure vertical velocity anomaly [w] unit: × 10^{-2} Pa s^{-1}).

4. NOVEL LIGHTNING FLASH DENSITIES FROM SPACE

—M. Füllekrug, E. Williams, C. Price, S. Goodman, R. Holzworth, S.-E. Enno, and B. Viticchie

The European Organisation for the Exploitation of Meteorological Satellites (EUMETSAT) recently launched the Lightning Imager (LI) onboard the Meteosat Third Generation (MTG) geostationary satellite in support of climate monitoring and lightning warning alerts as a proxy measure for high-impact weather. MTG-LI started to deliver publicly available lightning flash occurrence times and locations on 4 July 2024, 1500 UTC (EUMETSAT 2024). The optical emissions from lightning flashes are recorded with four cameras with slightly overlapping field of views which cover Europe, Africa, the Middle East, the eastern part of South America, and a large part of the Atlantic Ocean (EUMETSAT 2023). South America is also covered by the Geostationary Lightning Mapper (GLM) on the Geostationary Operational Environmental Satellite 16 (GOES-16) (Rudlosky and Virts 2021). The field of view of MGT-LI extends from 80°S to 80°N latitude to cover part of the Antarctic and Arctic, where lightning occurrence may increase as a result of fast rising near-surface temperatures (Holzworth et al. 2021). The lightning flash densities were accumulated in a map with a spatial resolution of 0.1° × 0.1° from July 2024 to January 2025 (Fig. 2.58). These lightning flash densities are largest ~177 fl km^{-2} yr^{-1} along the western side of the Virunga Mountains as part of the Albertine

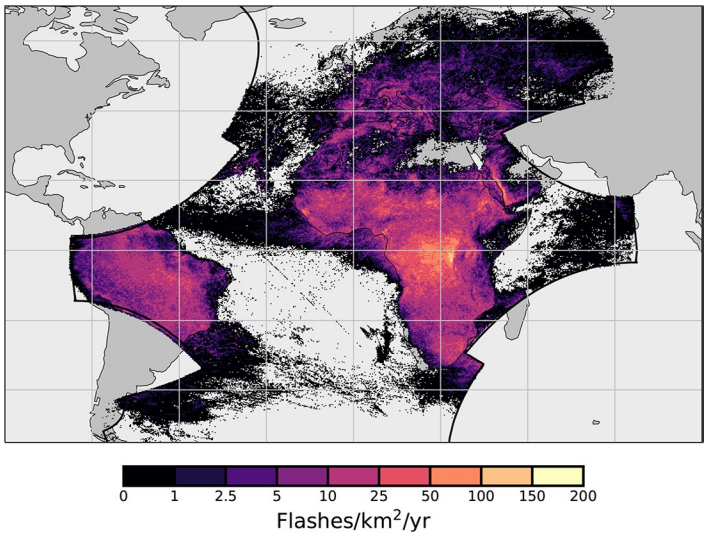

Fig. 2.58. Lightning flash densities (fl km^2 yr^{-1}) calculated from the European Organisation for the Exploitation of Meteorological Satellites' (EUMETSAT) Lightning Imager (LI) on the Meteosat Third Generation (MTG) geostationary satellite from Jul 2024 to Jan 2025. The largest lightning flash densities, ~177 fl km^2 yr^{-1}, are found west of the Virunga Mountains and Lake Kivu along the border between East and Central Africa. Many lightning flashes are detected over the Atlantic and Indian Oceans as part of thunderstorm systems driven by the trade winds.

Rift and Lake Kivu in Africa, where Rwanda, the Democratic Republic of Congo, and Uganda meet. Although lightning is mainly a continental phenomenon (Füllekrug et al. 2022), relatively large flash densities were observed over the Atlantic and Indian Oceans. These lightning flash densities follow the outflow of thunderstorms from the continents, for example westerlies at midlatitudes and easterlies at low latitudes. It is thought that many of the optical pulses recorded by MTG-LI are caused by in-cloud (IC) lightning flashes, which are more common than cloud-to-ground (CG) lightning flashes (Rakov and Uman 2003).

The lightning flash densities over the oceans and the continents have different seasonal variability. Figure 2.59 shows the differences between lightning flash densities during July and December 2024. Over the continents, the lightning flash densities migrate seasonally following the solar insolation, which increases surface temperature and thereby facilitates the development of deep convection. Over the oceans, the lightning flash densities are larger in December compared to July. Four key areas can be distinguished: 1) the Mediterranean Sea, the relative warmth of which interacts with cold European air to enhance instability and deep convection during the winter months, and where numerous particularly intense lightning discharges commonly known as superbolts occur (Holzworth et al. 2019); 2) the Cape Verde Islands, possibly linked to the Atlantic winter storm tracks; 3) the Mid-Atlantic off the coast of western Africa linked to the Intertropical Convergence Zone (ITCZ); and 4) the southern Atlantic off the coast of southern Brazil, due to cooler continental air in winter (July) moving out over the warm Brazil and South Atlantic currents. It is thought that the increase of lightning flash densities over the oceans are caused by the larger heat storing capacity of the oceans when compared to the continents during the winter months, and that warmer ocean currents might assist the initiation of deep convection (Virts et al. 2015; Füllekrug et al. 2002). In this context, it is interesting to note that Lake Victoria (Africa) exhibits a different diurnal cycle when compared to the land around it (Virts and Goodman 2020). It is expected that such regional and seasonal climatological differences will become more evident when MTG-LI lightning flashes accumulate over time, allowing for more detailed analyses with particular emphasis on annual anomalies. Thunderstorms over Lake Victoria are an important area of study because of the risks to local fishers (Thiery et al. 2016; Roberts et al. 2022). Another interesting area of research with EUMETSAT's novel lightning flash densities is the propagation of atmospheric instabilities associated with thunderstorms and lightning across the Atlantic, which have the potential to develop into hurricanes in the Caribbean and the southeastern United States (Price et al. 2009).

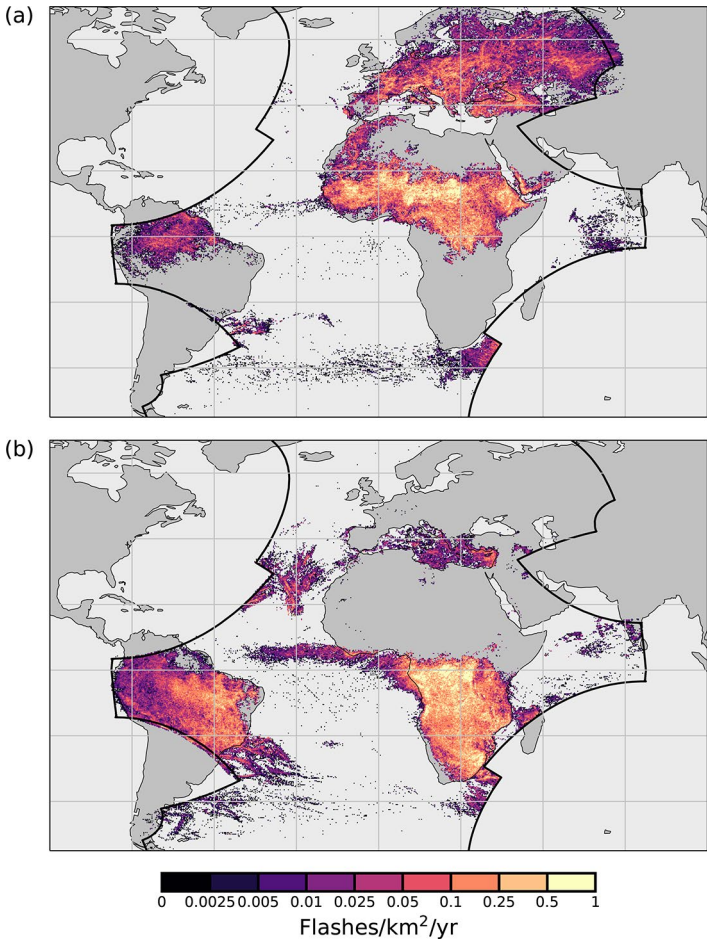

Fig. 2.59. Lightning flash densities (fl km^2 yr^{-1}) for (a) Jul 2024 and (b) Dec 2024.

f. Earth radiation budget

1. EARTH RADIATION BUDGET AT TOP-OF-ATMOSPHERE

—T. Wong, P. W. Stackhouse Jr., P. Sawaengphokhai, J. Garg, and N. G. Loeb

The Earth radiation budget (ERB) at top-of-atmosphere (TOA) is defined by the exchange of incoming total solar irradiance (TSI) and outgoing radiation from Earth given by the sum of reflected shortwave (RSW) and outgoing longwave radiation (OLR). This balance is vital in understanding Earth's climate system and global temperature variations. Over the past two decades, the climate system has amassed a large net positive imbalance, representing a sizeable surplus of energy to the Earth–atmosphere system (Loeb et al. 2021, 2022; von Schuckmann et al. 2023). This net positive imbalance continued in 2024 with a global annual mean of +0.85 W m^{-2} despite the transition from El Niño to La Niña-like conditions.

An analysis of the Clouds and the Earth's Radiant Energy System (CERES) TOA ERB measurements (Table 2.10) shows that the global annual-mean OLR increased by 0.35 W m^{-2} relative to 2023, and RSW by 0.65 W m^{-2}, while the corresponding TSI component remained unchanged in 2024 relative to 2023 (rounded to the nearest 0.05 W m^{-2}). As a consequence of the increase in both OLR and RSW, the global annual-mean net radiation decreased by 1.00 W m^{-2}. Figure 2.60 shows regional annual-mean difference maps in OLR and RSW between 2024 and 2023. The largest reductions in OLR and increases in RSW, indicative of the increases in deep convection, are observed over the tropical Indian Ocean, Australia, the region just east and southeast of

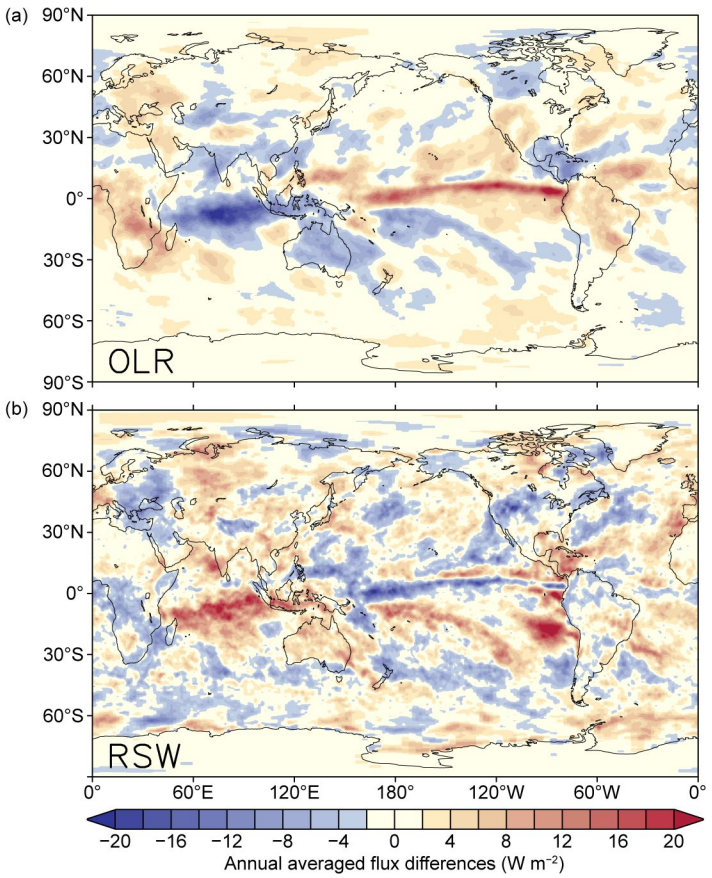

Fig. 2.60. Annual average top-of-atmosphere flux differences (W m^{-2}) between 2024 and 2023 for (a) outgoing longwave radiation (OLR) and (b) reflected shortwave radiation (RSW). The annual mean maps for 2024 were derived after adjusting Dec 2024 Fast Longwave and Shortwave Radiative Fluxes (FLASHFlux) version 4C data using the difference between Clouds and the Earth's Radiant Energy System (CERES) EBAF Ed4.2.1 and CERES FLASHFlux version 4C data in 2023.

Table 2.10. Global annual mean top-of-atmosphere (TOA) radiative flux changes between 2023 and 2024, the 2024 global annual mean radiative flux anomalies relative to their corresponding 2001–23 mean climatological values, the mean 2001–23 climatological values, and the 2-sigma interannual variabilities of the 2001–23 global annual mean fluxes (all units in W m^{-2}) for the outgoing longwave radiation (OLR), total solar irradiance (TSI), reflected shortwave (RSW), absorbed solar radiation (ASR, determined from TSI–RSW), and total net fluxes (Net). All flux values have been rounded to the nearest 0.05 W m^{-2} and only balance to that level of significance.

Global	One Year Change (2024 minus 2023) (W m^{-2})	2024 Anomaly (Relative to 2001–23) (W m^{-2})	Climatological Mean (2001–23) (W m^{-2})	Interannual Variability (2001–23) (W m^{-2})
OLR	+0.35	+1.15	240.40	±0.70
TSI	+0.00	+0.25	340.20	±0.20
RSW	+0.65	–0.85	98.90	±1.20
ASR	–0.65	+1.10	241.30	±1.25
Net	–1.00	–0.05	0.90	±0.95

the Australian continent, and the South Pacific Convergence Zone. The largest increases in OLR and decreases in RSW are observed to cover the entire extent of the equatorial Pacific Ocean. There is also an area of increased RSW off the west coast of South America that does not have a corresponding OLR decrease; this may be due to a thickening of stratocumulus clouds there. These large regional changes represent the response of the climate system as it transitioned from El Niño into La Niña-like conditions. Additional studies are required to understand fully the effects of this El Niño–Southern Oscillation (ENSO) transition as well as other climate drivers on the observed regional changes in the Earth radiation budget during the past year. While the 2024 global annual-mean anomalies, relative to their 2001–23 climatology, for TSI, RSW, and net anomalies (Table 2.10) were near or within their corresponding 2-sigma interannual variability, the 2024 OLR anomaly continued to be outside the range of natural variability observed during the past two decades. This large 2024 OLR anomaly illustrates that the Earth climate system continues to labor excessively to remove the large surplus of energy currently stored within its system.

The global monthly-mean TOA OLR anomaly varied between +0.80 W m^{-2} and +1.55 W m^{-2} in 2024 (Fig. 2.61). This variability is consistent with NOAA's High-resolution Infrared Radiation Sounder (HIRS; Lee and NOAA CDR Program 2018) and NASA's Atmospheric Infrared Sounder (AIRS; Susskind et al. 2012) OLR datasets (not shown). The 2024 global annual-mean TOA OLR anomaly was +1.15 W m^{-2}. The global monthly-mean TOA absorbed solar radiation (ASR, determined from TSI minus RSW) anomaly also remained positive between +0.55 W m^{-2} and +1.65 W m^{-2} in 2024. The 2024 global annual-mean TOA ASR anomaly was +1.10 W m^{-2}. The global monthly-mean TOA total net anomaly, which is calculated from ASR anomaly minus OLR anomaly, varied between –1.00 and +0.35 W m^{-2} in 2024. The global annual-mean TOA total net anomaly for 2024 was –0.05 W m^{-2}. Further analyses are needed to understand the significance and impacts of these observed global changes.

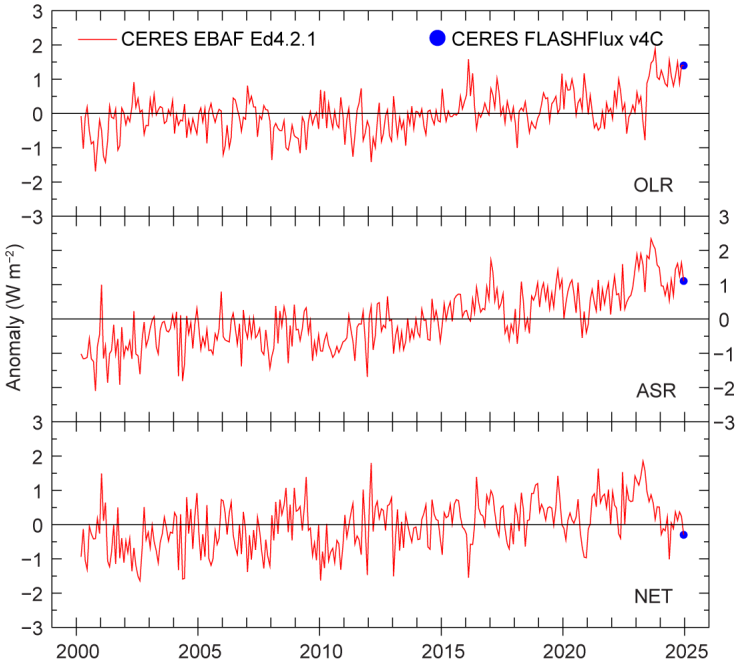

Fig. 2.61. Time series of global monthly mean deseasonalized anomalies (W m^{-2}) of top-of-atmosphere Earth radiation budget for outgoing longwave radiation (OLR; top), absorbed solar radiation (ASR, determined from total solar irradiance [TSI] minus reflected shortwave [RSW]; middle), and total net (TSI–RSW–OLR; bottom) from Mar 2000 to Dec 2024. Anomalies are relative to their calendar month climatology (2001–23). The time series show the Clouds and the Earth's Radiant Energy (CERES) EBAF Ed4.2.1 1-Deg data (Mar 2000–Nov 2024) in solid red line and the CERES Fast Longwave and Shortwave Radiative Fluxes (FLASHFlux) version 4C data (Dec 2024) in solid blue dot; see text for merging procedure (Sources: https://ceres-tool.larc.nasa.gov/ord-tool/jsp/EBAFTOA421Selection.jsp; https://ceres-tool.larc.nasa.gov/ord-tool/jsp/FLASH_TISASelection.jsp).

The TSI data are from a "Community-Consensus TSI Composite" using the methodology defined by Dudok de Wit et al. (2017). The TOA RSW and TOA OLR data are from two different CERES datasets. The data for March 2000–November 2024 are based on the CERES Energy Balanced and Filled (EBAF) Ed4.2.1 product (Loeb et al. 2009, 2012, 2018), which were constructed with measurements from the CERES instruments (Wielicki et al. 1996, 1998) aboard *Terra*, *Aqua*, and NOAA-20 spacecraft. The data for December 2024 are from the CERES Fast Longwave and Shortwave Radiative Fluxes (FLASHFlux) version 4C product (Kratz et al. 2014), which were created using CERES measurements from *Terra* and NOAA-20 spacecraft. The FLASHFlux to EBAF data normalization procedure (Stackhouse et al. 2016) results in 2-sigma monthly uncertainties of ±0.40 W m^{-2}, ±0.00 W m^{-2}, ±0.45 W m^{-2}, and ±0.50 W m^{-2} for the OLR, TSI, RSW, and total net radiation, respectively (rounded to the nearest 0.05 W m^{-2}).

2. MAUNA LOA APPARENT TRANSMISSION RECORD UPDATE FOR 2024

—J. A. Augustine, L. Soldo, K. O. Lantz, A. Baron, K. Smith, E. Asher, and J.-P. Vernier

Since 2018, the Northern Hemisphere (NH) lower stratosphere (LS) has been continuously infused with aerosols from a series of volcanic eruptions (e.g., Raikoke, Ulawun, La Soufriere, Hunga) and wildfire events (e.g., Pacific Northwest; Boone et al. 2020). These perturbations are evident from both a composite, multi-platform analysis from the Global Space-based Stratospheric Aerosol Climatology (GloSSAC; Thomason et al. 2018; Kovilakam et al. 2020) and from aerosol extinction time series imagery from the Stratospheric Aerosol and Gas Experiment (SAGE-III) limb sounder on board the International Space Station (ISS). Although the Hunga eruption occurred in the Southern Hemisphere (20.54°S), its stratospheric plume extended to the latitude of the Mauna Loa Observatory (MLO, 19.536°N, 155.576°W, elevation 3397 m a.s.l.) on the Big Island of Hawaii (Augustine et al. 2024). These events have kept the apparent atmospheric transmission at MLO near or below 0.93 since 2018.

Broadband pyrheliometer measurements of the direct solar beam at MLO have been used to derive atmospheric transmission since 1958 (Ellis and Pueschel 1971). The high altitude and pristine environment there makes transmission a fitting proxy of the extent and variability of stratospheric aerosols. Bodhaine et al. (1981) demonstrated that the principal tropospheric influence on the transmission is the perennial passage of dust from springtime storms in Asia. The complete time series (Fig. 2.62) begins with a very clean period, until the Agung eruption in 1963. That period serves as a baseline-level clean stratosphere, as there were no impactful volcanic events from the mid-1930s to 1963 (Ammann et al. 2003; Sato et al. 1993). Since Agung, a series of eruptions have kept the transmission generally lower than pre-1963 baseline levels.

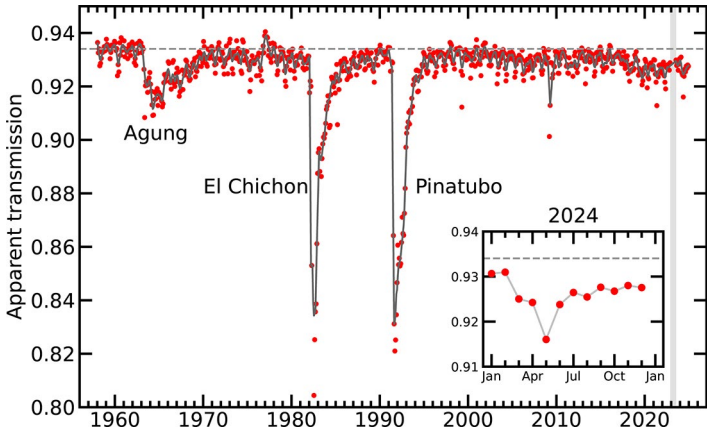

Fig. 2.62. Apparent transmission at Mauna Loa, Hawaii, from 1958 through 2024. Red dots are monthly averages of morning transmission and the black curve is a locally weighted scatterplot smoothing (LOWESS) fit with a six-month smoother applied. Inset shows new data for 2024. Horizontal dashed lines represent the average transmission of the clean period before the eruption of Agung (Ammann et al. 2003; Sato et al. 1993). The shaded area represents the period from Dec 2022 through Jun 2023 when the station was down due to the eruption of Mauna Loa in late Nov 2022.

The extended transmission reduction from 2018 through 2024 is evident in Fig. 2.62. New data for 2024, shown in the inset of Fig. 2.62, have an annual mean of 0.926±0.00387. The year began with a relatively high transmission of ~0.93 in January and February as the LS was recovering from the Hunga eruption. Reduction of the transmission in March and April was probably caused by dust because, after a lull in 2023, several strong spring storms in the desert regions of northwest China and Mongolia brought dust to Japan and Korea and then to Mauna Loa. The latter is supported by the aerosol optical depth (AOD) product from NASA's Moderate Resolution Imaging Spectroradiometer (https://earthobservatory.nasa.gov/global-maps/MODAL2_M_AER_OD). It shows relatively high AOD over Hawaii from March through May, followed by dramatic clearing in June as easterly tropospheric winds became more persistent. The sharp minimum in May was likely due to both Asian dust and stratospheric plumes from explosive eruptions of Ruang in Indonesia on 16 and 29 April 2024, which sent eruptive plumes 21,000 m and 19,000 m above mean sea level, well into the LS. Other NH explosive eruptions in 2024, e.g., Kanlaon in the Philippines, did not penetrate the tropopause. An aerosol layer in the LS centered at ~5°S is apparent in a latitudinal cross section of the aerosol extinction coefficient from SAGE for August 2024 (https://sage.nasa.gov/2024/09/sage-iii-iss-science-highlight/). Residual Hunga aerosol was supplemented in the tropics by Ruang and now extends beyond 30°N, overlying MLO.

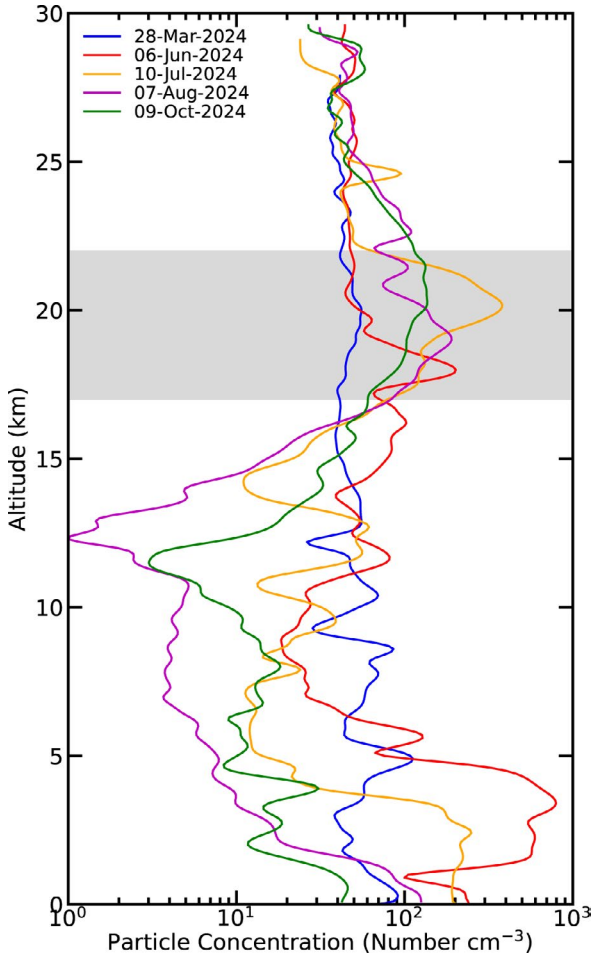

Fig. 2.63. Particle number concentration profiles at standard temperature and pressure (STP; number STP cm^{-3}) from the Portable Optical Particle Spectrometer (POPS) aboard the NOAA Global Monitoring Laboratory balloon platform launched from Hilo, Hawaii, ~60 km east of Mauna Loa. The shaded area highlights lower-stratosphere (LS) aerosol signals in Jun, Jul, Aug, and Oct 2024 that arose from the Ruang eruptions in Apr 2024.

Trajectories from the Hybrid Single-Particle Lagrangian Integrated Trajectory model (HYSPLIT; Stein et al. 2015) reveal that the stratospheric plume from Ruang reached the longitude of MLO around 14 May. NOAA balloon sondes (Todt et al. 2023; Asher et al. 2024) from Hilo, Hawaii, ~60 km east of MLO, on 6 June, 10 July, 7 August, and 9 October carrying the Portable Optical Particle Spectrometer (POPS; Gao et al. 2016) confirm the presence of the Ruang signal between 17,000 m and 22,000 m a.s.l. (Fig. 2.63). That signal was also sampled by a NASA balloon at Baura, Brazil, on 1 June 2024 (https://science.larc.nasa.gov/balneo/). The highest aerosol number concentrations were observed in June (200 Number cm^{-3}) and July (300 Number cm^{-3}), with back trajectories indicating that LS signals at Hilo were from Ruang. Slowly increasing transmission after July that is apparent in the inset of Fig. 2.62, along with the sequence of sondes in Fig. 2.63, reflect a diminishing Ruang signal to the end of the year.

Major wildfire activity in 2024 occurred in South and Central America and Canada from July through September (section 2h3). However, trajectory and the Copernicus Atmosphere Monitoring Service's (CAMS) analyses (https://atmosphere.copernicus.eu/south-america-sees-historic-emissions-during-2024-wildfire-season) suggest that smoke from those fires had little to no presence over Hawaii.

g. Atmospheric composition

1. LONG-LIVED GREENHOUSE GASES

—X. Lan, B. D. Hall, G. Dutton, and I. Vimont

In 2024, the atmospheric burdens of the three most important long-lived greenhouse gases (LLGHGs), carbon dioxide (CO_2), methane (CH_4), and nitrous oxide (N_2O), showed no sign of slowing in their increases. The globally averaged CO_2 level at Earth's surface in 2024—as derived from remote marine boundary layer measurements made by NOAA's Global Monitoring Laboratory—reached 422.8±0.1 ppm (parts per million by moles in dry air; Fig. 2.64a; Table 2.11; uncertainties are reported as one sigma in this section), a 52% increase from the pre-industrial level of ~278 ppm (Etheridge et al. 1996). Globally averaged CH_4 and N_2O levels reached 1930.0±0.6 ppb (parts per billion by moles in dry air) and 337.7±0.1 ppb in 2024, which are 165% and 25% increases from pre-industrial levels, respectively. Yet again, these three LLGHGs are setting record highs.

Carbon dioxide is the most important and abundant anthropogenic greenhouse gas (GHG). Annual growth in global-mean CO_2 has risen from 0.6±0.1 ppm yr^{-1} in the early 1960s to an average of 2.4 ppm yr^{-1} during 2011–20 (Lan et al. 2025a). The increase in CO_2 by 3.4 ppm from 2023 to 2024 tied with that of 2015/16 as the highest on record since systematic measurements started in the 1960s. The main driver of increasing atmospheric CO_2 is fossil fuel (FF) burning; overall emissions, including cement production, increased from 3.0±0.2 Pg C yr^{-1} in the 1960s to 9.7±0.5 Pg C yr^{-1} in the past decade (2014–23; Friedlingstein et al. 2025). Emissions in 2024 are estimated at 10.2±0.5 Pg C yr^{-1} (Friedlingstein et al. 2025). Together with the measured atmospheric increase, it is estimated that about 45% of the FF-emitted CO_2 since 1958 has remained in the atmosphere, with the remaining portion entering the oceans and terrestrial biosphere (Friedlingstein et al. 2025). While increasing emissions of CO_2 from FF combustion are roughly monotonic, the CO_2 growth rate varies from year to year (standard deviation = 0.4 ppm in 2015–24) with variability mostly driven by terrestrial biosphere exchange of CO_2. The El Niño–Southern Oscillation (ENSO) changes regional temperature and precipitation patterns and influences photosynthetic CO_2 uptake, respiratory release, and fires. It is the main driver of CO_2 interannual variability (Betts et al. 2016; Liu et al. 2017). The record-high CO_2 increase in 2024 was likely driven by the record-high global temperature and large fire carbon emissions during the year.

Atmospheric CH_4 is the second most important LLGHG, and in 2024 its globally averaged abundance at Earth's surface reached 1930.0±0.6 ppb (Lan et al. 2025b),

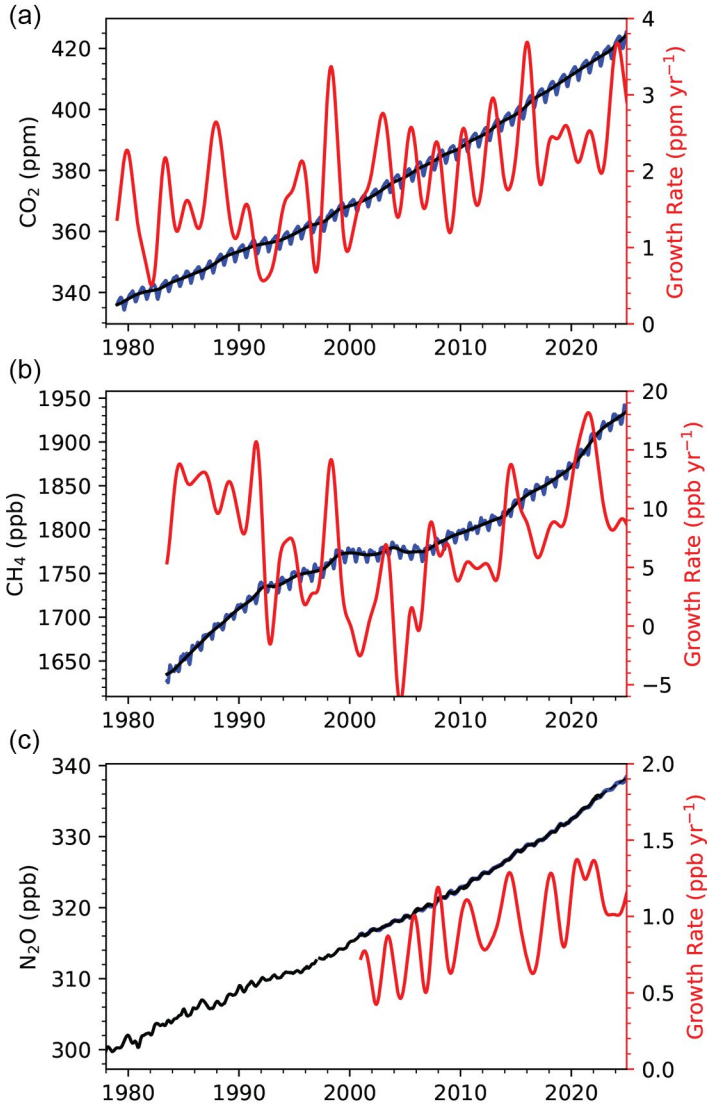

Fig. 2.64. Global mean dry-air remote surface mole fractions (approximately weekly data in blue and deseasonalized trend in black; left axis) and instantaneous growth rates (red, right axis) calculated as time derivatives of deseasonalized trend curves of (a) carbon dioxide (CO_2), (b) methane (CH_4), and (c) nitrous oxide (N_2O) derived from marine boundary layer measurements from the NOAA Global Greenhouse Gases Reference Network. See Dlugokencky et al. (1994) for methods. N_2O data prior to 2000 are insufficient and noisy, and therefore hinder the calculation of a growth rate.

about 2.65 times its pre-industrial level of 729±9 ppb (Mitchell et al. 2013). Global CH_4 increased by an average rate of 11.5±1.4 ppb yr^{-1} between 1984 and 1991, followed by a smaller increase of 5.4±1.8 ppb yr^{-1} between 1992 and 1998, and a further reduced rate near zero (0.7±3.0 ppb yr^{-1}) between 1999 and 2006. Atmospheric CH_4 growth restarted in 2007 and has accelerated since 2014, and further accelerated in 2020–24 with an average rate of increase of 12.6±2.0 ppb yr^{-1} (Fig. 2.64b). Atmospheric CH_4 increased by 8.4±0.4 ppb from 2023 to 2024.

Atmospheric CH_4 is emitted by anthropogenic sources such as fossil fuel exploitation, livestock, waste and landfills, and rice cultivation areas, as well as natural sources such as wetlands and shallow lakes. The ongoing reduction in atmospheric $\delta^{13}C$-CH_4 since 2008 (Michel et al. 2024) indicates increased emissions from microbial sources (Basu et al. 2022), including emissions from livestock as well as natural wetlands and lakes, which have more negative $\delta^{13}C$-CH_4 signatures. Small increases in FF emissions may also play a role in the post-2006 global CH_4 increase (Oh et al. 2023; Lan et al. 2019, 2021; Basu et al. 2022). The contribution of the hydroxyl radical, the main sink for CH_4, is still uncertain, but is less likely to be a major contributor (Morgenstern et al. 2025; Zhao et al. 2019; Lan et al. 2021). Recent studies suggest a dominant role of increased tropical wetland emissions in the post-2020 CH_4 surge (Lin et al. 2024; L. Feng et al. 2022; Peng et al. 2022). Sustained increases in wetland CH_4 emissions may be an indication of an emerging carbon climate feedback (Nisbet et al. 2023; Zhang et al. 2023).

Nitrous oxide (N_2O) is a potent greenhouse gas with an atmospheric lifetime of 120 years (Tian et al. 2024). It is produced by microbes that rely on nitrogen from natural and agricultural soils, animal manure, and the oceans (Davidson 2009). Increased agricultural emissions related to fertilizer usage are the major source of its long-term increase (Tian et al. 2023). The average global atmospheric abundance of N_2O in 2024 was 337.7±0.1 ppb, a 25% increase over its pre-industrial level of 270 ppb (Rubino et al. 2019). Recent growth reached an average rate of 1.3±0.1 ppb yr^{-1} from 2020 to 2022 (Fig. 2.64c), larger than the average rate between 2010 and 2019 (1.0±0.2 ppb yr^{-1}), strongly suggesting increased emissions (Tian et al. 2023). Atmospheric N_2O increased by 1.0±0.1 ppb from 2023 to 2024.

The impacts of LLGHGs on global climate can be estimated using the effective radiative forcing (ERF) of LLGHGs, the change of radiative energy caused by added LLGHGs to the atmosphere, following the approach used in the Intergovernmental Panel on Climate Change's Sixth Assessment Report (Forster et al. 2021). Increased atmospheric abundances of LLGHGs are largely responsible for increasing global temperature (Forster et al. 2023; IPCC 2013). Since the industrial era (1750), increasing atmospheric CO_2 has accounted for 64% of the increase in ERF by LLGHGs, reaching 2.33 W m^{-2} in 2024 (Fig. 2.65). The increase in CH_4 contributed a 0.57 W m^{-2} increase in ERF between 1750 and 2024 while the CH_4-related production of tropospheric ozone and stratospheric water vapor also contributes to ~0.30 W m^{-2} indirect radiative forcing (Myhre et al. 2014). The increase in atmospheric N_2O abundance contributed to a 0.23 W m^{-2} increase in ERF between 1750 and 2024.

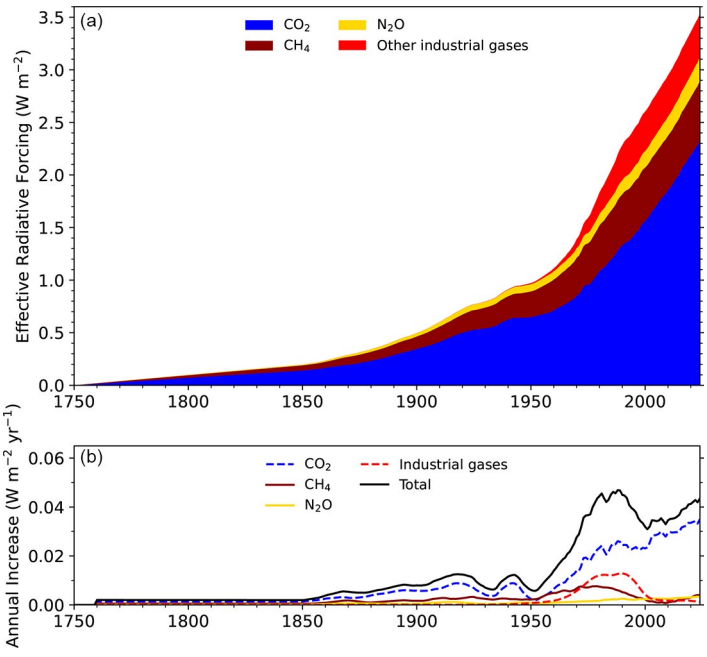

Fig. 2.65. (a) Effective radiative forcing (W m^{-2}) due to long-lived greenhouse gases (LLGHGs; see Table 2.11 for details on industrial gases). (b) Annual increase in effective radiative forcing (W m^{-2} yr^{-1}) smoothed by a 10-year running average.

Table 2.11. Summary table of long-lived greenhouse gases for 2024 (CO_2 mixing ratios are in ppm, N_2O and CH_4 in ppb, and all others in ppt).

Compound Class	Industrial Designation or Common Name	Chemical Formula	ERF[a]	Effective Rad. Efficiency (W m^{-2} ppb^{-1})[b]	Effective Rad. Forcing[a] (ERF or SARF) (W m^{-2})	Mean Surface Mole Fraction, 2024 [Change from Prior Year][c]	Lifetime (yrs)[b]
Acidic Oxide	Carbon Dioxide	CO_2	Y	1.33×10^{-5}	2.33	422.8 [3.4]	
Alkane	Methane	CH_4	Y	3.89×10^{-4}	0.57	1930.0 [8.4]	9.1
Nitride	Nitrous Oxide	N_2O	Y	3.20×10^{-3}	0.23	337.7 [1.0]	109
Chlorofluorocarbons	CFC-11	CCl_3F	N(Y)[e]	0.30	0.057 (0.063)	214.5 [–2.7][d]	52
Chlorofluorocarbons	CFC-12	CCl_2F_2	N(Y)[e]	0.36	0.156 (0.172)	481.5 [–3.9][d]	102
Chlorofluorocarbons	CFC-113	CCl_2FCClF_2	N	0.30	0.020	66.6 [–0.6][d,f]	93
Hydrochlorofluorocarbons	HCFC-22	$CHClF_2$	N	0.21	0.052	245.3 [–2.2]	11.6
Hydrochlorofluorocarbons	HCFC-141b	CH_3CCl_2F	N	0.16	0.004	24.4 [–0.1]	8.8
Hydrochlorofluorocarbons	HCFC-142b	CH_3CClF_2	N	0.19	0.004	20.7 [–0.3]	17.1
Hydrofluorocarbons	HFC-134a	CH_2FCF_3	N	0.17	0.022	134.7 [5.2]	13.5
Hydrofluorocarbons	HFC-152a	CH_3CHF_2	N	0.10	<0.001	7.73 [0.38]	1.5
Hydrofluorocarbons	HFC-143a	CH_3CF_3	N	0.17	0.005	32.4 [1.7]	52
Hydrofluorocarbons	HFC-125	CHF_2CF_3	N	0.23	0.01	47.5 [4.0]	31
Hydrofluorocarbons	HFC-32	CH_2F_2	N	0.11	0.003	38.2 [4.4]	5.3
Hydrofluorocarbons	HFC-23	CHF_3	N	0.19	0.007	37.8 [1.0]	228
Hydrofluorocarbons	HFC-365mfc	$CH_3CF_2CH_2CF_3$	N	0.24	<0.001	1.03 [0.04]	8.9
Hydrofluorocarbons	HFC-227ea	CF_3CHFCF_3	N	0.27	<0.001	2.39 [0.19]	36
Chlorocarbons	Methyl Chloroform	CH_3CCl_3	N	0.07	<0.001	0.87 [–0.11]	5
Chlorocarbons	Carbon Tetrachloride	CCl_4	N	0.17	0.012	73.0 [–0.8][d]	30
Chlorocarbons	Methyl Chloride	CH_3Cl	N	0.005	<0.001	550 [5]	0.9
Bromocarbons	Methyl Bromide	CH_3Br	N	0.004	<0.001	6.52 [0.08]	0.8
Bromocarbons	Halon 1211	$CBrClF_2$	N	0.31	0.001	2.75 [–0.09]	16
Bromocarbons	Halon 1301	$CBrF_3$	N	0.31	0.001	3.3 [0]	72
Bromocarbons	Halon 2402	$CBrF_2CBrF_2$	N	0.33	<0.001	0.390 [–0.005]	28
Fully Fluorinated Species	Sulfur Hexafluoride	SF_6	N	0.57	0.007	11.8 [0.4]	850–1280
Fully Fluorinated Species	PFC-14	CF_4	N	0.1	0.005	90.4 [1.0]	~50,000
Fully Fluorinated Species	PFC-116	C_2F_6	N	0.26	0.001	5.33 [0.09]	~10,000
Fully Fluorinated Species	PFC-218	C_3F_8	N	0.28	<0.001	0.78 [0.02]	~2600
Fully Fluorinated Species	PFC-318	c-C_4F_8	N	0.33	<0.001	2.18 [0.08]	~3200

[a] Effective Radiative Forcing (ERF) calculated by multiplying the stratospheric-temperature-adjusted radiative efficiency (SARF) by the global mole fraction (in ppb) and then applying a tropospheric adjustment factor for the species indicated based on recommended values from chapters 6 and 7 in the Intergovernmental Panel on Climate Change Sixth Assessment Report Working Group I (IPCC AR6 WGI) Report. The Radiative Forcing column is either ERF (where indicated) or SARF. The adjustments to the SARF are CO_2: 5%±5%, CH_4: –14%±15%, N_2O: 7%±13%–16%

[b] Effective radiative efficiencies and lifetimes were taken from Appendix A in WMO (2022) and Hodnebrog et al. (2020a), except CH_4 which is from Prather et al. (2012). For CO_2, numerous removal processes complicate the derivation of a global lifetime. AGGI = Annual Greenhouse Gas Index. For radiative forcing, see https://www.esrl.noaa.gov/gmd/aggi/aggi.html

[c] Mole fractions are global, annual, midyear surface means determined from the NOAA Cooperative Global Air Sampling Network (Hofmann et al. 2006), except for PFC-14, PFC-116, PFC-218, PFC-318, and HFC-23, which were measured by the Advanced Global Atmospheric Gases Experiment (AGAGE; Mühle et al. 2010; Miller et al. 2010). Changes indicated in brackets are the differences between the 2024 and 2023 means. All values are preliminary and subject to minor updates.

[d] Global mean estimates derived from multiple NOAA measurement programs ("Combined Dataset").

[e] ERF-calculated values for CFC-11 and CFC-12 are highly uncertain but recommended by the IPCC AR6 WGI Report. Thus, they are included in parentheses here as the lower confidence value. The adjustment to the SARF for these values is 12%±13% (Hodnebrog et al. (2020b).

[f] Measurements of CFC-113 are known to be a combination of CFC-113 and CFC-113a, with CFC-113a contributing approximately 0.3 ppt to the 2024 reported abundance of CFC-113.

2. OZONE-DEPLETING GASES

—I. J. Vimont, B. D. Hall, S. A. Montzka, G. Dutton, J. Mühle, M. Crotwell, K. Petersen, S. Clingan, and D. Nance

Since 1987, the Montreal Protocol (Montreal Protocol 1989) and its Amendments (The Protocol; https://ozone.unep.org/treaties/montreal-protocol) have regulated the production and consumption of ozone-depleting substances (ODSs) and their replacement chemicals. Controlled chemicals include chlorofluorocarbons, hydrochlorofluorocarbons, and hydrofluorocarbons, (CFCs, HCFCs, and HFCs, respectively), as well as halons and methyl bromide. While The Protocol was initially enacted to limit damage to the stratospheric ozone layer by limiting ODS production for dispersive uses, these controls have also limited the impact of these gases on Earth's radiation budget. Through the 2016 Kigali Amendment, The Protocol also limits production and consumption of some HFCs that do not destroy stratospheric ozone, but like the CFCs and HCFCs they replace, are strong greenhouse gases.

Emissions of a chemical do not necessarily cease once production has been phased out for dispersive uses, nor are emissions the only factor controlling the atmospheric abundance of a trace gas species. Reservoirs that exist, e.g., in equipment and insulating foams (known as "banks") can continue to emit controlled chemicals for years after the final phase-out of production has occurred. The observed atmospheric trends of ODSs and their replacements (Fig. 2.66) result from the combination of emissions and the rate at which compounds degrade via loss processes such as photolysis. As an example, CFC-11 and CFC-12 production for dispersive use was scheduled to be globally phased out in 2010, but they have long atmospheric lifetimes and remain present in large banks that continue to emit both compounds. CFC-12, the most abundant CFC, declined by 4 ppt in 2024 to 481.4 ppt (Table 2.11). Conversely, methyl chloroform (CH_3CCl_3) has relatively small banks and a short lifetime and, having been phased out in 2015, has declined in the atmosphere to 0.87 ppt, 99% lower than its peak abundance.

While the transition from CFCs to HCFCs resulted in an increase in the atmospheric abundance of several HCFCs during the 1990s and 2000s, the mole fractions of the three most abundant HCFCs (HCFC-22, HCFC-141b, and HCFC-142b) have started to decline (Fig. 2.66; Table 2.11). For example, HCFC-22 declined by 2.2 ppt in 2024 to 245.3 ppt. The combined radiative forcing from these three HCFCs peaked in 2021 and is now declining (Western et al. 2024). In contrast, mole fractions of several HFCs, used as replacements for HCFCs, have increased substantially since their introduction in the mid-1990s, in particular HFC-134a, HFC-32, and HFC-23. There is substantial interest in HFC-23 because it is a potent greenhouse gas and is emitted primarily as a by-product of HCFC-22 production (UNEP 2024). The production of chlorinated and fluorinated compounds such as HFCs and some plastics can also result in emissions of ODSs. Recent increases in abundances and emissions of CFC-13, CFC-112a, CFC-113a, CFC-114a, and CFC-115 (not shown), chemicals controlled by the Montreal Protocol, have been identified and could be related to uses and processes not controlled by the Montreal Protocol (Western et al. 2023). Of these, CFC-115 is the most abundant at ~8.8 ppt.

While global measurements of ODSs mainly represent the composition of the planetary boundary layer close to Earth's surface,

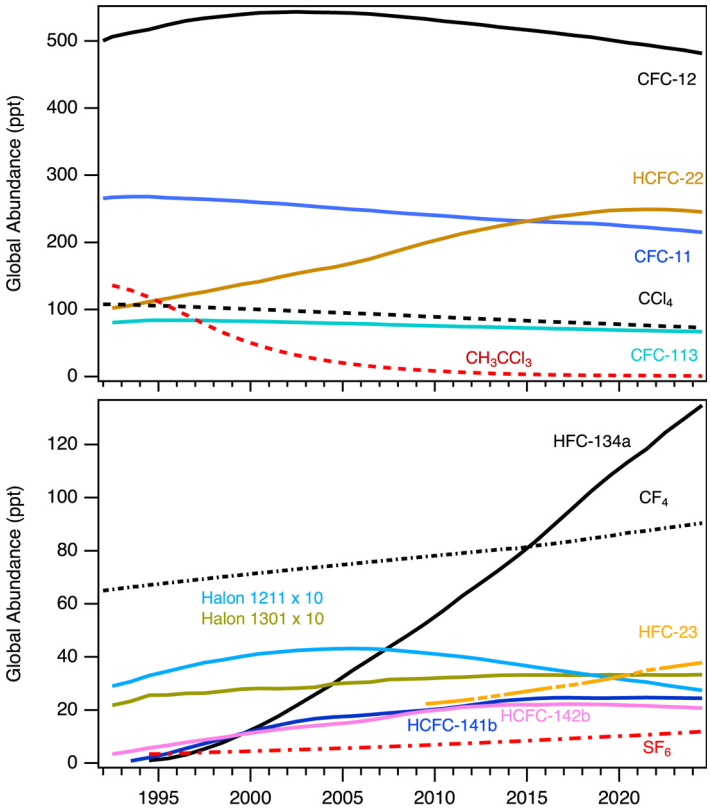

Fig. 2.66. Global mean abundances (mole fractions) at Earth's surface (ppt = pmol mol^{-1} in dry air) for several halogenated gases, many of which deplete stratospheric ozone. See Table 2.11 for the 2024 global mean mole fractions of these and other gases.

destruction of the ozone layer is dependent on the amount of reactive halogen in the stratosphere. In order to track progress towards the ozone layer's recovery, equivalent effective stratospheric chlorine (EESC) is used as a measure of the reactive halogen loading in the stratosphere based on globally distributed surface measurements, atmospheric transport, and chemical reactivity (Daniel et al. 1995; Newman et al. 2007). While EESC provides a measure of reactive stratospheric halogen, it is also useful to scale the EESC to provide context relative to stratospheric ozone recovery. The Ozone Depleting Gas Index (ODGI) assesses the EESC relative to 1980, where an ODGI of 0 represents the EESC level in 1980, and an ODGI of 100 represents peak EESC, which occurred in 1996/97 at midlatitudes and in 2001/02 over Antarctica. The EESC and, therefore, also the ODGI, are reported for the midlatitudes and the Antarctic in order to capture the range of ozone layer recovery timescales due to differences in transport and chemical degradation processes in the stratosphere. At the beginning of 2024, reactive halogen in the Antarctic (represented by air with a mean transit time from the surface of 5.5 years) had decreased 28% from the peak relative to the 1980 benchmark. Likewise, reactive halogen in the midlatitude region (represented by air with a mean transit time from the surface of three years) declined by 55% (Fig. 2.67; https://gml.noaa.gov/odgi/).

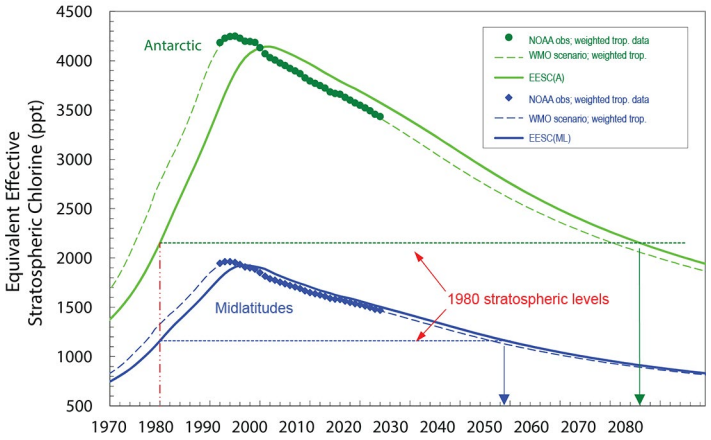

Fig. 2.67. Equivalent effective stratospheric chlorine (EESC) calculated for air representative of the Antarctic (green) and midlatitude (blue) stratosphere (EESC[A] and EESC[ML], respectively). Dashed lines represent tropospheric measurement-derived scenarios, based on past measurements and, for the future, full adherence to all controls from The Protocol based on the World Meteorological Organization (WMO)/United Nations Environment Programme 2018 Ozone Assessment. Solid blue and green arrows indicate currently predicted dates for the return of EESC to 1980s levels in midlatitudes (year 2048) and over the Antarctic (year 2076), respectively. Solid lines depict inferred stratospheric changes based on the measured tropospheric curves.

3. TROPOSPHERIC AEROSOLS

—S. Rémy, N. Bellouin, M. Parrington, M. Ades, M. Alexe, A. Benedetti, O. Boucher, E. di Tomaso, and Z. Kipling

Atmospheric aerosols play an important role in the climate system by scattering and absorbing radiation, and by affecting the life cycle, optical properties, and precipitation activity of clouds (IPCC AR6, chapter 6; Szopa et al. 2021). Aerosols in the boundary layer also represent a serious public health issue in many countries and are thus subject to monitoring and forecasting as part of air quality policies.

The Copernicus Atmosphere Monitoring Service (CAMS; https://atmosphere.copernicus.eu) runs near-real-time (NRT) global analyses and forecasts of aerosols and trace gases. CAMS also produces a reanalysis of global aerosols and trace gases that covers the years between 2003 and 2024 (CAMSRA; Inness et al. 2019) by combining state-of-the-art numerical modeling and aerosol remote sensing retrievals from the Moderate Resolution Imaging Spectroradiometer (MODIS) onboard the *Terra* and *Aqua* satellites (Levy et al. 2013) and the Advanced Along Track Scanning Radiometer (AATSR) onboard the Envisat satellite (Popp et al. 2016). This section uses data exclusively from the CAMS reanalysis, focusing on aerosol optical depth at 550 nm in the middle of the visible light spectrum (AOD550), as well as surface particulate matter (PM2.5) concentrations. AOD550 is a vertically integrated quantity while PM2.5 is a surface parameter.

AOD550 and PM2.5 absolute values in 2024 (Plates 2.1ab, ac, respectively) show maxima from pollution over the industrial regions of India and China, as well as from dust over the Sahara and the Middle East. High values in 2024 also arose from seasonal vegetation fires in equatorial Africa and the southern Amazon Basin, and occasionally from extreme fires, most notably across large parts of Canada and eastern Siberia. A strong seasonality appears in AOD550, driven mainly by dust episodes between March and July in the Sahara, Middle East, and Taklimakan/Gobi

regions, as well as seasonal biomass burning emissions in tropical regions of Africa, South America, and Indonesia (Fig. 2.68c). Globally averaged AOD550 in 2024 was the highest since 2019, driven by higher-than-usual fire activity over large parts of North and South America as well as equatorial Africa.

The AOD550 anomalies (Plate 2.1ab) are dominated by the large fire events over western Brazil, Canada, equatorial Africa, and eastern Siberia. The PM2.5 anomalies mostly match those in AOD, except for the PM2.5 anomalies caused by large fires, which caused elevated aerosol plumes with a clear AOD signature, but without a PM2.5 one. Over parts of South America, a series of recent years with positive anomalies led to a positive trend of AOD since 2012. Dust storm activity was higher than usual over the western Sahara (with the signal mostly in PM2.5) and the southern Arabian Peninsula, and lower than usual over the eastern Sahara. The negative anomalies of AOD and PM2.5 over East Asia, the eastern United States, and Europe can be explained by ongoing decreasing long-term trends in these regions. Conversely, the positive anomalies over India and Iran are associated with increasing long-term trends over these regions. The exceptional nature of the fires in the summer of 2024 in South America, Canada, and equatorial Africa is highlighted by Plate 2.1ad, which shows the number of extreme AOD days in 2024 as compared to the climatological distribution of daily AOD over the 2003–24 period. Interestingly, for the South American fires, the highest number of extreme AOD days is found over the Pacific and Atlantic Oceans from transported plumes of smoke originating from Bolivia and southern Brazil. Fires also caused a significant number over parts of Siberia, while the high values over India are mostly from anthropogenic sources.

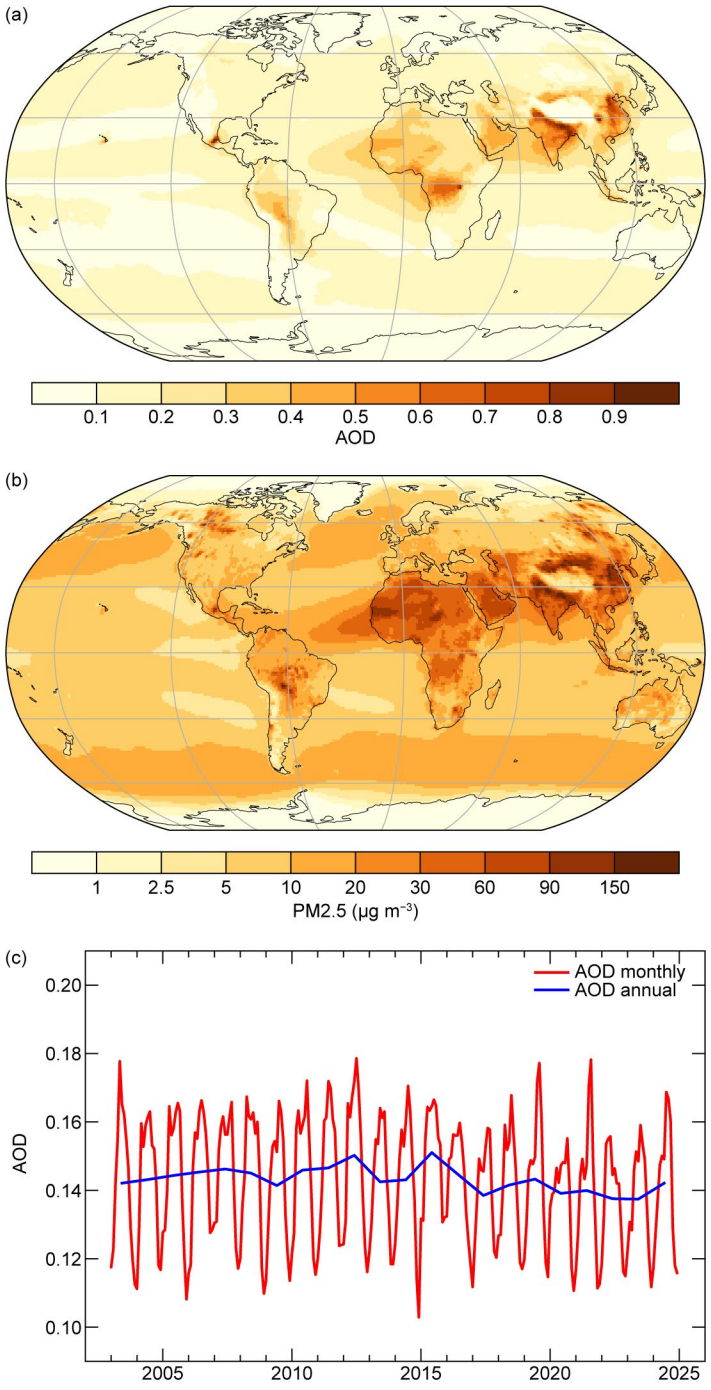

Fig. 2.68. (a) Global aerosol optical depth (AOD) at 550 nm in 2024. (b) Global surface particulate matter (PM2.5) concentrations (μg m^{-3}) in 2024. (c) Global average of total AOD at 550 nm averaged over monthly (red) and annual (blue) periods for the period 2003–24.

The AOD550 nm and PM2.5 2003–24 trends (Fig. 2.69a,b) are generally collocated, although discrepancies can occur, particularly in regions mainly affected by fires and dust transport. Between 2003 and 2024, there is a significant negative trend in both quantities over most of the United States, Europe, East Asia, and most of the eastern Sahara. The first three can be attributed to a decrease in anthropogenic emissions while the last is caused mainly by a decrease of desert dust emissions. Positive trends in AOD are noted over parts of Siberia, driven by biomass burning events, as well as over India and Iran, driven by an increase in anthropogenic emissions (Satheesh et al. 2017). Interestingly, the positive trend in AOD over Iran and the Indian subcontinent is not matched by a corresponding positive trend in PM2.5. This means that in the CAMS reanalysis, the increasing trend in aerosol burden over these areas is simulated aloft and not at surface, which could be an artefact, or because of elevated aerosol plumes such as those from desert dust or fire events.

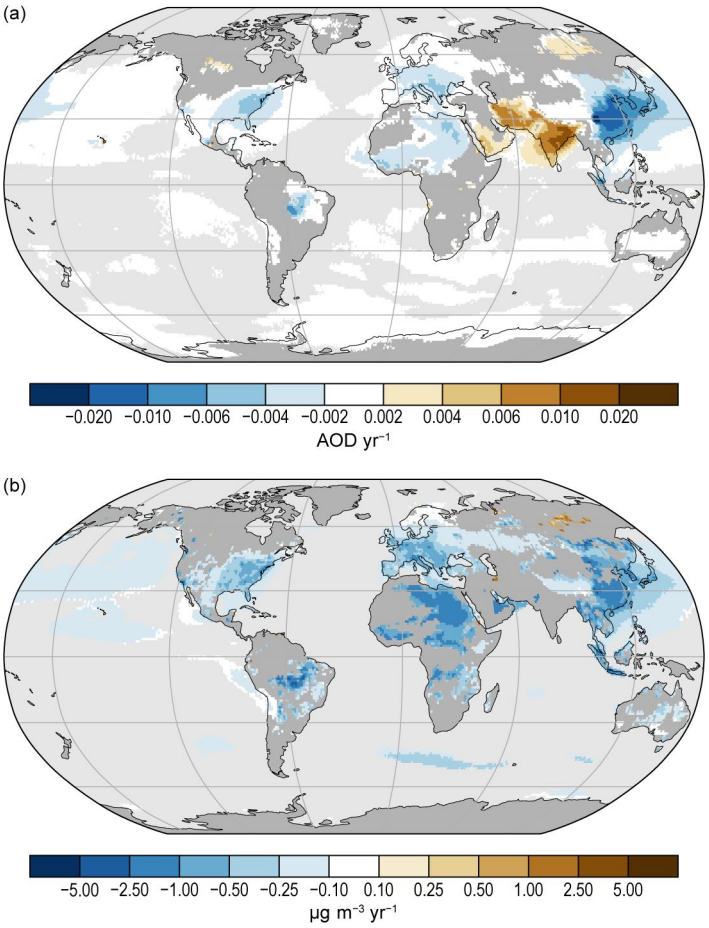

Fig. 2.69. (a),(b) linear trends of total aerosol optical depth (AOD yr^{-1}) and particulate matter (PM2.5), respectively, (μg m^{-3} yr^{-1}) for the period 2003–24. Only trends that are statistically significant (95% confidence level) are shown. Regions with decreasing trends include the eastern United States, most of Europe, and parts of Brazil and China, as well as the Korean peninsula and Japan.

Tarasick et al. 2019; Gulev et al. 2021; Chang et al. 2024). On the global scale, the tropospheric ozone burden (TOB) increased from the mid-1990s to 2019, based on a range of in situ and satellite observations. Last year's *State of the Climate* report (Cooper et al. 2024a) reported an apparent leveling-off of ozone for the period 2020–23, mainly at northern midlatitudes, likely initiated by the economic downturn associated with the Coronavirus disease 2019 (COVID-19) pandemic. However, the updated tropospheric ozone product from the Aura Ozone Monitoring Instrument (OMI) and the Microwave Limb Sounder (MLS) satellite instruments (based on the new OMI Collection 4 total ozone) does not support a sustained leveling-off of ozone on the global scale (Fig. 2.70a), and the long-term trend for the period 2004–24 is positive. Notably, 2024 experienced the highest TOB since the OMI/MLS record began in 2004.

Anthropogenic AOD and radiative forcing resulting from aerosol–radiation interactions (RFari) and aerosol–cloud interactions (RFaci) are shown in Appendix Fig. A2.12 for 2024 and the period 2003–24. They are estimated using the methods described in Bellouin et al. (2020). There was a small increase in anthropogenic AOD again this year, but aerosol radiative forcing has remained fairly flat recently.

4. TROPOSPHERIC OZONE

—O. R. Cooper, J. R. Ziemke, K.-L. Chang, and P. Effertz

Tropospheric ozone contributes to almost all of ozone's effective radiative forcing (tropospheric and stratospheric), estimated to be 0.51 (0.25–0.76) W m^{-2} for the period 1750–2023 (Forster et al. 2024). A short-lived climate forcer, its lifetime is on the order of three to four weeks (Archibald et al. 2020) and, therefore, its global distribution is highly variable and difficult to quantify (Gaudel et al. 2018;

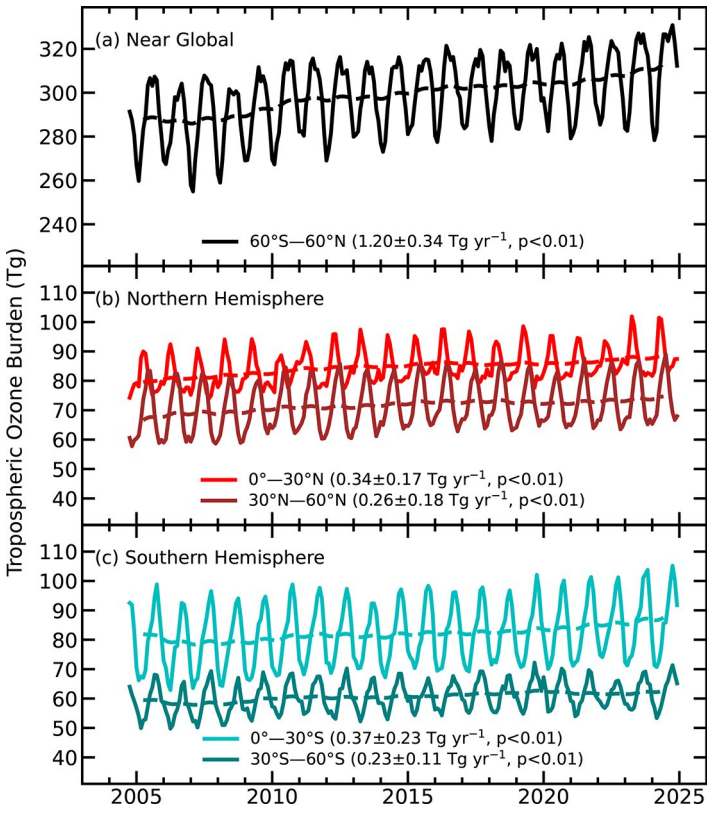

Fig. 2.70. Monthly averages (solid lines) and 12-month running means (dashed lines) of Ozone Monitoring Instrument (OMI)/Microwave Limb Sounder (MLS) tropospheric ozone burdens (Tg) from Oct 2004 through Dec 2024 for (a) near global (60°S–60°N; black), (b) the Northern Hemisphere tropics (0°–30°N; red) and midlatitudes (30°N–60°N; dark red), and (c) the Southern Hemisphere tropics (0°–30°S; blue) and midlatitudes (30°S–60°S; green). Slopes of linear fits to the data are presented with their 95%-confidence-level uncertainties.

Averaged over the entire year of 2024, and relative to 2005–23, positive ozone anomalies were widespread across the Northern Hemisphere (NH), with the largest anomalies found above central Asia, the tropical North Atlantic, the eastern North Pacific, and western North America (Plate 2.1ae). Anomalies in the Southern Hemisphere (SH) were generally positive across the tropics and across much of the midlatitudes, with weaker positive anomalies across southern Australia and the central South Pacific Ocean.

Over the full 20-year record, global (60°S–60°N) TOB increased at the average rate of 1.20±0.34 Tg yr^{-1}, equal to a total increase of ~8% (Fig. 2.70). Regarding the impact of COVID-19, the updated OMI/MLS product shows a brief leveling-off of ozone from 2019 to 2020 and into 2021, similar to other satellite products (Ziemke et al. 2022); however, by the end of 2021, ozone began to increase again through 2024. Regionally, the strongest trends (2004–24) have occurred above central and southern Asia and also across western North America and central South America (Fig. 2.71). Strong ozone decreases were not observed above any region of the globe.

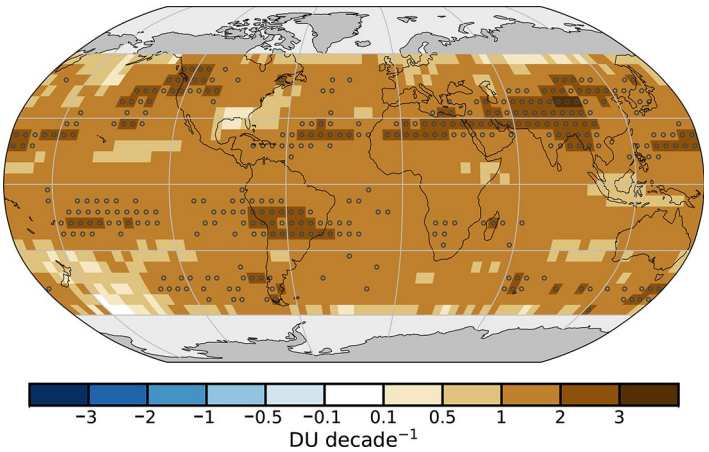

Fig. 2.71. Linear trends in Ozone Monitoring Instrument (OMI)/Microwave Limb Sounder (MLS) tropospheric column ozone (DU decade^{-1}) on a 5° × 5° grid from Oct 2004 through Dec 2024. Circles denote trends with p-values <0.05. Trends were calculated using a multivariate linear regression model (e.g., Randel and Cobb 1994 and references therein) that included a seasonal cycle fit and the Niño-3.4 index as an El Niño–Southern Oscillation proxy; trend uncertainties included autoregressive adjustment via Weatherhead et al. (1998).

Ozone trends at the surface are often decoupled from the trends in the free troposphere (Gulev et al. 2021; Chang et al. 2023), and the availability of long-term surface ozone records is too limited spatially to produce a globally representative surface ozone product (Sofen et al. 2016). However, global chemistry climate models can estimate surface ozone trends, and their output can be evaluated against reliable observations. Ozone trends from six surface sites are reported here, all located in remote environments and suitable for evaluating coarse resolution global models. These records are now 25 to 50 years in length (Fig. 2.72; Table 2.12). In the Arctic, Barrow Atmospheric Observatory (at sea level) reported a weak positive trend of 0.45±0.30 ppbv decade^{-1}, while the high-elevation site of Summit, Greenland, showed decreasing ozone since 2000 (–1.89±0.85 ppbv decade^{-1}). In the remote North Atlantic Ocean, Tudor Hill, Bermuda (sea level),

Table 2.12. Ozone trends at the six baseline monitoring sites shown in Fig. 2.72. Trends are estimated by the generalized least-squares method, based on monthly anomalies referenced to the monthly 2000–20 base period (Chang et al. 2021), and reported with 95% confidence intervals and *p*-values. The trends at the Mauna Loa Observatory (MLO) were adjusted to account for interannual meteorological variability following the methods of Chang et al. (2024), spanning the period 1974–2024.

Site Name — Latitude, Longitude, Elevation	Years With Data	Trend, ppbv decade^{-1}	*p*-value
Summit, Greenland — 72.6°N, 38.5°W, 3238 m	2000–present	–1.89±0.85	p<0.01
Barrow Atmospheric Observatory, Alaska — 71.3°N, 156.6°W, 11 m	1973–present	0.45±0.30	p<0.01
Tudor Hill, Bermuda — 32.3°N, 64.9°W, 30 m	1988–98, 2003–present	–0.65±1.04	p=0.21
Mauna Loa Observatory (MLO), Hawaii — 19.5°N, 155.6°W, 3397 m	1973–present	1.21±0.30	p<0.01
Arrival Heights, Antarctica — 77.8°S, 166.8°W, 50 m	1996–present	–0.04±0.52	p=0.88
South Pole, Antarctica — 90.0°S, 59.0°E, 2840 m	1975–present	0.35±0.33	p=0.03

reported high interannual variability and a weak negative trend (−0.65±1.04 ppbv decade^{-1}), while Mauna Loa (3400 m a.s.l.) in the tropical North Pacific Ocean showed a clear ozone increase since 1973 (1.21±0.30 ppbv decade^{-1}). The Antarctic site of Arrival Heights showed no trend since 1996, while ozone has increased slightly at South Pole (0.35±0.33 ppbv decade^{-1}).

The combined OMI/MLS satellite product (Ziemke et al. 2019) has been reported by the *State of the Climate* reports since 2012, covering most of the globe (60°S–60°N). The product now provides a continuous record of TOB spanning a full 20 years (2004–24). This edition of the *State of the Climate* report uses the latest version of the product, based on the new OMI Collection 4 L1b retrievals (Kleipool et al. 2022), which correct for instrument drift through the end of 2024. The vertical resolution of OMI/MLS monthly tropospheric column ozone is ~3 km near the tropopause with a regional precision (standard deviation) of ~2 Dobson units (DU; ~7%) in all latitude bands; trend uncertainties are about 0.5 DU decade^{-1} (1.5% decade^{-1}).

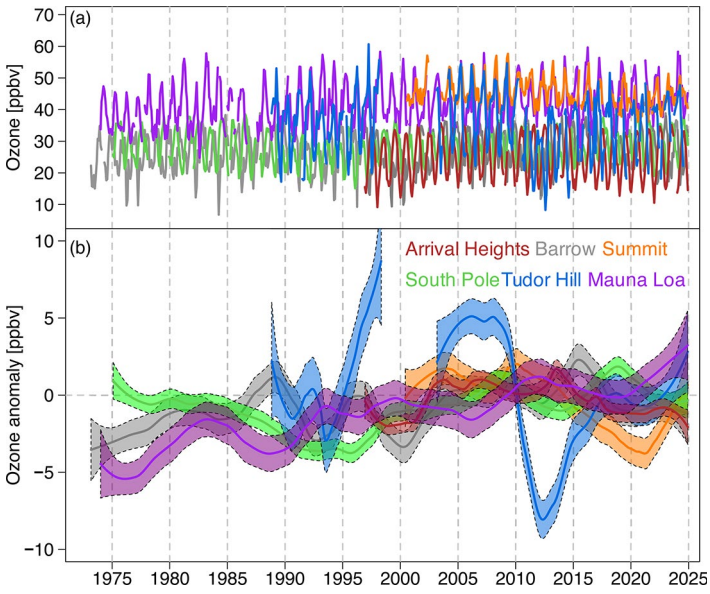

Fig. 2.72. (a) Monthly mean surface ozone (ppbv) at Barrow Observatory, Alaska (gray), Summit, Greenland (orange), Tudor Hill, Bermuda (blue), Mauna Loa, Hawaii (purple), Arrival Heights, Antarctica (red), and the South Pole (green). Monthly means are produced for months with at least 50% data availability using observations from all 24 hours of the day. The locations of each site are listed in Table 2.12. (b) The same time series after conversion to monthly anomalies referenced to the monthly climatological values over 2000–20 and smoothed using locally weighted scatterplot smoothing (LOWESS) regression (Chang et al. 2021).

5. STRATOSPHERIC AEROSOLS

—S. Khaykin, G. Taha, T. Sakai, I. Morino, and B. Liley

Stratospheric aerosols play a large role in the chemical and radiative balance of the atmosphere (Kremser et al. 2016). Explosive volcanic eruptions may directly inject sulfur dioxide (SO_2) and ash into the stratosphere, leading to significant perturbations of stratospheric aerosol burden at hemispheric and global scales that can last from several months to several years. Another important emerging source of particulate matter in the stratosphere is injection of smoke from wildfires via associated pyrocumulonimbus (pyroCb)—the fire-generated storms that can overshoot the tropopause (Peterson et al. 2021).

Despite the continued decay of the stratospheric aerosol perturbation produced by the eruption of the Hunga submarine volcano in January 2022, the stratospheric aerosol optical depth (sAOD) remained elevated above the background level in 2024 (Fig. 2.73a). Due to its extreme explosiveness, the Hunga eruption produced aerosol layers throughout the stratosphere (Taha et al. 2022) and resulted in the largest perturbation of the global sAOD in the last three decades (Khaykin et al. 2022). Augmenting the Hunga perturbation were additional lower stratospheric injections (up to 20 km–21 km) from two consecutive eruptions of the Ruang volcano in North Sulawesi, Indonesia, on 18 and 29 April 2024 (Dodangodage et al. 2025). Extrapolation of the stable decay of the Hunga southern hemispheric sAOD during early 2024 leads to an inference of the total lifetime of the Hunga-induced stratospheric aerosol load of 2.5 years, spanning from mid-January 2022 to mid-July 2024.

The eruption of Ruang ended the era of Hunga-induced sAOD perturbation. The Ruang aerosols spread throughout the tropics in less than two months and were transported farther into the southern extratropics during the austral winter (Fig. 2.73a). Figures 2.73b–e display quarterly zonal-mean extinction ratio (ER, aerosol-to-molecular extinction ratio) from the Ozone Mapping and Profiler Suite Limb Profiler (OMPS-LP) observations, summarizing the stratospheric aerosol latitude–altitude distribution during 2024. During the first three months of 2024, the Hunga aerosols were still present in the tropical mid-stratosphere (21 km–29 km) and the southern extratropical lower stratosphere (Fig. 2.73b). During the three months following the

Ruang eruption, the Ruang aerosols were observed at 18 km–23 km together with a possible contribution from remnants of Hunga above that layer (Fig. 2.73c). During July–September 2024, the Ruang layer intensified, and the isentropic transport of its aerosols to the southern extratropical lowermost stratosphere can be seen (Fig. 2.73d). Further transport of Ruang aerosols towards the southern high latitudes and their upwelling in the tropics to altitudes of 19 km–24 km in October–December, as well as a modest transport into the northern extratropics during this period, can be inferred from Fig. 2.73e.

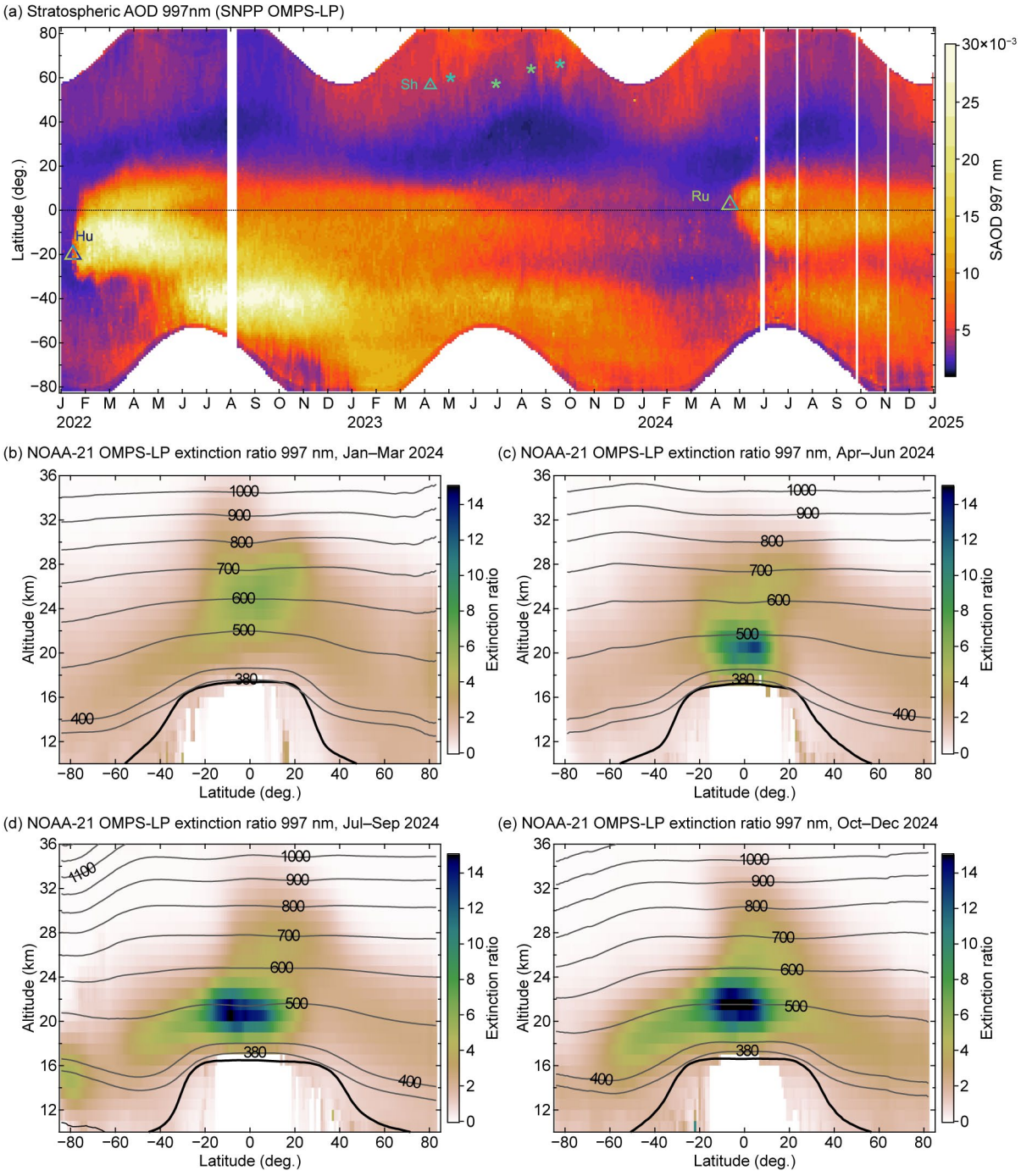

Fig. 2.73. Global evolution of the stratospheric aerosol from the Suomi National Polar-orbiting Partnership (SNPP) and NOAA-21 Ozone Mapping and Profiler Suite–Limb Profile (OMPS-LP) observations at 997 nm during 2022–24. (a) zonal-mean stratospheric aerosol optical depth (sAOD). The triangles indicate the eruptions of Hunga (Hu), Shiveluch (Sh), and Ruang (Ru) volcanoes, whereas the stars indicate the wildfire events with measurable stratospheric impact in Canada and Russia during summer 2023. (b)–(e) NOAA-21 OMPS-LP three-month zonal mean latitude–altitude section of the aerosol-to-molecular extinction ratio (ER) during 2024. The thick black line is the tropopause altitude, and the thin black lines are the potential temperature levels in Kelvin (K).

Figure 2.74 shows three decades of sAOD observations by ground-based Network for the Detection for Stratospheric Change (NDACC) lidars at Observatoire de Haute Provence (OHP; 43.9°N) and Lauder observatory (45°S) together with the corresponding zonally averaged satellite data from the International Space Station's (ISS) Stratospheric Aerosol and Gas Experiment III (SAGE III) instrument and the Global Space-based Stratospheric Aerosol Climatology (GloSSAC). These stations, located nearly antipodally on the globe, respectively represent the northern and southern extratropics. The OHP time series (Fig. 2.74a) during the twenty-first century is largely modulated by several moderate volcanic eruptions as well as by the extreme Pacific Northwest Event (PNE) wildfire outbreak in August 2017 (Khaykin et al. 2018; Peterson et al. 2018). The largest impact on the NH sAOD was caused by the Raikoke eruption in June 2019. Since that time, the OHP sAOD remained elevated, owing to contributions of boreal wildfires and the transport of Hunga aerosols (Khaykin et al. 2024). In late 2024, a subtle increase in sAOD was most likely related to the transport of Ruang aerosol into northern midlatitudes.

In the southern midlatitude stratosphere (Fig. 2.74b), the most significant sAOD perturbations were caused by the 2019/20 Australian New Year (ANY) wildfire super outbreak (Khaykin et al. 2020; Peterson et al. 2021) and the eruption of the Hunga submarine volcano in January 2022. The massive transport of Ruang sulfates into the southern extratropics is reflected in the SH extratropical sAOD enhancement peaking in October 2024 (Fig. 2.74b).

Unlike 2023, which had multiple pyrocumulonimbus clouds in the NH that reached the lowermost stratosphere (Zhang et al. 2024), there were no significant stratospheric intrusions of the smoke during 2024, and most of the aerosol seen in the NH stratosphere originated from the Hunga and Ruang eruptions.

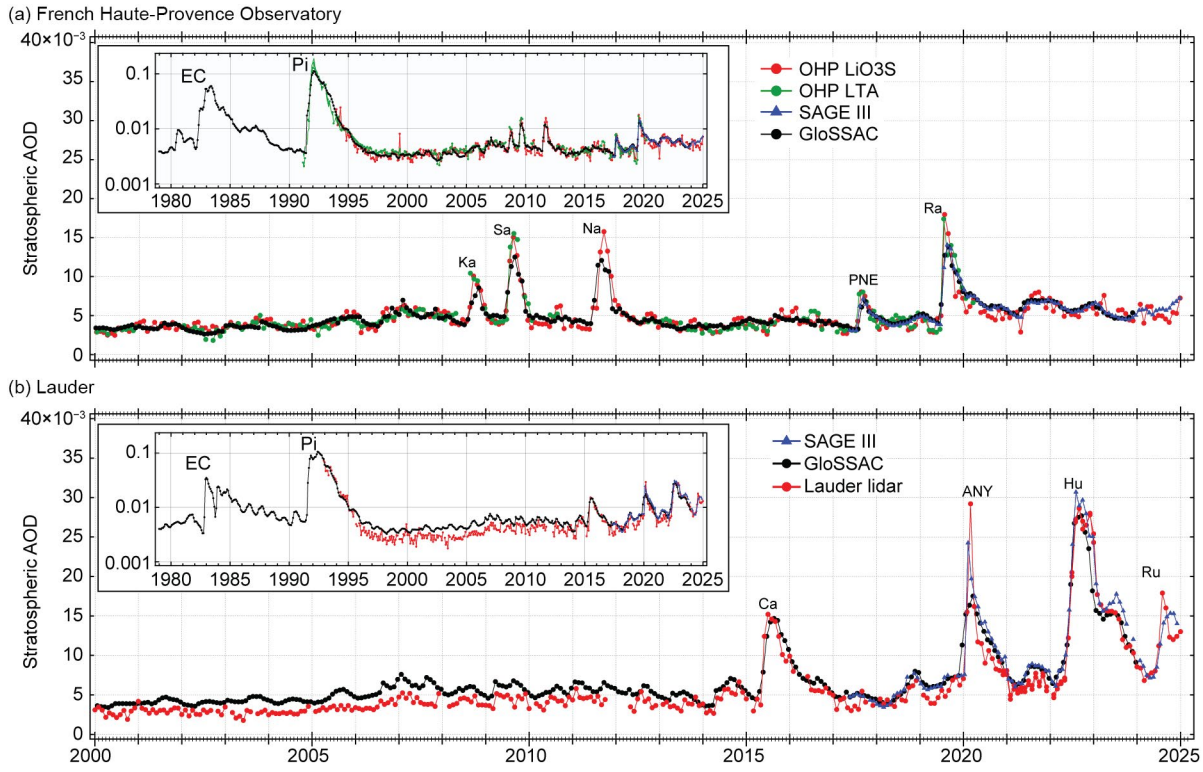

Fig. 2.74. Time series of monthly mean aerosol optical depth at 532 nm of the stratospheric overworld (380 K; 33 km) from ground-based lidars at (a) French Haute-Provence Observatory (OHP, 43.9°N, 5.7°E, Stratospheric Ozone Lidar at OHP [LiO3S] and the Lidar Temperature Aerosol [LTA] instruments) and (b) New Zealand's Lauder station (45°S, 179°E, Lauder aerosol lidar) and the corresponding monthly/zonal-mean values from satellite observations within 40°N–50°N and 50°S–40°S latitude bands from the ISS's Stratospheric Aerosol and Gas Experiment III (SAGE III) instrument and Global Space-based Stratospheric Aerosol Climatology (GloSSAC) merged satellite record. The embedded panels display the log-scaled time series from the beginning of the GloSSAC record. The literal notations indicate the most significant volcanic eruptions: El Chichón (EC), Pinatubo (Pi), Kasatochi (Ka), Sarychev (Sa), Nabro (Na), Raikoke (Ra), Calbuco (Ca), Hunga (Hu), Ruang (Ru); and wildfire events: Pacific Northwest Event (PNE, British Columbia, Canada) and Australian New Year (ANY) super outbreak.

6. STRATOSPHERIC OZONE

—M. Weber, W. Steinbrecht, C. Arosio, R. van der A, S. M. Frith, J. Anderson, L. M. Ciasto, M. Coldewey-Egbers, S. Davis, D. Degenstein, V. E. Fioletov, L. Froidevaux, J. de Laat, D. Loyola, A. Rozanov, V. Sofieva, K. Tourpali, R. Wang, T. Warnock, and J. D. Wild

About 90% of total column ozone resides in the stratosphere; only 10% resides in the troposphere. In 2024, total column ozone was well above the average of 1998–2008 over most of the globe except for two narrow zonal bands in the tropics and a patch over Antarctica (Plate 2.1af). In the NH, anomalies reached values of +60 DU or more in some regions, for example the Canadian Arctic. The time series in Fig. 2.75b show that the 2024 annual zonal mean at northern midlatitudes (35°N–60°N) was close to the high values observed during the 1960s. In March 2024, Arctic (60°N–90°N) total column ozone reached 475 DU, the highest value seen since 1979 (Fig. 2.75e). The variation in annual-mean total column ozone in the extratropics is largely driven by variations in the stratospheric circulation in winter/early spring. During boreal winter/spring 2024, the Brewer–Dobson (BD) circulation, which transports ozone from the tropical source region to middle and high latitudes, was particularly strong (Newman et al. 2024). Combined with the lower stratospheric quasi-biennial oscillation (QBO) in its easterly phase and the strong El Niño conditions in the first half of 2024, total column ozone was reduced in the tropics and strongly enhanced in the extratropics (Figs. 2.75a,b,d; Plate 2.1af; Baldwin et al. 2001; Oman et al. 2013; Butchart 2014; Domeisen et al. 2019).

In the SH midlatitudes and in October in the Antarctic (Fig. 2.75d,e), the last two years were closer to the high end of the range of interannual variability, ending the series of years of low total column ozone from 2020 to 2022, caused by Australian wildfires (Solomon et al. 2023) and a series of volcanic eruptions, including Hunga (Santee et al. 2023; Fleming et al. 2024).

Generally, observed total column ozone values in recent years have tended to be at the low end of projections from chemistry climate models (CCMs; see Figs. 2.75a–d), based on current scenarios for ODSs and GHGs. Overall, the data show the slow path of ozone recovery due to the ODS phase-out by the Montreal Protocol and its Amendments (WMO 2022).

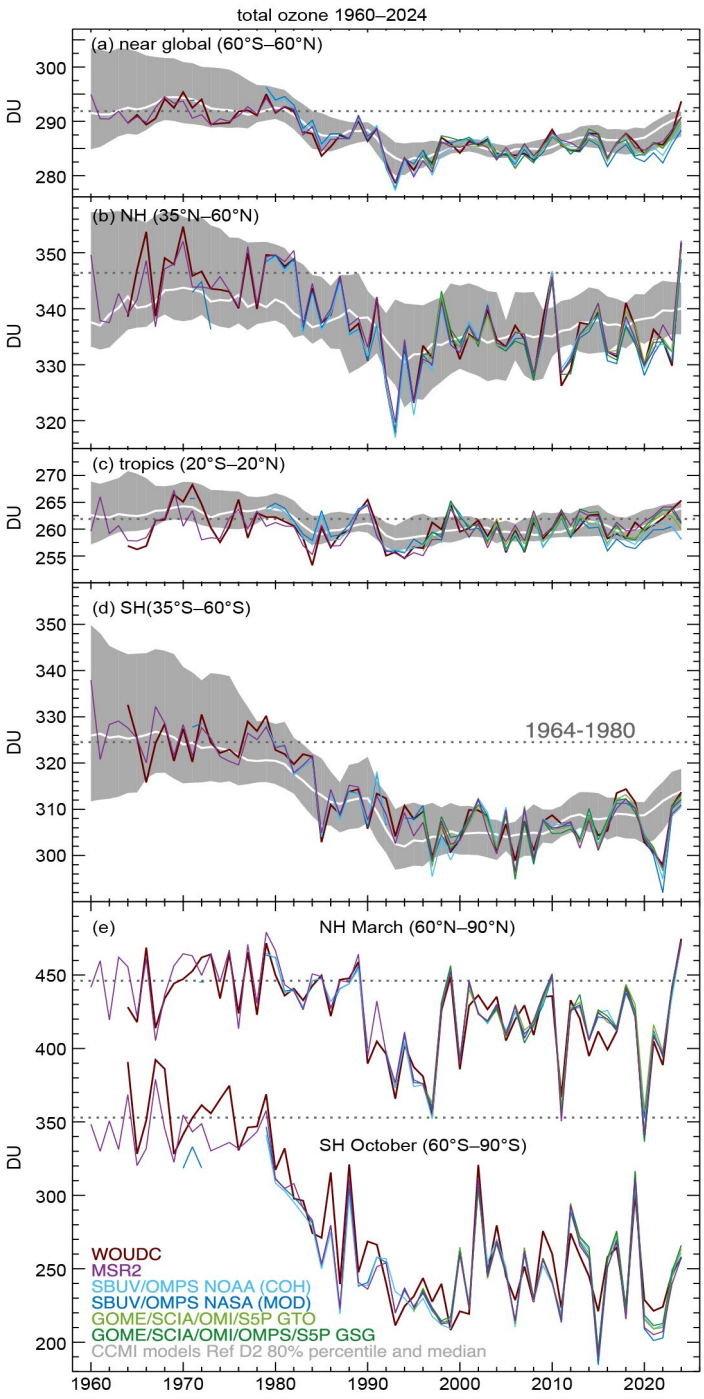

Fig. 2.75. Time series of annual mean total column ozone (DU) in (a)–(d) four zonal bands, and (e) polar (60°–90°) total column ozone in Mar (Northern Hemisphere; NH) and Oct (Southern Hemisphere; SH), the months when polar ozone losses usually are largest. Values are plotted at the tick mark start of each year. The dotted gray lines in each panel show the average ozone level for 1964–1980 calculated from the World Ozone and Ultraviolet Radiation Data Centre's (WOUDC) data. Most of the observational data for 2024 are preliminary. The thick white lines in (a)–(d) show the median from Chemistry-Climate Model Initiative (CCMI)-2022 ref D2 model runs (Plummer et al. 2021). The model data have been smoothed using a three-point triangle function. The gray-shaded areas provide the 80th percentile range. All datasets have been bias-corrected by subtracting individual data averages and adding the multi-instrument mean from the reference period 1998–2008.

Figure 2.76 shows the evolution of ozone profiles at two stratospheric levels and for three latitude bands. The 2-hPa level (or 42-km altitude) represents the upper stratosphere (Figs. 2.76a–c), and the 50-hPa level (or 22-km altitude) the lower stratosphere (Figs. 2.76d–f).

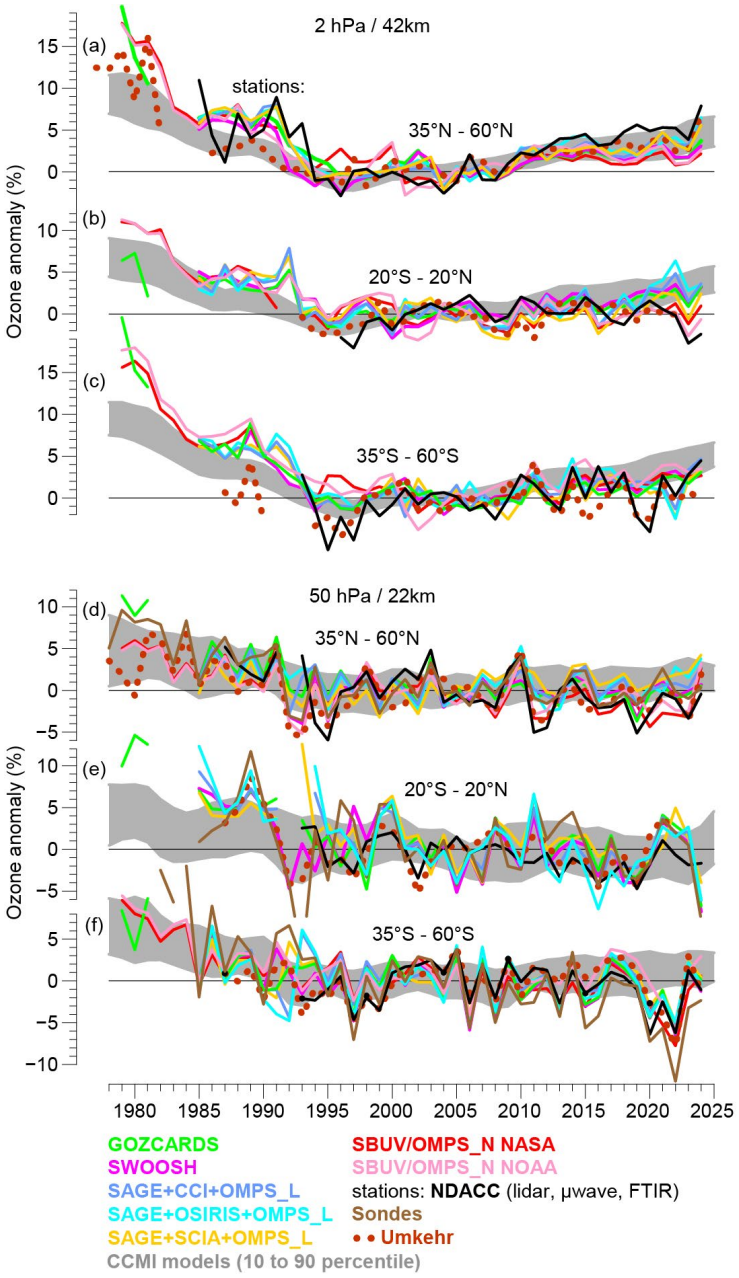

Ozone in the upper stratosphere is controlled to a large degree by photochemistry. The year 2024 continued the slow upper-stratospheric ozone increase due to declining ODSs and cooling of the upper stratosphere, as predicted by models (e.g., WMO 2022), although observed values in recent years have tended to be at the lower end of expectations from CCM simulations (gray-shaded region in Figs. 2.76a–c).

Ozone in the lower stratosphere (Figs. 2.76d–f) is controlled to a large degree by transport variations and is the main contributor to the already discussed total column ozone variations. Consistent with the strong El Niño and the easterly shear phase of the QBO in the lower stratosphere from January to April, ozone values were very low in the tropical band in 2024 (Fig. 2.76e; see also the El Niño years 1998 and 2016). In the Northern Hemisphere extratropical band in 2024 (Fig. 2.76d), ozone at 50 hPa was near the high end of recent values for almost all individual datasets. However, the enhancement was not as large as that seen for total column ozone in Fig. 2.75b, because a large fraction of the total column enhancement in 2024 came from levels lower than 50 hPa. In the SH (Fig. 2.76f) in 2024, ozone at 50 hPa from the zonal-mean satellite datasets again approached the range predicted by CCMs, ending the low excursions from 2020 to 2022 due to the Australian wildfires and recent volcanic eruptions, events which were not considered in the CCM projections.

Fig. 2.76. Annual mean anomalies of ozone in the (a)–(c) upper stratosphere near 42-km altitude or 2-hPa pressure, and in the (d)–(f) lower stratosphere near 22 km or 50 hPa for three zonal bands: (a),(d) 35°N–60°N, (b),(e) 20°S–20°N (tropics), and (c),(f) 35°S–60°S, respectively. Anomalies are referenced to the 1998–2008 baseline. Annual means are plotted at the tick marks of the start of each year. Colored lines are long-term records obtained by merging different limb (Global Ozone Chemistry and Related Trace Gas Data Records for the Stratosphere [GOZCARDS], Stratospheric Water and Ozone Satellite Homogenized [SWOOSH], Stratospheric Aerosol and Gas Experiment [SAGE]+Climate Change Initiative [CCI]+Ozone Mapping and Profiler Suite Limb Profiler [OMPS-LP], SAGE+Scanning Imaging Absorption Spectrometer for Atmospheric Chartography [SCIAMACHY]+OMPS-LP, SAGE+Optical Spectrograph and InfraRed Imaging System [OSIRIS]+OMPS-LP) and nadir-viewing (Solar Backscatter Ultraviolet Radiometer [SBUV], OMPS Nadir Profile [OMPS-NP]) satellite instruments. The nadir-viewing instruments have a much coarser altitude resolution than the limb-viewing instruments. This can cause differences in some years, especially at 50 hPa. Red dots are results from ground-based Umkehr data (Petropavlovskikh et al. 2025). The black line is from merging ground-based ozone records at seven Network for the Detection of Atmospheric Composition Change (NDACC) stations employing differential absorption lidars and microwave radiometers. See Steinbrecht et al. (2017), WMO (2022), and Arosio et al. (2019) for details on the various datasets. Gray shaded area shows the range of chemistry-climate model simulations from the Chemistry-Climate Model Initiative (CCMI)-1 refC2 (SPARC/IO3C/GAW 2019). Ozone data for 2024 are not yet complete for all instruments and are still preliminary.

7. STRATOSPHERIC WATER VAPOR

—S. M. Davis, K. H. Rosenlof, E. A. Asher, H. Vömel, and R. M. Stauffer

In 2024, stratospheric water vapor (WV) continued to be strongly influenced by the January 2022 eruption of the Hunga volcano (20.5°S, 175.4°W), which injected 150 Tg of WV into the stratosphere (~10% of the entire stratospheric burden; Millán et al. 2022; Vömel et al. 2022). In addition to the ongoing influence from the Hunga eruption, deseasonalized tropical lower-stratospheric WV anomalies (using a climatological base period of 2004–21) started the year positive following record-high values in 2023 (Davis et al. 2024), but then became negative for much of the year before returning to positive in November and December 2024 (Figs. 2.77a,c, 2.78, 2.79). Overall, 2024 continued the positive WV anomalies observed in the last five years in the global stratosphere (Konopka et al. 2022; Zolghadrshojaee et al. 2024) with some notable variability that was likely due to natural fluctuations.

Zonal-mean WV provided by satellite measurements (Fig. 2.77) shows that the lingering positive anomalies from Hunga were evident in the tropical upper stratosphere (above 10 hPa) in 2024 (Fig. 2.77a). In the tropics (Figs. 2.77a, 2.78), the positive anomaly decreased as the year progressed, with a return to near-normal values around July, likely driven by upward vertical transport of drier air that entered the stratosphere more recently and was not impacted by the Hunga eruption. At the start of 2024, the lingering effects of the Hunga WV perturbation were evident in the middle stratosphere (e.g., 26 hPa, Fig. 2.77b; see also Fig. 2.78) at extratropical latitudes in both hemispheres. Positive WV anomalies, including some record values (see hatched regions, Fig. 2.78), were also present in the lower stratosphere throughout 2024. Attribution of these extratropical lower-stratosphere anomalies is subject to ongoing research, but they are plausibly explained as some combination of poleward transport of the positive tropical lowermost stratosphere anomalies from the end of 2023 (Figs. 2.77a,c) as well as downward transport of Hunga-impacted air from above.

Even though the mid- and upper-stratospheric WV anomalies were still dramatically perturbed by Hunga in 2024, tropical lower-stratospheric WV anomalies (i.e., at pressures greater than ~30 hPa) followed a more typical progression influenced by other factors. Anomalies in this region are expected to be primarily caused by anomalies in tropical tropopause temperatures, which control freeze-drying of air ascending into the stratosphere (Mote et al. 1996). Indeed, lower-stratospheric satellite WV anomalies are highly correlated with tropical (15°S–15°N) cold-point tropopause (CPT) temperature anomalies (Figs. 2.79b,c). While 2022 and 2023 had the first- and second-warmest MERRA-2 tropical CPT temperatures on record (the annual-mean anomaly was +0.76 K in 2022 and +0.73 K in 2023), 2024 was cooler than average (–0.23 K), ranking 39th out of 45 years (since 1980, based on the MERRA-2 reanalysis). Accordingly, while 2023 and 2022 ranked as the first- and

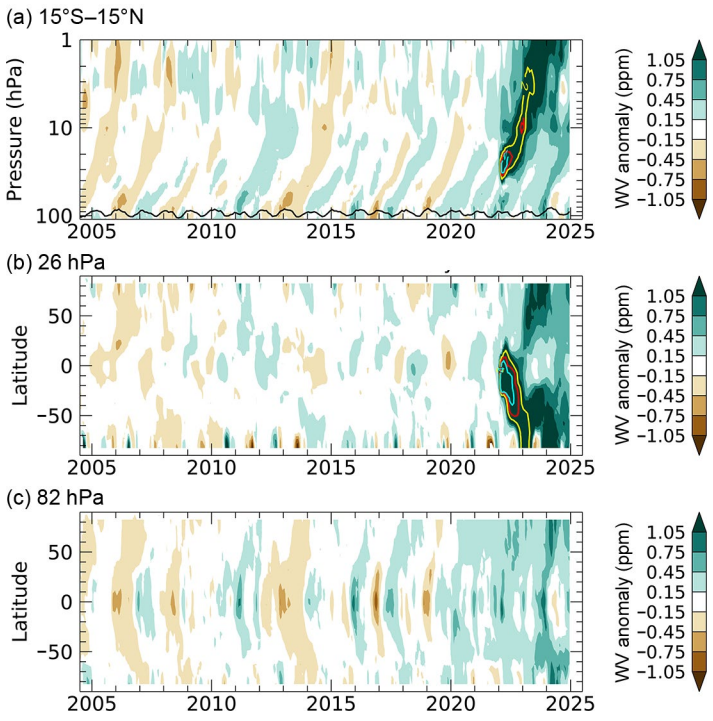

Fig. 2.77. (a) Pressure–time contour of tropical (15°S–15°N) lower-stratospheric water vapor (WV) anomalies, with the +2-, +3-, and +4-ppm values shown as yellow, red, and cyan contour lines, respectively. The black line shows the MERRA-2 tropical cold point pressure. (b),(c) Latitude–time contour of WV anomalies at (b) 26 hPa (middle stratosphere) and (c) 82 hPa (lower stratosphere), respectively. All panels are based on merged satellite data from the Stratospheric Water and Ozone Satellite Homogenized version 2.7 (SWOOSH v2.7) dataset (a combination of Aura Microwave Limb Sounder (MLS), Atmospheric Chemistry Experiment—Fourier Transform Spectrometer (ACE-FTS), and Stratospheric Aerosol and Gas Experiment III (SAGE III)/ISS WV data, Davis et al. 2016). Anomalies are differences from the mean 2004–21 water vapor mixing ratios (ppm) for each month. Tick marks denote the beginning of each year.

second-most positive annual-mean tropical (15°S–15°N) WV anomalies at 82 hPa (+0.39 ppm in 2023 and +0.27 ppm in 2022; parts per million, i.e., μmol mol^{-1}) based on the Stratospheric Water and OzOne Satellite Homogenized (SWOOSH) combined WV record (Davis et al. 2016), 2024 was near the median (10th out of the 20 years since 2005 with sufficient satellite sampling of the tropics) with an anomaly of +0.07 ppm. As is typical, the tropical lower-stratosphere WV anomalies propagate both upward and to higher latitudes, becoming evident at other frost-point measurement stations with a lag of several months at subtropical and midlatitude stations (Hurst et al. 2011).

Two important drivers of interannual variations in CPT temperatures and stratospheric WV concentrations entering the stratosphere are the ENSO and the QBO in equatorial stratospheric winds. Strong El Niño conditions were present at the beginning of 2024 through January–March, followed by a transition to ENSO-neutral conditions by April–June, and then La Niña-like conditions from September through the end of the year (see section 4f). During boreal winter, both La Niña and strong El Niño conditions are associated with a wetter tropical lowermost stratosphere (e.g., Garfinkel et al. 2021), which seems consistent with conditions at the beginning and end of 2024. However, also during the first half of 2024, there was easterly QBO shear between the 50-hPa and 70-hPa levels (section 2e3), which is consistent with stronger upwelling and cold CPT temperatures (e.g., Fig. 2.79c). This behavior is consistent with the anomalously dry

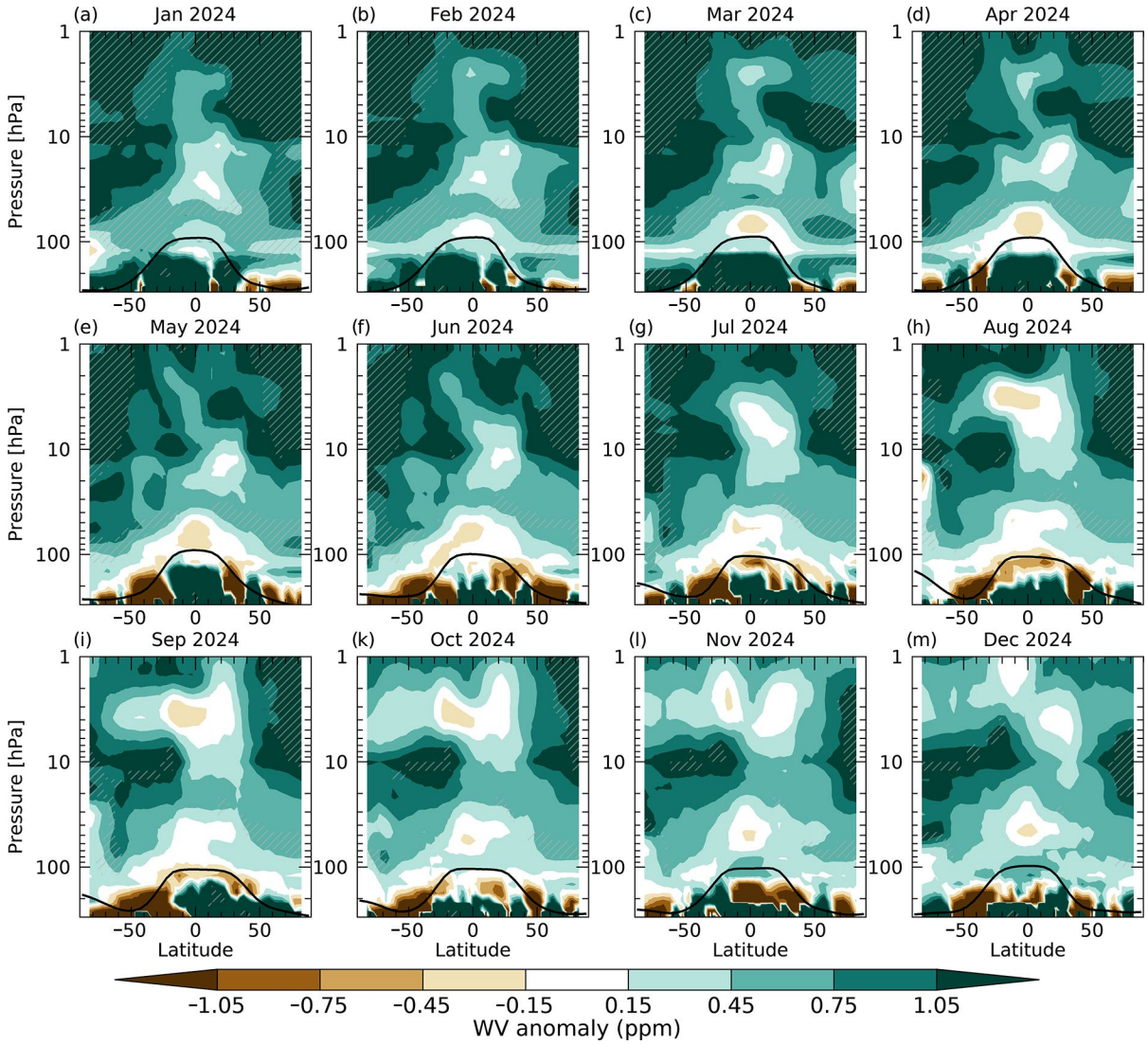

Fig. 2.78. Latitude–pressure cross-sections of zonally averaged water vapor (WV) anomalies (ppm; 2004–21 base period). Hatching shows where the zonal-mean WV was at record values for the given month. Black lines show the monthly mean tropopause pressure from the MERRA-2 reanalysis.

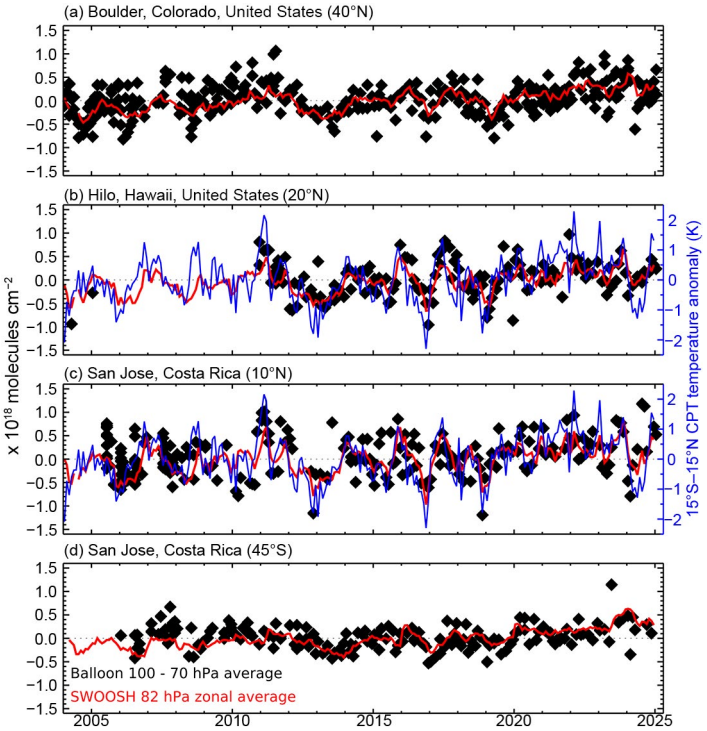

Fig. 2.79. Lower-stratospheric water vapor (WV) anomalies over four balloon-borne frost point (FP) hygrometer stations. Each panel shows the lower-stratospheric anomalies (relative to each station) of individual FP soundings (black diamonds) and of monthly zonal averages from Stratospheric Water and Ozone Satellite Homogenized (SWOOSH) data at 82 hPa in the 5° latitude band containing the FP station (red lines). High-resolution FP vertical profile data were averaged between 70 hPa and 100 hPa for comparison with the SWOOSH 82 hPa level. Anomalies for SWOOSH and FP data are calculated relative to the 2004–21 period for all sites except Hilo (2011–21). Tropical cold-point tropopause temperature anomalies based on the MERRA-2 reanalysis ([b],[c], blue lines) are generally well correlated with the tropical lower-stratospheric WV anomalies.

conditions in the tropical lower stratosphere during the middle of the year (Figs. 2.77a,c, 2.78c–f). After June, the 70-hPa–50-hPa wind shear then reversed to westerly for the remainder of the year, which is consistent with the anomalously wet conditions in the tropical lowermost stratosphere at the end of 2024.

8. CARBON MONOXIDE

—J. Flemming and A. Inness

The global burden of carbon monoxide (CO) in 2024 was the second highest since 2003, mainly because of exceptionally high emissions from wildfires in South America (Fig. 2.80). The emitted CO was transported in the adjacent outflow regions over the Pacific and Atlantic Oceans, leading to positive CO anomalies throughout the SH midlatitudes and tropics (Plate 2.1ag).

CO is emitted into the atmosphere by anthropogenic combustion processes, such as road transport and energy generation, as well as from wildfires. Similar in size to, or even larger than these emissions, is the chemical production of CO in the atmosphere from formaldehyde as part of the oxidation chains of methane, isoprene, and other volatile organic trace gases. Oxidation of CO by reaction with the hydroxyl radical (OH) is the main loss process for CO, resulting in an atmospheric lifetime of 1–2 months. The presence of CO contributes to the production of tropospheric ozone, a relatively short-lived species among radiatively important molecules that affect the climate.

According to the CAMS (https://atmosphere.copernicus.eu/) reanalysis of atmospheric composition, produced by the European Center for Medium-Range Weather Forecasts (ECMWF) and detailed in Inness et al. (2019), the global CO burden decreased between 2003 and 2014 because of decreased anthropogenic emissions in most parts of the world, along with a strong decrease in fire activities in South America. In recent years, positive global and regional CO anomalies occurred because of regionally intensified wildfires related to exceptional meteorological conditions, such as the intensive peat fires in Indonesia in 2015—which caused the highest global CO burden since 2003 (Fig. 2.80)—and the exceptional wildfires in South America in 2024. The latter led to the highest CO burden over the continent in the CAMS reanalysis record (Fig. 2.81). The increased fire intensity in South America was caused by anomalous dry and hot conditions, which started in mid-2023 (de Laat et al. 2025). While fires in the Amazon

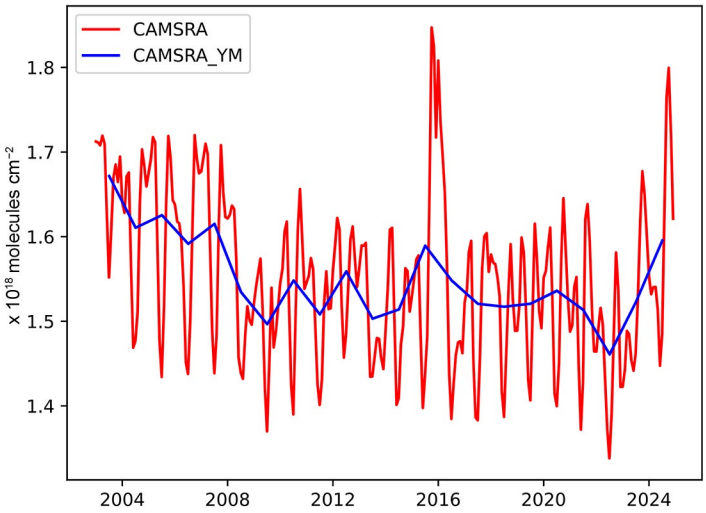

Fig. 2.80. Global monthly-mean (red) and yearly-mean (YM; blue) of the total-column carbon monoxide from the Copernicus Atmosphere Monitoring Service (CAMS) reanalysis for the period 2003–24.

region of Brazil and Bolivia in August–September 2024 were the main cause of the increased CO burden, fires in other regions contributed as well: Venezuela experienced strong fires in January–March, and the Pantanal wetlands in Brazil, the world's largest tropical wetland area, suffered from intensive peat fires in May.

As in previous years, boreal wildfires over Canada and Eastern Siberia in summer led to regional positive CO anomalies against the background of decreasing CO burden in the NH. Less-intensive fire activity over many parts of central and southern Africa contributed to a localized negative CO anomaly in 2024. India is a region where anthropogenic sources, including the burning of agricultural waste in winter, continued to increase the regional CO burden.

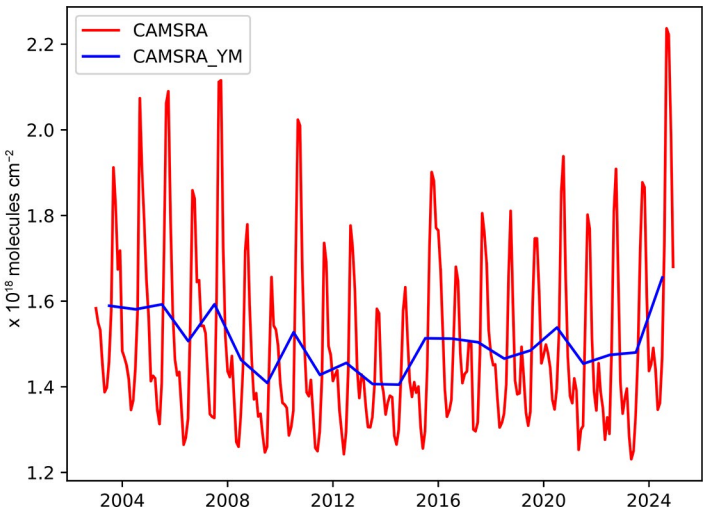

Fig. 2.81. Monthly-mean (red) and yearly-mean (YM; blue) of the total column carbon monoxide from the Copernicus Atmosphere Monitoring Service (CAMS) reanalysis over South America (70°S–10°N, 83°W–30°W) for the period 2003–24.

CAMS has produced a retrospective analysis of CO, aerosols, and ozone since 2003 by assimilating satellite retrievals of atmospheric composition with the ECMWF model (Inness et al. 2019). This CAMS reanalysis assimilated global thermal infrared total column CO retrievals (V6 from 2003 to 2016; NRT V7 from January 2017 to June 2019; NRT V8 from July 2019 to present) of the Measurement of Pollution in the Troposphere (MOPITT) satellite instrument (Deeter et al. 2014, 2017, 2019), excluding observations poleward of 65°N/S, using the ECWMF four-dimensional variational assimilation (4D-VAR) data assimilation system. The anthropogenic emissions were taken from the Monitoring Atmospheric Composition and Climate and CityZen (MACCity) inventory (Granier et al. 2011) that accounts for projected emission trends according to the emission scenario Representation Concentration Pathways (RCP) 8.5 scenario, but COVID-19-related emissions modifications were not applied. Biomass burning emissions were taken from the Global Fire Assimilation System (GFASv1.2; Kaiser et al. 2012; section 2h3) that is based on MODIS fire radiative power retrievals (Giglio et al. 2016). Monthly-mean biogenic emissions simulated by the Model of Emissions of Gases and Aerosols from Nature (MEGAN) 2.1 following Sindelarova et al. (2014) were used for the period 2003–17, and after 2017 a monthly climatology derived from the 2003–17 data was applied.

Sidebar 2.2: Operational satellite instruments monitor a range of indirect short-lived climate forcers

—O. R. COOPER, E. PENNINGTON, J. WORDEN, K. BOWMAN, S. KONDRAGUNTA, Z. WEI, AND K. YANG

Earth's effective radiative forcing (ERF) due to total anthropogenic activities since 1750 is 2.79 (1.78 to 3.61) W m^{-2}, which is a balance between the warming effect of greenhouse gases and the cooling effect of aerosols and land use change (surface albedo changes and effects of irrigation; Forster et al. 2024). Long-lived greenhouse gases (LLGHGs: carbon dioxide [CO_2], nitrous oxide [N_2O], and halogenated greenhouse gases) accumulate in the atmosphere on decadal to centennial time scales, while short-lived climate forcers (SLCFs) have lifetimes ranging from a few hours to about two decades. SLCFs that exert a climate effect through their radiative forcing are known as direct SLCFs (e.g., ozone, methane, primary and secondary aerosols), while indirect SLCFs are precursors of other direct climate forcers (IPCC 2021). For example, carbon monoxide (CO) and nitrogen oxides (NO_x = NO+NO_2) are ozone precursors, while ammonia (NH_3) is a precursor of secondary aerosols (e.g., ammonium nitrate).

In terms of SLCFs, previous editions of the *State of the Climate* report have focused on methane, tropospheric and stratospheric ozone (direct SLCFs; sections 2g1, 2g4, 2g6), and carbon monoxide (indirect SLCF; section 2g8). The *State of the Climate* also provides updates on aerosols (sections 2g3, 2g5), but no distinction is made between primary aerosols (direct SLCFs) and secondary aerosols (indirect SLCFs). Advances in satellite instrumentation and retrieval algorithms now allow for operational monitoring of several indirect SLCFs; here, three operational satellite products that can improve understanding of the regional and global scale production of tropospheric ozone and secondary aerosols are described.

Tropospheric column nitrogen dioxide (NO_2): NO_2 is an indirect SLCF that reacts with CO, methane, and volatile organic compounds (VOCs) in the presence of sunlight to produce ozone, which is both a SLCF and an air pollutant detrimental to human health and vegetation (Monks et al. 2015). Over the past two decades, several satellite instruments have monitored changes in tropospheric column NO_2, allowing scientists to identify regions where ozone production is increasing or decreasing (Duncan et al. 2016; He et al. 2024). The Ozone Mapping and Profiler Suite (OMPS) instrument is currently monitoring NO_2 on three NOAA operational polar-orbiting satellites (Suomi National Polar-orbiting Partnership [SNPP] since 2012, NOAA-20 since 2018, and NOAA-21 since 2023; Huang et al. 2022). Figure SB2.4a presents annual average tropospheric column NO_2 for the most recent five years (2020–24), showing well-known hotspots associated with fossil fuel combustion across North America, Europe, the Middle East, South Asia, East Asia, and southern Africa. A region of frequent biomass burning is also visible above south-central Africa. Figure SB2.4b presents the 2020–24 period as anomalies with respect to 2012–19. Previously documented NO_2 decreases have persisted across Mexico City (Mexico), South Africa, the northeastern United States, western Europe, and especially across East Asia (Duncan et al. 2016; Elshorbany et al. 2024). Notable increases are found above western Texas, eastern Europe, Iraq, Iran, and eastern India (Gyawali 2023; Elshorbany et al. 2024).

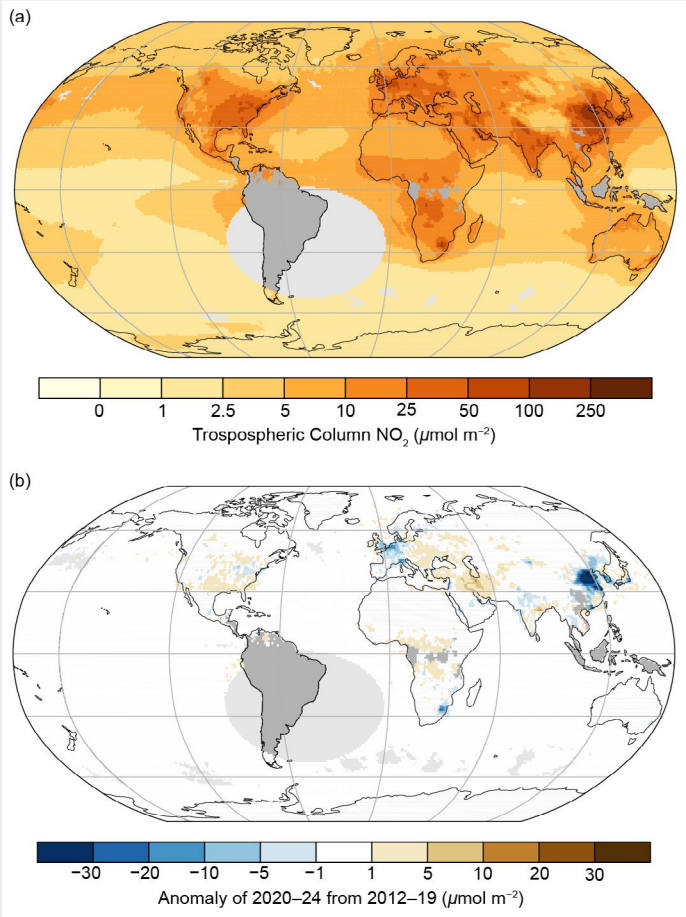

Fig. SB2.4. (a) Ozone Mapping and Profiler Suite (OMPS) tropospheric-column nitrogen dioxide (NO_2), 2020–24; (b) Anomalies of OMPS tropospheric column NO_2 for the period 2020–24, with reference to 2012–19. Units are µmol m^{-2}. Gray areas indicate regions with low data availability, and portions of South America and the South Atlantic are omitted due to instrument interference caused by the South Atlantic Anomaly (Finlay et al. 2020).

Ammonia (NH_3): Ammonia is produced from agricultural practices (Behera et al. 2013), fossil fuel combustion, and wildfires (Lindaas et al. 2021). When this indirect SLCF combines with nitric acid (HNO_3; an oxidation product of NO_2) it forms

ammonium nitrate (NH_4NO_3), a secondary aerosol and SLCF, which reflects sunlight (Nowak et al. 2012). The Cross-Track Infrared Sounder (CrIS) flies on the same NOAA operational satellites as the OMPS instrument, and provides midday retrievals of column ammonia, with a peak sensitivity of around 700 hPa (Bowman 2021a). Figure SB2.5a presents average CrIS ammonia for the year 2024, revealing three major hotspots. The enhancements above northeastern China and the Indo-Gangetic Plain are associated with anthropogenic activity and are similar to previous years (2020–23, not shown). In contrast, the enhancement above central South America is produced by wildfires and is elevated compared to previous years. Peak ammonia concentrations occurred in September (Fig. SB2.5b) during a period of record-breaking wildfires across Bolivia (CAMS 2024; sections 2g8, 2h3). The ammonia plume was prevented from spreading westward by the Andes Mountains and instead advected eastward across the South Atlantic Ocean.

Peroxyacetyl nitrate (PAN): Acyl peroxynitrates (PANs) are a class of thermally unstable reservoir species for nitrogen oxides, commonly produced by wildfires and fossil fuel combustion (Juncosa Calahorrano et al. 2021). CrIS detects PANs with highest sensitivity in the mid-troposphere (450 hPa; Bowman 2021b), with peroxyacetyl nitrate (PAN) being the most abundant species (Payne et al. 2022). PAN is stable at low temperatures and can therefore transport NO_x over long distances, especially in the free troposphere. When PAN descends to warmer layers of the atmosphere, its thermal decomposition releases NO_x, which is then available for ozone production (Fischer et al. 2014). CrIS detected enhanced PANs above North America during summer 2023, produced by the record-breaking Canadian wildfire season (Cooper et al. 2024b). Canada experienced its second strongest wildfire season in 2024 (CAMS 2024; section 2h3), and the CrIS PANs product shows strong enhancements above Canada and the central United States during July 2024 (Fig. SB2.6a), similar to the enhancements above the downwind region of the North Atlantic Ocean and to the enhancements above East Asia that are attributed to anthropogenic activity. By September, the PANs hotspots had shifted to the biomass burning regions of South America and southern Africa, with plumes of PANs extending from both regions into the South Atlantic Ocean (Fig. SB2.6b).

These examples demonstrate the unique capability of satellites to monitor indirect SLCFs on a global scale. The benefits of this knowledge go beyond the simple understanding of trace gas distributions, because the chemistry and transport connections between these trace gases amplify their impact on climate and air quality (Szopa et al. 2021). For example,

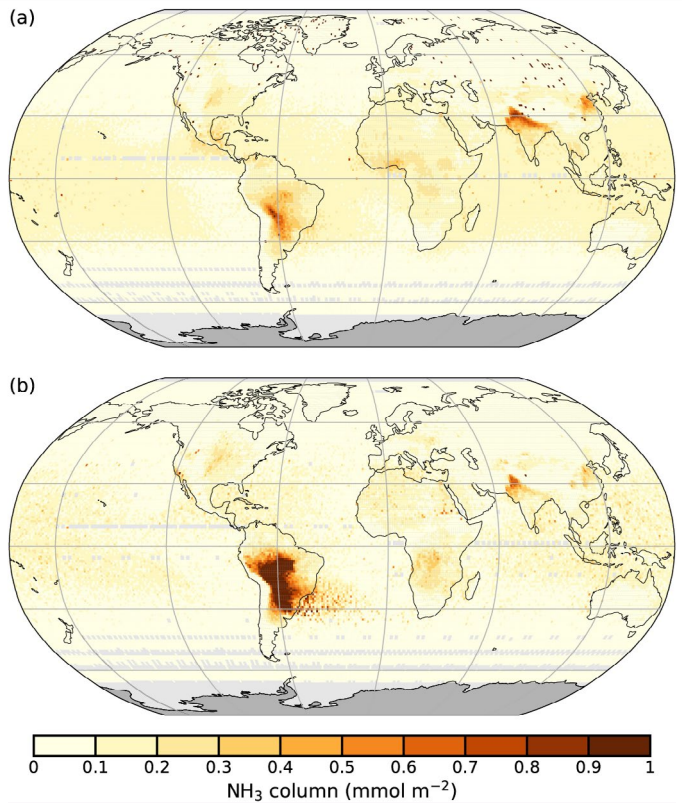

Fig. SB2.5. (a) Cross-Track Infrared Sounder (CrIS) ammonia (NH_3) averaged over the entire year of 2024; (b) CrIS NH_3 averaged over Sep 2024. Units are m mol m^{-2}. Both images show NH_3 for the total atmospheric column.

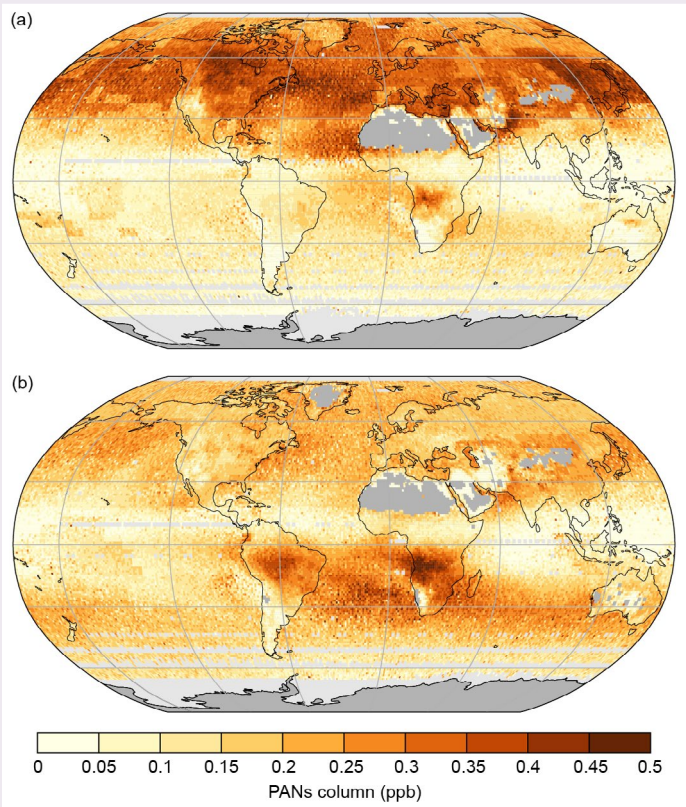

Fig. SB2.6. (a) Cross-Track Infrared Sounder (CrIS) acyl peroxynitrates (PANs) averaged over Jul 2024; (b) CrIS PANs averaged over Sep 2024. Units are ppb. Both images show PANs between 825 hPa and 215 hPa.

NO_2, NH_3, and PAN are all produced by biomass burning, and wildfires (many of which are ignited by humans) are becoming more intense due to climate change (Byrne et al. 2024). The connections of these indirect SLCFs with respect to ERF are as follows: NO_2 is a precursor of PAN, which then transports NO_x downwind where it can produce ozone far from its origin (potential ERF increase); the ozone produced from NO_2 subsequently impacts methane (direct SLCF) by reducing its lifetime (potential ERF decrease); NH_3 and NO_2 generated by fires can produce secondary aerosols (potential ERF decrease).

With existing and expanded data assimilation methods, satellite retrievals of indirect SLCFs can be assimilated into global atmospheric chemistry models, such as the Unified Forecast System (UFS; Jacobs 2021), Goddard Earth Observing System Composition Forecast Modeling System (GEOS-CF; Keller et al. 2021), or the Copernicus Atmosphere Monitoring Service (CAMS) European Centre for Medium-Range Weather Forecasts (ECMWF) reanalysis of atmospheric composition (Innes et al. 2019), to quantify their impact on air quality and Earth's radiation budget.

h. Land surface properties

1. TERRESTRIAL SURFACE ALBEDO DYNAMICS

—F. Cappucci, R. Urraca, and N. Gobron

The terrestrial surface albedo is a key variable controlling the amount of radiative energy absorbed by Earth's surface. Defined as the nondimensional ratio of reflected solar radiation to incident irradiance, the terrestrial surface albedo is influenced by a range of factors. An increase in vegetation density causes a "darkening" effect (negative anomalies) in the visible spectrum (0.3 μm–0.7 μm), as vegetation absorbs more radiation, while near-infrared (0.7 μm–5.0 μm) albedo increases slightly, due to healthy vegetation's higher reflectivity. In contrast, desertification or snow-covered surfaces result in a greater shortwave (0.3 μm–5.0 μm) albedo.

The 2024 anomaly (2003–20 reference period) of white sky albedo in visible spectrum (Plate 2.1ah, Fig. 2.82a) continued the darkening trend of Earth's surface as already seen in previous years (Cappucci et al. 2024; Duveiller and Gobron 2023).

The decrease in shortwave (Plate 2.1aj) white sky surface albedo over Canada was driven by the exceptional heatwaves that affected the region during the first half of 2024, which contributed to early snowmelt and large-scale wildfires. The decline in the shortwave albedo over central Europe, Scandinavia, and Greenland's coastline is also linked to the loss of snow and ice in all these areas (section 2c5).

The albedo brightening (positive anomaly) in the visible spectrum (Plate 2.1ah) over South America, (mainly Brazil, Bolivia, and Paraguay) and over southern Africa (including Zambia, Zimbabwe, Namibia, and Botswana) can be attributed to vegetation decline resulting from prolonged drought during the second and third quarters of the year, often associated with high temperatures (sections 2b1, 2d12). Surface darkening in the visible spectrum over northeastern Brazil and the Horn of Africa was characteristic of El Niño and the Indian Ocean dipole, respectively, where abundant precipitation occurring during the first half of the year contributed to healthier vegetation. A decrease in visible surface albedo, accompanied by an increase in near-infrared spectrum (Plate 2.1ai), was recorded in central and eastern Europe, eastern China, Japan, northern Australia, and sub-Saharan northeast Africa, characteristic of an increase in vegetation activity driven by the above-average precipitation that occurred over these areas during the first half of the year (section 2d6).

The patterns of the zonally averaged albedo anomalies in the shortwave (Fig. 2.83c) during 2024 exhibit a large decline in albedo at high latitudes (above 60°N), most evident in spring driven by early snowmelt, a tendency already consolidated since early in the century (Young 2023). The increased vegetation density over China and India has resulted in lowering the visible albedo (persistent negative anomalies) and increasing the near-infrared albedo (positive anomalies), which is clear between 10°N and 30°N for 2023 and 2024 (Figs. 2.83a,b, respectively). Over the southern tropical zone, surface visible brightening is evident during the second and third quarters of 2024, and is associated with a decline in vegetation health, particularly over South America and southern Africa. Between 30°S and 40°S, a persistent

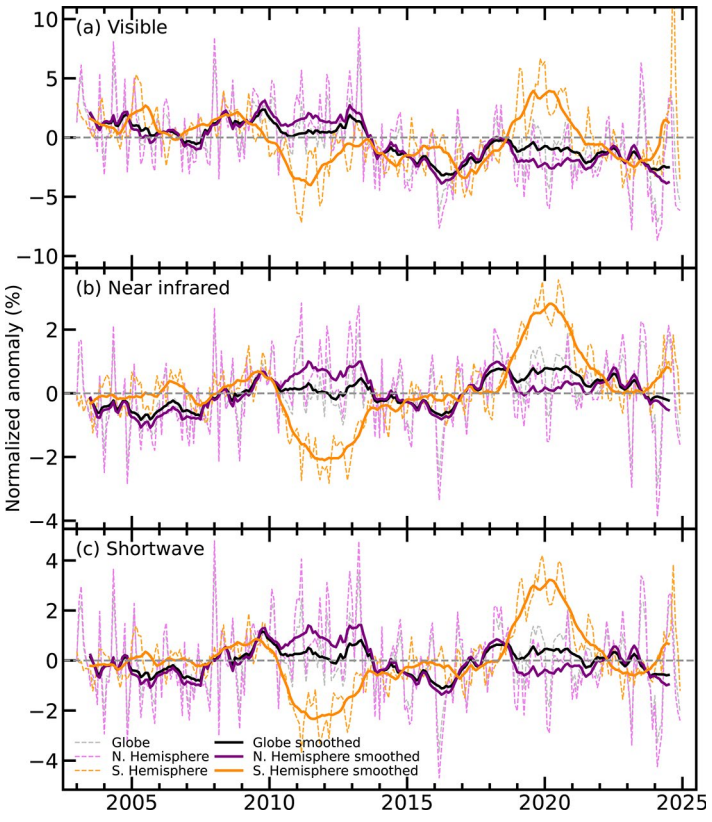

Fig. 2.82. Global (black lines), Northern Hemisphere (purple), and Southern Hemisphere (orange) land surface (a) visible, (b) near-infrared, and (c) shortwave broadband albedo anomalies (%; 2003–20 reference period) for the period 2003–24. Dotted lines denote monthly values; solid lines indicate the 12-month running averaged mean.

surface darkening trend in both visible and near-infrared domains, which had already started in 2022, is also evident in 2024.

The globally smoothed average anomaly (solid black line) enables the detection of long-term patterns of darkening or brightening in the terrestrial surface albedo over time. Although its amplitude shows minimal variability during the 2003–24 period, with fluctuations within ±3% in the visible domain and ±2% in the near-infrared and shortwave domains (Fig. 2.82), notable trends emerge.

A positive plateau in global shortwave albedo from 2018 to 2020 was followed by consecutive drops from 2021, with a persistent decline emerging in mid-2023 and consolidating through 2024 (Fig. 2.82c). Furthermore, 2024 saw the third-darkest (negative) shortwave anomalies since 2003 both globally (−0.58%) and in the Northern Hemisphere (NH; −0.96%). The acceleration of albedo decline in 2023/24 coincides with the record-positive anomalies in absorbed solar radiation (ASR), especially in 2023 (Fig. 2.61; section 2f1), as well as global surface temperature during these years. Surface albedo anomalies have a weak contribution to ASR on a global scale due to cloud masking, which attenuates surface albedo effect on ASR by a factor of about three. However, the decline in albedo caused by snow and ice loss above 55°N and ice loss above 55°S dominates polar ASR anomalies, contributing around +0.03°C of the +0.22°C ASR-driven warming in 2023 (Goessling et al. 2025).

This analysis is based on satellite products derived from the Moderate Resolution Imaging Spectroradiometer (MODIS) instrument on board the *Aqua* and *Terra* satellite platforms to generate a long-term record from 2002 to 2022 (Schaaf et al. 2002). The 2023 and 2024 data are derived from the Visible Infrared Imaging Radiometer Suite (VIIRS) on board the Suomi NPP satellite. Although the similarity in spectral band configuration makes VIIRS the optimal continuation of the MODIS archive (Liu et al. 2017), a small difference between VIIRS and MODIS surface albedo was noted, with VIIRS data being bias-corrected accordingly.

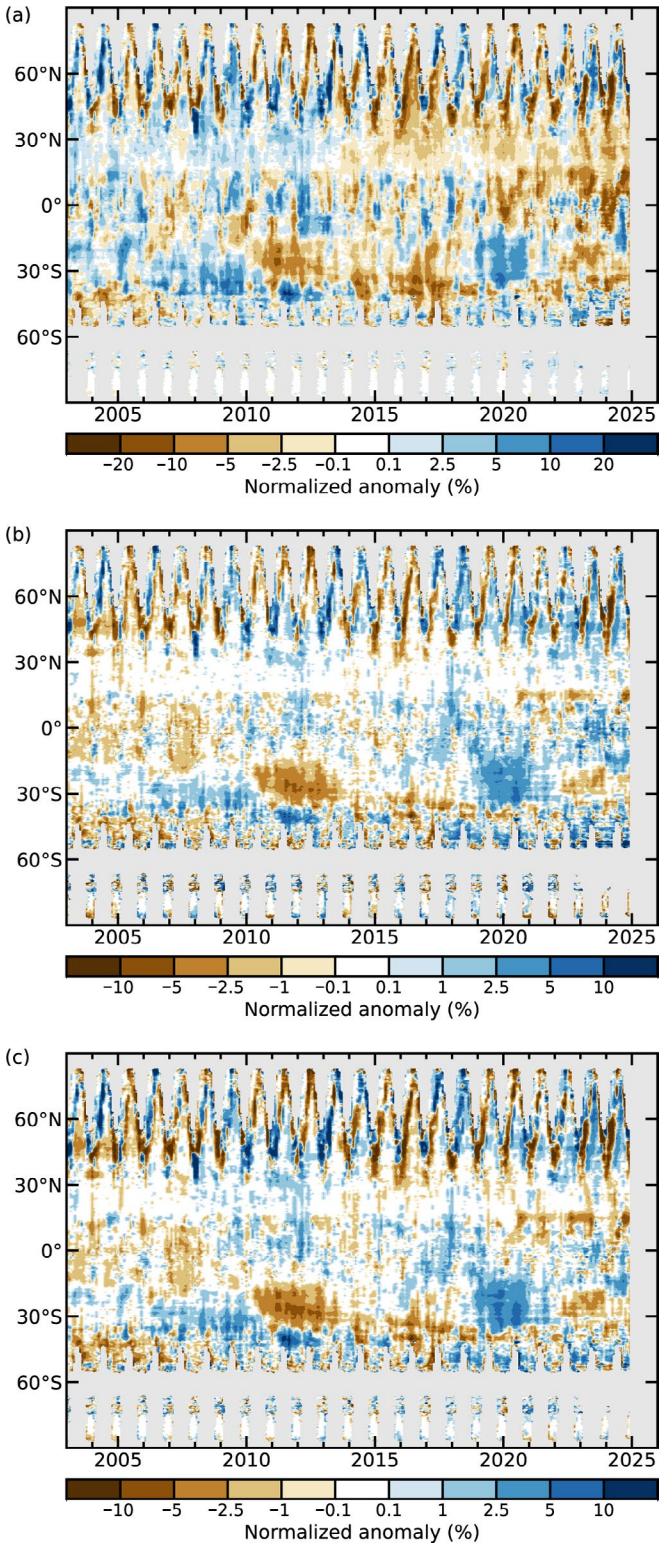

Fig. 2.83. Zonally averaged white-sky (a) visible, (b) near-infrared, and (c) shortwave broadband land surface albedo anomalies (%) for the period 2003–24 using a 2003–20 reference period.

2. TERRESTRIAL VEGETATION DYNAMICS

—N. Gobron and F. Cappucci

The fraction of absorbed photosynthetically active radiation (FAPAR) measures the amount of radiation absorbed by plant canopies. FAPAR is a key indicator of vegetation density, health, and productivity, and plays a crucial role in evaluating how effectively plants absorb carbon dioxide from the atmosphere. According to the FAPAR record in 2024, extreme deviations from

the 1998–2020 average (above 0.04 and below −0.04) accounted for 13% of land areas, with 11% showing an increase in productivity and 2% showing a decrease.

As illustrated in Plate 2.1ak, Earth's surfaces continued their greening trend in 2024 due to both higher temperatures (section 2b1) as well as plentiful rainfall (section 2d5). This is especially noticeable over continental Europe, excluding Bulgaria and Ukraine. The North American Arctic experienced an exceptional level of tundra greenness, with northern Alaska and central and eastern Canada all showing significantly above-average levels of greenness (Frost et al. 2024). In contrast, northeastern Siberia was again suffering from highly active wildfires. Northeastern Brazil vegetation recovered from 2023, particularly during the first half of the year. Positive anomaly patterns were seen in eastern Africa—including Kenya, Somalia, and Ethiopia—where, remarkably, overall green conditions were present due to extreme rainfall at the end of 2023; however, vegetated productivity declined in the second half of the year, especially in Somalia due to below-average rainfall between October and December. Northern and eastern Australia reported greener annual conditions, building on the higher-than-normal levels seen during the first six months of the year.

In Canada, forests in Quebec still bear the scars of fires in 2023, as evidenced by negative annual anomalies indicating that the area has not yet fully recovered. Additionally, there were persistent and large-scale fires that affected British Columbia and Alberta in July 2024 (section 2h3), and the number of wildfires increased in the Northwest Territories through August following heatwaves across the region.

The prolonged spring heatwaves that affected Central America contributed to vegetation decline in Chihuahua (Mexico) and Yucatan (Guatemala), and set records in high temperature and drought. Conversely, the state of Nuevo León (Mexico) experienced a significant increase in photosynthetic activity due to recovery of vegetation surfaces from last year.

Several regions in South America, including the Amazon and other areas of Brazil and Bolivia, experienced an extended period of drought, characterized by low rainfall and high temperatures. This led to severe summer wildfires affecting the forests. While the Sahel received excess rainfall (section 2d5), several countries in southern Africa, including Namibia, Botswana, Nigeria, Zambia, and Mozambique, experienced severe rainfall deficits and record-high temperatures. India and Pakistan, along with China, still exhibited a strong annual greenness due to agricultural intensification (Park et al. 2023) despite occasional heatwaves and floods.

The monthly anomalies of longitude-averaged FAPAR from 1998 to 2024 (compared to the 1998–2020 base period, Fig. 2.84) reveal that all latitudes between 2002 and 2013, particularly in the Southern Hemisphere (SH), experienced significant vegetation decline (values below −0.04). This was followed by an increasing greenness of surfaces in both hemispheres thereafter. Furthermore, during 2024, positive values were observed at almost all latitudes, with exceptionally high values (exceeding +0.04) noted around 50°N at the start of the year and shifting to around 10°N in the latter part of the year.

Figure 2.85 shows the global and hemispheric results, with the SH showing greater seasonal variability than the NH. FAPAR monthly anomalies over the SH were positive before 2002, in 2011, and after 2014, except for 2019. There were strong positive peaks (above +0.01) during the summers of 2000, 2017, and 2023, corresponding to fewer extreme events such as fire or drought, compared to the negative peaks (below −0.01) in 2008/09. A severe drought that affected a significant portion of South America and southern Africa led to an extreme negative deviation of −0.015 in October 2024. The NH was positive in 1998 but negative from 1999 to 2013 and positive thereafter, reaching a peak

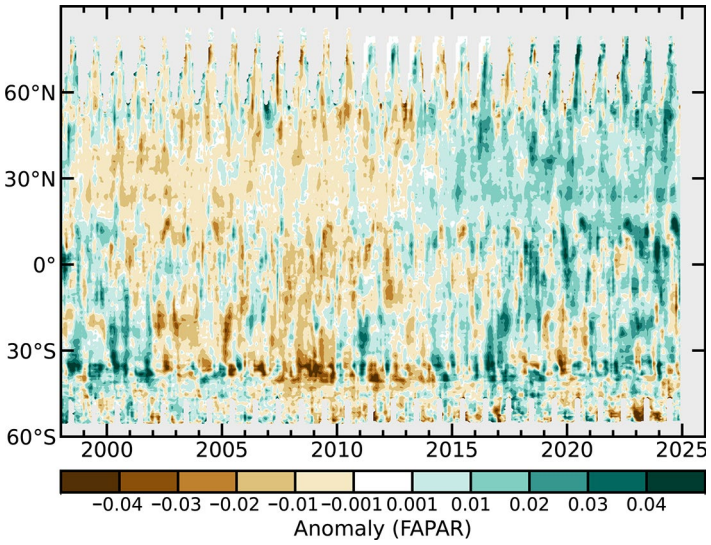

Fig. 2.84. Zonally averaged fraction of absorbed photosynthetically active radiation (FAPAR) anomalies for the period 1998–2024 (1998–2020 base period).

(above 0.014) in spring 2024. This greening trend is directly linked to the increase of land surface temperatures but also to the carbon dioxide fertilization effect (Zhu et al. 2016).

FAPAR, an essential climate variable (GCOS 2022), was estimated using optical space sensors. The 2024 analysis combines 27 years of global products from four optical sensors: the Sea-Viewing Wide Field-of-View Sensor (SeaWiFS; 1998–2002); Envisat/ Medium Resolution Imaging Spectrometer (MERIS; 2003–10), *Terra-Aqua*/MODIS (2011–16), and EU Copernicus Sentinel-3/Ocean and Land Colour Instrument (OLCI; 2017–24; Gobron et al. 2010, 2022; Pinty et al. 2011).

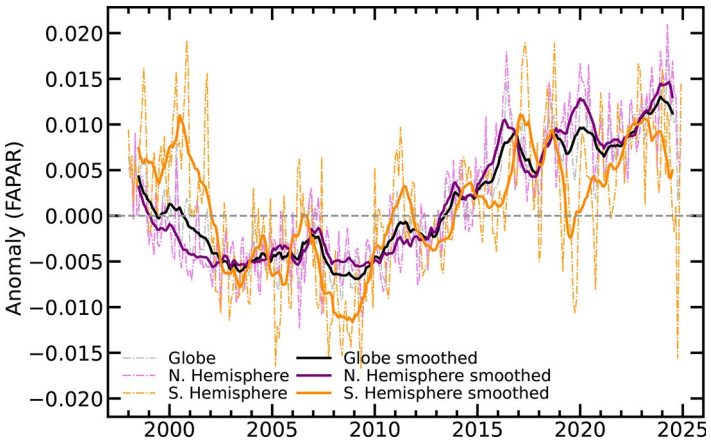

Fig. 2.85. Global (black line), Northern Hemisphere (purple), and Southern Hemisphere (orange) fraction of absorbed photosynthetically active radiation (FAPAR) anomalies for 1998–2024 (1998–2020 base period). Dotted lines denote each monthly period; solid lines indicate the six-month running averaged mean.

Uncertainties of the four datasets were derived through error propagation techniques and comparisons against multiple proxies using ground-based measurements (Bai et al. 2022) and radiative transfer simulations, all of which provide an estimate of the uncertainties and biases. This long-term FAPAR dataset has an estimated average uncertainty of approximately 5% to 10%.

3. BIOMASS BURNING

—J. W. Kaiser, M. Parrington, and D. Armenteras

Two distinct trends in global biomass burning were identified over the last decade, both of which persisted into 2024. Many savanna regions, which are responsible for most global fire emissions, have experienced a decline related to agricultural expansion. In contrast, many forested, wetland, and boreal regions have witnessed an increase in both the duration and intensity of wildfire episodes (see Plate 2.1al). This is attributable to climate change, which has led to increased drought periods and, consequently, heightened flammability of the landscape (e.g., Xing and Wang 2023 for the Arctic). The magnitude of biomass burning, denoted as "fire activity" or "wildfires", is here described as the quantity of carbon that is consumed by fire and released into the atmosphere. Of this, 80% to 95% is emitted as carbon dioxide (CO_2), with the remainder being oxidized to CO_2 in the atmosphere or released as particulate matter. In a stable ecosystem, the bulk of this CO_2 is typically assimilated through vegetation re-growth. However, it is estimated that 20% currently contributes to the long-term buildup of atmospheric CO_2 (Zheng et al. 2023).

Global annual total estimated fire emissions were below the 2003–20 average in 2024 by approximately 7%, but were still the second highest since 2016 (after 2023), according to the Copernicus Atmosphere Monitoring Service's (CAMS) Global Fire Assimilation System version 1.4 (GFASv1.4; Fig. 2.86; Table 2.13). The global total was affected by anomalously large-scale wildfires that burned persistently in forests across South and North America at different points throughout the year (Figs. 2.87, 2.88). In the latter, Canada again experienced an extreme year with fire activity above any year between 2003 and 2022, with the annual total having been second only to the record fires of 2023 (Fig. 2.88). The western United States experienced its seventh-highest annual total fire emissions since 2003 with a +22% anomaly. The year 2024 also saw an increase in

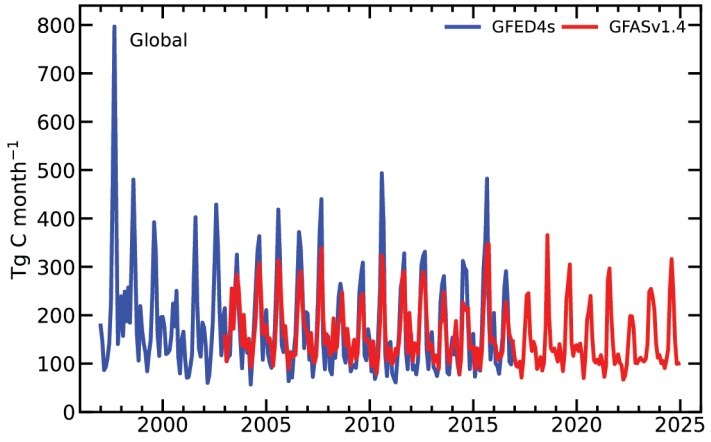

Fig. 2.86. Global monthly carbon consumption (Tg C month^{-1}) in biomass burning.

Table 2.13. Annual continental-scale biomass burning budgets in terms of carbon emission (Tg C yr^{-1}) from the Copernicus Atmosphere Monitoring Service Global Fire Assimilation System version 1.4 (CAMS-GFASv1.4).

Name of Region	Location	Biomass Burning 2003–20 Mean value (Range)	Biomass Burning 2024 Value	Biomass Burning 2024 Anomaly (%)
Global	–	1954 (1669–2293)	1812	–142 (–7%)
North America	30°N–75°N, 190°E–330°E	86 (58–114)	148	+62 (+71%)
Central America	13°N–30°N, 190°E–330°E	43 (29–62)	46	+3 (+7%)
South America	13°N–60°S, 190°E–330°E	352 (225–526)	486	+134 (+38%)
Europe and Mediterranean	30°N–75°N, 330°E–60°E	30 (16–58)	22	–8 (–28%)
N. Hem. Africa	0°–30°N, 330°E–60°E	394 (314–457)	305	–89 (–23%)
S. Hem. Africa	0°–35°S, 330°E–60°E	482 (429–544)	446	–36 (–7%)
Northern Asia	30°N–75°N, 60°E–190°E	185 (97–425)	156	–29 (–16%)
South-East Asia	10°N–30°N, 60°E–190°E	116 (80–153)	86	–31 (–26%)
Tropical Asia	10°N–10°S, 60°E–190°E	149 (24–448)	24	–125 (–84%)
Australia	10°S–50°S, 60°E–190°E	117 (49–221)	94	–22 (–19%)
Canada	47°N–75°N, 219°E–310°E	46 (10–80)	111	+65 (+141%)
Arctic	67°N–90°N, 0°–360°	7 (1–35)	16	+8 (+117%)

wildfire emissions from boreal Eurasia, following persistent wildfires in the Sakha Republic and Amur Oblast in the east of Russia. The first contributed to the third strongest wildfires in the Arctic after 2019/20 (Fig. 2.88). Overall, however, North Asia experienced a negative anomaly of –16%.

South America experienced its highest fire activity since 2007, but approximately equal with 2010, at 38% above the 2003–20 mean (Fig. 2.88). The spring seasonal fires in the northern tropics of South America led to Venezuela, Guyana, Suriname, and Brazil's Roraima state all experiencing their highest annual total emissions. In central regions, Bolivia, the Pantanal wetlands, and some parts of the Brazilian Amazon experienced historic fires with the highest emissions of the past two decades, largely driven by drought conditions (section 2d11). Bolivia experienced its highest fire activity since at least 2003, with each month during January to November exceeding its 2003–20 monthly mean. Fires in Pantanal burned 1.2 million hectares between January and August, 14% of which were on either indigenous lands or protected natural areas including the Pantanal wetlands (Alencar et al. 2024). In Brazil, Amazon fire emissions peaked higher than any year since 2010, with emissions in the states of Mato Grosso and Pará well above average, as El Niño-driven drought (see section 7d; Marengo et al. 2024)

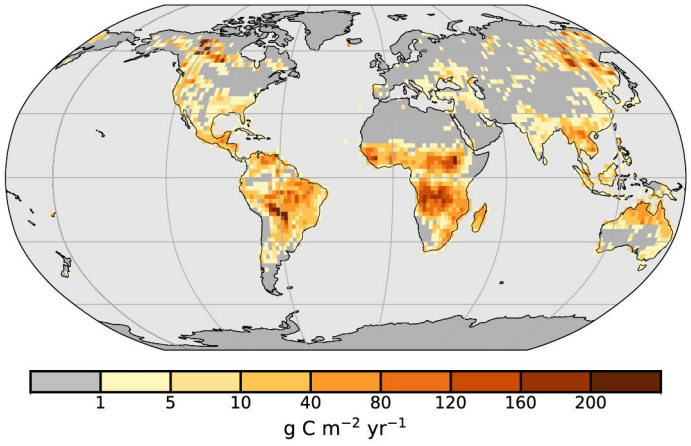

Fig. 2.87. Global map of fire activity in 2024 in terms of carbon consumption (g C m^{-2} yr^{-1}). (Source: Copernicus Atmosphere Monitoring Service Global Fire Assimilation System version 1.4 [CAMS-GFASv1.4.])

significantly increased fire risk despite reduced deforestation. Earlier seasonal drying also heightened flammability, leading to widespread fire outbreaks (Feron et al. 2024).

African fire carbon emissions accounted for roughly half of the total global emissions during the 2000s, but their contribution shrunk to ~40% during recent years (Fig. 2.87; Plate 2.1al). The decrease in savanna regions persisted in 2024 over Northern Hemisphere Africa with emissions 23% below the 2003–20 average, the fourth successive year with lower fire activity than any years in the record prior to 2019. Southern Hemisphere Africa also contributed to the trend despite increased fire activity in several regions, including the central African tropical forest. Fire activity in southeast and tropical Asia generally continued reducing trends. In the latter—including Indonesia—El Niño-induced drought combined with land-clearing fires on palm, pulp, and rice plantations have led to extreme fires in the past. However, the fire activity of 2024 was lower than during any year from 2003 to 2016 (Fig. 2.88) despite the El Niño conditions at the beginning of the year. Increased wildfire emissions occurred in tropical regions of Australia between September and November, related to warmer and drier conditions (Plate 2.1al).

GFAS is operated by CAMS and produces global fire emission estimates (Kaiser et al. 2012) in near-real-time based on the MODIS Fire Radiative Power products (Giglio et al. 2016). A combination of near-real-time and consistently reprocessed products are used here, with input from MODIS Collection 6 for the entire period of 2003–24. The biases with respect to Collection 5 and between satellites have been corrected, and a more extensive spurious signal mask has been applied. Archived MODIS input is used for 1 January 2003 to 18 December 2016 and August 2024, and near-real-time (NRT) input is used otherwise. The replacement for August 2024 is necessary due to corrupt NRT input, and uses an updated land cover map. The time series in Fig. 2.86 also places GFAS in the context of the Global Fire Emissions Database version 4.1 (GFED4s), which is primarily based on burnt area observation and dates back to 1997 (van der Werf et al. 2017).

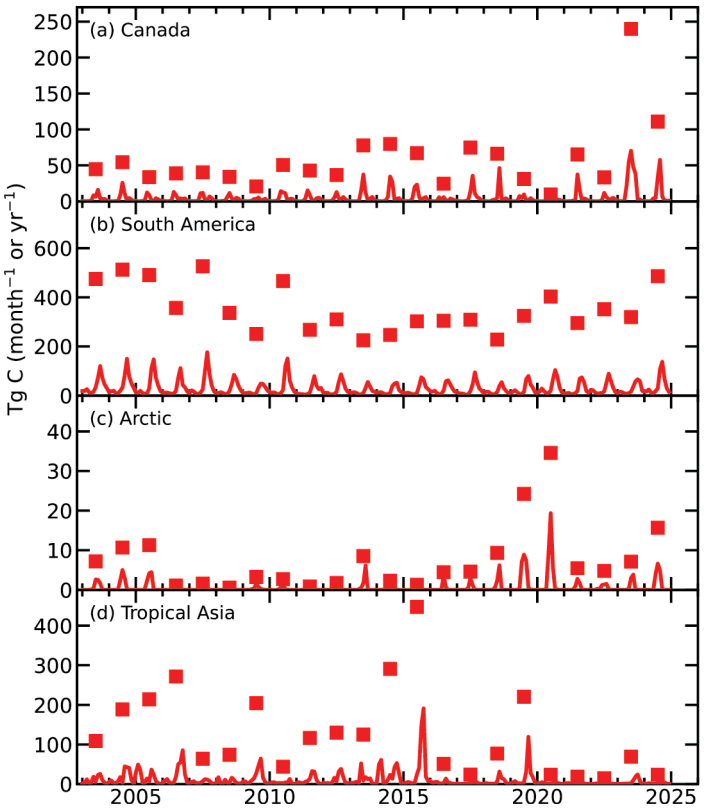

Fig. 2.88. Regional time series of monthly (lines in Tg C month^{-1}) and annual (symbols in Tg C yr^{-1}) biomass burning activity in (a) Canada, (b) South America, (c) the Arctic, and (d) tropical Asia.

4. PHENOLOGY

—D. L. Hemming, O. Anneville, Y. Aono, T. Crimmins, N. Estrella, R. Holliday, S.-I. Matsuzaki, A. Menzel, I. Mrekaj, J. O'Keefe, A. D. Richardson, J. Rozkošný, T. Rutishauser, R. Shinohara, S. J. Thackeray, A. J. H. van Vliet, and J. Garforth

Vegetation phenology, "the rhythm of the seasons", is strongly influenced by climate variations and can modify climate through land–atmosphere exchanges of energy, moisture, and carbon (Hassan et al. 2024).

PhenoCam (https://phenocam.nau.edu/) is a network of over 900 automated digital cameras monitoring phenological changes in a wide range of ecosystems around the world (Richardson 2019; Seyednasrollah et al. 2019). The highest-density and longest-running PhenoCam sites (there are over 75 with more than 10 years of observations) are in the United States. Indicators of 'start of season' (SOS_{PC}) and 'end of season' (EOS_{PC}) were estimated from PhenoCam data (Table 2.14) and ground observation of red oak (*Quercus rubra*; SOS_{GO}, EOS_{GO}) in Harvard Forest, a deciduous forest in Massachusetts in the United States (Richardson and O'Keefe 2009; O'Keefe and VanScoy 2024), and from red oak observations across the northeastern United States

contributed to *Nature's Notebook* (SOS_{NN}, EOS_{NN}), the USA National Phenology Network (USA NPN) phenology monitoring platform (Rosemartin et al. 2014; Crimmins et al. 2022). Interannual variations in the start and end of season dates at Harvard Forest are broadly consistent with larger-scale data from USA NPN's *Nature's Notebook* program (Figs. 2.89a,b; Table 2.15). In 2024, SOS_{PC}, SOS_{GO}, and SOS_{NN} were three, six, and four days later, respectively, than in 2023, while EOS_{PC}, EOS_{GO}, and EOS_{NN} were seven, four, and four days earlier. SOS_{PC} (EOS_{PC}) was two days earlier (one day earlier) than the 2011–20 baseline mean, resulting in a growing season length of 168 days: 10 days shorter than in 2023, and one day longer than the baseline.

The USA NPN's extended Spring Index (SI-x), a model that reflects the onset of spring-season biological activity (Schwartz et al. 2013; Crimmins et al. 2017), estimated widespread later "first leaf" in 2024 across the eastern and southern United States and earlier first leaf across the western and central United States compared with 2023. In contrast, compared with the baseline (2011–20 mean), first leaf in 2024 was early across most of the eastern United States, and late across the west (Figs. 2.89a,b). Consistent with the SOS_{PC} and SOS_{GO} observations at Harvard Forest, first leaf was later (by three days) in 2024 than in 2023 and earlier (by one day) in 2024 compared to the baseline. Likewise, first leaf and SOS_{PC} observations from a selection of nine other sites across the USA showed consistent patterns (see Fig. 2.89 for details).

Start- and end-of-season indicators for native oak trees (*Quercus robur* and/or *Quercus petraea*) at European sites in Germany (D), the Netherlands (NL), Slovakia (SK), and the

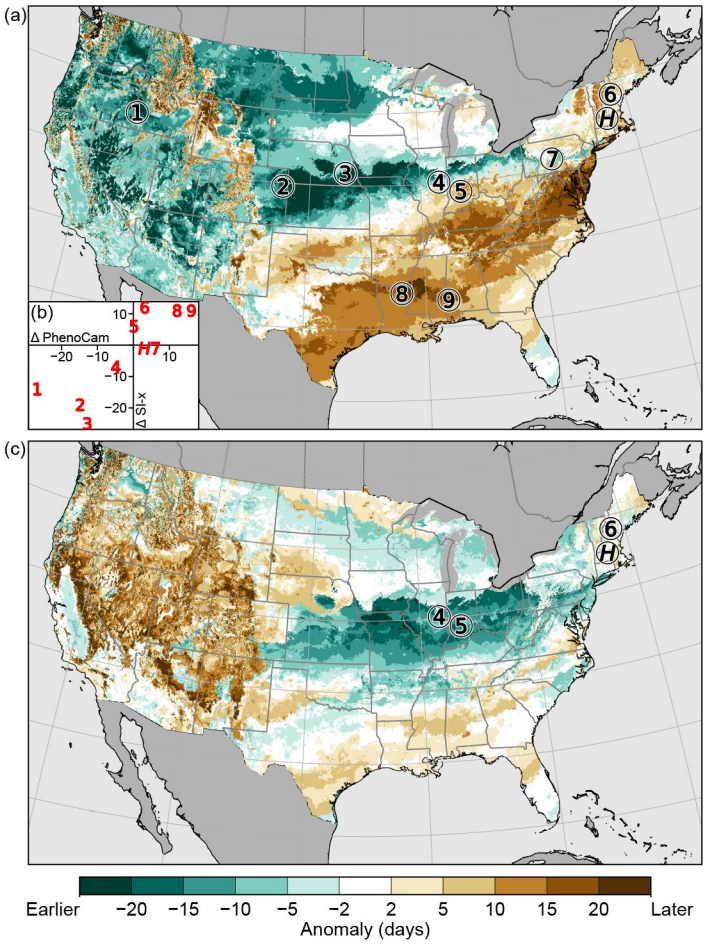

Fig. 2.89. 2024 "first leaf" date anomalies across the United States relative to (a) 2023 and (c) the 2011–20 baseline, estimated using the USA National Phenological Network (USA NPN) extended Spring Index (SI-x) model (Source: USA NPN data—https://www.usanpn.org/data). Negative (green) values show earlier first-leaf estimates in 2024 and positive (brown) are later. First-leaf SI-x anomalies are generally consistent with start of season PhenoCam (SOS_{PC}) anomalies at the 10 selected sites highlighted on map (a), see Table 2.14 for details. The scatter plot (b, inset in [a]) shows PhenoCam date anomalies on the x axis, and first-leaf SI-x date anomalies on the y axis (Deming regression, y = 1.02±0.04 x – 0.29±0.49, r^2 = 0.69). Map (c) shows the four sites from (a) for which the data record is long enough to calculate the 2011–20 baseline.

Table 2.14. PhenoCam sites across USA used in this assessment.

PhenoCam Site Name (#)	Location	Ecosystem Type
ARS Great Basin (1)	Reynolds Creek, Idaho	Shrub Community
NEON Site – D10 Central Plains (2)	Arikaree River, Colorado	Grass Community
Nine Mile Prairie, University of Nebraska (3)	Lancaster County, Nebraska	Grass Community
University of Illinois Energy Farm (4)	Urbana, Illinois	Restored Prairie Community
Morgan Monroe State Forest (5)	Indiana	Deciduous Forest
Bartlett Experimental Forest (6)	New Hampshire	Deciduous Forest
Susquehanna Shale Hills Critical Zone Observatory (7)	Pennsylvania	Deciduous Forest
Russell Sage State Wildlife Management Area (8)	Louisiana	Deciduous Forest
NEON Site – D08 Ozarks Complex (9)	Lenoir Landing, Alabama	Deciduous Forest
Harvard Forest (H)	Petersham, Massachusetts	Deciduous Forest

United Kingdom (UK) are represented by observations of first leaf (SOS) and leaf fall or "bare tree" (EOS; Table 2.15; Figs. 2.90c,d). They have been shown to be strongly influenced by spring and autumn/winter temperatures across Europe (Menzel et al. 2020). Compared to the baseline (2000–20 mean), SOS dates in D, NL, SK, and UK were all earlier by 11, 13, 12, and 8 days, respectively, while EOS dates were mostly later by 2, 5, 3, and 0 days (Table 2.15). Spring temperatures in D, NL, UK, and SK were much warmer (record high in SK; see section 7f) than average, resulting in very early 2024 SOS in D and SK, and the earliest SOS on record in NL and UK. Above-average temperatures in autumn/winter combined with ample precipitation across most of Europe resulted in generally later-than-average EOS dates. In some locations of SK, where extreme summer drought occurred (see section 7f), very early yellowing and leaf fall was observed at the end of August. With the warmer autumn/winter and consequently later EOS dates, the growing season length in 2024 was significantly longer than the baseline.

In Kyoto, Japan, the full bloom date (FBD) for native cherry tree (*Prunus jamasakura*) in 2024 was two days earlier than the baseline (2000–20 mean; Table 2.15; Fig. 2.90e), but 10 days later than the record set in 2023. Annual FBDs have been recorded since 812 AD (Aono and Kazui 2008), and for the Arashiyama district of Kyoto, they are recorded in newspapers and on web sites from daily observations at train stations by railway passengers.

Monitoring data on lake water concentrations of the photosynthetic pigment chlorophyll-*a* were available to estimate spring phytoplankton phenology in 10 Northern Hemisphere lakes (Fig. 2.91). The seasonal timing was estimated for 'start of season' (SOS_L; Park et al. 2016), 'day of maximum concentration' (DOM_L), and 'center of gravity' (COG_L), which is an estimate of the mid-point of the plankton bloom (Edwards and Richardson 2004). The lake basins showed great interannual variation and mixed phenological behavior in 2024 relative to 2000–20. The SOS_L and COG_L occurred earlier than the baseline median for most of the lakes—8 and 7 of 10, respectively—whereas no consistent pattern was observed for DOM_L (5 earlier and 5 later than the baseline median).

Table 2.15. Day of year (doy) and date of start of season (SOS), end of season (EOS) and full bloom date (FBD; cherry tree observations only) for land phenology records in USA (Harvard: PhenoCam, red oak, and USA National Phenology Network [USA-NPN] mean covering northeastern USA), Europe oak records (Germany, Netherlands, Slovakia, and United Kingdom), and Japan (native cherry tree observations in Japan). The baseline period is 2000–20 for all records except PhenoCam and USA-NPN, which have baseline periods of 2011–20. Growing season length for 2024 and the baseline mean are calculated as EOS minus SOS or FBD as appropriate for the record. Negative/positive values represent earlier/later dates for 2024 relative to the baseline.

Location / Record	SOS/FBD **2024** (doy, date)	SOS/FBD **Baseline** (doy, date)	SOS/FBD **Difference 2024 – Baseline** (days)	EOS **2024** (doy, date)	EOS **Baseline** (doy, date)	EOS **Difference 2024 – Baseline** (days)	Growing Season **EOS – SOS 2024** (days)	Growing Season **EOS – SOS Baseline Mean** (days)
Harvard PhenoCam	125 4 May	127 6 May	–2	293 19 Oct	294 20 Oct	–1	168	167
Harvard Red oak	128 7 May	128 7 May	0	295 21 Oct	293 19 Oct	+2	167	164
USA-NPN	120 29 Apr	126 5 May	–6	268 24 Sep	276 2 Oct	–8	148	150
Germany	107 17 Apr	118 28 Apr	–11	312 8 Nov	310 6 Nov	+2	205	192
Netherlands	97 6 Apr	110 20 Apr	–13	336 1 Dec	331 27 Nov	+5	239	221
Slovakia	104 14 Apr	116 26 Apr	–12	294 20 Oct	291 17 Oct	+3	190	175
UK	106 15 Apr	114 23 Apr	–8	334 29 Nov	334 29 Nov	0	228	221
Japan	95 4 Apr	97 6 Apr	–2	-	-	-	-	-

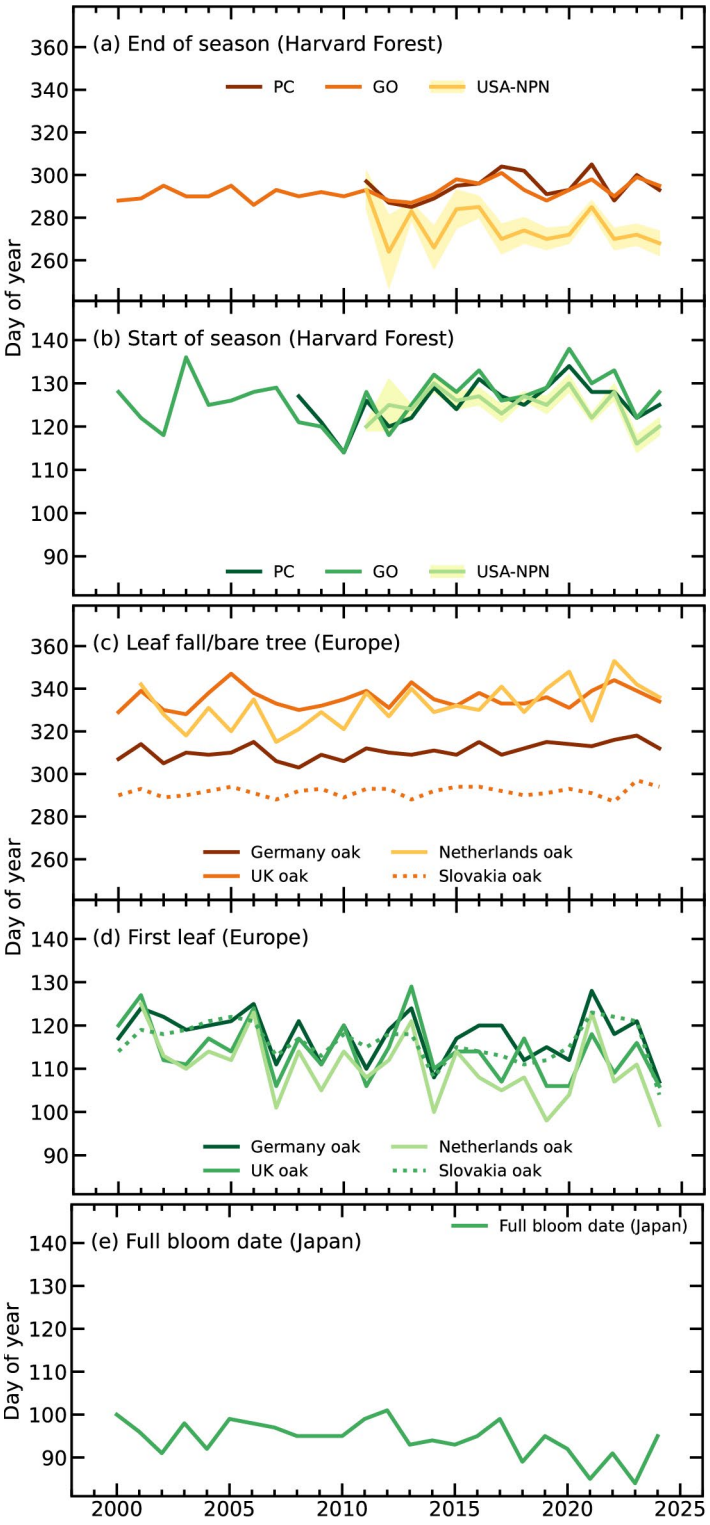

Fig. 2.90. Day of year of spring (green shades) and autumn (orange and yellow) vegetation phenology indicators for (a),(b) Harvard Forest, Massachusetts, derived from PhenoCam (PC), ground observations (GO) of red oak (*Quercus rubra*), and the USA National Phenology Network (USA NPN) regional-scale means of red oak observations (calculated across the northeastern states of Pennsylvania, New Jersey, New York, Connecticut, Rhode Island, Massachusetts, Vermont, New Hampshire, and Maine, with ±1 std. error shaded); (c),(d) Germany, United Kingdom, Netherlands, and Slovakia mean of native oak observations (*Quercus robur* or *Quercus petraea*), and (e) full bloom date observations of native cherry trees (*Prunus jamasakura*) in Kyoto (Arashiyama district), Japan.

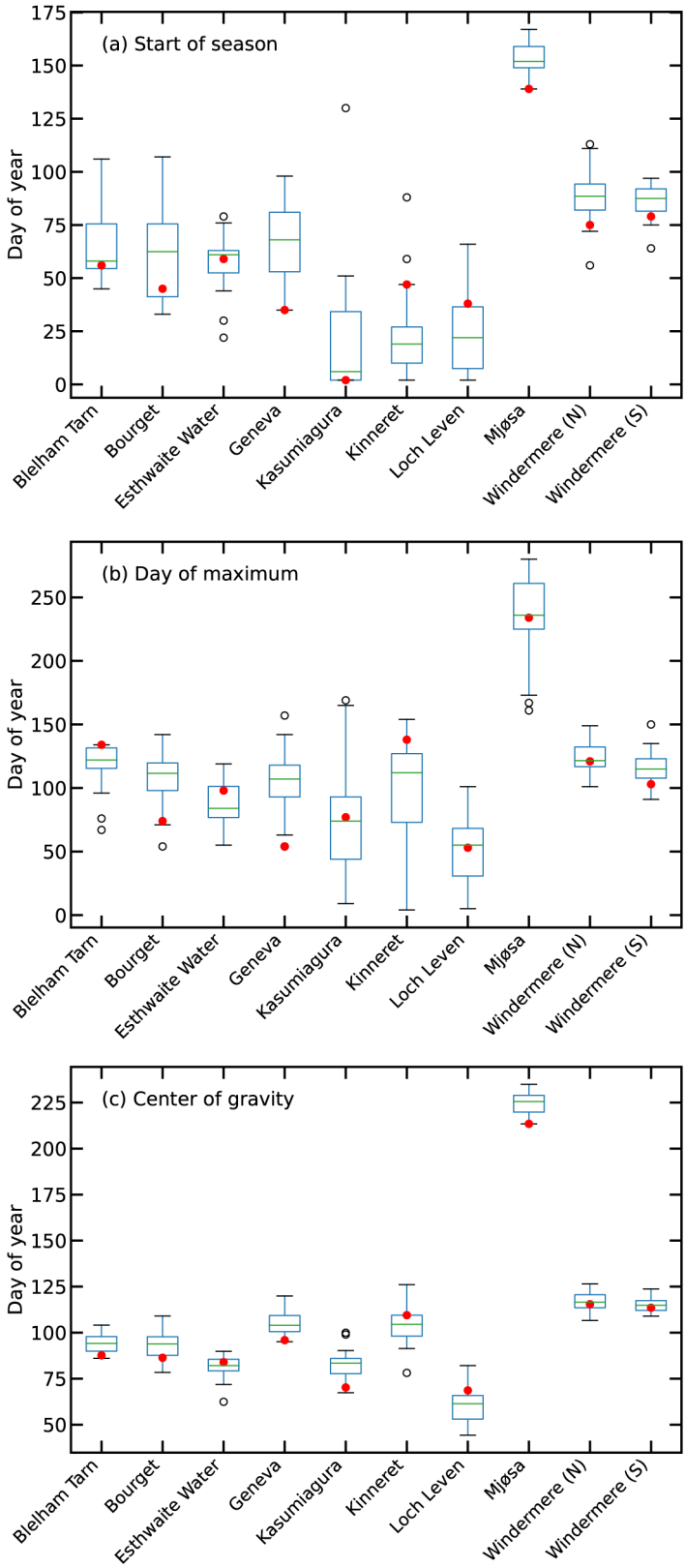

Fig. 2.91. Phenological metrics based on lake chlorophyll-*a* concentrations as a proxy of phytoplankton biomass: (a) start of season, (b) day of maximum, and (c) center of gravity. Boxplots show variation during the 2000–20 baseline period, and red dots show 2024 values. The 10 lakes are in the Northern Hemisphere (Blelham Tarn in the United Kingdom, Bourget in France, Esthwaite Water in the United Kingdom, Geneva in France/Switzerland, Kasumigaura in Japan, Kinneret in Israel, Loch Leven in the United Kingdom, Mjøsa in Norway, and north and south basins of Windermere in the United Kingdom).

5. VEGETATION OPTICAL DEPTH

—R. M. Zotta, W. Preimesberger, R. De Jeu, T. Frederikse, and W. Dorigo

Vegetation optical depth (VOD) is a radiative transfer model parameter derived from space-borne passive microwave sensors that indicates the attenuation of Earth's emitted or reflected radiation by vegetation. It serves as an indicator of vegetation water content (VWC) and vegetation density. VOD has proven valuable in many applications, including vegetation condition monitoring (Moesinger et al. 2022; Vreugdenhil et al. 2022). Positive VOD anomalies indicate above-average vegetation development, while negative anomalies indicate stressed or underdeveloped vegetation with lower VWC compared to normal conditions, either due to stressed vegetation, overall lower biomass, or both.

In 2024, the overall VOD anomaly in the NH was similar to that observed in 2023 (Zotta et al. 2023; Fig. 2.92). In contrast, in the SH, where vegetation development is influenced by variations in the El Niño–Southern Oscillation (ENSO; Miralles et al. 2014; Martens et al. 2017), overall VOD was lower than in 2023 (Figs. 2.92, 2.93). Here, negative anomalies prevailed, especially in the first quarter of the year (Appendix Fig. A2.13), during the strong El Niño event.

Widespread positive anomalies (Plate 2.1am), which intensified relative to 2023 (Appendix Fig. A2.14), were observed in large regions across Australia and parts of eastern Africa. In Australia, these patterns were likely driven by above-average rainfall (section 7h4) boosting vegetation growth. Substantial positive anomaly patterns were observed during the first half of 2024 across large parts of Kenya, Somalia, Ethiopia, and South Sudan (Appendix Fig. A2.13), likely a consequence of two consecutive seasons of wetter-than-normal conditions facilitating vegetation recovery after an extended drought period (WFP 2024). Additionally, notable positive VOD anomaly patterns emerged in the Sahel starting in September, likely driven by substantial rainfall (section 7e5) that boosted vegetation activity. At the monthly time scale (Appendix Fig. A2.13), striking positive patterns were observed in North America across portions of the Plains and Midwest, where exceptionally warm temperatures led to favorable winter crop conditions (USDA and USDC 2024) in the year's first quarter. Strong positive VOD anomaly patterns also emerged in Spain in October, likely due to record rainfall amounts (section 7f4).

Large-scale negative anomaly patterns in VOD were identified across multiple regions, including extended areas in Africa, Mexico, Central and South America, and Eastern Europe (Plate 2.1am). During the first quarter of 2024, lower-than-usual VOD continued to be evident in southern

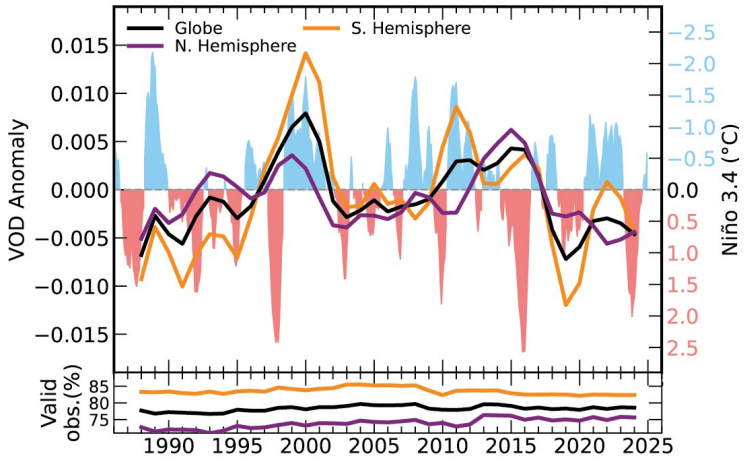

Fig. 2.92. Yearly vegetation optical depth (VOD) anomaly averages computed from the 1991–2020 climatology and yearly Niño-3.4 index. The Niño-3.4 index tracks the state of the El Nino–Southern Oscillation (ENSO). A negative Niño-3.4 index corresponds to a negative ENSO phase. (Source: VOD Climate Archive version 2 [VODCA v2]; NOAA Physical Sciences Laboratory [https://psl.noaa.gov/data/timeseries/month/DS/Nino34/].)

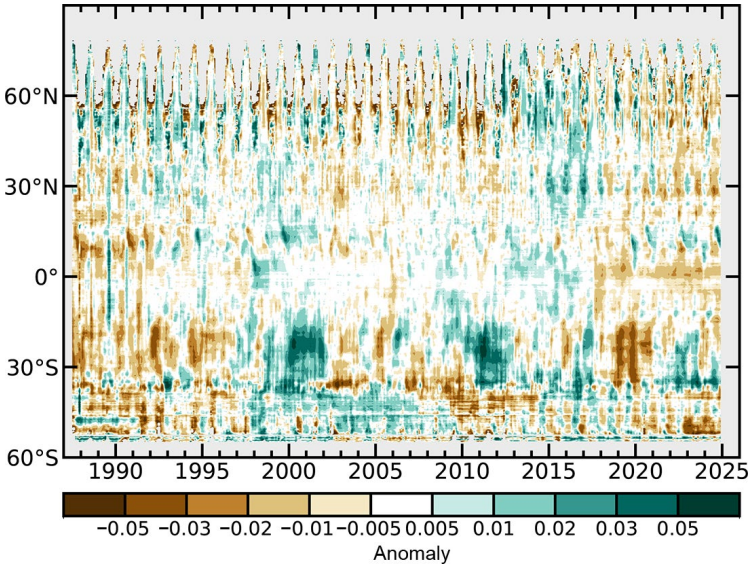

Fig. 2.93. Time–latitude diagram of monthly vegetation optical depth (VOD) anomalies (1991–2020 base period). Data are masked where no retrieval is possible or where the quality of the retrieval is not assured and flagged due to frozen soil, radio frequency interference, etc. (Source: VOD Climate Archive version 2 [VODCA v2].)

Africa (Appendix Fig. A2.13), where ENSO is a significant factor in agricultural productivity (UNOCHA 2024). Specifically, negative VOD anomalies in February and March were recorded in Namibia, Botswana, Zimbabwe, Zambia, and Angola. These regions experienced their driest conditions in decades (Van Dijk et al. 2025), which deteriorated the vegetation (UNOCHA 2024). In Zambia, severe drought and high temperatures devastated agricultural production (Van Dijk et al. 2025). In the Americas, Mexico experienced a prolonged dry spell which, combined with intense heatwaves (section 7b3), severely impacted crop growth (Climate.gov 2024). The reduction in VOD observed in the Pantanal region in Brazil is likely a result of extreme drought (NASA 2024). Persistent drought conditions significantly affected vegetation condition across West, Central, and North Africa during the first half of the year, contributing to the observed negative VOD anomalies (Appendix Fig. A2.13; Toreti et al. 2024a). Similarly, declines in VOD in Romania, Ukraine, and southern Russia are likely attributable to extended drought conditions that adversely affected local vegetation (Toreti et al. 2024b).

Long-term patterns associated with land-use changes persisted in 2024 (Plate 2.1am; Zotta et al. 2023). Regions including northern Mongolia, Bolivia, Paraguay, and Brazil experienced below-average VOD due to deforestation and land degradation (Song et al. 2018). Conversely, intensified agricultural practices in India and reforestation efforts in northeastern China contributed to above-average VOD (Song et al. 2018).

The VOD data originate from the VOD Climate Archive version 2 (VODCA v2, Zotta et al. 2024a,b). VODCA combines VOD observations derived with the Land Parameter Retrieval Model (Meesters et al. 2005; van der Schalie et al. 2017) from various space-borne radiometers—including the Special Sensor Microwave/Imager (SSM/I), Tropical Rainfall Measuring Mission (TRMM), WindSat, Advanced Microwave Scanning Radiometer for the Earth Observing System (AMSR-E), and Advanced Microwave Scanning Radiometer 2 (AMSR2)—into a long-term, harmonized dataset. Here, VODCA CXKu, which integrates C-, X-, and Ku-band observations and provides daily data at 0.25° spatial resolution, was used.

Acknowledgments

a Introduction

R.J.H.D., J.B., and K.M.W. were supported by the Met Office Hadley Centre Climate Programme funded by the U.K. Department for Science, Innovation and Technology (DSIT). G.A.M. is supported by NOAA. The editors thank Emily Carlisle, John Kennedy, David Parker, Jessica Poulton, Nick Rayner, Ruben Urraca, and the five anonymous reviewers for their insight, thoughts, and suggestions while reviewing this chapter. We also thank Fumi Sezaki and Ayaka Bunno (Japanese Meteorological Association [JMA]), Julien Nicolas (European Centre for Medium-Range Weather Forecasts [ECMWF]), and Mike Bosilovich (NASA) for their help in providing the reanalysis data used in this chapter. Many of the figures in this chapter were produced with the help of the Matplotlib version 3.7.2 (Hunter et al. 2007), Iris version 3.7.0 (Hattersley et al. 2023), and Cartopy version 0.21.1 (Elson et al. 2022) packages.

b2 Lake Surface Temperatures

Lake surface water temperatures from satellite data have been generated within the Climate Change Initiative Lakes project funded by the European Space Agency (ESA) (4000125030/18/I-NB) with adaptation funded by the E.U. Copernicus Climate Change Service (C3S) programme and extensions by the U.K. Earth Observation Climate Information Service (EOCIS) project (NE/X019071/1). Part of the in situ data used for the validation of the satellite data and for this report have kindly been made publicly available by the Fisheries and Oceans Canada (FOC), the National Data Buoy Center from NOAA, the Hungarian Meteorological Office, the Upper Great Lakes Observing System (UGLOS), and the North Temperate Lakes Long-Term Ecological Research (NTL-LTER). The authors gratefully acknowledge the late Alon Rimmer for always supplying data for Lake Kinneret.

b3 Night Marine Air Temperatures

R.C. and E. K. were supported by the Natural Environmental Research Council (NERC) through National Capability funding (AtlantiS: NE/Y005589/1). R. J. was supported by funding from the U.S. Department of Energy (DOE) (DE-SC0023332).

b4 Surface Temperature Extremes

R.J.H.D. was supported by the Met Office Hadley Centre Climate Programme funded by DSIT.

b5 Tropospheric Temperature

Work performed by Stephen Po-Chedley at Lawrence Livermore National Laboratory (LLNL) was supported by the Regional and Global Model Analysis Program (RGMA) of the Office of Science at the DOE and performed under the auspices of the DOE under Contract DE- AC52-07NA27344. Work performed by Cheng-Zhi Zou was supported by NOAA/Office of Low Earth Orbit (LEO) Proving Ground and Risk Reduction (PGRR) Program.

b7 Equivalent Temperature

Paul Stoy was supported by the U.S. National Science Foundation (NSF) (Hydrological Sciences award 2422397). Tom Matthews and Tom Wood were supported by a U.K. Research and Innovation Future Leaders Fellowship (grant MR/X03450X/1).

c1 Permafrost Temperatures and Active-Layer Thickness

Research on James Ross Island was supported by the Czech Antarctic Research Programme and the Czech Science Foundation project (GM22-28659M). The Circumpolar Active Layer Monitoring (CALM) program is funded by the NSF Project 1836377. The Svalbard permafrost data is part of the Svalbard Integrated Earth Observing System (SIOS). The Swiss Permafrost Monitoring Network (PERMOS) is financially supported by MeteoSwiss (in the framework of Global Climate Observing System [GCOS] Switzerland), the Federal Office for the Environment, and the Swiss Academy of Sciences, and acknowledges the contribution of its partner

institutions. The French Network PermaFRANCE is financially supported by the Grenoble Observatory for Sciences of the Universe and the French Research Infrastructure Critical Zone Observatories: Research and Application (OZCAR). The Chinese Permafrost Monitoring Network is financially supported by the Chinese National Science Foundation (41931180) and Cryosphere Research Station on Qinghai–Xizang Plateau, Chinese Academy of Sciences (CAS).

c2 Rock Glacier Velocity

Rock glacier monitoring at Hinteres Langtalkar and Dösen rock glaciers (AT) is supported by the Hohe Tauern National Park Carinthia through its long-term permafrost monitoring program. Laurichard (FR) survey is supported by "Observation and Experimentation System for Environmental Research" (SOERE/All'envi-OZCAR Research Infrastructure) and the PermaFrance observatory "Monitoring the mountain permafrost in the French Alps" as well as French National Research Agency in the framework of the Investments for the Future programs: Risk@UGA (ANR-15-IDEX-02) and LabEx OSUG@2020 (ANR10 LABX56). The Ecrins National Park has been supporting field surveys since the early 2000s. PERMOS is financially supported by MeteoSwiss in the framework of GCOS Switzerland, the Federal Office for the Environment, and the Swiss Academy of Sciences. PERMOS acknowledges the important contribution of the partner institutions and principal investigators. The time series for Central Asian rock glaciers was compiled within the ESA Permafrost Climate Change Initiative (Permafrost_CCI) project (4000123681/18/I-NB). The time series for the Dry Andes was supported by the Center for Advanced Studies in Arid Zones (CEAZA) and the Leading House for the Latin American Region (University of St. Gallen), grant number MOB1829.

c3 Alpine Glaciers

The World Glacier Monitoring Service mass balance dataset is the primary data used in the section.

c4 Lake Ice Cover

We thank Al and Sue Stangel, Alexander Mills, Ann LaLiberte, Beth Kohlman, B.J. Bauer, Bob Katzenberger, Bonny Pederson, Brendan Wiltse, Brian D. Neill, Brian Vlach, John Barten, Rick Brascke, Calvin Maurer, Carl C. Nelson, Carol Wendorf, Cheryl and Dorothy Zingler, Clare and Dan Shirley, Craig Hillman, Dale Robertson, Dan Brumm, Daniel L. Anderson, Dave and Lynda J. Urshan, David Kahan, Don Pierson, Don McClanathan, Donald and Mureil Fornasiere, Doug Fitzgerald, Douglas Pierzina, Dr. Neal D. Mundahl, Duane Williams and Edie Evarts, Duncan A. Brown, Earl Cook, Fred Buckley, Gary Teigen, Gay Alberts Ruby, Gene Cooper, George Grevich, Greg Sass, Holly Waterfield, Huaxia Yao, James and Sharon Fenner, James W. Danielson, Jan Henning L'Abée-Lund, Jeff Goelzer, Jeffrey G. Lowe, Jerry Evans, Jerry Sondreal, Jim and Judy Daugherty, Joe Jenkins, Joel Rasmussen, John and Catherine Bart, John Maier, Jonathan Ross, Dan Drumm, Martin Kainz, Joy Krubsack, Kay and Rich Rezanka, Kay Olson, Kay Wepfer, Kay Wepfer, Ken Blumenfeld, Larry and Marlene Lotto, Larry Peterson, Lars Rudstam, Lolita Olson, Lowell Dague, Marge Kellor, Mark Biller, Mark Holland, Mark J. and Rosie Peters, Mary Jane Dillingham, Mary Lou Fry, Randell Fry, Merja Pulkkanen, Michael Allen, Michael Bradley, Michael Kolecheck, Michael Traufler, Mickey and Dennis Chick, Mike, Jeff, and Thomm Backus, Molly Hibbard, Morris and Doris Whiting, Mr. and Mrs. Jay R. Mackie, Mr. and Mrs. William Bergersen, Mrs. Gale Wheeler, Mrs. Kathy Elhard, Mrs. Margery Armstrong, Myron Hagelstrom, Nancy Putnam, Nancy Steenport, Patricia Bebak, Patrick Collins, Paulette Janssen, Pete Boulay, Peter Bearup, Rachel Dahlke, Raymond (Joe) Jenkins, Richard L. Tamke, Rock Anderson, Ron Pabich, Ronald Jones, Ross Swain, Sally Ketchen, Sandra Anderson, Scott Schoepp, Sogee Spinner, Sharon Natzel, Shin-Ichiro Matsuzaki, Susan Reineking, Susan Verhaalen, Tana McNutt, Theodore (Ted) Peters, Thomas Sommerfeldt, Tom Stangl, Travis Campbell, Virgil Luehrs, Walt and Nancy Quillinan, Walter R. Brown, Water Dahlke III, William and Brenda Jones, and William Hanson for their dedication and efforts to collect and share in situ ice phenological records with us. A part of this research was enabled by an intern, Jessica Ollinik, from the Canadian Institute of Ecology and Evolution's Living Data Project, which is funded by the Government of Canada through a Natural Sciences and Engineering Research Council of Canada (NSERC) Collaborative Research and Training Experience (CREATE) grant.

c5 Northern Hemisphere Continental Snow Cover Extent

This work is funded in part by NOAA's Climate Data Record (CDR) Program at the National Centers for Environmental Information.

d1 Surface Humidity

Kate Willett was supported by the Met Office Hadley Centre Climate Programme funded by DSIT.

d2 Humid-Heat extremes

Kate Willett was supported by the U.K.–China Research & Innovation Partnership Fund through the Met Office Climate Science for Service Partnership (CSSP) China under the International Science Partnerships Fund (ISPF). Kate Willett was also supported by the Met Office Hadley Centre Climate Programme funded by DSIT.

Cassandra Rogers was supported by the Australian Climate Service.

Thank you to Mitchell Black and Ulrike Bende-Michl from the Bureau of Meteorology for providing initial reviews of this section.

d6 Precipitation Extremes

The National Center for Atmospheric Research is sponsored by the National Science Foundation under Cooperative Agreement No. 1852977. Stephen Blenkinsop was supported by the UK NERC funded grant no. NE/Y503241/1.

d7 Cloudiness

Clouds and the Earth's Radiant Energy System (CERES) Energy Balanced and Filled (EBAF) data were obtained from the NASA Langley Research Center CERES ordering tool at https://ceres.larc.nasa.gov/data/.

d9 River Discharge

The Global Flood Awareness System (GloFAS) is part of the Copernicus Emergency Management Service, which is funded by the European Union Space Program.

d10 Groundwater and Terrestrial Water Storage

This work was supported by NASA's Gravity Recovery and Climate Experiment Follow-On (GRACE-FO) Science Team.

d11 Soil Moisture

This study uses satellite soil moisture observations from the C3S's Climate Data Store (CDS; 2025): Soil moisture gridded data from 1978 to present. Accessed on 11 February 2025, 10.24381/cds.d7782f18

d12 Monitoring Drought using the Self-Calibrating Palmer Drought Severity Index

Jonathan Barichivich was supported by the European Research Council (ERC) under the Horizon Europe research and innovation programme (ERC-starting grant CATES, grant agreement No. 101043214). Tim Osborn received funding from the U.K. NERC (NE/S015582/1). Ian Harris and Amee Gollop received funding from U.K. National Centre for Atmospheric Science (NCAS). The research presented in the drought section was carried out on the High-Performance Computing Cluster supported by the Research and Specialist Computing Support service at the University of East Anglia.

d13 Land Evaporation

D.G.M. acknowledges support from the European Research Council (ERC) under grant agreement no. 101088405 (HEAT). H.E.B. is supported by the King Abdullah University of Science and Technology (KAUST).

e1 Mean Sea Level Pressure and Related Modes of Variability

David Fereday was supported by the Met Office Hadley Centre Climate Programme funded by DSIT.

e2 Surface Winds

C.A.M. was supported by the Spanish National Research Council (CSIC), University of Valencia (UV), Generalitat Valenciana (GVA) and funded by PROMETEO Grant CIPROM/2023/38, International Global Change Laboratory (LINCGLOBAL)-CSIC ref. LINCG24042, and the Interdisciplinary Thematic Platform for Climate and Climate Services (PTI-CLIMA). R.J.H.D. was supported by the Met Office Hadley Centre Climate Programme funded by DSIT. L.R. was supported by NASA Ocean Vector Wind Science Team grant 80NSSC23K0984. Z.Z. was supported by the National Natural Science Foundation of China grant 42071022.

e4 Lightning

The work of M.F. was sponsored by the Royal Society (U.K.) grant NMG/R1/180252 and NERC (U.K.) under grants NE/L012669/1 and NE/H024921/1.

E.W. is supported for studies on global circuit response to climate change from the Physical and Dynamic Meteorology Program at the NSF on grant no. 6942679.

C.P. was supported in his lightning research by the Israel Science Foundation (ISF) grant 2701/17, and the Ministry of Energy grant no. 220-17-002. S.G. was supported by NASA Grant 80NSSC21K0923 and NASA Contract 80GSFC20C044. The authors wish to thank Peter Thorne at Maynooth University in Ireland and at the ECMWF for suggesting and initiating this work and for recommending that lightning be made an essential climate variable. The Meteosat Third Generation Lightning Imager (MTG-LI) data used to generate the Figures are available from https://user.eumetsat.int/resources/user-guides/mtg-data-access-guide.

f1 Earth Radiation Budget at Top-of-Atmosphere

This research has been supported by the NASA CERES project. The resources of the NASA Langley Atmospheric Sciences Data Center are utilized to process the instantaneous Single Scanner Footprint (SSF) data used as input to EBAF Ed4.2.1 and processes the Fast Longwave and Shortwave Radiative Fluxes (FLASHFlux) Time Interpolated and Spatially Averaged (TISA) version 4C. We further acknowledge the efforts of Walt Miller and Pam Mlynczak of the CERES team, who monitor CERES data production and produce the FLASHFlux TISA version 4C monthly averaged data products, respectively.

f2 Mauna Loa Clear-Sky Atmospheric Solar Transmission

Key balloon data from Hilo used in this 2024 update of the Mauna Loa apparent atmospheric transmission would not have been possible without the generous cooperation afforded by Global Monitoring Laboratory (GML) staff, Matthew Martinsen, Darryl Kuniyuki, and David Nardini, at the Mauna Loa Observatory.

g1 Long-Lived Greenhouse Gases

This research was supported in part by NOAA cooperative agreement NA22OAR4320151, for the Cooperative Institute for Earth System Research and Data Science (CIESRDS).

g2 Ozone-Depleting Gases

This research was supported in part by NOAA cooperative agreement NA22OAR4320151, for the Cooperative Institute for Earth System Research and Data Science (CIESRDS).

g3 Tropospheric Aerosols

This research has been supported by the Copernicus Atmospheric Monitoring Service (CAMS) program managed by ECMWF (Framework Agreement ECMWF/Copernicus/2021/CAMS2_35_HYGEOS) on behalf of the European Commission. A large number of observational datasets are used in the CAMS reanalysis; the authors would like to thank all the actors that created and made public the remote sensing products assimilated in the CAMS Reanalysis: NASA, NOAA, the European Organisation for the Exploitation of Meteorological Satellites (EUMETSAT), and the ESA.

g4 Tropospheric Ozone

The NOAA Proving Ground and Risk Reduction (PGRR) Program supported the contributions by O. R. Cooper and K.-L. Chang. K.-L. Chang was also supported by NOAA cooperative agreement NA22OAR4320151. P. Effertz was supported by NOAA cooperative agreement NA22OAR4320151. Funding for J. Ziemke for this research was provided in part by NASA NNH14ZDA001N-DSCOVR, NASA Suomi National Polar-orbiting Partnership (SNPP) and Joint Polar Satellite System (JPSS) Satellites Standard Products for Earth System Data Records, and Code 614 programmatic support for long-term ozone trends.

g5 Stratospheric Aerosols

Lidar observations at the Haute-Provence Observatory (OHP) are funded by the French National Centre for Scientific Research/National Institute of Sciences of the Universe (CNRS/INSU) and the National Centre for Space Studies (CNES). S. Khaykin's work is supported by National Agency for Research (ANR) PyroStrat 21-CE01- 335 0007-01 project. We thank Christine David, Alain Hauchecorne, Julien Jumelet, Philippe Keckhut (Laboratory for Atmospheres, Observations, and Space [LATMOS]) and the lidar station operators for their contributions to long-term monitoring of stratospheric aerosol at OHP. Lidar observation at Lauder are funded in part by the Greenhouse gases Observing SATellite (GOSAT) project. We thank Richard Querel (National Institute of Water and Atmospheric Research [NIWA]), Osamu Uchino, Tomohiro Nagai (Meteorological Research Institute [MRI]) and Yushitaka Jin (MRI) for their contributions to long-term monitoring of stratospheric aerosol at Lauder. G. Taha's work is supported by the NASA Earth Science Division grant 80NSSC23K1037.

g6 Stratospheric Ozone

Carlo Arosio, Melanie Coldewey-Egbers, Diego Loyola, Viktoria Sofieva, Alexei Rozanov, and Mark Weber are grateful to the E.U. C3S, C3S2_312a_Lot2 Ozone, and to the ESA's Climate Change Initiative Ozone (CCI+) projects for supporting the generation and extension of the Global Ozone Monitoring Experiment-type Total Ozone Essential Climate Variable (GTO-ECV) total ozone and Stratospheric Aerosol and Gas Experiment (SAGE) CCI Ozone Mapping and Profiler Suite (OMPS) data records. Carlo Arosio, Viktoria Sofieva, Kleareti Tourpali, Alexei Rozanov, and Mark Weber are grateful for the support of the ESA project Ozone Recovery from Merged Observational Data and Model Analysis (OREGANO). The OSIRIS Team is grateful for the support of the Canadian Space Agency since 1993. The NASA Long Term Measurement of Ozone program WBS 479717 supports Stacey M. Frith. Lucien Froidevaux's contribution, with the assistance of Ryan Fuller, was performed at the California Institute of Technology's Jet Propulsion Laboratory (JPL), under contract with NASA. Jeannette Wild was supported by NOAA grant NA19NES4320002 (Cooperative Institute for Satellite Earth System Studies [CISESS]) at the University of Maryland's Earth System Science Interdisciplinary Center (ESSIC). Melanie Coldewey-Egbers and Diego Loyola acknowledge the partial support by the German Aerospace Center (DLR) projects "Methods for analyzing and assessing changes in the atmosphere and the climate system" (MABAK) and INPULS.

g7 Stratospheric Water Vapor

We would like to acknowledge assistance with water vapor sonde launches from NOAA GML staff in Boulder, Colorado, and Hilo, Hawaii, and international collaborators in San Jose, Costa Rica, and Lauder, New Zealand. This research was supported by the NASA Upper Atmosphere Composition Observations (UACO) program.

g8 Carbon Monoxide

CAMS is funded by the E.U.

h2 Terrestrial Vegetation Dynamics

The authors thank the providers of the remote sensing dataset needed to perform this analysis and the Joint Research Centre's (JRC) Big Data Analytics Platform (BDAP) (https://doi.org/10.5281/zenodo.10214201).

h4 Phenology

Deborah Hemming and Rebecca Holliday acknowledge support from the Met Office Hadley Centre Climate Programme funded by DSIT. Andrew Richardson acknowledges support from the NSF LTER (award 1832210); John O'Keefe and Greta VanScoy also acknowledge support from the NSF through the LTER (award 1832210) program. Nature's Calendar (Woodland Trust) in the U.K. thanks all its volunteer recorders and support from players of People's Postcode Lottery. Theresa Crimmins and the USA National Phenology Network (NPN) acknowledge support from the NSF through the Division of Biological Infrastructure (award 2404760), the U.S. Fish and Wildlife Service (agreements F16AC01075 and F19AC00168), and the U.S. Geological Survey (G14AC00405 and G18AC00135). The USA NPN thanks the many participants contributing phenology observations to Nature's Notebook. De Natuurkalender (Nature's Calendar) program in the Netherlands thanks all the volunteers and school children in the Global Learning and Observations to Benefit the Environment (GLOBE) program for their many observations. The Slovak Hydrometeorological Institute thanks all its volunteer observers for participating in the phenological observation program. Orlane Anneville acknowledges support from the National Institute of Agricultural Research (INRAE). Stephen Thackeray thanks Werner Eckert, Heidrun Feuchtmayr, Alba Alemany, Shin-Ichiro Matsuzaki, Ryuichiro Shinohara, Jan-Erik Thrane, Linda May, and all field and lab workers associated with the provision of the lake chlorophyll-*a* data. We acknowledge funding from Vassdragsforbundet for Mjøsa med tilløpselver (https://www.vassdragsforbundet.no/om-oss/). Windermere, Blelham Tarn, Esthwaite Water, and Loch Leven monitoring were supported by NERC award numbers NE/R016429/1 and NE/Y006208/1 as part of the U.K. Status, Change and Projections of the Environment (UK-SCAPE) and U.K. Challenges Programmes delivering National Capability. Data for Lakes Geneva and Bourget were contributed by the Observatory on LAkes (OLA), © Observation and Experimentation System for Environmental Research (SOERE) OLA-IS, AnaEE-France, INRAE of Thonon-les-Bains, International Commission for the Protection of the Waters of Lake Geneva (CIPEL), Intercommunity Committee for the Sanitation of Lake Bourget (CISALB).

h5 Vegetation Optical Depth

R. M. Zotta and W. Dorigo acknowledge the TU Wien Wissenschaftspreis 2015, a personal grant awarded to W. Dorigo. We also acknowledge support from the ESA CCI and the C3S.

Sidebar 2.1 Super Extreme Land Surface Temperature Hotspots

This study has been funded through the ESA within the framework of the Land Surface Temperature project under the CCI (LST_cci), contract number 4000123553/18/I-NB, and was supported by NERC [NERC grant reference number NE/X019071/1, "U.K. EO Climate Information Service"] and the U.K.–China Research & Innovation Partnership Fund through the Met Office Climate Science for Service Partnership (CSSP) China under the International Science Partnerships Fund (ISPF). The authors are grateful to the ESA for creating the CCI program, which has strengthened the consistency of the many research communities related to developing, processing, qualifying, and using satellite CDRs.

Appendix 1: Acronyms

4D-VAR	four-dimensional variational assimilation
AAO	Antarctic Oscillation
AATSR	Advanced Along-Track Scanning Radiometer
ACE-FTS	Atmospheric Chemistry Experiment—Fourier Transform Spectrometer
AIRS	Atmospheric Infrared Sounder
ALT	active-layer thickness
AMSR2	Advanced Microwave Scanning Radiometer 2
AMSR-E	Advanced Microwave Scanning Radiometer for the Earth Observing System
ANR	National Agency for Research
ANT_EAST	East Antarctic
ANT_PEN	Antarctic Peninsula
ANT_SVL	Antarctic: southern Victoria Land
ANY	Australian New Year
AOD	aerosol optical depth
AOD550	aerosol optical depth at 550 nm
ASCAT	Advanced Scatterometer
ASR	absorbed solar radiation
AT	Austria
BAR_WS	Barents Sea region—West Siberia
BCS	Beaufort Chukchi Sea—Arctic Alaska and Mackenzie Delta region
BD	Brewer–Dobson
BDAP	Big Data Analytics Platform
C3S	Copernicus Climate Change Service
Ca	Calbuco
CALM	Circumpolar Active Layer Monitoring
CAMS	Copernicus Atmosphere Monitoring Service
CAMSRA	Copernicus Atmosphere Monitoring Service reanalysis
CAN	Canada
CAS	Chinese Academy of Sciences
CCI+	Climate Change Initiative Ozone
CCM	chemistry climate model
CCMI	Chemistry-Climate Model Initiative
CDR	Climate Data Record
CEAZA	Center for Advanced Studies in Arid Zones
CENT_SIB	Central Siberia
CERES	Clouds and the Earth's Radiant Energy System
CFC	chlorofluorocarbon
CG	cloud-to-ground
CH	Switzerland
CH_3CCl_3	methyl chloroform
CH_4	methane
CI	confidence interval
CIESRDS	Cooperative Institute for Earth System Research and Data Science
CIPEL	International Commission for the Protection of the Waters of Lake Geneva
CISALB	Intercommunity Committee for the Sanitation of Lake Bourget
CISESS	Cooperative Institute for Satellite Earth System Studies
CLASSnmat	Climate Linked Atlantic Sector Science Night Marine Air Temperature
CNES	National Centre for Space Studies
CNRS	French National Centre for Scientific Research

CO	carbon monoxide
CO_2	carbon dioxide
COGL	center of gravity
COSMIC	Constellation Observing System for Meteorology, Ionosphere, and Climate
COVID-19	Coronavirus disease 2019
C_p	specific heat capacity of air
CPT	cold-point tropopause
CREATE	Collaborative Research and Training Experience
CrIS	Cross-Track Infrared Sounder
CRU TS	Climatic Research Unit terrestrial series
CRUTEM5	Climatic Research Unit temperature version 5
CSIC	Spanish National Research Council
CSSP	Climate Science for Service Partnership
D	Germany
DE	Germany
DLR	German Aerospace Center
DOE	U.S. Department of Energy
DOML	day of maximum concentration
DU	Dobson unit
EAST_SIB	East Siberia
EBAF	Energy Balanced and Filled
EC	El Chichón
ECMWF	European Center for Medium-Range Weather Forecasts
ECOSTRESS	Ecosystem Spaceborne Thermal Radiometer Experiment on Space Station
EESC	equivalent effective stratospheric chlorine
EESC[A]	equivalent effective stratospheric chlorine calculated for air representative of the Antarctic
EESC[ML]	equivalent effective stratospheric chlorine calculated for air representative of the midlatitude stratosphere
ENSO	El Niño–Southern Oscillation
EOCIS	Earth Observation Climate Information Service
EOS	end of season
ER	extinction ratio
ERB	Earth radiation budget
ERC	European Research Council
ERF	effective radiative forcing
ESA	European Space Agency
ESSIC	Earth System Science Interdisciplinary Center
ET	evapotranspiration
EUMETSAT	European Organisation for the Exploitation of Meteorological Satellites
EUR	Europe
FAPAR	fraction of absorbed photosynthetically active radiation
FBD	full bloom date
FF	fossil fuel
FLASHFlux	Fast Longwave and Shortwave Radiative Fluxes
FOC	Fisheries and Oceans Canada
FP	frost point
FR	France
GCOS	Global Climate Observing System
GEOS-CF	Goddard Earth Observing System Composition Forecast Modeling System
GFAS	Global Fire Assimilation System
GFED4S	Global Fire Emissions Database version 4.1

GHCN	Global Historical Climatology Network
GHCNDEX	Global Historical Climatology Network Daily Extremes
GHCNh	Global Historical Climatology Network hourly
GHG	greenhouse gas
GISS	Goddard Institute for Space Studies
GISTEMP	Goddard Institute for Space Studies Surface Temperature Analysis
GLEAM4	Global Land Evaporation Amsterdam Model version 4
GLM	Geostationary Lightning Mapper
GLOBE	Global Learning and Observations to Benefit the Environment
GloFASv4	Global Flood Awareness System version 4
GloSSAC	Global Space-based Stratospheric Aerosol Climatology
GMI	Global Precipitation Measurement Microwave Imager
GMST	global mean surface temperature
GNSS	Global Navigation Satellite System
GNSS-RO	Global Navigation Satellite System Radio Occultation
GO	ground observation
GOES	Geostationary Operational Environmental Satellite
GOSAT	Greenhouse gases Observing SATellite
GOZCARDS	Global Ozone Chemistry and Related Trace Gas Data records for the Stratosphere
GPCC	Global Precipitation Climatology Centre
GPCP	Global Precipitation Climatology Project
GRACE	Gravity Recovery and Climate Experiment
GRACE-FO	Gravity Recovery and Climate Experiment Follow-On
GREALM	Global Reservoirs and Lakes Monitor
GSL	Global Snow Lab
Gt	gigaton
GTO-ECV	Global Ozone Monitoring Experiment-type Total Ozone Essential Climate Variable
GVA	Generalitat Valenciana
HadCRUT5	Met Office Hadley Centre/Climatic Research Unit Temperature version 5
HadEX3	Met Office Hadley Centre Extremes Dataset version 3
HadISD3	Met Office Hadley Centre Integrated Surface Dataset 3
HadISDH	Met Office Hadley Centre Integrated Surface Dataset of Humidity
HadISDH.blend	Met Office Hadley Centre Integrated Surface Dataset of Humidity over Land and Ocean
HadISDH.extremes	Met Office Hadley Centre Integrated Surface Dataset of Humidity Extremes
HadISDH.land	Met Office Hadley Centre Integrated Surface Dataset of Humidity over Land
HadISDH.marine	Met Office Hadley Centre Integrated Surface Dataset of Humidity over Ocean
HadSST4	Met Office Hadley Centre Sea Surface Temperature Dataset version 4
HCFC	hydrochlorofluorocarbon
HFC	hydrofluorocarbon
HIRS	High-resolution Infrared Radiation Sounder
HNO_3	nitric acid
Hu	Hunga
HYSPLIT	Hybrid Single-Particle Lagrangian Integrated Trajectory
IAK_CMV	Interior Alaska and central Mackenzie Valley, Northwest Territories
IC	in-cloud
ICESat-2	Ice, Cloud, and land Elevation Satellite 2
INRAE	National Institute of Agricultural Research
INSU	National Institute of Sciences of the Universe
IOD	Indian Ocean dipole
IR	infrared
ISF	Israel Science Foundation
ISPF	International Science Partnerships Fund

ISS	International Space Station
IT	Italy
ITCZ	Intertropical Convergence Zone
JMA	Japanese Meteorological Agency
JPSS	Joint Polar Satellite System
JRA-3Q	Japanese Reanalysis for Three Quarters of a Century
JRA-55	Japanese 55-year Reanalysis
JRC	Joint Research Centre
K	Kelvin
Ka	Kasatochi
KAUST	King Abdullah University of Science and Technology
KOMPSAT-5	Korea Multi-Purpose Satellite-5
L	latent heat of vaporization
LATMOS	Laboratory for Atmospheres, Observations, and Space
LEO	Office of Low Earth Orbit
LI	Lightning Imager
LINCGLOBAL	International Global Change Laboratory
LiO3s	Stratospheric Ozone Lidar at Haute-Provence Observatory
LLGHG	long-lived greenhouse gases
LLNL	Lawrence Livermore National Laboratory
LOWESS	locally weighted scatterplot smoothing
LS	lower stratosphere
LST	land surface temperature
LST_cci	Climate Change Initiative for Land Surface Temperature
LSWT	lake surface water temperature
LTA	Lidar Temperature Aerosol
LTT	lower-tropospheric temperature
LWCRE	longwave cloud radiative effect
MABAK	Methods for analyzing and assessing changes in the atmosphere and the climate system
MACCity	Monitoring Atmospheric Composition and Climate and CityZen
MCM	million cubic meters
MEGAN	Model of Emissions of Gases and Aerosols from Nature
MERIS	Medium Resolution Imaging Spectrometer
MetOp	Meteorological Operational satellite
MLO	Mauna Loa Observatory
MLS	Microwave Limb Sounder
MNT_FRA	French Alps
MNT_IT	Italian Alps
MNT_NOR	Norwegian mountains
MNT_QTP	Qinghai–Tibet Plateau
MNT_SWI	Swiss Alps
MODIS	Moderate Resolution Imaging Spectroradiometer
MOPITT	Measurement of Pollution in the Troposphere
MRI	Meteorological Research Institute
MSLP	mean sea-level pressure
MSU	Microwave Sounding Unit
MSWEP	Multi-Source Weighted-Ensemble Precipitation
MTG	Meteosat Third Generation
MWR	Microwave Radiometer
N_2O	nitrous oxide
Na	Nabro
NA	North America

NAO	North Atlantic Oscillation
NCAS	National Centre for Atmospheric Science
NCEP	National Centers for Environmental Prediction
NDACC	Network for the Detection for Stratospheric Change
NERC	Natural Environmental Research Council
NH	Northern Hemisphere
NH_3	ammonia
NH_4NO_3	ammonium nitrate
NIWA	National Institute of Water and Atmospheric Research
NL	The Netherlands
NMAT	night marine air temperature
NO	Norway
NO_2	nitrogen dioxide
NOAAGlobalTemp	NOAA Merged Land Ocean Global Surface Temperature Analysis
NOx	nitrogen oxides
NRT	near-real-time
NSERC	Natural Sciences and Engineering Research Council of Canada
NSF	National Science Foundation
NTL-LTER	North Temperate Lakes Long-Term Ecological Research
ODGI	Ozone Depleting Gas Index
ODS	ozone-depleting substance
OH	hydroxyl radical
OHP	Haute-Provence Observatory
OLA	Observatory of alpine LAkes
OLCI	Ocean and Land Colour Instrument
OLR	outgoing longwave radiation
OLS	ordinary least-squares
OMI	Ozone Monitoring Instrument
OMPS	Ozone Mapping and Profiler Suite
OMPS-LP	Ozone Mapping and Profiler Suite Limb Profiler
OMPS-NP	Ozone Mapping and Profiler Suite Nadir Profile
ONI	Oceanic Niño Index
OSIRIS-REx	Origins, Spectral Interpretation, Resource Identification, and Security—Regolith Explorer
OZCAR	Critical Zone Observatories: Research and Application
PAN	Peroxyacetyl nitrate
PANs	Acyl peroxynitrates
PC	PhenoCam
PDO	Pacific Decadal Oscillation
Permafrost_CCI	Permafrost Climate Change Initiative
PERMOS	Swiss Permafrost Monitoring Network
PGRR	Proving Ground and Risk Reduction
Pi	Pinatubo
PM2.5	particulate matter
PNA	Pacific–North American
PNE	Pacific Northwest Event
POPS	Portable Optical Particle Spectrometer
PSA	Pacific–South American
PTI-CLIMA	Interdisciplinary Thematic Platform for Climate and Climate Services
pyroCb	pyrocumulonimbus
q	specific humidity
QBO	quasi-biennial oscillation
QTP	Qinghai–Tibet Plateau

QuickSCAT	Quick Scatterometer
Ra	Raikoke
RATPAC	Radiosonde Atmospheric Temperature Products for Assessing Climate
RCP	Representation Concentration Pathways
RFaci	aerosol–cloud interactions
RFari	aerosol–radiation interactions
RGMA	Regional and Global Model Analysis Program
RGV	rock glacier velocity
RH	relative humidity
RSS	Remote Sensing Systems
RSW	reflected shortwave
Ru	Ruang
Rx1day	one-day maxima
Rx5day	accumulated five-day maxima
Sa	Sarychev
SAGE III	Stratospheric Aerosol and Gas Experiment III
SAM	Southern Annular Mode
sAOD	stratospheric aerosol optical depth
SAT	surface high temperature
SBUV	Solar Backscatter Ultraviolet Radiometer
SCE	snow cover extent
SCIAMACHY	Scanning Imaging Absorption Spectrometer for Atmospheric Chartography
scPDSI	self-calibrating Palmer Drought Severity Index
SeaWiFS	Sea-Viewing Wide Field-of-View Sensor
SEH	super extreme hotspot
Sh	Shiveluch
SH	Southern Hemisphere
SIOS	Svalbard Integrated Earth Observing System
SI-x	Spring Index
SJ	Svalbard
SK	Slovakia
SLCF	short-lived climate forcer
SLSTR/A	Sea and Land Surface Temperature Radiometer onboard the Sentinel-3A platform
SLSTR/B	Sea and Land Surface Temperature Radiometer onboard the Sentinel-3B platform
SNPP	Suomi National Polar-orbiting Partnership
SO_2	sulfur dioxide
SOERE	Observation and Experimentation System for Environmental Research
SOI	Southern Oscillation Index
SOS	start of season
SSF	Single Scanner Footprint
SSM/I	Special Sensor Microwave/Imager
SSMIS	Special Sensor Microwave Imager/Sounder
SST	sea surface temperature
SSU	Stratospheric Sounding Unit
SSW	sudden stratospheric warming
STP	standard temperature and pressure
SW	shortwave
SWCRE	shortwave cloud radiative effect
SWOOSH	Stratospheric Water and OzOne Satellite Homogenized
SWOT	Surface Water and Ocean Topography
T	dry-bulb air temperature
T12	water vapor channel

T2	upper-tropospheric temperature
T2m	near-surface air temperature at ~1.5 m^{-2} m above the surface
TCWV	total column water vapor
TDX	TerraSAR-X add-on for Digital Elevation Measurement
Teq	equivalent temperature
TISA	Time Interpolated and Spatially Averaged
TLS	Lower-stratosphere temperatures
TMI	Tropical Rainfall Measuring Mission Microwave Imager
TOA	top-of-atmosphere
TOB	tropospheric ozone burden
Tq	latent temperature
TRISHNA	Thermal Infrared Imaging Satellite for High-resolution Natural Resource Assessment
TRMM	Tropical Rainfall Measuring Mission
TROPOMI	Tropospheric Monitoring Instrument
TSI	total solar irradiance
TSX	TerraSAR-X
TTT	tropical tropospheric temperatures
T_w	wet-bulb temperature
T_wN	minimum humid-heat intensity
TWS	terrestrial water storage
T_wX	humid-heat intensity
TXx	highest annual maximum temperature
U.K.	United Kingdom
U.S.	United States
UACO	Upper Atmosphere Composition Observations
UAHNMAT	University of Alabama in Huntsville Night Marine Air Temperature
UFS	Unified Forecast System
UGLOS	Upper Great Lakes Observing System
UK-SCAPE	United Kingdom Status, Change and Projections of the Environment
UNIS	University Centre in Svalbard
USA NPN	USA National Phenology Network
UT	upper troposphere
UTH	upper tropospheric humidity
UV	University of Valencia
VIIRS	Visible Infrared Imaging Radiometer Suite
VOC	volatile organic compound
VOD	vegetation optical depth
VODCA	Vegetation Optical Depth Climate Archive
VWC	vegetation water content
w.e.	water equivalent
WGMS	World Glacier Monitoring Service
WMO	World Meteorological Organization
WOUDC	World Ozone and Ultraviolet Radiation Data Centre
WV	water vapor
YM	yearly mean

Appendix 2: Datasets and sources

Section 2b Temperature			
Sub-section	**General Variable or Phenomenon**	**Specific Dataset or Variable**	**Source**
2b1	Temperature, [Near] Surface	Berkeley Earth	https://berkeleyearth.org/data/
2b1, 2b4, 2b7	Temperature, [Near] Surface	ERA5	https://www.ecmwf.int/en/forecasts/dataset/ecmwf-reanalysis-v5
2b1	Temperature, [Near] Surface	HadCRUT5	https://www.metoffice.gov.uk/hadobs/hadcrut5/
2b1	Temperature, [Near] Surface	Climatic Research Unit Temperature Version 5 (CRUTEM5)	https://www.metoffice.gov.uk/hadobs/crutem5/
2b1, 2b3	Temperature, [Near] Surface	Met Office Hadley Centre Sea Surface Temperature Dataset (HadSST) Version 4	https://www.metoffice.gov.uk/hadobs/hadsst4/
2b1, 2b4, 2b7	Temperature, [Near] Surface	Japanese Reanalysis for Three Quarters of a Century (JRA-3Q)	https://search.diasjp.net/en/dataset/JRA3Q
2b1, 2b2	Temperature, [Near] Surface	NASA/Goddard Institute for Space Studies (GISS) Global Temperature Version 4	https://data.giss.nasa.gov/gistemp/
2b1	Temperature, [Near] Surface	NOAA/NCEI NOAAGlobalTemp	https://www.ncei.noaa.gov/products/land-based-station/noaa-global-temp
2b2	Lake Temperature	Full Lake Surface Temperature Water Dataset	https://cds.climate.copernicus.eu/datasets/satellite-lake-water-temperature
2b2	Lake Temperature	National Buoy Data Center Great Lakes Buoys	https://www.ndbc.noaa.gov/mobile/region.php?reg=great_lakes
2b2	Lake Temperature	Balaton Lakes	https://odp.met.hu/climate/observations_hungary/hourly/historical/
2b2	Lake Temperature	Canadian Lakes	https://www.meds-sdmm.dfo-mpo.gc.ca/isdm-gdsi/waves-vagues/data-donnees/index-eng.asp
2b2	Lake Temperature	Biel and Thun Lakes (Switzerland); Biwa and Mikata Lakes (Japan)	https://portal.gemstat.org/applications/public.html?publicuser=PublicUser
2b2	Lake Temperature	Trout Lake	https://portal.edirepository.org/nis/metadataviewer?packageid=knb-lter-ntl.116.10
2b2	Lake Temperature	European Space Agency (ESA) Climate Change Initiative (CCI) LAKES Lake Surface Water Temperature (LSWT) Version 2.0.2	https://catalogue.ceda.ac.uk/uuid/a07deacaffb8453e93d57ee214676304

Sub-section	General Variable or Phenomenon	Specific Dataset or Variable	Source
2b3	Nighttime Marine Air Temperature	Climate Linked Atlantic Sector Science Night Marine Air Temperature (CLASSnmat)	https://catalogue.ceda.ac.uk/uuid/5bbf48b128bd488dbb10a56111feb36a
2b3	Nighttime Marine Air Temperature	University of Alabama in Huntsville Night Marine Air Temperature (UAHNMAT) Version 1	https://www.nsstc.uah.edu/climate/; https://doi.org/10.1002/joc.6354
2b4	Temperature, [Near] Surface	MERRA-2	https://gmao.gsfc.nasa.gov/gmao-products/merra-2/
2b4	Temperature, [Near] Surface	Global Historical Climatology Network Daily Extremes (GHCNDEX)	https://www.climdex.org/
2b5	Temperature, Upper Atmosphere	ERA5	https://www.ecmwf.int/en/forecasts/dataset/ecmwf-reanalysis-v5
2b5	Temperature, Upper Atmosphere	MERRA-2	https://gmao.gsfc.nasa.gov/gmao-products/merra-2/
2b5	Temperature, Upper Atmosphere	JRA-3Q	https://search.diasjp.net/en/dataset/JRA3Q
2b5	Temperature, Upper Atmosphere	NOAA National Environmental Satellite, Data, and Information Service (NESDIS) Center for Satellite Applications and Research (STAR) Microwave Sounding Unit (MSU) Version 5	https://www.star.nesdis.noaa.gov/data/mscat/MSU_AMSU_v5.0/Monthly_Atmospheric_Layer_Mean_Temperature/
2b5	Temperature, Upper Atmosphere	Radiosone Observation Correction Using Reanalyses (RAOBCORE) Radiosonde Innovation Composite Homogenization (RICH) Version 1.9	https://webdata.wolke.img.univie.ac.at/haimberger/v1.9/
2b5	Temperature, Upper Atmosphere	Radiosonde Atmospheric Temperature Products for Assessing Climate (RATPAC) A2	https://www.ncei.noaa.gov/products/weather-balloon/radiosonde-atmospheric-temperature-products
2b5	Temperature, Upper Atmosphere	Remote Sensing Systems (RSS) Version 4.0	https://www.remss.com/measurements/upper-air-temperature/
2b5	Temperature, Upper Atmosphere	University of Alabama in Huntsville (UAH) Microwave Sounding Unit (MSU) Version 6.1	https://www.nsstc.uah.edu/data/msu/v6.1/
2b5	Sea Surface Temperature	Niño 3.4 Index	https://psl.noaa.gov/data/timeseries/month/DS/Nino34_CPC/

Sub-section	General Variable or Phenomenon	Specific Dataset or Variable	Source
2b6	Temperature, Upper Atmosphere	Aura Microwave Limb Sounder (MLS)	https://discnrt1.gesdisc.eosdis.nasa.gov/data/Aura_MLS_NRT/ML2T_NRT.005/
2b7	Equivalent Temperature, [Near] Surface	Met Office Hadley Centre International Surface Dataset of Humidity Over Land (HadISDH.land).4.6.1.2024f	https://www.metoffice.gov.uk/hadobs/hadisdh/
2b7	Equivalent Temperature, [Near] Surface	ERA5	https://www.ecmwf.int/en/forecasts/dataset/ecmwf-reanalysis-v5

Section 2c Cryosphere

Sub-section	General Variable or Phenomenon	Specific Dataset or Variable	Source
2c1	Permafrost	Global Terrestrial Network for Permafrost (GTN-P)	http://gtnpdatabase.org/
2c1	Permafrost	GTN-P Global Mean Annual Ground Temperature Data for Permafrost	https://doi.org/10.1594/PANGAEA.884711
2c1	Permafrost	Permafrost Temperature at Chinese Qinghai–Tibet Plateau (QTP) Sites	https://nsidc.org/data/GGD700/versions/1
2c1	Permafrost	Permafrost Temperature in European Mountains	https://zenodo.org/records/13628540
2c1	Permafrost	Permafrost Temperature at French Sites	https://permafrance.osug.fr
2c1	Permafrost	Permafrost Temperature at Norwegian Sites	https://cryo.met.no/
2c1, 2c2	Permafrost	Permafrost Temperature at Swiss Sites (Swiss Permafrost Monitoring Network [PERMOS])	https://www.permos.ch; https://www.permos.ch/doi/permos-dataset-2022-1
2c1	Active Layer Depth	Circumpolar Active Layer Monitoring (CALM)	https://www.gwu.edu/~calm/
2c2	Rock Glacier Velocity	Regional Rock Glacier Velocity	Available from authors upon request. Austria: V. Kaufmann and A. Kellerer-Pirklbauer, Central Asia: A. Kääb, Dry Andes: S. Vivero, France: X. Bodin, D. Cusicanqui and E. Thibert, Switzerland: R. Delaloye, J. Noetzli and C. Pellet
2c3	Glacier Mass, Area or Volume	World Glacier Monitoring Service	https://dx.doi.org/10.5904/wgms-fog-2022-09
2c4	Lake Ice	ERA5	https://www.ecmwf.int/en/forecasts/dataset/ecmwf-reanalysis-v5

Sub-section	General Variable or Phenomenon	Specific Dataset or Variable	Source
2c4	Lake Ice	Lake Ice Clearance and Formation Data for Green Lakes Valley, 1968—Ongoing. Version 6. Environmental Data Initiative	https://doi.org/10.6073/pasta/e89a9a6984ebbcdbbc85c16d65298dd2
2c4	Lake Ice	Global Lake and River Ice Phenology Database, Version 1	https://doi.org/10.7265/N5W66HP8
2c4	Lake Ice	Mountain Lake Biology, Chemistry, Physics, and Climate Data Since 1959 at Castle Lake Version 1. Environmental Data Initiative	https://doi.org/10.6073/pasta/a8e3b81cfe5864731b29ad42506c65d7
2c4	Lake Ice	Great Lakes Annual Maximum Ice Cover (%)	https://www.glerl.noaa.gov/data/ice/
2c4	Lake Ice	Great Lakes Ice	https://www.glerl.noaa.gov/data/ice
2c4	Lake Ice	Geographic Variation and Temporal Trends in Ice Phenology in Norwegian Lakes During a Century, Dryad	https://datadryad.org/stash/dataset/doi:10.5061/dryad.bk3j9kd9x
2c4	Lake Ice	Lake Surface Water Temperature and Ice Cover in Subalpine Lake Lunz, Austria	https://doi.org/10.1080/20442041.2017.1294332
2c4	Temperature, [Near] Surface	NASA/Goddard Institute for Space Studies (GISS) Global Temperature	https://data.giss.nasa.gov/gistemp/
2c5	Snow Properties	Northern Hemisphere (NH) Snow Cover Extent (SCE) Version 1	https://doi.org/10.7289/V5N014G9; https://www.snowcover.org

Section 2d Hydrological cycle			
Sub-section	**General Variable or Phenomenon**	**Specific Dataset or Variable**	**Source**
2d1	Humidity, [Near] Surface	ERA5	https://www.ecmwf.int/en/forecasts/dataset/ecmwf-reanalysis-v5
2d1, 2d2	Humidity, [Near] Surface	Met Office Hadley Centre Integrated Surface Dataset of Humidity over Land (HadISDH.land.4.6.1.2024f), Met Office HadISDH over Ocean (HadISDH.marine.1.6.1.2024), Met Office HadISDH over Land and Ocean (HadISDH.blend.1.5.1.2024f), Met Office HadISDH of Humidity Extremes (HadISDH.extremes.1.2.0.2024f)	https://www.metoffice.gov.uk/hadobs/hadisdh
2d1	Humidity, [Near] Surface	Japanese Reanalysis for Three Quarters of a Century (JRA-3Q)	https://jra.kishou.go.jp/JRA-3Q/index_en.html
2d1	Humidity, [Near] Surface	MERRA-2	https://disc.gsfc.nasa.gov/datasets/M2T1NXSLV_5.12.4/summary
2d3	Water Vapor, Total Column	Constellation Observing System for Meteorology, Ionosphere and Climate (COSMIC)	https://cdaac-www.cosmic.ucar.edu/
2d3	Water Vapor, Total Column	ERA5	https://www.ecmwf.int/en/forecasts/dataset/ecmwf-reanalysis-v5
2d3	Water Vapor, Total Column	Global Navigation Satellite System (GNSS) Ground-Based Total Column Water Vapor	https://doi.org/10.25326/68
2d3	Water Vapor, Total Column	JRA-3Q	https://jra.kishou.go.jp/JRA-3Q/index_en.html
2d3	Water Vapor, Total Column	MERRA-2	https://gmao.gsfc.nasa.gov/gmao-products/merra-2/
2d3	Water Vapor, Total Column	Special Sensor Microwave Imager (SSM/I)–Advanced Microwave Scanning Radiometer for Earth Observing System (AMSR-E) Ocean Total Column Water Vapor	https://www.remss.com
2d4	Humidity, Upper Atmosphere	Upper-Troposphere Humidity (UTH)	Available on request to Brian Soden (bsoden@miami.edu)
2d4	Humidity, Upper Atmosphere	ERA5	https://www.ecmwf.int/en/forecasts/dataset/ecmwf-reanalysis-v5
2d4	Humidity, Upper Atmosphere	High Resolution Infrared Sounder (HIRS)	https://www.ncei.noaa.gov/products/climate-data-records/hirs-ch12-brightness-temperature

Sub-section	General Variable or Phenomenon	Specific Dataset or Variable	Source
2d4	Temperature, Upper Atmosphere	NOAA National Environmental Satellite, Data, and Information Service (NESDIS) Center for Satellite Applications and Research (STAR) Microwave Sounding Unit (MSU) Version 5	https://www.star.nesdis.noaa.gov/pub/smcd/emb/mscat/data/MSU_AMSU_v5.0/Monthly_Atmospheric_Layer_Mean_Temperature/
2d5, 2d6	Precipitation	Global Precipitation Climatology Centre (GPCC)	https://www.dwd.de/EN/ourservices/gpcc/gpcc.html
2d5	Precipitation	GPCPv2.3	https://www.ncei.noaa.gov/products/global-precipitation-climatology-project; https://rda.ucar.edu/datasets/d728008/dataaccess/
2d6	Precipitation	Multi-Source Weighted-Ensemble Precipitation (MSWEP)	https://www.gloh2o.org/mswep/
2d6	Precipitation	Met Office Hadley Centre Dataset of Extreme Indices (HadEX3) Version 3	https://www.metoffice.gov.uk/hadobs/hadex3/
2d6	Precipitation	ERA5	https://cds.climate.copernicus.eu/datasets/reanalysis-era5-single-levels
2d6	Precipitation	Global Historical Climatology Network Daily Extremes (GHCNDEX)	https://www.climdex.org
2d6	Precipitation	MERRA-2	https://gmao.gsfc.nasa.gov/gmao-products/merra-2/ https://disc.gsfc.nasa.gov/datasets/M2SMNXEDI_2/summary
2d7	Cloud properties	PATMOS-xv6.0	https://www.ncei.noaa.gov/products/climate-data-records/avhrr-hirs-cloud-properties-patmos
2d7	Cloud Properties	Clouds and the Earth's Radiant Energy System Energy Balance and Filled (CERES EBAF) Version 4.2	https://ceres.larc.nasa.gov/data/
2d8	Lake Water Storage and Level	'GloLakes' Lake and Reservoir Storage	https://doi.org/10.5194/essd-16-201-2024
2d8	Lake Water Storage and Level	Global Lakes and Reservoir Monitor (GREALM) Lake Level	https://ipad.fas.usda.gov/cropexplorer/global_reservoir/
2d9	River Discharge	Global Flood Awareness System Version (GloFAS) 4	https://ewds.climate.copernicus.eu/datasets/cems-glofas-historical; https://data.jrc.ec.europa.eu/dataset/68050d73-9c06-499c-a441-dc5053cb0c86
2d9	River Discharge	ERA5	https://cds.climate.copernicus.eu/datasets/reanalysis-era5-single-levels
2d10	Groundwater and Terrestrial Water Storage	Gravity Recovery and Climate Experiment (GRACE)/GRACE Follow-On (GRACE-FO)	https://podaac.jpl.nasa.gov/dataset/TELLUS_GRAC-GRFO_MASCON_CRI_GRID_RL06.3_V4

Sub-section	General Variable or Phenomenon	Specific Dataset or Variable	Source
2d11	Soil Moisture	Copernicus Climate Change Service (C3S) Version 202012 product based on the ESA Climate Change Initiative for Soil Moisture (ESA CCI SM) Version 05.2 Merging Algorithm	https://cds.climate.copernicus.eu/datasets/satellite-soil-moisture
2d12	Drought	Climatic Research Unit Gridded Time Series (CRU TS) 4.09	https://crudata.uea.ac.uk/cru/data/drought/
2d13	Land Evaporation	Global Land Evaporation Amsterdam Model (GLEAM)	https://www.gleam.eu/
2d13	Modes of Variability	Niño 3.4 index	https://psl.noaa.gov/data/timeseries/month/DS/Nino34

Section 2e Atmospheric circulation

Sub-section	General Variable or Phenomenon	Specific Dataset or Variable	Source
2e1, 2e3	Modes of Variability	Antarctic Oscillation (AAO)/Southern Annular Mode (SAM)	https://ftp.cpc.ncep.noaa.gov/cwlinks/norm.daily.aao.index.b790101.current.ascii
2e1	Pressure, Sea Level or Near-Surface	ERA5	https://www.ecmwf.int/en/forecasts/dataset/ecmwf-reanalysis-v5
2e2	Wind, [Near] Surface	ERA5	https://www.ecmwf.int/en/forecasts/dataset/ecmwf-reanalysis-v5
2e2	Wind, [Near] Surface	Met Office Hadley Centre Integrated Surface Dataset (HadISD) Version v3.4.1.2024f	https://hadleyserver.metoffice.gov.uk/hadisd/v341_2024f/index.html
2e2	Wind, [Near] Surface	Global Historical Climate Network hourly (GHCNh)	https://www.ncei.noaa.gov/products/global-historical-climatology-network-hourly
2e2	Wind, [Near] Surface	MERRA-2	https://gmao.gsfc.nasa.gov/gmao-products/merra-2/
2e2	Wind, [Near] Surface	Remote Sensing System (RSS) Merged 1-Degree Monthly Radiometer Winds	https://www.remss.com/measurements/wind/
2e2	Wind, [Near] Surface	Remote Sensing System (RSS) Advanced Scatterometer (ASCAT)	https://www.remss.com/missions/ascat/
2e2	Wind, [Near] Surface	Remote Sensing System (RSS) QuickScat4	https://www.remss.com/missions/qscat/
2e3	Modes of Variability	Pacific Decadal Oscillation	https://psl.noaa.gov/data/timeseries/month/data/pdo.timeseries.sstens.data

Sub-section	General Variable or Phenomenon	Specific Dataset or Variable	Source
2e3	Wind, [Upper Atmosphere]	Quasi-biennial Oscillation (QBO)	https://www.atmohub.kit.edu/data/singapore2023.dat
2e3	Wind, [Upper Atmosphere]	ERA5 Hourly Data on Pressure Levels from 1940 to Present. Copernicus Climate Change Service (C3S) Climate Data Store (CDS)	https://cds.climate.copernicus.eu/datasets/reanalysis-era5-single-levels
2e3	Wind, [Upper Atmosphere]	MERRA-2	https://gmao.gsfc.nasa.gov/gmao-products/merra-2/
2e3	Wind, [Upper Atmosphere]	Japanese 55-Year Reanalysis (JRA-55) Atmospheric Reanalysis	https://jra.kishou.go.jp/JRA-55/index_en.html
2e3	Wind, [Upper Atmosphere]	Japanese Reanalysis for Three-Quarters of a Century (JRA-3Q)	https://jra.kishou.go.jp/JRA-3Q/index_en.html
2e4	Lightning	European Organisation for the Exploitation of Meteorological Satellites (EUMETSAT)	https://www.eumetsat.int/features/animations-europes-first-lightning-imager; https://user.eumetsat.int/news-events/news/mtg-lightning-imager-li-level-2-data-available

Section 2f Earth's radiation budget

Sub-section	General Variable or Phenomenon	Specific Dataset or Variable	Source
2f1	TOA Earth Radiation Budget	Clouds and the Earth's Radiant Energy System (CERES) Energy Balanced and Filled (EBAF) Version 4.2.1	https://ceres-tool.larc.nasa.gov/ord-tool/jsp/EBAFTOA421Selection.jsp
2f1	TOA Earth Radiation Budget	CERES Fast Longwave And Shortwave Radiative Fluxes (FLASHflux) Version 4C	https://ceres-tool.larc.nasa.gov/ord-tool/jsp/FLASH_TISASelection.jsp
2f1	TOA Earth Radiation Budget	Community-Consensus Total Solar Irradiance (TSI) Composit	https://spot.colorado.edu/~koppg/TSI/TSI_Composite-SIST.txt
2f2	Solar Transmission, Apparent	Mauna Loa Observatory	https://www.esrl.noaa.gov/gmd/webdata/grad/mloapt/mauna_loa_transmission.dat
2f2	Aerosol Optical Depth	NASA's Moderate Resolution Imaging Spectroradiometer (MODIS)	https://earthobservatory.nasa.gov/global-maps/MODAL2_M_AER_OD
2f2	Aerosol Optical Depth	Copernicus Atmosphere Monitoring Service (CAMS)	https://atmosphere.copernicus.eu/south-america-sees-historic-emissions-during-2024-wildfire-season

Sub-section	General Variable or Phenomenon	Specific Dataset or Variable	Source
2f2	Aerosol Extinction Coefficient	Stratospheric Aerosol and Gas Experiment (SAGE) Limb Sounder	https://sage.nasa.gov/2024/09/sage-iii-iss-science-highlight/
2f2	Stratospheric Aerosol Loadings	Balloon Network for Stratospheric Aerosol Observations (BalNeO)	https://science.larc.nasa.gov/balneo/
2f2	Stratospheric Aerosol Loadings	Balloon Baseline Stratospheric Aerosol Profiles (B2SAP)	https://csl.noaa.gov/projects/b2sap/pops.php?loc=HIH

Section 2g Atmospheric composition

Sub-section	General Variable or Phenomenon	Specific Dataset or Variable	Source
2g1	Trace Gases	Atmospheric Gas Trends	https://gml.noaa.gov/ccgg/trends/
2g1	Trace Gases	Global Greenhouse Gas Reference Network	https://gml.noaa.gov/ccgg/about.html
2g1	Trace Gases	Atmospheric Greenhouse Gas Index (AGGI)	https://gml.noaa.gov/ccgg/trends/
2g2	Trace Gases	Halocarbons and Other Atmospheric Trace Species	https://gml.noaa.gov/hats/data.html
2g2	Trace Gases	Ozone-Depleting Gas Index (ODGI)	https://gml.noaa.gov/odgi/
2g3	Aerosols	Copernicus Atmosphere Monitoring Service Reanalysis (CAMSRA)	https://www.ecmwf.int/en/research/climate-reanalysis/cams-reanalysis
2g4	Ozone, Surface	NOAA Global Monitoring Laboratory	https://gml.noaa.gov/aftp/data/ozwv/SurfaceOzone/
2g4	Ozone, Tropospheric	Ozone Monitoring Instrument (OMI)/ Microwave Limb Sounder (MLS)	https://acdb-ext.gsfc.nasa.gov/Data_services/cloud_slice/; https://avdc.gsfc.nasa.gov/
2g5	Stratospheric Aerosols	Haute-Provence Observatory (OHP) Lidar Temperature Aerosol (LTA) Lidar	https://www-air.larc.nasa.gov/missions/ndacc/data.html?station=haute.provence/ames/lidar/
2g5	Stratospheric Aerosols	Stratospheric Ozone Lidar at Haute-Provence Observatory (LiO3S)	https://www-air.larc.nasa.gov/missions/ndacc/data.html?station=haute.provence/ames/lidar/
2g5	Stratospheric Aerosols	Lauder Aerosol Lidar	https://www-air.larc.nasa.gov/missions/ndacc/data.html?station=lauder/ames/lidar/

Sub-section	General Variable or Phenomenon	Specific Dataset or Variable	Source
2g5	Stratospheric Aerosols	Stratospheric Aerosol and Gas Experiment III (SAGE III) Version 5.3	https://asdc.larc.nasa.gov/project/SAGE%20III-ISS/g3bssp_53
2g5	Stratospheric Aerosols	Global Space-based Stratospheric Aerosol Climatology (GloSSAC) Version 2	https://asdc.larc.nasa.gov/project/GloSSAC
2g5	Stratospheric Aerosols	Ozone Mapping and Profiler Suite Limb Profiler (OMPS-LP) Version 2.1	https://disc.gsfc.nasa.gov/datasets/OMPS_NPP_LP_L2_AER_DAILY_2/summary
2g6	Ozone, Total Column and Stratospheric	Global Ozone Monitoring Experiment (GOME)/ Scanning Imaging Absorption Spectrometer for Atmospheric Cartography (SCIAMACHY)/GOME2 (GSG) Merged Total Ozone	https://www.iup.uni-bremen.de/UVSAT/data/wfdoas/
2g6	Ozone, Total Column and Stratospheric	GOME/SCIAMACHY/GOME2 (GTO) Merged Total Ozone	https://atmos.eoc.dlr.de/app/products/gto-ecv
2g6	Ozone, Total Column and Stratospheric	Global Ozone Chemistry and Related Trace Gas Data Records (GOZCARDS) Ozone Profiles	https://disc.gsfc.nasa.gov/datasets/GozMmlpO3_1/summary
2g6	Ozone, Total Column and Stratospheric	Multi Sensor Reanalysis (MSR-2) of Total Ozone	https://www.temis.nl/protocols/O3global.html
2g6	Ozone, Total Column and Stratospheric	NASA Backscatter Ultraviolet Radiometer (BUV)/Solar Backscatter Ultraviolet Radiometer (SBUV)/Ozone Mapping and Profiler Suite (OMPS) Version 8.7 (MOD) Merged Ozone	https://acd-ext.gsfc.nasa.gov/Data_services/merged/
2g6	Ozone, Total Column and Stratospheric	NOAA SBUV V8.6 OMPS V4r1 Cohesive Dataset (COH)	https://ftp.cpc.ncep.noaa.gov/SBUV_CDR/
2g6	Ozone, Total Column and Stratospheric	Network for the Detection of Atmospheric Composition Change (NDACC) Lidar, Microwave, and Fourier Transform Infrared Spectroscopy (FTIR)	https://www-air.larc.nasa.gov/missions/ndacc
2g6	Ozone, Total Column and Stratospheric	Chemistry-Climate Model Initiative (CCMI)-2022 Model Runs	https://blogs.reading.ac.uk/ccmi/ccmi-2022/
2g6	Ozone, Total Column and Stratospheric	SAGE-Climate Change Initiative (CCI)-OMPS	https://climate.esa.int/en/projects/ozone/data

Sub-section	General Variable or Phenomenon	Specific Dataset or Variable	Source
2g6	Ozone, Total Column and Stratospheric	SAGE/Origins, Spectral Interpretation, Resource Identification, and Security (OSIRIS)	https://doi.org/10.5194/amt-11-489-2018 https://research-groups.usask.ca/osiris/
2g6	Ozone, Total Column and Stratospheric	SAGE-SCIA-OMPS	https://doi.org/10.5194/amt-2018-275 https://www.iup.uni-bremen.de/DataRequest/
2g6	Ozone, Total Column and Stratospheric	Stratospheric Water and Ozone Satellite Homogenized (SWOOSH)	https://csl.noaa.gov/groups/csl8/swoosh/
2g6	Ozone, Total Column and Stratospheric	World Ozone and Ultraviolet Radiation Data Centre (WOUDC) Ground-Based Ozone	https://woudc.org/data/dataset_info.php?id=totalozone
2g7	Stratospheric Water Vapor	The Aura Microwave Limb Sounder Version 5.0 Data, as Merged Into SWOOSH	https://csl.noaa.gov/groups/csl8/swoosh/
2g7	Tropopause Temperature	MERRA-2	https://gmao.gsfc.nasa.gov/gmao-products/merra-2/
2g7	Stratospheric Water Vapor	NOAA Frostpoint Hygrometer (FPH)	https://gml.noaa.gov/aftp/data/ozwv/WaterVapor/
2g7	Stratospheric Water Vapor	Cryogenic Frostpoint Hygrometer (CFH)	https://ndacc.org
2g8	Trace Gases	Copernicus Atmosphere Monitoring Service Reanalysis (CAMSRA) for Carbon Monoxide	https://ads.atmosphere.copernicus.eu/datasets/cams-global-radiative-forcing-auxilliary-variables?tab=overview

Section 2h Land surface properties

Sub-section	General Variable or Phenomenon	Specific Dataset or Variable	Source
2h1	Albedo	Moderate Resolution Imaging Spectroradiometer (MODIS)/Terra+Aqua Bidirectional Reflectance Distribution Function (BDRF)/Albedo Albedo Daily L3 Global 0.05 Deg Climate Modeling Grid (CMG) Version 061	https://www.earthdata.nasa.gov/centers/lp-daac
2h1	Albedo	VIIRS VNP43C3 Collection 1.0	https://www.earthdata.nasa.gov/centers/lp-daac

Sub-section	General Variable or Phenomenon	Specific Dataset or Variable	Source
2h2	Fraction of Absorbed Photosynthetically Active Radiation (FAPAR)	Joint Research Centre (JRC) Two-Stream Inversion Package (TIP) MODIS	https://fapar.jrc.ec.europa.eu
2h2	FAPAR	Medium Resolution Imaging Spectrometer (MERIS)	https://fapar.jrc.ec.europa.eu
2h2	FAPAR	Sea-Viewing Wide Field-of-View Sensor (SeaWIFS) FAPAR	https://fapar.jrc.ec.europa.eu/
2h2	FAPAR	Ocean and Land Colour Instrument (OLCI)	https://dataspace.copernicus.eu/
2h3	Biomass, Greenness or Burning	Global Fire Assimilation System Version (GFAS) 1.2	https://ads.atmosphere.copernicus.eu/cdsapp#!/dataset/cams-global-fire-emissions-gfas v1.4 available upon request
2h3	Biomass, Greenness or Burning	Global Fire Emissions Database	https://www.globalfiredata.org/data.html
2h4	Phenology	MODIS Normalized Difference Vegetative Index (NDVI)	https://modis.gsfc.nasa.gov/data/dataprod/mod13.php
2h4	Temperature [Near] Surface	MERRIS-2 Monthly Temperature	https://goldsmr4.gesdisc.eosdis.nasa.gov/data/MERRA2_MONTHLY/M2TMNXLND.5.12.4/
2h4	Phenology	USA-National Phenology Network (NPN) Phenology Data	https://www.usanpn.org/data/observational
2h4	Phenology	USA-National Phenology Network (NPN) Spring Index Raster Data Products	https://data.usanpn.org/geoserver-request-builder/
2h4	Phenology	German Oak Phenology Data	https://opendata.dwd.de/
2h4	Phenology	Harvard Forest	https://harvardforest1.fas.harvard.edu/exist/apps/datasets/showData.html?id=hf003
2h4	Phenology	Natures Calendar	https://naturescalendar.woodlandtrust.org.uk/
2h4	Phenology	PhenoCam	https://phenocam.sr.unh.edu
2h4	Phenology	UK Cumbrian Lakes Data	https://catalogue.ceh.ac.uk/documents/bf30d6aa-345a-4771-8417-ffbcf8c08c28/
2h4	Phenology	UK Loch Leven	https://catalogue.ceh.ac.uk/documents/ac973b0d-2c99-4e00-8931-22aa0881006d
2h4	Phenology	Dutch Oak Phenology Data	https://www.natuurkalender.nl/
2h4	Phenology	Lakes Geneva and Bourget Data	https://si-ola.inrae.fr/si_lacs/login.jsf

Sub-section	General Variable or Phenomenon	Specific Dataset or Variable	Source
2h5	Vegetation Optical Depth	Global Long-term Microwave Vegetation Optical Depth Climate Archive Version 2 (VODCAv2)	https://researchdata.tuwien.ac.at/records/t74ty-tcx62
2h5	Modes of Variability	Niño 3.4 Index	https://psl.noaa.gov/data/timeseries/month/DS/Nino34

Sidebar 2.1 Super extreme land surface temperature hotspots

Sub-section	General Variable or Phenomenon	Specific Dataset or Variable	Source
SB2.1	Temperature [Near] Surface	Climatic Research Unit Temperature Version 5 (CRUTEM5)	https://www.metoffice.gov.uk/hadobs/crutem5/
SB2.1	Temperature [Near] Surface	Centre for Environmental Data Analysis (CEDA) Archive, European Space Agency (ESA) Land Surface Temperature Climate Change Initiative (LST_cci)—Sea and Land Surface Temperature Radiometer Onboard the Sentinel-3B Platform (SLSTR-B)	https://catalogue.ceda.ac.uk/uuid/5f66a881adf846bfaad58b0e6068f0ea/
SB2.1	Temperature [Near] Surface	CEDA Archive, Earth Observation Climate Information Service (EOCIS)—SLSTR-B	https://catalogue.ceda.ac.uk/uuid/fc0bc3d5887d441296091a8025f8f45d/

Sidebar 2.2 Short-lived greenhouse gases

Sub-section	General Variable or Phenomenon	Specific Dataset or Variable	Source
SB2.2	Trace Gases [NH3]	Cross-track Infrared Sounder (CrIS) Column NH3	https://doi.org/10.5067/7I3KMUCCJNEN
SB2.2	Trace Gases [PAN]	CrIS Partial Column Acyl Peroxynitrates (PANs) Data	https://doi.org/10.5067/W0W6L8M6J85X
SB2.2	Total Column Ozone	Ozone Mapping and Profiler Suite (OMPS) Satellite Instrument Data	https://www.ncei.noaa.gov/metadata/geoportal/rest/metadata/item/gov.noaa.ncdc%3AC01464/html

Appendix 3: Supplemental materials

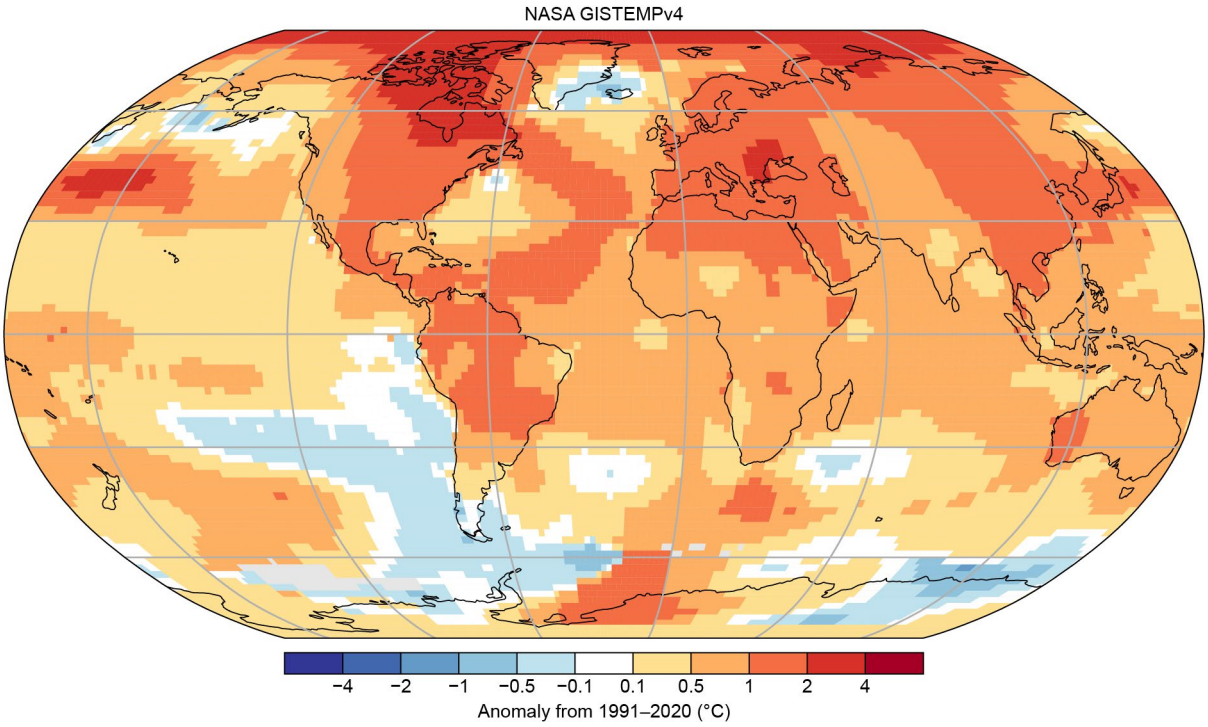

Fig. A2.1. Global surface temperature anomalies (°C). (Source: NASA Goddard Institute for Space Studies Surface Temperature Analysis version 4 [GISTEMPv4].)

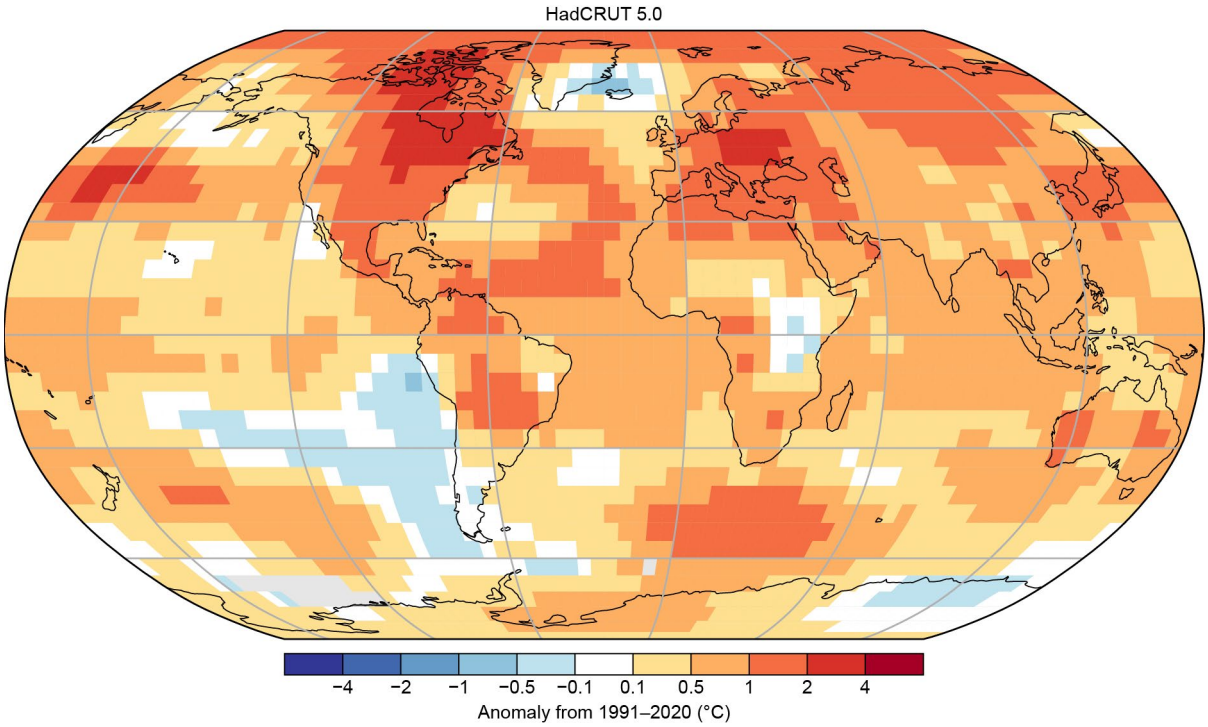

Fig. A2.2. Global surface temperature anomalies (°C). (Source: HadCRUTS.)

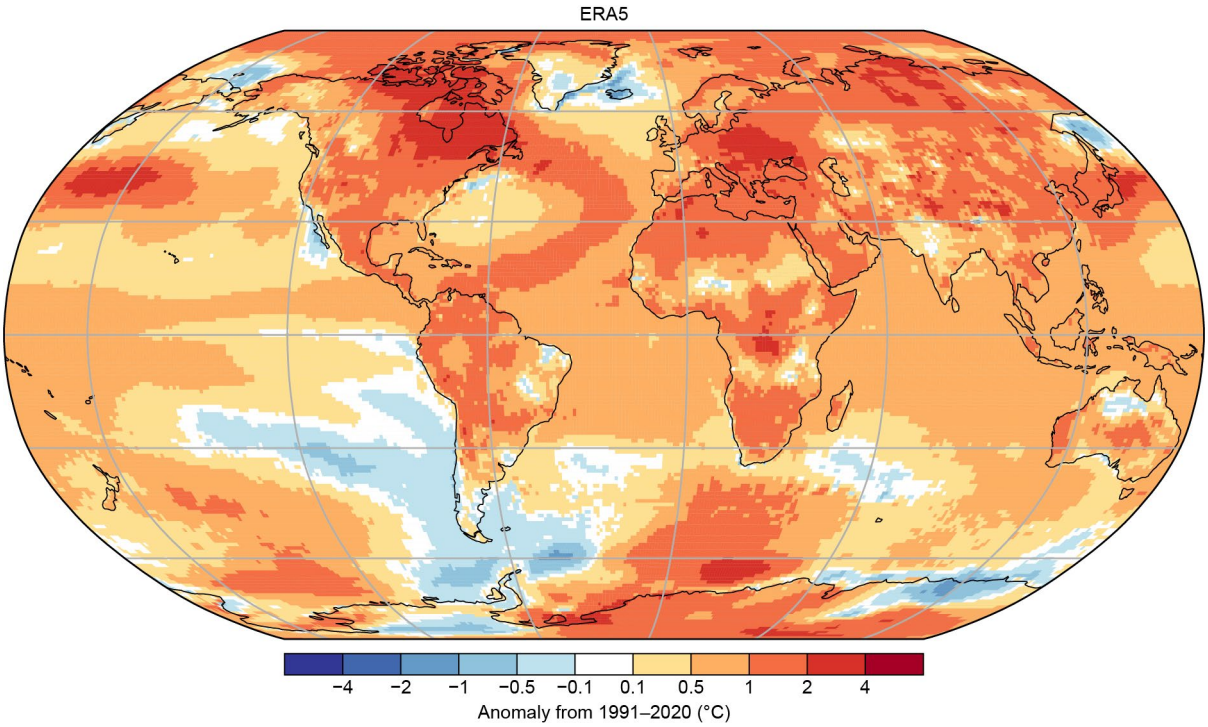

Fig. A2.3. Global surface temperature anomalies (°C). (Source: ERA5.)

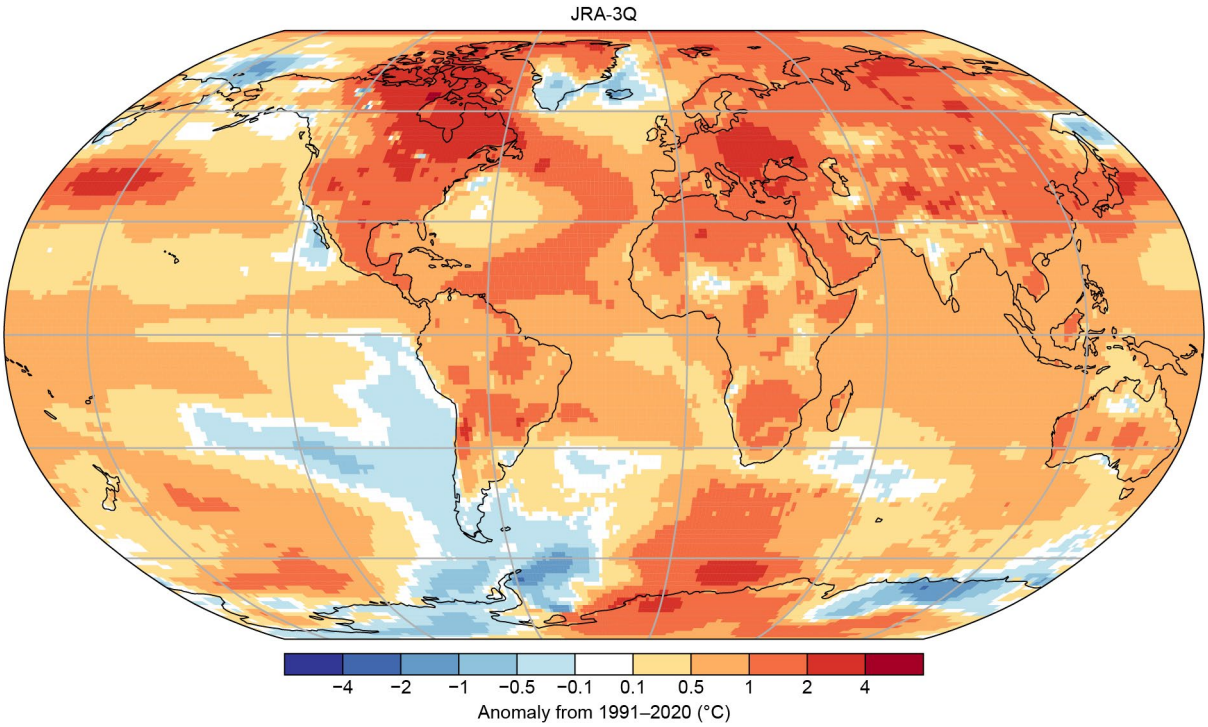

Fig. A2.4. Global surface temperature anomalies (°C). (Source: Japanese Reanalysis for Three Quarters of a Century [JRA-3Q].)

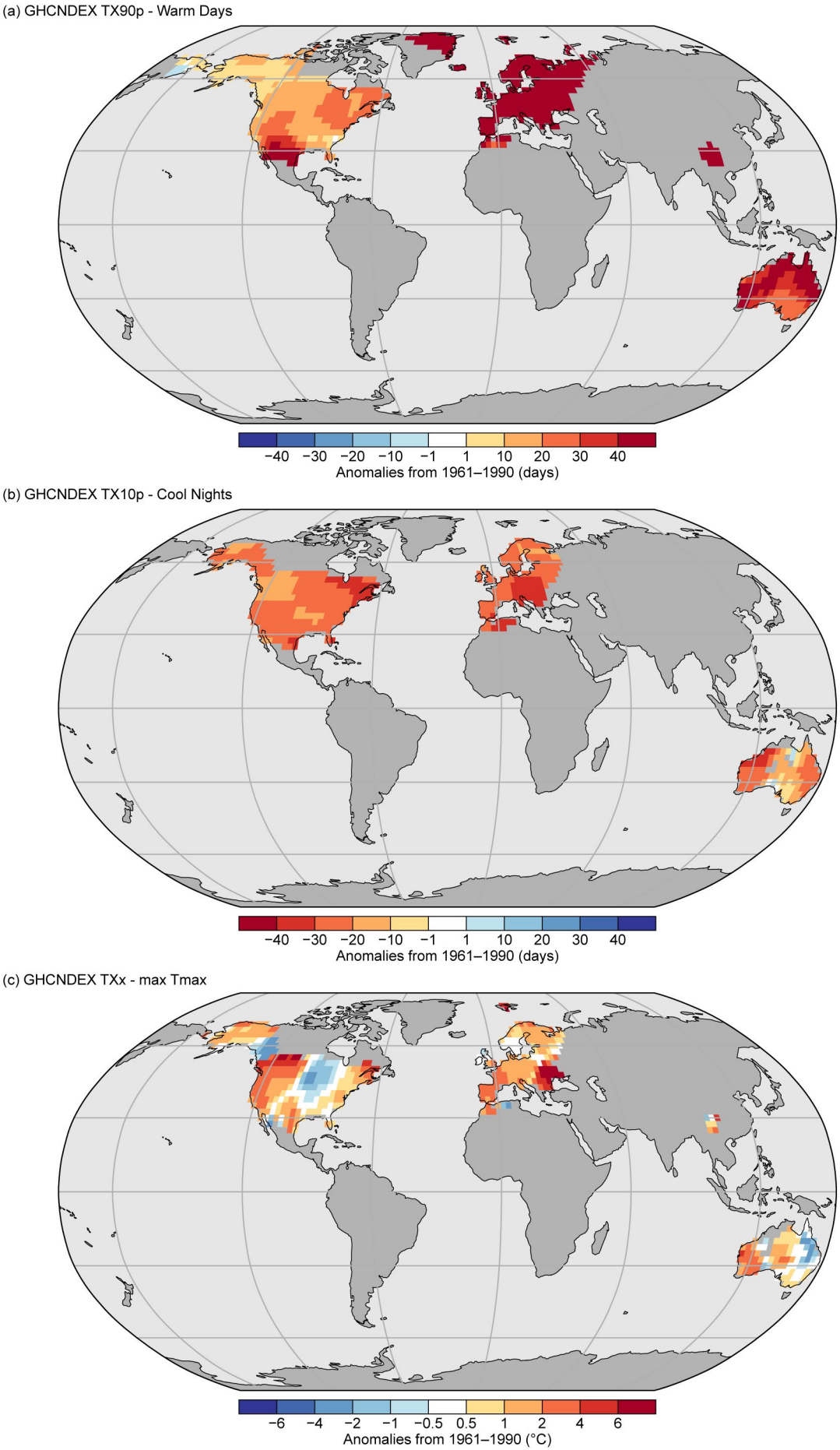

Fig. A2.5. Global Historical Climatology Network Daily Extremes (GHCNDEX) (a) warm day threshold exceedance (TX90p), (b) cool night threshold exceedance (TN10p), and (c) annual highest daily maximum temperature (TXx).

Table A2.1. Ten highest annual global equivalent temperature anomalies (Teq) and their constituent parts (air temperature [Ta]; latent temperature [Tq]) in °C (1991–2020 base period) since 1979 for ERA5.

Rank	Ta Year	Ta (°C)	Tq Year	Tq (°C)	Teq (Year)	Teq (°C)
1	2024	0.72	2024	0.85	2024	1.57
2	2023	0.60	2023	0.59	2023	1.19
3	2016	0.44	2016	0.50	2016	0.94
4	2020	0.43	2019	0.44	2019	0.84
5	2019	0.40	2020	0.38	2020	0.82
6	2017	0.34	2017	0.33	2017	0.68
7	2022	0.30	1998	0.27	2015	0.53
8	2021	0.27	2015	0.27	2018	0.52
9	2018	0.26	2018	0.25	2021	0.41
10	2015	0.26	2010	0.15	2022	0.40

Table A2.2. Ten highest annual global equivalent temperature anomalies (Teq) and their constituent parts (air temperature [Ta]; latent temperature [Tq]) in °C (1991–2020 base period) since 1979 for the Japanese Reanalysis for Three Quarters of a Century (JRA-3Q).

Rank	Ta Year	Ta (°C)	Tq Year	Tq (°C)	Teq (Year)	Teq (°C)
1	2024	0.67	2024	0.98	2024	1.65
2	2023	0.57	2023	0.74	2023	1.30
3	2016	0.42	2016	0.45	2016	0.86
4	2020	0.38	2020	0.41	2020	0.79
5	2019	0.36	1998	0.33	2019	0.68
6	2017	0.30	2019	0.32	2017	0.52
7	2015	0.25	2015	0.24	2015	0.49
8	2022	0.24	2017	0.23	2022	0.44
9	2018	0.22	2022	0.21	2021	0.38
10	2021	0.19	2021	0.19	1998	0.36

Table A2.3. Top ten ranked global equivalent temperature anomalies (Teq) and their constituent parts (air temperature [Ta]; latent temperature [Tq]) in °C (1991–2020 base period) since 1979 for the Met Office Hadley Centre Integrated Surface Dataset of Humidity (HadISDH; land-only).

Rank	Ta Year	Ta (°C)	Tq Year	Tq (°C)	Teq (Year)	Teq (°C)
1	2024	0.96	2024	1.13	2024	2.04
2	2023	0.74	2023	0.74	2023	1.49
3	2020	0.58	2016	0.61	2016	1.14
4	2016	0.55	1998	0.58	2020	1.03
5	2019	0.44	2020	0.46	1998	0.72
6	2015	0.42	2010	0.35	2017	0.67
7	2017	0.39	2022	0.31	2019	0.64
8	2021	0.37	2017	0.29	2021	0.63
9	2022	0.33	2021	0.27	2022	0.62
10	2018	0.24	2019	0.21	2015	0.60

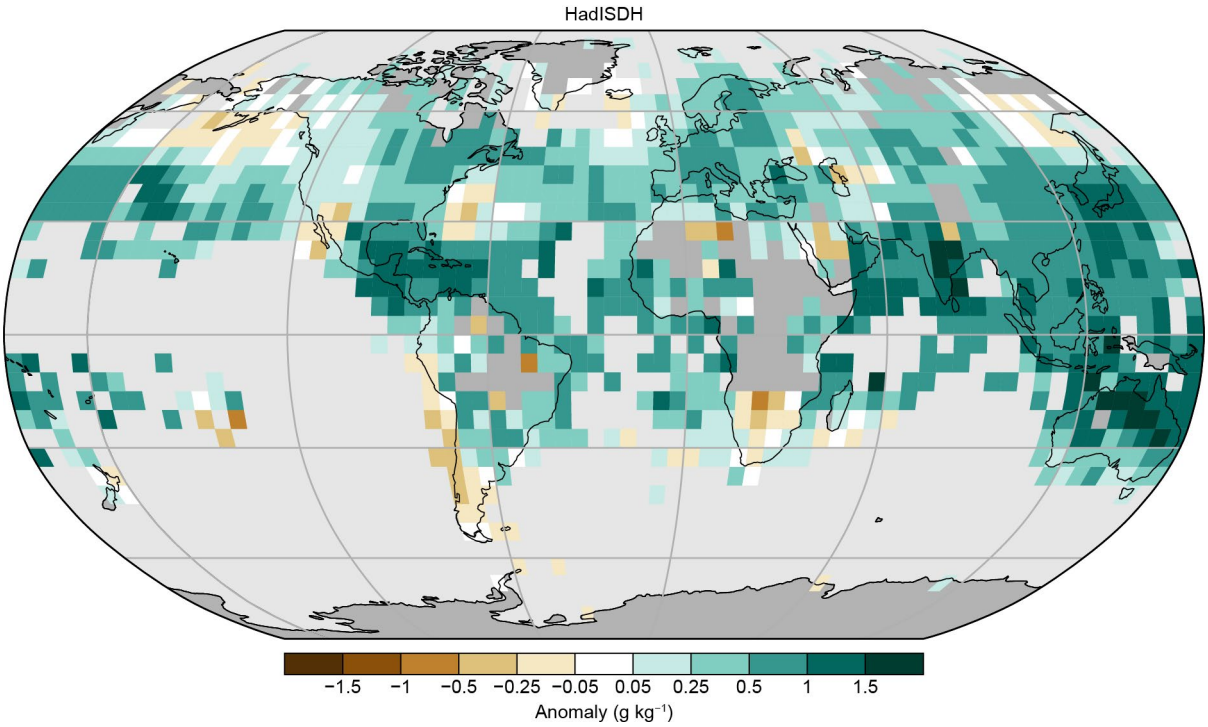

Fig. A2.6. Surface specific humidity anomaly (g kg^{-1}) relative to 1991–2020 from Met Office Hadley Centre Integrated Surface Dataset of Humidity Blend (HadISDH.blend.1.5.1.2024f).

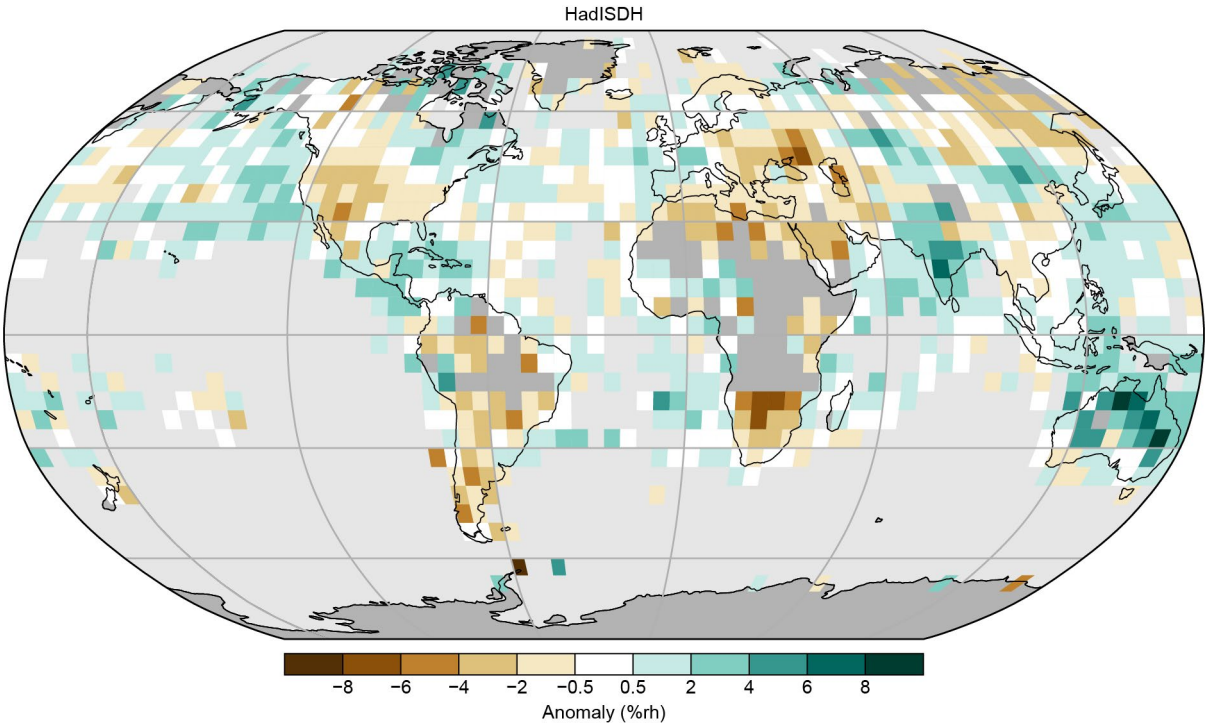

Fig. A2.7. Surface relative humidity anomaly (%rh) relative to 1991–2020 from Met Office Hadley Centre Integrated Surface Dataset of Humidity over Land and Ocean (HadISDH.blend.1.5.1.2024f).

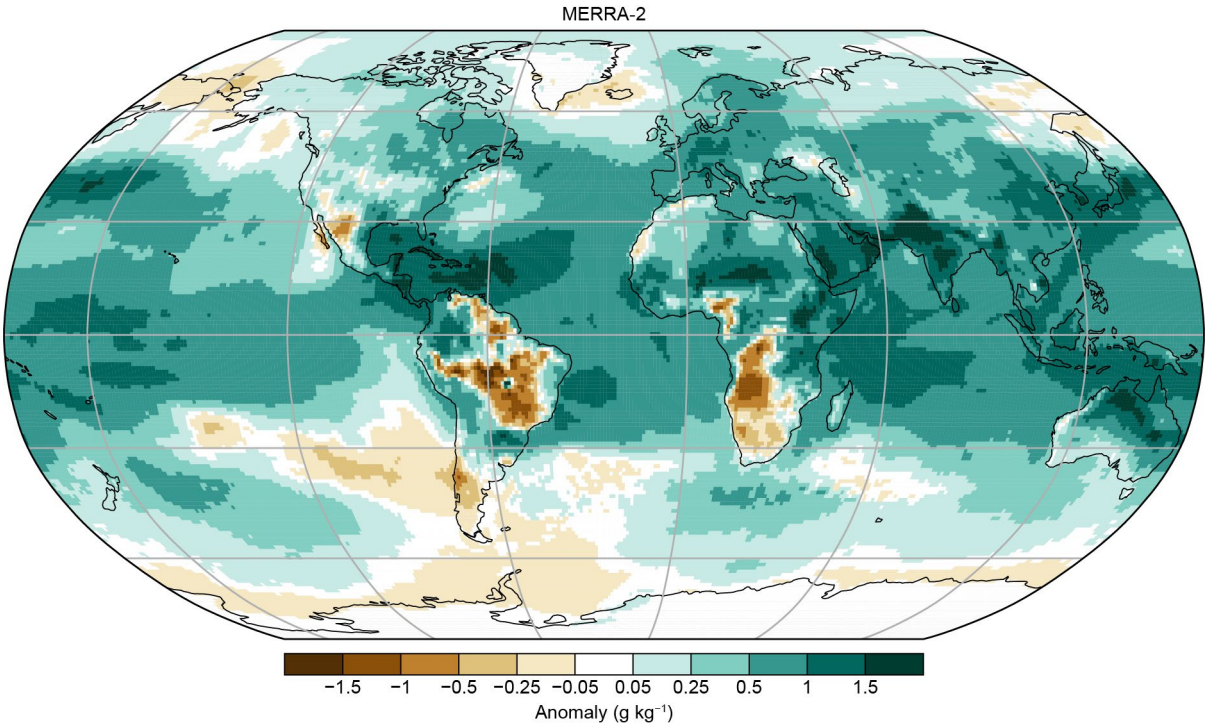

Fig. A2.8. Surface specific humidity anomaly (g kg^{-1}) relative to 1991–2020 from MERRA-2.

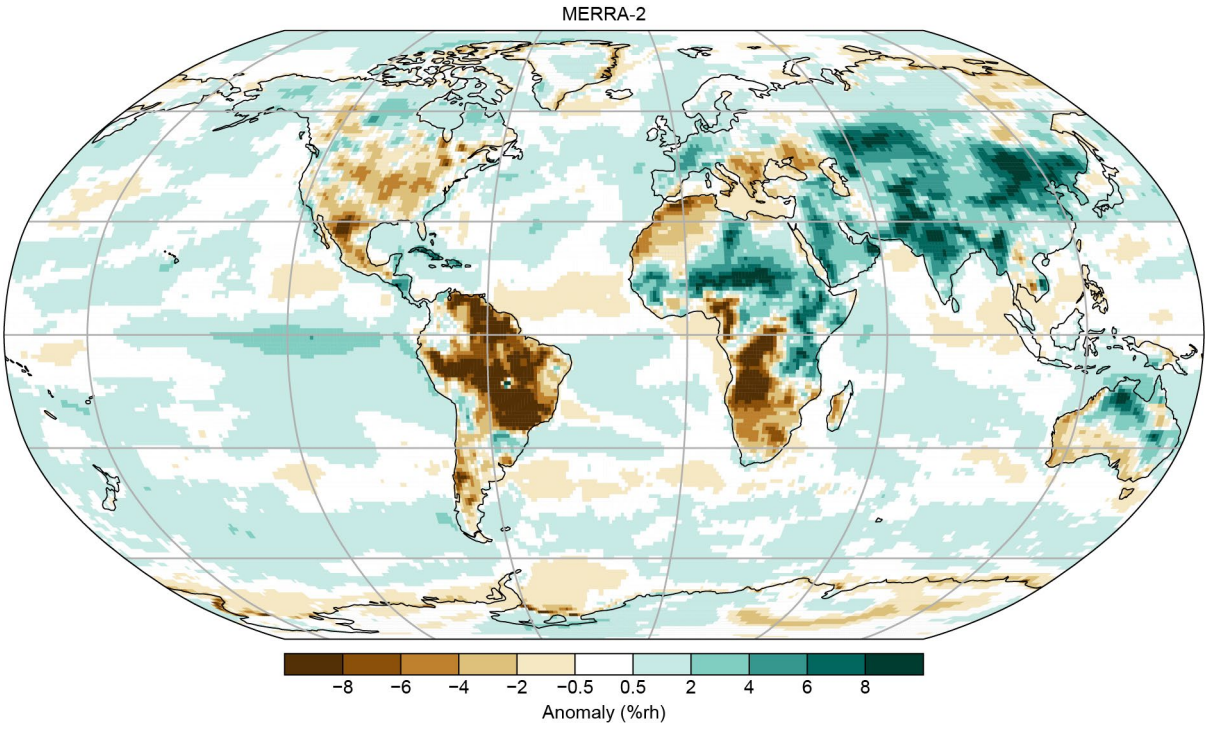

Fig. A2.9. Surface relative humidity anomaly (%rh) relative to 1991–2020 from MERRA-2.

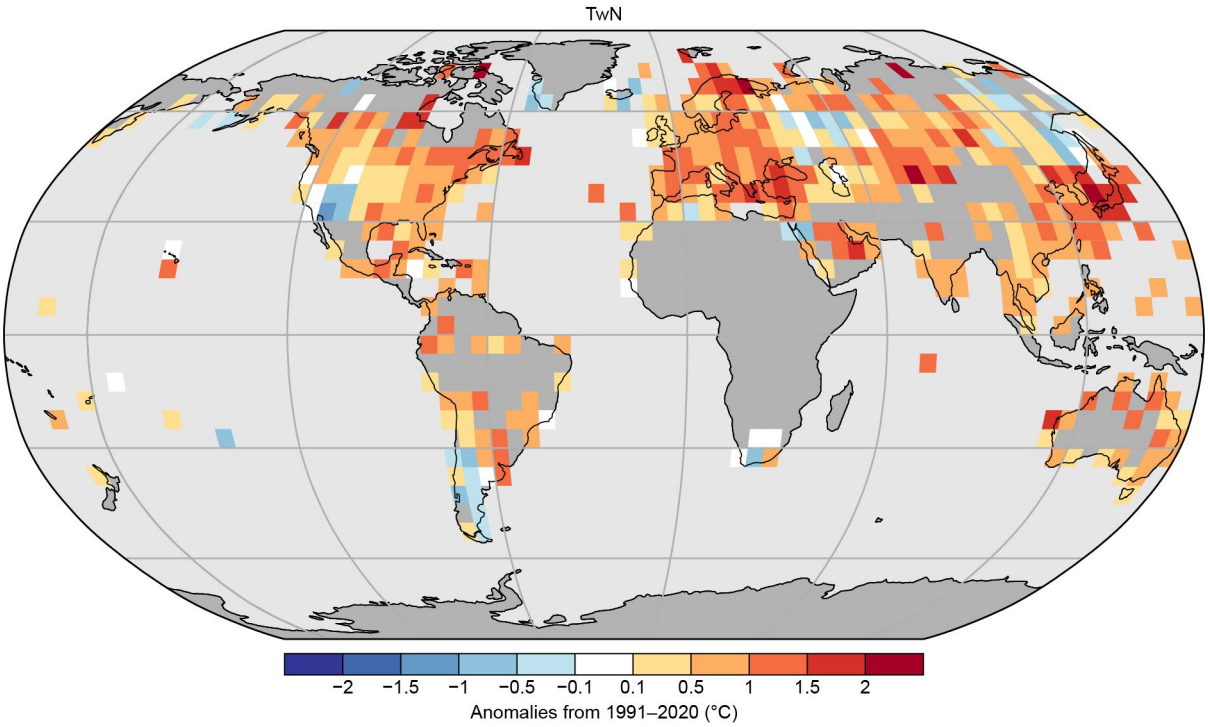

Fig. A2.10. 2024 minimum humid-heat intensity as measured by the annual median of the global median monthly minimum of the daily minimum wet-bulb temperature (T_wN; °C) from the Met Office Hadley Centre Integrated Surface Dataset of Humidity Extremes (HadISDH.extremes). Gray gridboxes (over land) represent regions with insufficient data.

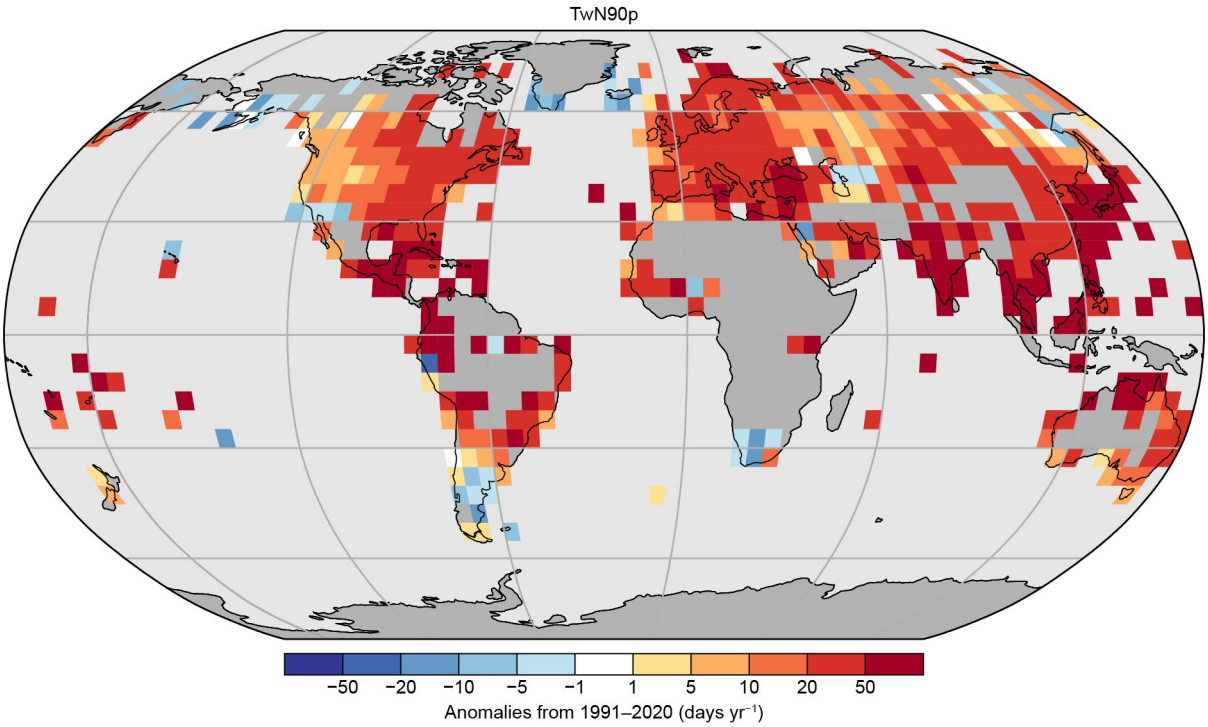

Fig. A2.11. 2024 high daily minimum humid-heat frequency anomalies as measured by the number of days where the daily minimum wet-bulb temperature exceeds the local daily 90th percentile (T_wN90p; days yr^{-1}; calculated over the 1991–2020 period) from the Met Office Hadley Centre Integrated Surface Dataset of Humidity Extremes (HadISDH.extremes). Gray gridboxes (over land) represent regions with insufficient data.

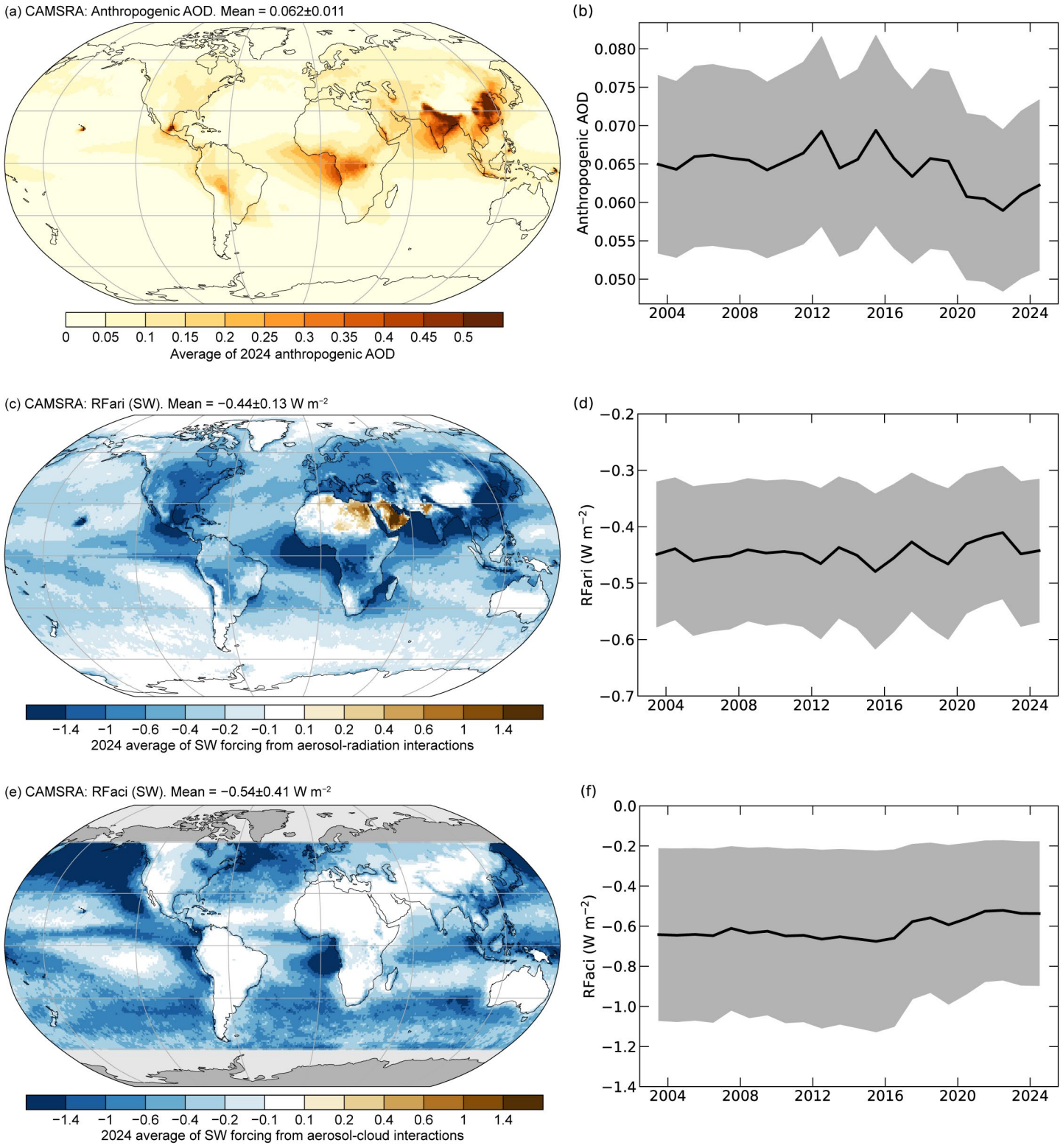

Fig. A2.12. Copernicus Atmosphere Monitoring Service reanalysis (CAMSRA) (a) 2024 average of anthropogenic aerosol optical depth (AOD); (b) global annual average of anthropogenic AOD from 2003 to 2024. Radiative forcing in the shortwave (SW) spectrum due to (c),(d) aerosol-radiation (RFari) and (e),(f) aerosol-cloud interactions (RFaci). The left column shows the distributions for the year 2024. The right column shows the time series of global averages for the period 2003–24, with the mean ±1-σ uncertainties of these estimates shown in gray.

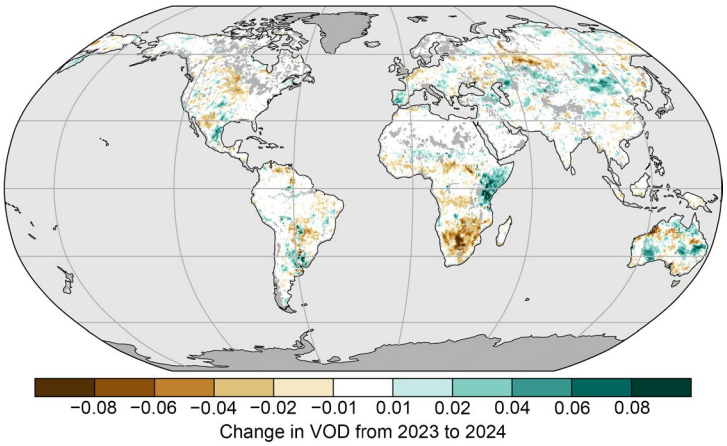

Fig. A2.13. The difference in average CXKu vegetation optical depth (VOD) between the years 2023 and 2024. Brown (green) colors indicate areas where VOD in 2024 were lower (higher) than in 2023. (Source: Vegetation Optical Depth Climate Archive version 2 [VODCAv2]).

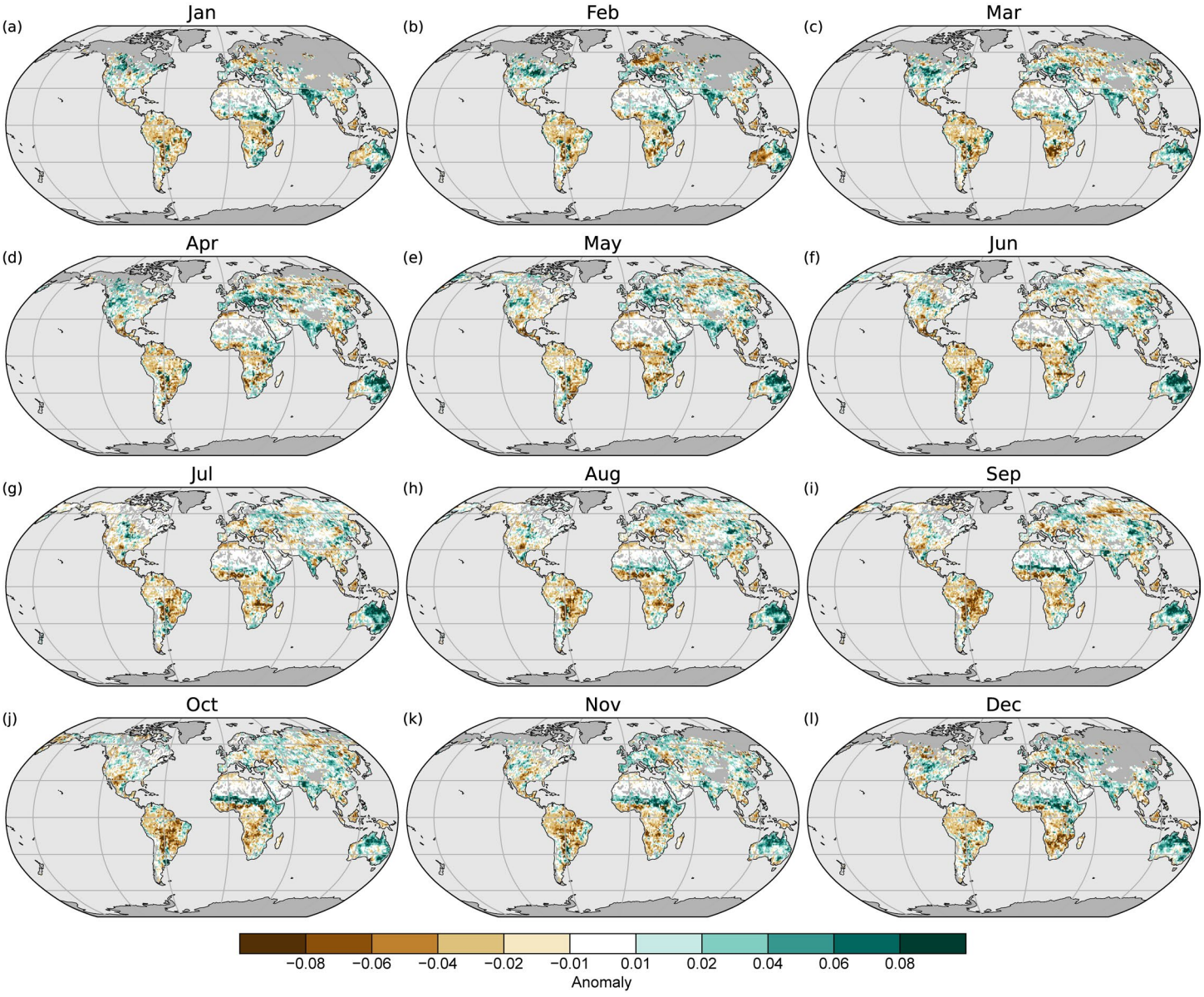

Fig. A2.14. Vegetation Optical Depth Climate Archive (VODCA) monthly CXKu vegetation optical depth (VOD) anomalies in 2024 (1991–20 base period). VOD cannot be retrieved over frozen or snow-covered areas, which is why they are masked out in winter.

References

Alencar, A., and Coauthors, 2024: Fogo no Brasil em 2024: O retrato fundiário da área queimada nos biomas. Tech. Note IPAM (Amazon Environmental Research Institute), Map-Biomas Network, 21 pp., https://ipam.org.br/wp-content/uploads/2024/10/NT_Fogo_Fundiario_ENG_v01.pdf.

Allan, R. J., J. A. Lindesay, and D. E. Parker, 1996: *El Niño Southern Oscillation and Climatic Variability*. CSIRO Publishing, 405 pp.

Ammann, C. M., G. A. Meehl, W. M. Washington, and C. S. Zender, 2003: A monthly and latitudinally varying volcanic forcing dataset in simulations of 20th century climate. *Geophys. Res. Lett.*, **30**, 1657, https://doi.org/10.1029/2003GL016875.

Aono, Y., and K. Kazui, 2008: Phenological data series of cherry tree flowering in Kyoto, Japan, and its application to reconstruction of springtime temperatures since the 9th century. *Int. J. Climatol.*, **28**, 905–914, https://doi.org/10.1002/joc.1594.

Archibald, A. T., and Coauthors, 2020: Tropospheric ozone assessment report. *Elementa*, **8**, 034, https://doi.org/10.1525/elementa.2020.034.

Arguez, A., and Coauthors, 2020: Should we expect each year in the next decade (2019–28) to be ranked among the top 10 warmest years globally? *Bull. Amer. Meteor. Soc.*, **101**, E655–E663, https://doi.org/10.1175/BAMS-D-19-0215.1.

Arosio, C., A. Rozanov, E. Malinina, M. Weber, and J. P. Burrows, 2019: Merging of ozone profiles from SCIAMACHY, OMPS and SAGE II observations to study stratospheric ozone changes. *Atmos. Meas. Tech.*, **12**, 2423–2444, https://doi.org/10.5194/amt-12-2423-2019.

Asher, E., and Coauthors, 2024: Balloon baseline stratospheric aerosol profiles (B^2SAP)—Perturbations in the Southern Hemisphere, 2019–2022. *J. Geophys. Res. Atmos.*, **129**, e2024JD041581, https://doi.org/10.1029/2024JD041581.

Augustine, J. A., K. O. Lantz, J.-P. Vernier, and L. Soldo, 2024: Mauna Loa apparent transmission record update for 2023 [in "State of the Climate in 2023"]. *Bull. Amer. Meteor. Soc.*, **105** (8), S1–S484, https://doi.org/10.1175/2024BAMSStateoftheClimate.1.

Azisov, E., M. Hoelzle, S. Vorogushyn, T. Saks, R. Usubaliev, M. Esenaman Uulu, and M. Barandun, 2022: Reconstructed centennial mass balance change for Golubin glacier, northern Tien Shan. *Atmosphere*, **13**, 954, https://doi.org/10.3390/atmos13060954.

Azorin-Molina, C., and Coauthors, 2023: Biases in wind speed measurements due to anemometer changes. *Atmos. Res.*, **289**, 106771, https://doi.org/10.1016/j.atmosres.2023.106771.

—— , R. J. H. Dunn, L. Ricciardulli, C. A. Mears, J. P. Nicolas, T. R. McVicar, Z. Zeng, and M. G. Bosilovich, 2024: Land and ocean surface winds [in "State of the Climate in 2023"]. *Bull. Amer. Meteor. Soc.*, **105** (8), S76–S79, https://doi.org/10.1175/BAMS-D-24-0116.1.

Bai, G., and Coauthors, 2022: GBOV (Ground-Based Observation for Validation): A copernicus service for validation of land products. *IGARSS 2022 – 2022 IEEE Int. Geoscience and Remote Sensing Symp.*, Kuala Lumpur, Malaysia, Institute of Electrical and Electronics Engineers, 4304–4307, https://doi.org/10.1109/IGARSS46834.2022.9883162.

Bai, X., J. Wang, C. Sellinger, A. Clites, and R. Assel, 2012: Interannual variability of Great Lakes ice cover and its relationship to NAO and ENSO. *J. Geophys. Res.*, **117**, C03002, https://doi.org/10.1029/2010JC006932.

Baldwin, M. P., and T. J. Dunkerton, 2001: Stratospheric harbingers of anomalous weather regimes. *Science*, **294**, 581–584, https://doi.org/10.1126/science.1063315.

—— , and Coauthors, 2001: The quasi-biennial oscillation. *Rev. Geophys.*, **39**, 179–299, https://doi.org/10.1029/1999RG000073.

Barichivich, J., E. Gloor, P. Peylin, R. J. Brienen, J. Schöngart, J. C. Espinoza, and K. C. Pattnayak, 2018: Recent intensification of Amazon flooding extremes driven by strengthened Walker circulation. *Sci. Adv.*, **4**, eaat8785, https://doi.org/10.1126/sciadv.aat8785.

—— , T. J. Osborn, I. Harris, G. van der Schrier, and P. D. Jones, 2024: Monitoring global drought using the self-calibrating palmer drought severity index [in "State of the Climate in 2023"]. *Bull. Amer. Meteor. Soc.*, **105** (8), S70–S71, https://doi.org/10.1175/2024BAMSStateoftheClimate.1.

Basu, S., and Coauthors, 2022: Estimating emissions of methane consistent with atmospheric measurements of methane and δ^{13}C of methane. *Atmos. Chem. Phys.*, **22**, 15 351–15 377, https://doi.org/10.5194/acp-22-15351-2022.

Beck, H. E., E. F. Wood, M. Pan, C. K. Fisher, D. G. Miralles, A. I. J. M. Van Dijk, T. R. McVicar, and R. F. Adler, 2019: MSWEP V2 global 3-hourly 0.1° precipitation: Methodology and quantitative assessment. *Bull. Amer. Meteor. Soc.*, **100**, 473–500, https://doi.org/10.1175/BAMS-D-17-0138.1.

Becker, A., P. Finger, A. Meyer-Christoffer, B. Rudolf, K. Schamm, U. Schneider, and M. A. Ziese, 2013: A description of the global land-surface precipitation data products of the Global Precipitation Climatology Centre with sample applications including centennial (trend) analysis from 1901–present. *Earth Syst. Sci. Data*, **5**, 71–99, https://doi.org/10.5194/essd-5-71-2013.

Behera, S. N., M. Sharma, V. P. Aneja, and R. Balasubramanian, 2013: Ammonia in the atmosphere: A review on emission sources, atmospheric chemistry and deposition on terrestrial bodies. *Environ. Sci. Pollut. Res.*, **20**, 8092–8131, https://doi.org/10.1007/s11356-013-2051-9.

Bell, B., and Coauthors, 2021: The ERA5 global reanalysis: Preliminary extension to 1950. *Quart. J. Roy. Meteor. Soc.*, **147**, 4186–4227, https://doi.org/10.1002/qj.4174.

Bellouin, N., and Coauthors, 2020: Radiative forcing of climate change from the Copernicus reanalysis of atmospheric composition. *Earth Syst. Sci. Data*, **12**, 1649–1677, https://doi.org/10.5194/essd-12-1649-2020.

Bessenbacher, V., D. L. Schumacher, M. Hirschi, S. I. Seneviratne, and L. Gudmundsson, 2023: Gap-filled multivariate observations of global land–climate interactions. *J. Geophys. Res. Atmos.*, **128**, e2023JD039099, https://doi.org/10.1029/2023JD039099.

Betts, R. A., C. D. Jones, J. R. Knight, R. F. Keeling, and J. J. Kennedy, 2016: El Niño and a record CO_2 rise. *Nat. Climate Change*, **6**, 806–810, https://doi.org/10.1038/nclimate3063.

Birkett, C., C. Reynolds, B. Beckley, and B. Doorn, 2011: From research to operations: The USDA global reservoir and lake monitor. Coastal Altimetry, S. Vignudelli et al., Eds., Springer, 19–50.

Bock, O., 2025: Global GNSS integrated water vapour data, 19942024. AERIS, accessed 15 July 2025, https://doi.org/10.25326/68.

—— , C. Mears, S. P. Ho, and S. Xi, 2024: Total column water vapor [in "State of the Climate in 2023"]. *Bull. Amer. Meteor. Soc.*, **105** (8), S57–S59, https://doi.org/10.1175/BAMS-D-24-0116.1.

Bodhaine, B. A., B. G. Mendonca, J. M. Harris, and J. M. Miller, 1981: Seasonal variations in aerosols and atmospheric transmission at Mauna Loa observatory. *J. Geophys. Res.*, **86**, 7395–7398, https://doi.org/10.1029/JC086iC08p07395.

Boone, C. D., P. F. Bernath, and M. D. Fromm, 2020: Pyrocumulonimbus stratospheric plume injections measured by the ACE-FTS. *Geophys. Res. Lett.*, **47**, e2020GL088442, https://doi.org/10.1029/2020GL088442.

Bowman, K. W., 2021a: TROPESS CrIS-JPSS1 L2 ammonia for forward stream, standard product V1. GES DISC, accessed 31 January 2025, https://doi.org/10.5067/7I3KMUCCJNEN.

——, 2021b: TROPESS CrIS-JPSS1 L2 peroxyacetyl nitrate for forward stream, standard product V. GES DISC, accessed 31 January 2025, https://doi.org/10.5067/W0W6L8M6J85X.

Brohan, P., J. J. Kennedy, I. Harris, S. F. Tett, and P. D. Jones, 2006: Uncertainty estimates in regional and global observed temperature changes: A new data set from 1850. *J. Geophys. Res.*, **111**, D12106, https://doi.org/10.1029/2005JD006548.

Brutsaert, W., 2017: Global land surface evaporation trend during the past half century: Corroboration by Clausius-Clapeyron scaling. *Adv. Water Resour.*, **106**, 3–5, https://doi.org/10.1016/j.advwatres.2016.08.014.

Burek, P., J. van der Knijff, and A. de Roo, 2013: LISFLOOD, distributed water balance and flood simulation model – Revised user manual 2013. Publications Office, 139 pp., https://doi.org/10.2788/24719.

Butchart, N., 2014: The Brewer-Dobson circulation. *Rev. Geophys.*, **52**, 157–184, https://doi.org/10.1002/2013RG000448.

Byrne, B., and Coauthors, 2024: Carbon emissions from the 2023 Canadian wildfires. *Nature*, **633**, 835–839, https://doi.org/10.1038/s41586-024-07878-z.

Caine, T. N. (Nel), J. F. Morse, and Niwot Ridge LTER, 2024: Lake ice clearance and formation data for Green Lakes Valley, 1968—Ongoing. Environmental Data Initiative, https://doi.org/10.6073/PASTA/947534B780396B2E79D2206C98640262.

Campos, D., and R. Rondanelli, 2023: ENSO-related precipitation variability in Central Chile: The role of large scale moisture transport. *J. Geophys. Res. Atmos.*, **128**, e2023JD038671, https://doi.org/10.1029/2023JD038671.

CAMS, 2024: CAMS Global wildfires review 2024: A harsh year for the Americas. https://atmosphere.copernicus.eu/cams-global-wildfires-review-2024-harsh-year-americas.

Capotondi, A., and Coauthors, 2015: Understanding ENSO diversity. *Bull. Amer. Meteor. Soc.*, **96**, 921–938, https://doi.org/10.1175/BAMS-D-13-00117.1.

Cappucci, F., N. Gobron, and G. Duveiller, 2024: Land surface properties: Terrestrial surface albedo dynamics [in "State of the Climate in 2023"]. *Bull. Amer. Meteor. Soc.*, **105** (8), S12–S155, https://doi.org/10.1175/BAMS-D-24-0116.1.

Carrea, L., O. Embury, and C. J. Merchant, 2015: Datasets related to in-land water for limnology and remote sensing applications: Distance-to-land, distance-to-water, water-body identifier and lake-Centre co-ordinates. *Geosci. Data J.*, **2**, 83–97, https://doi.org/10.1002/gdj3.32.

——, and Coauthors, 2019: Lake surface temperature [in "State of the Climate in 2018"]. *Bull. Amer. Meteor. Soc.*, **100** (8), S13–S14, https://doi.org/10.1175/2019BAMSStateoftheClimate.1.

——, and Coauthors, 2020: Lake surface temperature [in "State of the Climate in 2019"]. *Bull. Amer. Meteor. Soc.*, **101** (8), S26–S28, https://doi.org/10.1175/BAMS-D-20-0104.1.

——, and Coauthors, 2021: Lake surface water temperature [in "State of the Climate in 2020"]. *Bull. Amer. Meteor. Soc.*, **102** (8), S28–S31, https://doi.org/10.1175/BAMS-D-21-0098.1.

——, and Coauthors, 2022a: Lake surface water temperature [in "State of the Climate in 2021"]. *Bull. Amer. Meteor. Soc.*, **103** (8), S28–S30, https://doi.org/10.1175/BAMS-D-22-0092.1.

——, and Coauthors, 2022b: ESA Lakes climate change initiative (Lakes_cci): Lake products, version 2.0.2. NERC EDS Centre for Environmental Data Analysis, accessed 6 July 2022, https://doi.org/10.5285/a07deacaffb8453e93d57ee214676304.

——, and Coauthors, 2023a: Satellite-derived multivariate worldwide lake physical variable timeseries for climate studies. *Sci. Data*, **10**, 30, https://doi.org/10.1038/s41597-022-01889-z.

——, and Coauthors, 2023b: Lake surface temperature [in "State of the Climate in 2022"]. *Bull. Amer. Meteor. Soc.*, **104** (9), S1–S516, https://doi.org/10.1175/2023BAMSStateoftheClimate.1.

——, and Coauthors, 2024: Lake surface temperature [in "State of the Climate in 2023"]. *Bull. Amer. Meteor. Soc.*, **105** (8), S1–S484, https://doi.org/10.1175/2024BAMSStateoftheClimate.1.

Cassidy, E., 2024: Typhoons line up in the western Pacific. NASA Earth Observatory, https://earthobservatory.nasa.gov/images/153575/typhoons-line-up-in-the-western-pacific.

Cattiaux, J., A. Ribes, and E. Cariou, 2024: How extreme were daily global temperatures in 2023 and early 2024? *Geophys. Res. Lett.*, **51**, e2024GL110531, https://doi.org/10.1029/2024GL110531.

Chandra, S., E. K. Suenaga, F. Scordo, and T. A. Daniel, 2023: Mountain Lake Chemistry and physics profile data since 2015 at Castle Lake. Environmental Data Initiative, accessed 5 February 2025, https://doi.org/10.6073/PASTA/72811937CB436A198EC9B10483EDC2A4.

Chang, K. L., M. G. Schultz, X. Lan, A. McClure-Begley, I. Petropavlovskikh, X. Xu, and J. R. Ziemke, 2021: Trend detection of atmospheric time series: Incorporating appropriate uncertainty estimates and handling extreme events. *Elementa*, **9**, 00035, https://doi.org/10.1525/elementa.2021.00035.

——, and Coauthors, 2023: Diverging ozone trends above western North America: Boundary layer decreases versus free tropospheric increases. *J. Geophys. Res. Atmos.*, **128**, e2022JD038090, https://doi.org/10.1029/2022JD038090.

——, O. R. Cooper, A. Gaudel, I. Petropavlovskikh, P. Effertz, G. Morris, and B. C. McDonald, 2024: Technical note: Challenges in detecting free tropospheric ozone trends in a sparsely sampled environment. *Atmos. Chem. Phys.*, **24**, 6197–6218, https://doi.org/10.5194/acp-24-6197-2024.

Cheng, L., and Coauthors, 2025: Record high temperatures in the ocean in 2024. *Adv. Atmos. Sci.*, **42**, 1092–1109, https://doi.org/10.1007/s00376-025-4541-3.

Choulga, M., F. Moschini, C. Mazzetti, S. Grimaldi, J. Disperati, H. Beck, P. Salamon, and C. Prudhomme, 2024: Technical note: Surface fields for global environmental modelling. *Hydrol. Earth Syst. Sci.*, **28**, 2991–3036, https://doi.org/10.5194/hess-28-2991-2024.

Christy, J. R., 2017: Lower and mid-tropospheric temperature [in "State of the Climate in 2016"]. *Bull. Amer. Meteor. Soc.*, **98** (8), S16–S17, https://doi.org/10.1175/2017BAMSStateoftheClimate.1.

Chung, E., B. Soden, and V. O. John, 2013: Intercalibrating microwave satellite observations for monitoring long-term variations in upper- and midtropospheric water vapor. *J. Atmos. Oceanic Technol.*, **30**, 2303–2319, https://doi.org/10.1175/JTECH-D-13-00001.1.

—— , —— , B. J. Sohn, and L. Shi, 2014: Upper-tropospheric moistening in response to anthropogenic warming. *Proc. Natl. Acad. Sci. USA*, **111** (32) 11636-11641, https://doi.org/10.1073/pnas.1409659111.

—— , —— , X. Huang, L. Shi, and V. O. John, 2016: An assessment of the consistency between satellite measurements of upper tropospheric water vapor. *J. Geophys. Res. Atmos.*, **121**, 2874–2887, https://doi.org/10.1002/2015JD024496.

Ciasto, L., and A. Butler, 2024: And that's a wrap on this season's stratospheric polar vortex. NOAA, https://www.climate.gov/news-features/blogs/polar-vortex/and-thats-wrap-seasons-stratospheric-polar-vortex.

Cicoira, A., J. Beutel, J. Faillettaz, and A. Vieli, 2019: Water controls the seasonal rhythm of rock glacier flow. *Earth Planet. Sci. Lett.*, **528**, 115844, https://doi.org/10.1016/j.epsl.2019.115844.

Climate.gov, 2024: Multi-year drought and heat waves across Mexico. NOAA, accessed 1 February 2025, https://www.climate.gov/news-features/event-tracker/multi-year-drought-and-heat-waves-across-mexico-2024.

Cooper, O. R., J. R. Ziemke, and K.-L. Chang, 2024a: Tropospheric ozone [in "State of the Climate in 2023"]. *Bull. Amer. Meteor. Soc.*, **105** (8), S94–S96, https://doi.org/10.1175/BAMS-D-24-0116.1.

—— , and Coauthors, 2024b: Early season 2023 wildfires generated record-breaking surface ozone anomalies across the U.S. Upper Midwest. *Geophys. Res. Lett.*, **51**, e2024GL111481, https://doi.org/10.1029/2024GL111481.

Cornes, R. C., and R. Junod, 2024: Night marine air temperature [in "State of the Climate in 2023"]. *Bull. Amer. Meteor. Soc.*, **105** (8), S35–S37, https://doi.org/10.1175/2024BAMSStateoftheClimate.1.

—— , E. C. Kent, D. I. Berry, and J. J. Kennedy, 2020: CLASSnmat: A global night marine air temperature data set, 1880–2019. *Geosci. Data J.*, **7**, 170–184, https://doi.org/10.1002/gdj3.100.

—— , T. Cropper, R. Junod, and E. C. Kent, 2023: Night marine air temperature [in "State of the Climate in 2022"]. *Bull. Amer. Meteor. Soc.*, **104** (9), S31–S32, https://doi.org/10.1175/2023BAMSStateoftheClimate.1.

Crimmins, T. M., R. L. Marsh, J. Switzer, M. A. Crimmins, K. L. Gerst, A. H. Rosemartin, and J. F. Weltzin, 2017: USA National Phenology Network gridded products documentation. USGS Open-File Rep. 2017-1003, 34 pp., https://doi.org/10.3133/ofr20171003.

—— , E. G. Denny, E. E. Posthumus, A. H. Rosemartin, R. Croll, M. Montano, and H. Panci, 2022: Science and management advancements made possible by the USA National Phenology Network's nature's notebook platform. *BioScience*, **72**, 908–920, https://doi.org/10.1093/biosci/biac061.

Cusicanqui, D., P. Lacroix, X. Bodin, B. A. Robson, A. Kääb, and S. MacDonell, 2024: Detection and reconstruction of rock glaciers kinematic over 24 years (2000-2024) from Landsat imagery. EGUsphere, https://doi.org/10.5194/egusphere-2024-2393.

Daniel, J. S., S. Solomon, and D. L. Albritton, 1995: On the evaluation of halocarbon radiative forcing and global warming potentials. *J. Geophys. Res.*, **100**, 1271–1285, https://doi.org/10.1029/94JD02516.

Davidson, E. A., 2009: The contribution of manure and fertilizer nitrogen to atmospheric nitrous oxide since 1860. *Nat. Geosci.*, **2**, 659–662, https://doi.org/10.1038/ngeo608.

Davies, B., and Coauthors, 2024: Accelerating glacier volume loss on Juneau icefield driven by hypsometry and melt-accelerating feedbacks. *Nat. Commun.*, **15**, 5099, https://doi.org/10.1038/s41467-024-49269-y.

Davis, S. M., and Coauthors, 2016: The Stratospheric Water and Ozone Satellite Homogenized (SWOOSH) database: A long-term database for climate studies. *Earth Syst. Sci. Data*, **8**, 461–490, https://doi.org/10.5194/essd-8-461-2016.

—— , K. Rosenlof, E. Asher, H. Vömel, R. Stauffer, and D. Hurst, 2024: Stratospheric water vapor [in "State of the Climate in 2023"]. *Bull. Amer. Meteor. Soc.*, **105** (8), S101–S103, https://doi.org/10.1175/BAMS-D-24-0116.1.

Deeter, M. N., and Coauthors, 2014: The MOPITT version 6 product: Algorithm enhancements and validation. *Atmos. Meas. Tech.*, **7**, 3623–3632, https://doi.org/10.5194/amt-7-3623-2014.

—— , D. P. Edwards, G. L. Francis, J. C. Gille, S. Martínez-Alonso, H. M. Worden, and C. Sweeney, 2017: A climate-scale satellite record for carbon monoxide: The MOPITT version 7 product. *Atmos. Meas. Tech.*, **10**, 2533–2555, https://doi.org/10.5194/amt-10-2533-2017.

—— , and Coauthors, 2019: Radiance-based retrieval bias mitigation for the MOPITT instrument: The version 8 product. *Atmos. Meas. Tech.*, **12**, 4561–4580, https://doi.org/10.5194/amt-12-4561-2019.

de Laat, A. T. J., N. Andela, M. Forkel, V. Huijnen, D. Kinalzcyzk, and D. van Wees, 2025: Sentinel-5p reveals unexplained large wildfire carbon emissions in the Amazon in 2024. ESS Open Archive, https://doi.org/10.22541/essoar.173869416.69575859/v1.

de Pablo, M. A., M. Ramos, G. Vieira, A. Molina, R. Ramos, C. N. Maior, M. Prieto, and J. Ruiz-Fernández, 2024: Interannual variability of ground surface thermal regimes in Livingston and deception islands, Antarctica (2007–2021). Land Degrad. *Dev.*, **35**, 378–393, https://doi.org/10.1002/ldr.4922.

Dijk, V., and Coauthors, 2025: Global Water Monitor 2024 summary report. Global Water Monitor Consortium, 57 pp., https://www.globalwater.online/globalwater/report/#gallery.

Dlugokencky, E. J., L. P. Steele, P. M. Lang, and K. A. Masarie, 1994: The growth rate and distribution of atmospheric methane. *J. Geophys. Res.*, **99**, 17021–17043, https://doi.org/10.1029/94JD01245.

Dodangodage, R., P. F. Bernath, M. Wyatt, and C. Boone, 2025: Atmospheric chemistry experiment (ACE) satellite observations of aerosols and SO_2 emissions from the 2024 Ruang volcanic eruption. *J. Quant. Spectrosc. Radiat. Transfer*, **333**, 109333, https://doi.org/10.1016/j.jqsrt.2024.109333.

Domeisen, D. I. V., C. I. Garfinkel, and A. H. Butler, 2019: The teleconnection of El Niño Southern Oscillation to the stratosphere. *Rev. Geophys.*, **57**, 5–47, https://doi.org/10.1029/2018RG000596.

Donat, M. G., L. V. Alexander, H. Yang, I. Durre, R. Vose, and J. Caesar, 2013: Global Land-Based datasets for monitoring climatic extremes. *Bull. Amer. Meteor. Soc.*, **94**, 997–1006, https://doi.org/10.1175/BAMS-D-12-00109.1.

Dorigo, W., W. Preimesberger, C. Reimer, R. Van der Schalie, A. Pasik, R. De Jeu, and C. Paulik, 2025: Soil moisture gridded data from 1978 to present, v202312.0.0. Copernicus Climate Change Service (C3S) Climate Data Store (CDS), accessed 10 February 2025, https://doi.org/10.24381/cds.d7782f18.

Dudok de Wit, T., G. Kopp, C. Fröhlich, and M. Schöll, 2017: Methodology to create a new total solar irradiance record: Making a composite out of multiple data records. *Geophys. Res. Lett.*, **44**, 1196–1203, https://doi.org/10.1002/2016GL071866.

Duncan, B. N., L. N. Lamsal, A. M. Thompson, Y. Yoshida, Z. Lu, D. G. Streets, M. M. Hurwitz, and K. E. Pickering, 2016: A space-based, high-resolution view of notable changes in urban NO_x pollution around the world (2005–2014). J. Geophys. *Res. Atmos.*, **121**, 976–996, https://doi.org/10.1002/2015JD024121.

Dunn, R. J., 2019: HadISD version 3: Monthly updates. Hadley Centre Tech. Note 103, 10 pp., https://www.metoffice.gov.uk/research/library-and-archive/publications/science/climate-science-technical-notes.

——, K. M. Willett, P. W. Thorne, E. V. Woolley, I. Durre, A. Dai, D. E. Parker, and R. S. Vose, 2012: HadISD: A quality-controlled global synoptic report database for selected variables at long-term stations from 1973–2011. *Climate Past*, **8**, 1649–1679, https://doi.org/10.5194/cp-8-1649-2012.

——, ——, D. E. Parker, and L. Mitchell, 2016: Expanding HadISD: Quality-controlled, sub-daily station data from 1931. *Geosci. Instrum. Method Data Syst.*, **5**, 473–491, https://doi.org/10.5194/gi-5-473-2016.

——, C. Azorin-Molina, M. J. Menne, Z. Zeng, N. W. Casey, and C. Shen, 2022a: Reduction in reversal of global stilling arising from correction to encoding of calm periods. *Environ. Res. Commun.*, **4**, 061003, https://doi.org/10.1088/2515-7620/ac770a.

——, M. G. Donat, and L. V. Alexander, 2022b: Comparing extremes indices in recent observational and reanalysis products. *Front. Climate*, **4**, 989505, https://doi.org/10.3389/fclim.2022.989505.

Dunn, R. J. H., and C. P. Morice, 2022: On the effect of reference periods on trends in percentile-based extreme temperature indices. *Environ. Res. Lett.*, **17**, 034026, https://doi.org/10.1088/1748-9326/ac52c8.

——, and Coauthors, 2020: Development of an updated global land in situ–based data set of temperature and precipitation extremes: HadEX3. *J. Geophys. Res. Atmos.*, **125**, e2019JD032263, https://doi.org/10.1029/2019JD032263.

——, M. G. Donat, R. W. Schlegel, and M. G. Bosilovich, 2024a: Surface temperature extremes [in "State of the Climate in 2023"]. *Bull. Amer. Meteor. Soc.*, **105** (8), S37–S39, https://doi.org/10.1175/BAMS-D-24-0116.1.

——, and Coauthors, 2024b: Observed global changes in sector-relevant climate extremes indices—An extension to HadEX3. *Earth Space Sci.*, **11**, e2023EA003279, https://doi.org/10.1029/2023EA003279.

Duveiller, G., and N. Gobron, 2023: Land surface properties: Terrestrial surface albedo dynamics [in "State of the Climate in 2022"]. *Bull. Amer. Meteor. Soc.*, **104** (9), S102–S103, https://doi.org/10.1175/BAMS-D-23-0090.1.

DW, 2024: Pakistan: Lahore records heaviest rainfall in years. Accessed 13 February 2025, https://www.dw.com/en/pakistan-lahore-records-heaviest-rainfall-in-years/a-69829897.

ECMWF, 2025: Global Climate Highlights 2024. Climate Copernicus, accessed 13 February 2025, https://climate.copernicus.eu/global-climate-highlights-2024.

Edwards, M., and A. Richardson, 2004: Impact of climate change on marine pelagic phenology and trophic mismatch. *Nature*, **430**, 881–884, https://doi.org/10.1038/nature02808.

Ellis, H. T., and R. F. Pueschel, 1971: Solar radiation: Absence of air pollution trends at Mauna Loa. *Science*, **172**, 845–846, https://doi.org/10.1126/science.172.3985.845.

Elshorbany, Y., and Coauthors, 2024: Tropospheric ozone precursors: Global and regional distributions, trends, and variability. *Atmos. Chem. Phys.*, **24**, 12 225–12 257, https://doi.org/10.5194/acp-24-12225-2024.

Elson, P., and Coauthors, 2022: SciTools/cartopy: v0.21.1 (v0.21.1). Zenodo, https://doi.org/10.5281/zenodo.7430317.

Estilow, T. W., A. H. Young, and D. A. Robinson, 2015: A long-term Northern Hemisphere snow cover extent data record for climate studies and monitoring. *Earth Syst. Sci. Data*, **7**, 137–142, https://doi.org/10.5194/essd-7-137-2015.

Etheridge, D. M., L. P. Steele, R. L. Langenfelds, R. J. Francey, J. M. Barnola, and V. I. Morgan, 1996: Natural and anthropogenic changes in atmospheric CO_2 over the last 1000 years from air in Antarctic ice and firn. *J. Geophys. Res.*, **101**, 4115–4128, https://doi.org/10.1029/95JD03410.

Etzelmüller, B., and Coauthors, 2020: Twenty years of European Mountain permafrost dynamics—The PACE legacy. *Environ. Res. Lett.*, **15**, 104070, https://doi.org/10.1088/1748-9326/abae9d.

——, K. Isaksen, J. Czekirda, S. Westermann, C. Hilbich, and C. Hauck, 2023: Rapid warming and degradation of Mountain permafrost in Norway and Iceland. *Cryosphere*, **17**, 5477–5497, https://doi.org/10.5194/tc-17-5477-2023.

EUMETSAT, 2023: Animations from Europe's first lightning imager. https://www.eumetsat.int/features/animations-europes-first-lightning-imager.

——, 2024: MTG lightning imager data available. https://user.eumetsat.int/news-events/news/mtg-lightning-imager-li-level-2-data-available.

Feng, L., P. I. Palmer, S. Zhu, R. J. Parker, and Y. Liu, 2022: Tropical methane emissions explain large fraction of recent changes in global atmospheric methane growth rate. *Nat. Commun.*, **13**, 1378, https://doi.org/10.1038/s41467-022-28989-z.

Feng, Y., and Coauthors, 2022: Decadal lake volume changes (2003–2020) and driving forces at a global scale. *Remote Sens.*, **14**, 1032, https://doi.org/10.3390/rs14041032.

Feron, S., and Coauthors, 2024: South America is becoming warmer, drier, and more flammable. *Commun. Earth Environ.*, **5**, 501, https://doi.org/10.1038/s43247-024-01654-7.

Finlay, C. C., C. Kloss, N. Olsen, M. D. Hammer, L. Tøffner-Clausen, A. Grayver, and A. Kuvshinov, 2020: The CHAOS-7 geomagnetic field model and observed changes in the South Atlantic anomaly. *Earth Planets Space*, **72**, 156, https://doi.org/10.1186/s40623-020-01252-9.

Fischer, E. V., and Coauthors, 2014: Atmospheric peroxyacetyl nitrate (PAN): A global budget and source attribution. *Atmos. Chem. Phys.*, **14**, 2679–2698, https://doi.org/10.5194/acp-14-2679-2014.

Fisher, J. B., and Coauthors, 2020: ECOSTRESS: NASA's next generation mission to measure evapotranspiration from the international space station. *Water Resour. Res.*, **56**, e2019WR026058, https://doi.org/10.1029/2019WR026058.

Fleming, E. L., P. A. Newman, Q. Liang, and L. D. Oman, 2024: Stratospheric temperature and ozone impacts of the hunga Tonga-hunga Ha'apai water vapor injection. *J. Geophys. Res. Atmos.*, **129**, e2023JD039298, https://doi.org/10.1029/2023JD039298.

Fogt, R. L., and G. J. Marshall, 2020: The Southern annular mode: Variability, trends, and climate impacts across the Southern Hemisphere. *Wiley Interdiscip. Rev.: Climate Change*, **11**, e652, https://doi.org/10.1002/wcc.652.

Folland, C. K., J. Knight, H. W. Linderholm, D. Fereday, S. Ineson, and J. W. Hurrell, 2009: The summer North Atlantic oscillation: Past, present, and future. *J. Climate*, **22**, 1082–1103, https://doi.org/10.1175/2008JCLI2459.1.

Forster, P., and Coauthors, 2021: The Earth's energy budget, climate feedbacks, and climate sensitivity. *Climate Change 2021: The Physical Science Basis*, V. Masson-Delmotte et al., Eds., Cambridge University Press, 923–1054, https://doi.org/10.1017/9781009157896.009.

Forster, P. M., and Coauthors, 2023: Indicators of global climate change 2022: Annual update of large-scale indicators of the state of the climate system and human influence. *Earth Syst. Sci. Data*, **15**, 2295–2327, https://doi.org/10.5194/essd-15-2295-2023.

—— ., and Coauthors, 2024: Indicators of global climate change 2023: Annual update of key indicators of the state of the climate system and human influence. *Earth Syst. Sci. Data*, **16**, 2625–2658, https://doi.org/10.5194/essd-16-2625-2024.

Foster, M. J., C. Phillips, A. K. Heidinger, E. E. Borbas, Y. Li, W. P. Menzel, A. Walther, and E. Weisz, 2023: PATMOS-x version 6.0: 40 years of merged AVHRR and HIRS global cloud data. *J. Climate*, **36**, 1143–1160, https://doi.org/10.1175/JCLI-D-22-0147.1.

Free, M., D. J. Seidel, J. K. Angel, J. Lanzante, I. Durre, and T. C. Peterson, 2005: Radiosonde atmospheric temperature products for assessing climate (RATPAC): A new data set of large-area anomaly time series. *J. Geophys. Res.*, **110**, D22101, https://doi.org/10.1029/2005JD006169.

Friedlingstein, P., and Coauthors, 2025: Global Carbon Budget 2024. *Earth Syst. Sci. Data*, **17**, 965–1039, https://doi.org/10.5194/essd-17-965-2025.

Frost, G. V., and Coauthors, 2024: NOAA Arctic Report Card 2024: Tundra greenness. NOAA Tech. Rep. OAR ARC 24-09, 9 pp., https://doi.org/10.25923/5t2g-fm41.

Füllekrug, M., E. Williams, and C. Price, 2002: Intense oceanic lightning. *Ann. Geophys.*, **20**, 133–137, https://doi.org/10.5194/angeo-20-133-2002.

——, ——, ——, S. Goodman, R. Holzworth, K. Virts, and D. Buechler, 2022: Sidebar 2.1: Lightning [in "State of the Climate in 2021"]. *Bull. Amer. Meteor. Soc.*, **103** (8), S79, https://doi.org/10.1175/2022BAMSStateoftheClimate.1.

Gao, R. S., and Coauthors, 2016: A light-weight, high-sensitivity particle spectrometer for $PM_{2.5}$ aerosol measurements. *Aerosol Sci. Technol.*, **50**, 88–99, https://doi.org/10.1080/02786826.2015.1131809.

Garfinkel, C. I., and Coauthors, 2021: Influence of the El Niño–Southern Oscillation on entry stratospheric water vapor in coupled chemistry–ocean CCMI and CMIP6 models. *Atmos. Chem. Phys.*, **21**, 3725–3740, https://doi.org/10.5194/acp-21-3725-2021.

Garreaud, R., and Coauthors, 2025: Hyperdroughts in central Chile: Drivers, impacts and projections. EGUsphere, https://doi.org/10.5194/egusphere-2025-517.

Garreaud, R. D., J. P. Boisier, R. Rondanelli, A. Montecinos, H. H. Sepúlveda, and D. Veloso-Aguila, 2020: The central Chile mega drought (2010–2018): A climate dynamics perspective. *Int. J. Climatol.*, **40**, 421–439, https://doi.org/10.1002/joc.6219.

Gaudel, A., and Coauthors, 2018: Tropospheric ozone assessment report: Present-day distribution and trends of tropospheric ozone relevant to climate and global atmospheric chemistry model evaluation. *Elementa*, **6**, 39, https://doi.org/10.1525/elementa.291.

GCOS, 2022: The 2022 Global Climate Observing System (GCOS) implementation plan. WMO GCOS-244, 98 pp., https://gcos.wmo.int/en/publications/gcos-implementation-plan2022.

Gelaro, R., and Coauthors, 2017: The Modern-Era Retrospective Analysis for Research and Applications, version 2 (MERRA-2). J. Climate, **30**, 5419–5454, https://doi.org/10.1175/JCLI-D-16-0758.1.

Getirana, A., S. Kumar, M. Girotto, and M. Rodell, 2017: Rivers and floodplains as key components of global terrestrial water storage variability. *Geophys. Res. Lett.*, **44**, 10 359–10 310, https://doi.org/10.1002/2017GL074684.

Gettelman, A., and Coauthors, 2024: Has reducing ship emissions brought forward global warming? *Geophys. Res. Lett.*, **51**, e2024GL109077, https://doi.org/10.1029/2024GL109077.

Ghent, D. J., J. S. Anand, K. Veal, and J. J. Remedios, 2024: The operational and climate land surface temperature products from the sea and land surface temperature radiometers on Sentinel-3A and 3B. Remote Sens., **16**, 3403, https://doi.org/10.3390/rs16183403.

Giglio, L., W. Schroeder, and C. O. Justice, 2016: The Collection 6 MODIS active fire detection algorithm and fire products. *Remote Sens. Environ.*, **178**, 31–41, https://doi.org/10.1016/j.rse.2016.02.054.

GISTEMP Team, 2025: GISS Surface Temperature Analysis (GISTEMP), version 4. NASA Goddard Institute for Space Studies, accessed 20 January 2025, https://data.giss.nasa.gov/gistemp/.

Gobron, N., B. Belward, P. Pinty, and W. Knorr, 2010: Monitoring biosphere vegetation 1998–2009. *Geophys. Res. Lett.*, **37**, L15402, https://doi.org/10.1029/2010GL043870.

—— , and Coauthors, 2022: Evaluation of Sentinel-3A and Sentinel-3B ocean land colour instrument green instantaneous fraction of absorbed photosynthetically active radiation. *Remote Sens. Environ.*, **270**, 112850, https://doi.org/10.1016/j.rse.2021.112850.

Goessling, H. F., T. Rackow, and T. Jung, 2025: Recent global temperature surge intensified by record-low planetary albedo. *Science*, **387**, 68–73, https://doi.org/10.1126/science.adq7280.

Good, E. J., 2016: An in situ–based analysis of the relationship between land surface "skin" and screen-level air temperatures. *J. Geophys. Res. Atmos.*, **121**, 8801–8819, https://doi.org/10.1002/2016JD025318.

—— , D. J. Ghent, C. E. Bulgin, and J. J. Remedios, 2017: A spatiotemporal analysis of the relationship between near-surface air temperature and satellite land surface temperatures using 17 years of data from the ATSR series. *J. Geophys. Res. Atmos.*, **122**, 9185–9210, https://doi.org/10.1002/2017JD026880.

—— , F. M. Aldred, D. J. Ghent, K. L. Veal, and C. Jimenez, 2022: An analysis of the stability and trends in the LST_cci land surface temperature datasets over Europe. *Earth Space Sci.*, **9**, e2022EA002317, https://doi.org/10.1029/2022EA002317.

Granier, C., and Coauthors, 2011: Evolution of anthropogenic and biomass burning emissions of air pollutants at global and regional scales during the 1980–2010 period. *Climatic Change*, **109**, 163–190, https://doi.org/10.1007/s10584-011-0154-1.

Gruber, A., W. A. Dorigo, W. Crow, and W. Wagner, 2017: Triple Collocation-Based merging of satellite soil moisture retrievals. *IEEE Trans. Geosci. Remote Sens.*, **55**, 6780–6792, https://doi.org/10.1109/TGRS.2017.2734070.

—— , T. Scanlon, R. van der Schalie, W. Wagner, and W. Dorigo, 2019: Evolution of the ESA CCI soil moisture climate data records and their underlying merging methodology. *Earth Syst. Sci. Data*, **11**, 717–739, https://doi.org/10.5194/essd-11-717-2019.

Gulev, S. K., and Coauthors, 2021: Changing state of the climate system. Climate Change 2021: The Physical Science Basis, V. Masson-Delmotte et al., Eds., Cambridge University Press, 287–422, https://doi.org/10.1017/9781009157896.004.

Gyawali, M. S., and Coauthors, 2023: Tracking NO_2 pollution changes over Texas: Synthesis of in situ and satellite observations. *J. Geophys. Res. Atmos.*, **128**, e2022JD037473, https://doi.org/10.1029/2022JD037473.

Haimberger, L., C. Tavolato, and S. Sperka, 2012: Homogenization of the global radiosonde temperature dataset through combined comparison with reanalysis background series and neighboring stations. *J. Climate*, **25**, 8108–8131, https://doi.org/10.1175/JCLI-D-11-00668.1.

Han, Y., Q. Lin, S. Huang, C. Du, J. Shen, and K. Zhang, 2024: Human impacts dominate global loss of lake ecosystem resilience. *Geophys. Res. Lett.*, **51**, e2024GL109298, https://doi.org/10.1029/2024GL109298.

Hansen, J., R. Ruedy, M. Sato, and K. Lo, 2010: Global surface temperature change. *Rev. Geophys.*, **48**, RG4004, https://doi.org/10.1029/2010RG000345.

Harris, I., T. J. Osborn, P. D. Jones, and D. H. Lister, 2020: Version 4 of the CRU TS monthly high-resolution gridded multivariate climate dataset. *Sci. Data*, **7**, 109, https://doi.org/10.1038/s41597-020-0453-3.

Hassan, T., R. Gulzar, M. Hamid, R. Ahmad, S. A. Waza, and A. A. Khuroo, 2024: Plant phenology shifts under climate warming: A systematic review of recent scientific literature. *Environ. Monit. Assess.*, **196**, 36, https://doi.org/10.1007/s10661-023-12190-w

Hattersley, R., and Coauthors, 2023: SciTools/iris: v3.7.0 (v3.7.0). Zenodo, https://doi.org/10.5281/zenodo.8305232.

He, J., and Coauthors, 2024: COVID-19 perturbation on US air quality and human health impact assessment. *PNAS Nexus*, **3**, pgad483, https://doi.org/10.1093/pnasnexus/pgad483.

Hersbach, H., and Coauthors, 2020: The ERA5 global reanalysis. *Quart. J. Roy. Meteor. Soc.*, **146**, 1999–2049, https://doi.org/10.1002/qj.3803.

Hirschi, M., and Coauthors, 2024: Soil moisture [in "State of the Climate in 2023"]. *Bull. Amer. Meteor. Soc.*, **105** (8), Si–S484, https://doi.org/10.1175/2024BAMSStateoftheClimate.1.

Ho, S.-P., and Coauthors, 2020: The COSMIC/FORMOSAT-3 radio occultation mission after 12 years: Accomplishments, remaining challenges, and potential impacts of COSMIC-2. *Bul. Amer. Meteor. Sci.*, **101**, E1107–E1136, https://doi.org/10.1175/BAMS-D-18-0290.1.

Hodnebrog, Ø., and Coauthors, 2020a: Updated global warming potentials and radiative efficiencies of halocarbons and other weak atmospheric absorbers. *Rev. Geophys.*, **58**, e2019RG000691, https://doi.org/10.1029/2019RG000691.

——, and Coauthors, 2020b: The effect of rapid adjustments to halocarbons and N_2O on radiative forcing. *npj Climate Atmos. Sci.*, **3**, 43, https://doi.org/10.1038/s41612-020-00150-x.

Hoell, A., C. Funk, J. Zinke, and L. Harrison, 2017: Modulation of the southern Africa precipitation response to the El Niño Southern Oscillation by the subtropical Indian Ocean dipole. *Climate Dyn.*, **48**, 2529–2540, https://doi.org/10.1007/s00382-016-3220-6.

Hofmann, D. J., J. H. Butler, E. J. Dlugokencky, J. W. Elkins, K. Masarie, S. A. Montzka, and P. Tans, 2006: The role of carbon dioxide in climate forcing from 1979 to 2004: Introduction of the annual greenhouse gas index. *Tellus*, **58B**, 614–619, https://doi.org/10.1111/j.1600-0889.2006.00201.x.

Holzworth, R. H., M. P. McCarthy, J. B. Brundell, A. R. Jacobson, and C. J. Rodger, 2019: Global distribution of superbolts. *J. Geophys. Res. Atmos.*, **124**, 9996–10 005, https://doi.org/10.1029/2019JD030975.

——, J. B. Brundell, M. P. McCarthy, A. R. Jacobson, C. J. Rodger, and T. S. Anderson, 2021: Lightning in the Arctic. *Geophys. Res. Lett.*, **48**, e2020GL091366, https://doi.org/10.1029/2020GL091366.

Hou, J., A. I. J. M. Van Dijk, L. J. Renzullo, and P. R. Larraondo, 2024: GloLakes: Water storage dynamics for 27 000 Lakes globally from 1984 to present derived from satellite altimetry and optical imaging. *Earth Syst. Sci. Data*, **16**, 201–218, https://doi.org/10.5194/essd-16-201-2024.

Hrbáček, F., and Coauthors, 2023: Active layer and permafrost thermal regimes in the ice-free areas of Antarctica. *Earth-Sci. Rev.*, **242**, 104458, https://doi.org/10.1016/j.earscirev.2023.104458.

Hu, G., and Coauthors, 2024: Spatiotemporal characteristics and variability in the thermal state of permafrost on the Qinghai–Tibet Plateau. *Permafrost Periglacial Processes*, **35**, 143–156, https://doi.org/10.1002/ppp.2219.

Hu, Y., and Coauthors, 2025: Rock glacier velocity: An essential climate variable quantity for permafrost. *Rev. Geophys.*, **63**, e2024RG000847, https://doi.org/10.1029/2024RG000847.

Huang, X., K. Yang, S. Kondragunta, Z. Wei, L. Valin, J. Szykman, and M. Goldberg, 2022: NO_2 retrievals from NOAA-20 OMPS: Algorithm, evaluation, and observations of drastic changes during COVID-19. *Atmos. Environ.*, **290**, 119367, https://doi.org/10.1016/j.atmosenv.2022.119367.

Huffman, G. J., R. Adler, A. Behrangi, D. Bolvin, E. Nelkin, G. Gu, and M. Ehsani, 2023: The new version 3.2 Global Precipitation Climatology Project (GPCP) Monthly and Daily precipitation products. *J. Climate*, **36**, 7635–7655, https://doi.org/10.1175/JCLI-D-23-0123.1.

Hunter, J. D., 2007: Matplotlib: A 2D graphics environment. *Comput. Sci. Eng.*, **9**, 90–95, https://doi.org/10.1109/MCSE.2007.55.

Hurst, D. F., S. J. Oltmans, H. Vömel, K. H. Rosenlof, S. M. Davis, E. A. Ray, E. G. Hall, and A. F. Jordan, 2011: Stratospheric water vapor trends over boulder, Colorado: Analysis of the 30 year boulder record. *J. Geophys. Res.*, **116**, D02306, https://doi.org/10.1029/2010JD015065.

Ingram, W., 2010: A very simple model for the water vapour feedback on climate change. *Quart. J. Roy. Meteor. Soc.*, **136**, 30–40, https://doi.org/10.1002/qj.546.

Inness, A., and Coauthors, 2019: The CAMS reanalysis of atmospheric composition. *Atmos. Chem. Phys.*, **19**, 3515–3556, https://doi.org/10.5194/acp-19-3515-2019.

IPCC, 2013: *Climate Change 2013: The Physical Science Basis.* T. F. Stocker et al., Eds., Cambridge University Press, 1535 pp.

——, 2021: Annex VII: Glossary. *Climate Change 2021: The Physical Science Basis*, V. Masson-Delmotte et al., Eds., Cambridge University Press, 2215–2256, https://doi.org/10.1017/9781009157896.022.

Isaksen, K., and Coauthors, 2022: Exceptional warming over the Barents area. *Sci. Rep.*, **12**, 9371, https://doi.org/10.1038/s41598-022-13568-5.

Jacobs, N. A., 2021: Open innovation and the case for community model development. *Bull. Amer. Meteor. Soc.*, **102**, E2002–E2011, https://doi.org/10.1175/BAMS-D-21-0030.1.

Jasinski, M. F., and Coauthors, 2023: ATLAS/ICESat-2 L3A along track inland surface water data, version 6. NASA National Snow and Ice Data Center Distributed Active Archive Center, accessed 31 December 2024, https://doi.org/10.5067/ATLAS/ATL13.006.

John, V. O., L. Shi, E.-S. Chung, R. P. Allan, S. A. Buehler, and B. J. Soden, 2024: Upper tropospheric humidity [in "State of the Climate in 2023"]. *Bull. Amer. Meteor. Soc.*, **105** (8), S59–60, https://doi.org/10.1175/2024BAMSStateoftheClimate.1.

Joint Research Centre–European Commission, 2025: Global flood awareness system. Accessed 12 February 2025, https://global-flood.emergency.copernicus.eu/.

Juncosa Calahorrano, J. F., V. H. Payne, S. Kulawik, B. Ford, F. Flocke, T. Campos, and E. V. Fischer, 2021: Evolution of acyl peroxynitrates (PANs) in wildfire smoke plumes detected by the cross-track infrared sounder (CrIS) over the western U.S. during summer 2018. *Geophys. Res. Lett.*, **48**, e2021GL093405, https://doi.org/10.1029/2021GL093405.

Junod, R. A., and J. R. Christy, 2020: A new compilation of globally gridded night-time marine air temperatures: The UAHNMATv1 dataset. *Int. J. Climatol.*, **40**, 2609–2623, https://doi.org/10.1002/joc.6354.

Kääb, A., and J. Røste, 2024: Rock glaciers across the United States predominantly accelerate coincident with rise in air temperatures. *Nat. Commun.*, **15**, 7581, https://doi.org/10.1038/s41467-024-52093-z.

——, T. Strozzi, T. Bolch, R. Caduff, H. Trefall, M. Stoffel, and A. Kokarev, 2021: Inventory and changes of rock glacier creep speeds in Ile Alatau and Kungöy Ala-Too, Northern Tien Shan, since the 1950s. *Cryosphere*, **15**, 927–949, https://doi.org/10.5194/tc-15-927-2021.

Kainz, M. J., R., Ptacnik, S., Rasconi, and H. H. Hager, 2017: Irregular changes in lake surface water temperature and ice cover in subalpine Lake Lunz, Austria. *Inland Waters*, **7**, 27–33, https://doi.org/10.1080/20442041.2017.1294332.

Kaiser, J. W., and Coauthors, 2012: Biomass burning emissions estimated with a global fire assimilation system based on observed fire radiative power. *Biogeosciences*, **9**, 527–554, https://doi.org/10.5194/bg-9-527-2012.

Kamal, M., T. I. Sanjid, A. Rony, and F. Piya, 2024: The August 2024 Bangladesh flood: Examining meteorological triggers, forecasting limitations, and Cross-Border water dynamics. ESS Open Archive, https://doi.org/10.22541/essoar.173257596.62658483/v1.

Kaplan, A., 2011: Patterns and indices of climate variability [in "State of the Climate in 2010"]. *Bull. Amer. Meteor. Soc.*, **92** (6), S20–S25, https://doi.org/10.1175/1520-0477-92.6.S1.

Keller, C. A., and Coauthors, 2021: Description of the NASA GEOS composition forecast modeling system GEOS-CF v1.0. *J. Adv. Model. Earth Syst.*, **13**, e2020MS002413, https://doi.org/10.1029/2020MS002413.

Kellerer-Pirklbauer, A., and Coauthors, 2024: Acceleration and interannual variability of creep rates in Mountain permafrost landforms (rock glacier velocities) in the European Alps over the time period 1995–2022 based on geodetic surveys: Climatic factors versus site-specific effects. *Environ. Res. Lett.*, **19**, 034022, https://doi.org/10.1088/1748-9326/ad25a4.

Kennedy, J. J., N. A. Rayner, C. P. Atkinson, and R. E. Killick, 2019: An ensemble data set of sea surface temperature change from 1850: The Met Office Hadley Centre HadSST.4.0.0.0 data set. *J. Geophys. Res. Atmos.*, **124**, 7719–7763, https://doi.org/10.1029/2018JD029867.

Khaykin, S., and Coauthors, 2020: The 2019/20 Australian wildfires generated a persistent smoke-charged vortex rising up to 35 km altitude. *Commun. Earth Environ.*, **1**, 22, https://doi.org/10.1038/s43247-020-00022-5.

——, and Coauthors, 2022: Global perturbation of stratospheric water and aerosol burden by Hunga eruption. *Commun. Earth Environ.*, **3**, 316, https://doi.org/10.1038/s43247-022-00652-x.

——, and Coauthors, 2024: Stratospheric aerosols [in "State of the Climate in 2023"]. *Bull. Amer. Meteor. Soc.*, **105** (8), S96–S98, https://doi.org/10.1175/BAMS-D-24-0116.1.

Khaykin, S. M., S. Godin-Beekmann, A. Hauchecorne, J. Pelon, F. Ravetta, and P. Keckhut, 2018: Stratospheric smoke with unprecedentedly high backscatter observed by lidars above Southern France. *Geophys. Res. Lett.*, **45**, 1639–1646, https://doi.org/10.1002/2017GL076763.

Kleipool, Q., and Coauthors, 2022: Ozone Monitoring Instrument (OMI) collection 4: Establishing a 17-year-long series of detrended level-1b data. *Atmos. Meas. Tech.*, **15**, 3527–3553, https://doi.org/10.5194/amt-15-3527-2022.

Kobayashi, S., and Coauthors, 2015: The JRA-55 reanalysis: General specifications and basic characteristics. *J. Meteor. Soc. Japan*, **93**, 5–48, https://doi.org/10.2151/jmsj.2015-001.

Kodera, K., H. Mukougawa, P. Maury, M. Ueda, and C. Claud, 2016: Absorbing and reflecting sudden stratospheric warming events and their relationship with tropospheric circulation. *J. Geophys. Res. Atmos.*, **121**, 80–94, https://doi.org/10.1002/2015JD023359.

Konopka, P., M. Tao, F. Ploeger, D. F. Hurst, M. L. Santee, J. S. Wright, and M. Riese, 2022: Stratospheric moistening after 2000. *Geophys. Res. Lett.*, **49**, e2021GL097609, https://doi.org/10.1029/2021GL097609.

Kosaka, Y., and Coauthors, 2024: The JRA-3Q reanalysis. *J. Meteor. Soc. Japan*, **102**, 49–109, https://doi.org/10.2151/jmsj.2024-004.

Kothari, R., 2024: Cleanup begins in Valencia after Spain's worst floods in history claim over 200 lives. The Watchers, https://watchers.news/2024/11/01/valencia-cleanup-spain-worst-flood-record-october-2024/.

Kovilakam, M., L. W. Thomason, N. Ernest, L. Rieger, A. Bourassa, and L. Millán, 2020: The global space-based stratospheric aerosol climatology (version 2.0): 1979–2018. *Earth Syst. Sci. Data*, **12**, 2607–2634, https://doi.org/10.5194/essd-12-2607-2020.

Kraemer, B. M., A. Seimon, R. Adrian, and P. B. McIntyre, 2020: Worldwide lake level trends and responses to background climate variation. *Hydrol. Earth Syst. Sci.*, **24**, 2593–2608, https://doi.org/10.5194/hess-24-2593-2020.

Kratz, D. P., P. W. Stackhouse Jr., S. K. Gupta, A. C. Wilber, P. Sawaengphokhai, and G. R. McGarragh, 2014: The fast longwave and shortwave flux (FLASHFlux) data product: Single-Scanner footprint fluxes. *J. Appl. Meteor. Climatol.*, **53**, 1059–1079, https://doi.org/10.1175/JAMC-D-13-061.1.

Kremser, S., and Coauthors, 2016: Stratospheric aerosol-observations, processes, and impact on climate. *Rev. Geophys.*, **54**, 278–335, https://doi.org/10.1002/2015RG000511.

Lagouarde, J.-P., and Coauthors, 2018: The Indian-French TRISHNA Mission: Earth Observation in the thermal infrared with high spatio-temporal resolution. *IGARSS 2018 – 2018 IEEE Int. Geoscience and Remote Sensing Symp.*, Valencia, Spain, Institute of Electrical and Electronics Engineers, 4078–4081, https://doi.org/10.1109/IGARSS.2018.8518720.

Lambiel, C., and R. Delaloye, 2004: Contribution of real-time kinematic GPS in the study of creeping Mountain permafrost: Examples from the western Swiss Alps. *Permafrost Periglacial Processes*, **15**, 229–241, https://doi.org/10.1002/ppp.496.

Lan, X., and Coauthors, 2019: Long-term measurements show little evidence for large increases in total U.S. methane emissions over the past decade. *Geophys. Res. Lett.*, **46**, 4991–4999, https://doi.org/10.1029/2018GL081731.

——, and Coauthors, 2021: Improved constraints on global methane emissions and sinks using $\delta^{13}C\text{-}CH_4$. *Global Biogeochem. Cycles*, **35**, e2021GB007000, https://doi.org/10.1029/2021GB007000.

——, P. Tans, and K. W. Thoning, 2025a: Trends in globally-averaged CO_2 determined from NOAA global monitoring laboratory measurements, version 2025-05. Accessed 1 June 2025, https://doi.org/10.15138/9N0H-ZH07.

——, K. W. Thoning, and E. J. Dlugokencky, 2025b: Trends in globally-averaged CH_4, N_2O, and SF_6 determined from NOAA global monitoring laboratory measurements, version 2025-05. Accessed 1 June 2025, https://doi.org/10.15138/P8XG-AA10.

Landerer, F. W., and Coauthors, 2020: Extending the global mass change data record: GRACE follow-on instrument and science data performance. *Geophys. Res. Lett.*, **47**, e2020GL088306, https://doi.org/10.1029/2020GL088306.

Lavers, D. A., A. Simmons, F. Vamborg, and M. J. Rodwell, 2022: An evaluation of ERA5 precipitation for climate monitoring. *Quart. J. Roy. Meteor. Soc.*, **148**, 3152–3165, https://doi.org/10.1002/qj.4351.

Lee, H.-T., and NOAA CDR Program, 2018: NOAA Climate Data Record (CDR) of Monthly Outgoing Longwave Radiation (OLR), version 2.7. NOAA National Centers for Environmental Information, accessed 5 January 2023, https://doi.org/10.7289/V5W37TKD.

Lee, S. H., A. H. Butler, and G. L. Manney, 2025: Two major sudden stratospheric warmings during winter 2023/2024. *Weather*, **80**, 45–53, https://doi.org/10.1002/wea.7656.

Lehner, B., and Coauthors, 2011: High-resolution mapping of the world's reservoirs and dams for sustainable river-flow management. *Front. Ecol. Environ.*, **9**, 494–502, https://doi.org/10.1890/100125.

Lenssen, N. J. L., G. A. Schmidt, J. E. Hansen, M. J. Menne, A. Persin, R. Ruedy, and D. Zyss, 2019: Improvements in the GISTEMP uncertainty model. *J. Geophys. Res. Atmos.*, **124**, 6307–6326, https://doi.org/10.1029/2018JD029522.

Levene, H., 1960: Robust tests for equality of variances. *Contributions to Probability and Statistics: Essays in Honor of Harold Hotelling*, Ingram Olkin, Harold Hotelling et al., Eds., Stanford University Press, 278–292.

Levy, R. C., S. Mattoo, L. A. Munchak, L. A. Remer, A. M. Sayer, F. Patadia, and N. C. Hsu, 2013: The Collection 6 MODIS aerosol products over land and ocean. *Atmos. Meas. Tech.*, **6**, 2989–3034, https://doi.org/10.5194/amt-6-2989-2013.

L'Heureux, M. L., D. S. Harnos, E. Becker, B. Brettschneider, M. Chen, N. C. Johnson, A. Kumar, and M. K. Tippett, 2024: How well do seasonal climate anomalies match expected El Niño–Southern Oscillation (ENSO) impacts? *Bull. Amer. Meteor. Soc.*, **105**, E1542–E1551, https://doi.org/10.1175/BAMS-D-23-0252.1.

Lin, X., and Coauthors, 2024: Recent methane surges reveal heightened emissions from tropical inundated areas. *Nat. Commun.*, **15**, 10894, https://doi.org/10.1038/s41467-024-55266-y.

Lindaas, J., and Coauthors, 2021: Emissions of reactive nitrogen from western U.S. wildfires during summer 2018. *J. Geophys. Res. Atmos.*, **126**, e2020JD032657, https://doi.org/10.1029/2020JD032657.

Liu, J., and Coauthors, 2017: Contrasting carbon cycle responses of the tropical continents to the 2015–2016 El Niño. *Science*, **358**, eaam5690, https://doi.org/10.1126/science.aam5690.

Liu, R., X. Zhang, W. Wang, Y. Wang, H. Liu, M. Ma, and G. Tang, 2024: Global-scale ERA5 product precipitation and temperature evaluation. *Ecol. Indic.*, **166**, 112481, https://doi.org/10.1016/j.ecolind.2024.112481.

Liu, Y., and Coauthors, 2017: Evaluation of the VIIRS BRDF, albedo and NBAR products suite and an assessment of continuity with the long term MODIS record. *Remote Sens. Environ.*, **201**, 256–274, https://doi.org/10.1016/j.rse.2017.09.020.

——, L. Zhou, Y. Qin, C. Azorin-Molina, C. Shen, R. Xu, and Z. Zeng, 2024: Impacts of anemometer changes, site relocations and processing methods on wind speed trends in China. *Atmos. Meas. Tech.*, **17**, 1123–1131, https://doi.org/10.5194/amt-17-1123-2024.

Loeb, N. G., B. A. Wielicki, D. R. Doelling, G. L. Smith, D. F. Keyes, S. Kato, N. Manalo-Smith, and T. Wong, 2009: Toward optimal closure of the earth's top-of-atmosphere radiation budget. *J. Climate*, **22**, 748–766, https://doi.org/10.1175/2008JCLI2637.1.

——, S. Kato, W. Su, T. Wong, F. G. Rose, D. R. Doelling, J. R. Norris, and X. Huang, 2012: Advances in understanding top-of-atmosphere radiation variability from satellite observations. *Surv. Geophys.*, **33**, 359–385, https://doi.org/10.1007/s10712-012-9175-1.

——, and Coauthors, 2018: Clouds and the Earth's Radiant Energy System (CERES) Energy Balanced and Filled (EBAF) Top-of-Atmosphere (TOA) edition-4.0 data product. *J. Climate*, **31**, 895–918, https://doi.org/10.1175/JCLI-D-17-0208.1.

——, G. C. Johnson, T. J. Thorsen, J. M. Lyman, F. G. Rose, and S. Kato, 2021: Satellite and ocean data reveal marked increase in earth's heating rate. *Geophys. Res. Lett.*, **48**, e2021GL093047, https://doi.org/10.1029/2021GL093047.

——, and Coauthors, 2022: Evaluating twenty-year trends in earth's energy flows from observations and reanalyses. *J. Geophys. Res. Atmos.*, **127**, e2022JD036686, https://doi.org/10.1029/2022JD036686.

MacCallum, S. N., and C. J. Merchant, 2012: Surface water temperature observations of large Lakes by optimal estimation. *Can. J. Remote Sens.*, **38**, 25–45, https://doi.org/10.5589/m12-010.

Maciel, D. A., Lousada, F. Fassoni-Andrade, A. Pacheco Quevedo, R. Barbosa, C. C. F. Paule-Bonnet, and E. M. L. D. M. Novo, 2024: Sentinel-1 data reveals unprecedented reduction of open water extent due to 2023-2024 drought in the central Amazon basin. *Environ. Res. Lett.*, **19**, 124034, https://doi.org/10.1088/1748-9326/ad8a71.

Magnin, F., L. Ravanel, X. Bodin, P. Deline, E. Malet, J. Krysiecki, and P. Schoeneich, 2023: Main results of permafrost monitoring in the French Alps through the PermaFrance network over the period 2010–2022. *Permafrost Periglacial Processes*, **35**, 3–23, https://doi.org/10.1002/ppp.2209.

Magnusson, L., and Coauthors, 2025: Severe rain in central Europe from Storm Boris. ECMWF, accessed 29 May 2025, https://www.ecmwf.int/en/newsletter/182/news/severe-rain-central-europe-storm-boris.

Marengo, J., and Coauthors, 2024: The drought of Amazonia in 2023-2024. *Amer. J. Climate Change*, **13**, 567–597, https://doi.org/10.4236/ajcc.2024.133026.

Martens, B., and Coauthors, 2017: GLEAM v3: Satellite-based land evaporation and root-zone soil moisture. *Geosci. Model Dev.*, **10**, 1903–1925, https://doi.org/10.5194/gmd-10-1903-2017.

—— , W. Waegeman, W. A. Dorigo, N. E. C. Verhoest, and D. G. Miralles, 2018: Terrestrial evaporation response to modes of climate variability. *npj Climate Atmos. Sci.*, **1**, 43, https://doi.org/10.1038/s41612-018-0053-5.

Matthews, T., M. Byrne, R. Horton, C. Murphy, R. Pielke Sr., C. Raymond, P. Thorne, and R. L. Wilby, 2022: Latent heat must be visible in climate communications. *Wiley Interdiscip. Rev.: Climate Change*, **13**, e779, https://doi.org/10.1002/wcc.779.

—— , —— , P. C. Stoy, and K. M. Willett, 2024: Sidebar 2.2: Near-surface equivalent temperature as a key climate change metric [in "State of the Climate in 2023"]. *Bull. Amer. Meteor. Soc.*, **105** (8), S30–S32, https://doi.org/10.1175/2024BAMS-StateoftheClimate.1.

—— , C. Raymond, J. Foster, J. W. Baldwin, C. Ivanovich, Q. Kong, P. Kinney, and R. M. Horton, 2025: Mortality impacts of the most extreme heat events. *Nat. Rev. Earth Environ.*, **6**, 193–210, https://doi.org/10.1038/s43017-024-00635-w.

Mayer, M., L. Haimberger, C. T. Sabeerali, V. Schenzinger, D. E. Surendran, and O. P. Sreejith, 2023: Upper air winds [in "State of the Climate in 2022"]. *Bull. Amer. Meteor. Soc.*, **104** (9), S74–S76, https://doi.org/10.1175/BAMS-D-23-0090.1.

McCabe, M. F., B. Aragon, R. Houborg, and J. Mascaro, 2017: CubeSats in hydrology: Ultrahigh-resolution insights into vegetation dynamics and terrestrial evaporation. *Water Resour. Res.*, **53**, 10 017–10 024, https://doi.org/10.1002/2017WR022240.

McCarthy, M. P., and R. Toumi, 2004: Observed interannual variability of tropical troposphere relative humidity. *J. Climate*, **17**, 3181–3191, https://doi.org/10.1175/1520-0442(2004)017<3181:OIVOTT>2.0.CO;2.

McVicar, T. R., and Coauthors, 2012: Global review and synthesis of trends in observed terrestrial near-surface wind speeds: Implications for evaporation. J. Hydrol., 416–417, 182–205, https://doi.org/10.1016/j.jhydrol.2011.10.024.

Mears, C. A., and F. J. Wentz, 2016: Sensitivity of satellite-derived tropospheric temperature trends to the diurnal cycle adjustment. *J. Climate*, **29**, 3629–3646, https://doi.org/10.1175/JCLI-D-15-0744.1.

—— , A. D. Smith, K. L. Ricciardulli, J. Wang, H. Huelsing, and F. J. Wentz, 2018: Construction and uncertainty estimation of a satellite-derived total precipitable water data record over the world's oceans. *Earth Space Sci.*, **5**, 197–210, https://doi.org/10.1002/2018EA000363.

—— , J. P. Nicolas, O. Bock, S. P. Ho, and X. Zhou, 2023: Total column water vapor [in "State of the Climate in 2022"]. *Bull. Amer. Meteor. Soc.*, **104** (9), S54–S55, https://doi.org/10.1175/BAMS-D-23-0090.1.

Meesters, A. G., R. A. M. De Jeu, and M. Owe, 2005: Analytical derivation of the vegetation optical depth from the microwave polarization difference index. *IEEE Geosci. Remote Sens. Lett.*, **2**, 121–123, https://doi.org/10.1109/LGRS.2005.843983.

Menne, M. J., and Coauthors, 2025: The Global Historical Climatology Network hourly (GHCNh) dataset. *29th Conf. of Applied Climatology*, New Orleans, LA, Amer. Meteor. Soc., 9.1, https://ams.confex.com/ams/105ANNUAL/meetingapp.cgi/Paper/446924.

Menzel, A., Y. Yuan, M. Matiu, T. Sparks, H. Scheifinger, R. Gehrig, and N. Estrella, 2020: Climate change fingerprints in recent European plant phenology. *Global Change Biol.*, **26**, 2599–2612, https://doi.org/10.1111/gcb.15000.

Messager, M. L., B. Lehner, G. Grill, I. Nedeva, and O. Schmitt, 2016: Estimating the volume and age of water stored in global Lakes using a geo-statistical approach. *Nat. Commun.*, **7**, 13603, https://doi.org/10.1038/ncomms13603.

MeteoSwiss, 2025: Klimabulletin Jahr 2024. 14 pp.

Michel, S. E., and Coauthors, 2024: Rapid shift in methane carbon isotopes suggests microbial emissions drove record high atmospheric methane growth in 2020-2022. *Proc. Natl. Acad. Sci. USA*, **121**, e2411212121, https://doi.org/10.1073/pnas.2411212121.

Mildrexler, D. J., M. Zhao, and S. W. Running, 2006: Where are the hottest spots on earth? *EoS, Trans. Amer. Geophys. Union*, **87**, 461–467, https://doi.org/10.1029/2006EO430002.

Millán, L., and Coauthors, 2022: The Hunga Tonga-Hunga Ha'apai hydration of the stratosphere. *Geophys. Res. Lett.*, **49**, e2022GL099381, https://doi.org/10.1029/2022GL099381.

Miller, B. R., and Coauthors, 2010: HFC-23 (CHF_3) emission trend response to HCFC-22 ($CHClF_2$) production and recent HFC-23 emission abatement measures. *Atmos. Chem. Phys.*, **10**, 7875–7890, https://doi.org/10.5194/acp-10-7875-2010.

Minola, L., H. Reese, H. W. Lai, C. Azorin-Molina, J. A. Guijarro, S. W. Son, and D. Chen, 2022: Wind stilling–reversal across Sweden: The impact of land-use and large-scale atmospheric circulation changes. *Int. J. Climatol.*, **42**, 1049–1071, https://doi.org/10.1002/joc.7289.

Miralles, D. G., and Coauthors, 2014: El Niño–La Niña cycle and recent trends in continental evaporation. *Nat. Climate Change*, **4**, 122–126, https://doi.org/10.1038/nclimate2068.

—— , P. Gentine, S. I. Seneviratne, and A. J. Teuling, 2019: Land-atmospheric feedbacks during droughts and heatwaves: State of the science and current challenges. *Ann. N. Y. Acad. Sci.*, **1436**, 19–35, https://doi.org/10.1111/nyas.13912.

—— , and Coauthors, 2025: GLEAM4: Global land evaporation and soil moisture dataset at 0.1 resolution from 1980 to near present. *Sci. Data*, **12**, 416, https://doi.org/10.1038/s41597-025-04610-y.

Mitchell, L., E. Brook, J. E. Lee, C. Buizert, and T. Sowers, 2013: Constraints on the late Holocene anthropogenic contribution to the atmospheric methane budget. *Science*, **342**, 964–966, https://doi.org/10.1126/science.1238920.

Moesinger, L., R.-M. Zotta, R. van Der Schalie, T. Scanlon, R. de Jeu, and W. Dorigo, 2022: Monitoring vegetation condition using microwave remote sensing: The standardized vegetation optical depth index (SVODI). *Biogeosciences*, **19**, 5107–5123, https://doi.org/10.5194/bg-19-5107-2022.

Mollaret, C., C. Hilbich, C. Pellet, A. Flores-Orozco, R. Delaloye, and C. Hauck, 2019: Mountain permafrost degradation documented through a network of permanent electrical resistivity tomography sites. *Cryosphere*, **13**, 2557–2578, https://doi.org/10.5194/tc-13-2557-2019.

Monks, P. S., and Coauthors, 2015: Tropospheric ozone and its precursors from the urban to the global scale from air quality to short-lived climate forcer. *Atmos. Chem. Phys.*, **15**, 8889–8973, https://doi.org/10.5194/acp-15-8889-2015.

Montreal Protocol, 1989: Montreal Protocol on substances that deplete the ozone layer. Final act 1987. *J. Environ. Law*, **1**, 128–136, https://doi.org/10.1093/jel/1.1.128.

Morán-Tejeda, E., J. L. Ceballos, K. Peña, J. Lorenzo-Lacruz, and J. I. López-Moreno, 2018: Recent evolution and associated hydrological dynamics of a vanishing tropical Andean glacier: Glaciar de Conejeras, Colombia. *Hydrol. Earth Syst. Sci.*, **22**, 5445–5461, https://doi.org/10.5194/hess-22-5445-2018.

Morgenstern, O., and Coauthors, 2025: Radiocarbon monoxide indicates increasing atmospheric oxidizing capacity. *Nat. Commun.*, **16**, 249, https://doi.org/10.1038/s41467-024-55603-1.

Morice, C. P., and Coauthors, 2021: An updated assessment of near-surface temperature change from 1850: The HadCRUT5 data set. *J. Geophys. Res. Atmos.*, **126**, e2019JD032361, https://doi.org/10.1029/2019JD032361.

Mote, P. W., and Coauthors, 1996: An atmospheric tape recorder: The imprint of tropical tropopause temperatures on stratospheric water vapor. *J. Geophys. Res.*, **101**, 3989–4006, https://doi.org/10.1029/95JD03422.

Mühle, J., and Coauthors, 2010: Perfluorocarbons in the global atmosphere: Tetrafluoromethane, hexafluoroethane, and octafluoropropane. *Atmos. Chem. Phys.*, **10**, 5145–5164, https://doi.org/10.5194/acp-10-5145-2010.

Myhre, G., D. Shindell, and J. Pongratz, 2014: Anthropogenic and natural radiative forcing. *Climate Change 2013: The Physical Science Basis*, T. F. Stocker et al., Eds., Cambridge University Press, 659–740.

NASA, 2024: NASA, NOAA: Sun reaches maximum phase in 11-year solar cycle. Accessed 28 February 2025, https://science.nasa.gov/science-research/heliophysics/nasa-noaa-sun-reaches-maximum-phase-in-11-year-solar-cycle/.

NASA Earth Observatory, 2024: Intense, widespread drought grips South America. Accessed 10 February 2025, https://earthobservatory.nasa.gov/images/153447/intense-widespread-drought-grips-south-america.

Newman, P. A., J. S. Daniel, D. W. Waugh, and E. R. Nash, 2007: A new formulation of equivalent effective stratospheric chlorine (EESC). *Atmos. Chem. Phys.*, **7**, 4537–4552, https://doi.org/10.5194/acp-7-4537-2007.

—— , L. R. Lait, N. A. Kramarova, L. Coy, S. M. Frith, L. D. Oman, and S. S. Dhomse, 2024: Record high March 2024 Arctic total column ozone. *Geophys. Res. Lett.*, **51**, e2024GL110924, https://doi.org/10.1029/2024GL110924.

Nisbet, E. G., and Coauthors, 2023: Atmospheric methane: Comparison between methane's record in 2006–2022 and during glacial terminations. *Global Biogeochem. Cycles*, **37**, e2023GB007875, https://doi.org/10.1029/2023GB007875.

NOAA, 2024: Great Lakes ice coverage reaches historic low. https://research.noaa.gov/great-lakes-ice-coverage-reaches-historic-low/.

—— , 2025: Great Lakes ice cover database 1973-2024. GLERL, accessed 2 June 2025, https://www.glerl.noaa.gov/data/ice/#historical.

NOAA/NCEI, 2024: Monthly Global Climate Report for November 2024. https://www.ncei.noaa.gov/access/monitoring/monthly-report/global/202411#precip.

—— , 2025a: Global Climate Report Annual 2024. https://www.ncei.noaa.gov/access/monitoring/monthly-report/global/202413.

—— , 2025b: Monthly Drought Report for Annual 2024. Accessed 11 February 2025, https://www.ncei.noaa.gov/access/monitoring/monthly-report/drought/202413.

Noetzli, J., and Coauthors, 2024a: Enhanced warming of European Mountain permafrost in the early 21st century. *Nat. Commun.*, **15**, 10508, https://doi.org/10.1038/s41467-024-54831-9.

Nowak, J. B., and Coauthors, 2012: Ammonia sources in the California South Coast air basin and their impact on ammonium nitrate formation. *Geophys. Res. Lett.*, **39**, L07804, https://doi.org/10.1029/2012GL051197.

O'Gorman, P. A., and C. J. Muller, 2010: How closely do changes in surface and column water vapor follow Clausius–Clapeyron scaling in climate change simulations? *Environ. Res. Lett.*, **5**, 025207, https://doi.org/10.1088/1748-9326/5/2/025207.

Oh, Y., and Coauthors, 2023: CarbonTracker CH_4 2023. Accessed 1 June 2025, https://doi.org/10.25925/40jt-qd67.

Okamoto-Mizuno, K., K. Mizuno, S. Michie, A. Maeda, and S. Iizuka, 1999: Effects of humid heat exposure on human sleep stages and body temperature. *Sleep*, **22**, 767–773, https://doi.org/10.1093/sleep/22.6.767.

O'Kane, T. J., and C. L. Franzke, 2025: Pacific–South American pattern. *Atmospheric Oscillations*, Elsevier, 171–181, https://doi.org/10.1016/B978-0-443-15638-0.00008-3.

O'Keefe, J., and G. VanScoy, 2024: Phenology of woody species at Harvard Forest since 1990. Harvard Forest Data Archive: HF003, accessed 1 February 2025, https://harvardforest1.fas.harvard.edu/exist/apps/datasets/showData.html?id=HF003.

Oman, L. D., A. R. Douglass, J. R. Ziemke, J. M. Rodriguez, D. W. Waugh, and J. E. Nielsen, 2013: The ozone response to ENSO in aura satellite measurements and a chemistry–climate simulation. *J. Geophys. Res. Atmos.*, **118**, 965–976, https://doi.org/10.1029/2012JD018546.

O'Neill, H. B., S. L. Smith, C. R. Burn, C. Duchesne, and Y. Zhang, 2023: Widespread permafrost degradation and thaw subsidence in northwest Canada. *J. Geophys. Res. Earth Surf.*, **128**, e2023JF007262, https://doi.org/10.1029/2023JF007262.

Osborn, T. J., P. D. Jones, D. H. Lister, C. P. Morice, I. R. Simpson, J. P. Winn, E. Hogan, and I. C. Harris, 2021: Land surface air temperature variations across the globe updated to 2019: The CRUTEM5 data set. *J. Geophys. Res. Atmos.*, **126**, e2019JD032352, https://doi.org/10.1029/2019JD032352.

Pakistan Meteorological Department, 2025: State of Pakistan Climate 2024. Climate Data Processing Center, 23 pp., https://cdpc.pmd.gov.pk/Pakistan_Climate_2024.pdf.

Pandey, K., and R. Sengupta, 2024: Climate India 2024: An assessment of extreme weather events. Center for Science and Environment Down to Earth Rep., 60 pp., https://www.cseindia.org/climate-india-2024-an-assessment-of-extreme-weather-events-12460.

Park, T., and Coauthors, 2016: Changes in growing season duration and productivity of Northern vegetation inferred from long-term remote sensing data. *Environ. Res. Lett.*, **11**, 084001, https://doi.org/10.1088/1748-9326/11/8/084001.

—— , M. K. Gumma, W. Wang, P. Panjala, S. K. Dubey, and R. R. Nemani, 2023: Greening of human-dominated ecosystems in India. *Commun. Earth Environ.*, **4**, 419, https://doi.org/10.1038/s43247-023-01078-9.

Payne, V. H., and Coauthors, 2022: Satellite measurements of peroxyacetyl nitrate from the Cross-Track infrared sounder: Comparison with ATom aircraft measurements. *Atmos. Meas. Tech.*, **15**, 3497–3511, https://doi.org/10.5194/amt-15-3497-2022.

Pellet, C., and Coauthors, 2024: Rock glacier velocity [in "State of Climate 2023"]. *Bull. Amer. Meteor. Soc.*, **105** (8), 44–46, https://doi.org/10.1175/BAMS-D-24-0116.1.

Pelto, M., 2024: Alpine Glaciers [in "State of the Climate in 2023"]. *Bull. Amer. Meteor. Soc.*, **105** (8), S46–S47, https://doi.org/10.1175/BAMS-D-24-0116.1.

Pelto, M. S., and J. Pelto, 2025: The loss of ice worm glacier, North Cascade range, Washington USA. Water, **17**, 432, https://doi.org/10.3390/w17030432.

Peng, S., and Coauthors, 2022: Wetland emission and atmospheric sink changes explain methane growth in 2020. *Nature*, **612**, 477–482, https://doi.org/10.1038/s41586-022-05447-w.

PERMOS, 2024: *Swiss Permafrost Bulletin 2023* (Annual Report of the Swiss Permafrost Monitoring Network PERMOS No. 5). Swiss Permafrost Monitoring Network PERMOS, 25 pp., https://doi.org/10.13093/permos-bull-2024.

—— , 2025: *Swiss Permafrost Bulletin 2024* (Annual Report of the Swiss Permafrost Monitoring Network PERMOS No. 6). Swiss Permafrost Monitoring Network PERMOS, https://doi.org/10.13093/permos-bull-2025.

Peterson, D. A., J. Campbell, E. Hyer, M. Fromm, G. Kablick, J. Cossuth, and M. DeLand, 2018: Wildfire-driven thunderstorms cause a volcano-like stratospheric injection of smoke. *npj Climate Atmos. Sci.*, **1**, 30, https://doi.org/10.1038/s41612-018-0039-3.

—— , and Coauthors, 2021: Australia's Black Summer pyrocumulonimbus super outbreak reveals potential for increasingly extreme stratospheric smoke events. *npj Climate Atmos. Sci.*, **4**, 38, https://doi.org/10.1038/s41612-021-00192-9.

Peterson, T. C., K. M. Willett, and P. W. Thorne, 2011: Observed changes in surface atmospheric energy over land. *Geophys. Res. Lett.*, **38**, L16707, https://doi.org/10.1029/2011GL048442.

Petropavlovskikh, I., and Coauthors, 2025: Ozone trends in homogenized Umkehr, ozonesonde, and COH overpass records. *Atmos. Chem. Phys.*, **25**, 2895–2936, https://doi.org/10.5194/acp-25-2895-2025.

Phillips, C., and M. Foster, 2024: Cloudiness [in "State of the Climate in 2023"]. *Bull. Amer. Meteor. Soc.*, **105** (8), S63–S65, https://doi.org/10.1175/BAMS-D-24-0116.1.

Pi, X., and Coauthors, 2022: Mapping global lake dynamics reveals the emerging roles of small Lakes. *Nat. Commun.*, **13**, 5777, https://doi.org/10.1038/s41467-022-33239-3.

Pinto, I., and Coauthors, 2024: Conflict, poverty and water management issues exposing vulnerable communities in Africa to extreme floods that are now common events because of climate change. Imperial College London, 33 pp., https://spiral.imperial.ac.uk/server/api/core/bitstreams/a494f174-d954-4905-9569-0039d372762c/content.

Pinty, B., and Coauthors, 2011: Exploiting the MODIS albedos with the Two-stream Inversion Package (JRC-TIP): 2. Fractions of transmitted and absorbed fluxes in the vegetation and soil layers. *J. Geophys. Res.*, **116**, D09106, https://doi.org/10.1029/2010JD015373.

Plummer, D., and Coauthors, 2021: CCMI-2022: A new set of Chemistry-Climate Model Initiative (CCMI) community simulations to update the assessment of models and support upcoming ozone assessment activities. *SPARC Newsletter*, No. 57, 22–30, https://www.sparc-climate.org/wp-content/uploads/sites/5/2021/07/ SPARCnewsletter_Jul2021_web.pdf.

Po-Chedley, S., J. R. Christy, L. Haimberger, and C. A. Mears, 2021: Tropospheric temperature [in "State of the Climate in 2020"]. *Bull. Amer. Meteor. Soc.*, **102** (8), S34–S37, https://doi.org/10.1175/BAMS-D-21-0098.1.

—— , —— , —— , —— , and C.-Z. Zou, 2024: Tropospheric temperature [in "State of the Climate in 2023"]. *Bull. Amer. Meteor. Soc.*, **105** (8), S39–S41, https://doi.org/10.1175/BAMS-D-24-0116.1.

Pogliotti, P., E. Cremonese, and U. Morra di Cella, 2023: Warming permafrost in the western Alps: A further evidence of elevation dependent warming? *J. Alp. Res.*, **111** (2), https://doi.org/10.4000/rga.11784.

Popp, T., and Coauthors, 2016: Development, production and evaluation of aerosol climate data records from European satellite observations (Aerosol_cci). Remote Sens., **8**, 421, https://doi.org/10.3390/rs8050421.

Prather, M. J., C. D. Holmes, and J. Hsu, 2012: Reactive greenhouse gas scenarios: Systematic exploration of uncertainties and the role of atmospheric chemistry. *Geophys. Res. Lett.*, **39**, L09803, https://doi.org/10.1029/2012GL051440.

Price, C., M. Asfur, and Y. Yair, 2009: Maximum hurricane intensity preceded by increase in lightning frequency. *Nat. Geosci.*, **2**, 329–332, https://doi.org/10.1038/ngeo477.

Pucik, T., 2024: Meteorological analysis of extreme flash flood situation in the Valencia region. European Severe Storms Laboratory, accessed 29 May 2025, https://www.essl.org/cms/meteorological-analysis-of-extreme-flash-flood-situation-in-the-valencia-region/.

Raghuraman, S. P., B. Soden, A. Clement, G. Vecchi, S. Menemenlis, and W. Yang, 2024: The 2023 global warming spike was driven by the El Niño–Southern Oscillation. *Atmos. Chem. Phys.*, **24**, 11 275–11 283, https://doi.org/10.5194/acp-24-11275-2024.

Rakov, V. A., and M. A. Uman, 2003: *Lightning Physics and Effects.* Cambridge University Press, 687 pp., https://doi.org/10.1017/CBO9781107340886.

Randel, W. J., and J. B. Cobb, 1994: Coherent variations of monthly mean total ozone and lower stratospheric temperature. *J. Geophys. Res.*, **99**, 5433–5447, https://doi.org/10.1029/93JD03454.

—— , X. Wang, J. Starr, R. R. Garcia, and D. Kinnison, 2024: Long-term temperature impacts of the Hunga volcanic eruption in the stratosphere and above. *Geophys. Res. Lett.*, **51**, e2024GL111500, https://doi.org/10.1029/2024GL111500.

RGIK, 2023a: Guidelines for inventorying rock glaciers: Baseline and practical concepts (version 1.0). IPA Action Group Rock Glacier Inventories and Kinematics, 26 pp., https://doi.org/10.51363/unifr.srr.2023.002.

—— , 2023b: Rock glacier velocity as an associated parameter of ECV permafrost: Baseline concepts (version 3.2). IPA Action Group Rock Glacier Inventories and Kinematics, 13 pp.

Ricciardulli, L., and F. J. Wentz, 2015: A scatterometer geophysical model function for climate-quality winds: QuikSCAT Ku-2011. *J. Atmos. Oceanic Technol.*, **32**, 1829–1846, https://doi.org/10.1175/JTECH-D-15-0008.1.

—— , and A. Manaster, 2021: Intercalibration of ASCAT scatterometer winds from MetOp-A, -B, and -C, for a stable climate data record. *Remote Sens.*, **13**, 3678, https://doi.org/10.3390/rs13183678.

Richardson, A. D., 2019: Tracking seasonal rhythms of plants in diverse ecosystems with digital camera imagery. *New Phytol.*, **222**, 1742–1750, https://doi.org/10.1111/nph.15591.

—— , and J. O'Keefe, 2009: Phenological differences between understory and overstory. *Phenology of Ecosystem Processes*, A. Noormets, Ed., Springer, 87–117.

Roberts, R., and Coauthors, 2022: Taking the HIGHWAY to save lives on Lake Victoria. *Bull. Amer. Meteor. Soc.*, **103**, E485–E510, https://doi.org/10.1175/BAMS-D-20-0290.1.

Rodell, M., and B. Li, 2023: Changing intensity of hydroclimatic extreme events revealed by GRACE and GRACE-FO. Nat. *Water*, **1**, 241–248, https://doi.org/10.1038/s44221-023-00040-5.

—— , J. S. Famiglietti, D. N. Wiese, J. T. Reager, H. K. Beaudoing, F. W. Landerer, and M. H. Lo, 2018: Emerging trends in global freshwater availability. *Nature*, **557**, 651–659, https://doi.org/10.1038/s41586-018-0123-1.

—— , and Coauthors, 2024: An abrupt decline in global terrestrial water storage and its relationship with sea level change. *Surv. Geophys.*, **45**, 1875–1902, https://doi.org/10.1007/s10712-024-09860-w.

Rohde, R. A., and Z. Hausfather, 2020: The Berkeley Earth land/ocean temperature record. *Earth Syst. Sci. Data*, **12**, 3469–3479, https://doi.org/10.5194/essd-12-3469-2020.

Rosemartin, A. H., and Coauthors, 2014: Organizing phenological data resources to inform natural resource conservation. *Biol. Conserv.*, **173**, 90–97, https://doi.org/10.1016/j.biocon.2013.07.003.

Rubino, M., and Coauthors, 2019: Revised records of atmospheric trace gases CO_2, CH_4, N_2O, and $\delta^{13}C$-CO_2 over the last 2000 years from Law Dome, Antarctica. *Earth Syst. Sci. Data*, **11**, 473–492, https://doi.org/10.5194/essd-11-473-2019.

Rudlosky, S. D., and K. S. Virts, 2021: Dual geostationary lightning mapper observations. *Mon. Wea. Rev.*, **149**, 979–998, https://doi.org/10.1175/MWR-D-20-0242.1.

Rutllant, J. A., and H. Fuenzalida, 1991: Synoptic aspects of the central Chile rainfall variability associated with the Southern Oscillation. *Int. J. Climatol.*, **11**, 63–76, https://doi.org/10.1002/joc.3370110105.

Santee, M. L., and Coauthors, 2023: Strong evidence of heterogeneous processing on stratospheric sulfate aerosol in the extrapolar Southern Hemisphere following the 2022 Hunga Tonga-Hunga Ha'apai eruption. *J. Geophys. Res. Atmos.*, **128**, e2023JD039169, https://doi.org/10.1029/2023JD039169.

Santer, B. D., and Coauthors, 2008: Consistency of modelled and observed temperature trends in the tropical troposphere. *Int. J. Climatol.*, **28**, 1703–1722, https://doi.org/10.1002/joc.1756.

Satheesh, S. K., and Coauthors, 2017: Variability of atmospheric aerosols over India. Observed Climate Variability and Change over the Indian Region, Springer, 221–248, https://doi.org/10.1007/978-981-10-2531-0_13.

Sato, M., J. E. Hansen, M. P. McCormick, and J. B. Pollack, 1993: Stratospheric aerosol optical depths, 1850–1990. *J. Geophys. Res.*, **98**, 22 987–22 994, https://doi.org/10.1029/93JD02553.

Schaaf, C. B., and Coauthors, 2002: First operational BRDF, albedo nadir reflectance products from MODIS. Remote Sens. *Environ.*, **83**, 135–148, https://doi.org/10.1016/S0034-4257(02)00091-3.

Schwartz, M. D., T. R. Ault, and J. L. Betancourt, 2013: Spring onset variations and trends in the continental United States: Past and regional assessment using temperature-based indices. *Int. J. Climatol.*, **33**, 2917–2922, https://doi.org/10.1002/joc.3625.

Sen, P. K., 1968: Estimates of the regression coefficient based on Kendall's tau. *J. Amer. Stat. Assoc.*, **63**, 1379–1389, https://doi.org/10.1080/01621459.1968.10480934.

Seneviratne, S. I., T. Corti, E. L. Davin, M. Hirschi, E. B. Jaeger, I. Lehner, B. Orlowsky, and A. J. Teuling, 2010: Investigating soil moisture–climate interactions in a changing climate: A review. *Earth-Sci. Rev.*, **99**, 125–161, https://doi.org/10.1016/j.earscirev.2010.02.004.

Seyednasrollah, B., A. M. Young, K. Hufkens, T. Milliman, M. A. Friedl, S. Frolking, and A. D. Richardson, 2019: Publisher correction: Tracking vegetation phenology across diverse biomes using version 2.0 of the PhenoCam dataset. *Sci. Data*, **6**, 261, https://doi.org/10.1038/s41597-019-0270-8.

Shao, X., S.-P. Ho, X. Jing, X. Zhou, Y. Chen, T.-C. Liu, B. Zhang, and J. Dong, 2023: Characterizing the tropospheric water vapor spatial variation and trend using 2007–2018 COSMIC radio occultation and ECMWF reanalysis data. *Atmos. Chem. Phys.*, **23**, 14 187–14 218, https://doi.org/10.5194/acp-23-14187-2023.

Sharma, S., and Coauthors, 2021: Loss of ice cover, shifting phenology, and more extreme events in Northern Hemisphere lakes. *J. Geophys. Res. Biogeosci.*, **126**, e2021JG006348, https://doi.org/10.1029/2021JG006348.

——, and Coauthors, 2022: Author correction: Long-term ice phenology records spanning up to 578 years for 78 lakes around the Northern Hemisphere. *Sci. Data*, **9**, 419, https://doi.org/10.1038/s41597-022-01531-y.

Shi, L., and J. J. Bates, 2011: Three decades of intersatellite-calibrated High-Resolution Infrared Radiation Sounder upper tropospheric water vapor. *J. Geophys. Res.*, **116**, D04108, https://doi.org/10.1029/2010JD014847.

Simmons, A. J., 2022: Trends in the tropospheric general circulation from 1979 to 2022. *Wea. Climate Dyn.*, **3**, 777–809, https://doi.org/10.5194/wcd-3-777-2022.

Simpson, I. R., K. A. McKinnon, D. Kennedy, D. M. Lawrence, F. Lehner, and R. Seager, 2024: Observed humidity trends in dry regions contradict climate models. *Proc. Natl. Acad. Sci. USA*, **121**, e2302480120, https://doi.org/10.1073/pnas.2302480120.

Sindelarova, K., and Coauthors, 2014: Global data set of biogenic VOC emissions calculated by the MEGAN model over the last 30 years. *Atmos. Chem. Phys.*, **14**, 9317–9341, https://doi.org/10.5194/acp-14-9317-2014.

Smith, S. L., H. B. O'Neill, K. Isaksen, J. Noetzli, and V. E. Romanovsky, 2022: The changing thermal state of permafrost. *Nat. Rev. Earth Environ.*, **3**, 10–23, https://doi.org/10.1038/s43017-021-00240-1.

——, V. E. Romanovsky, K. Isaksen, K. E. Nyland, N. I. Shiklomanov, D. A. Streletskiy, and H. H. Christiansen, 2024: Permafrost [in "State of the Climate in 2023"]. *Bull. Amer. Meteor. Soc.*, **105** (8), 314–317, https://doi.org/10.1175/BAMS-D-24-0116.1.

Soci, C., and Coauthors, 2024: The ERA5 global reanalysis from 1940 to 2022. *Quart. J. Roy. Meteor. Soc.*, **150**, 4014–4048, https://doi.org/10.1002/qj.4803.

Sofen, E. D., D. Bowdalo, and M. J. Evans, 2016: How to most effectively expand the global surface ozone observing network. *Atmos. Chem. Phys.*, **16**, 1445–1457, https://doi.org/10.5194/acp-16-1445-2016.

Solomon, S., K. Stone, P. Yu, D. M. Murphy, D. Kinnison, A. R. Ravishankara, and P. Wang, 2023: Chlorine activation and enhanced ozone depletion induced by wildfire aerosol. *Nature*, **615**, 259–264, https://doi.org/10.1038/s41586-022-05683-0.

Song, F., G. J. Zhang, V. Ramanathan, and L. R. Leung, 2022: Trends in surface equivalent potential temperature: A more comprehensive metric for global warming and weather extremes. *Proc. Natl. Acad. Sci. USA*, **119**, e2117832119, https://doi.org/10.1073/pnas.2117832119.

Song, X.-P., M. C. Hansen, S. V. Stehman, P. V. Potapov, A. Tyukavina, E. F. Vermote, and J. R. Townshend, 2018: Global land change from 1982 to 2016. *Nature*, **560**, 639–643, https://doi.org/10.1038/s41586-018-0411-9.

Sorg, A., A. Kääb, A. Roesch, C. Bigler, and M. Stoffel, 2015: Contrasting responses of central Asian rock glaciers to global warming. *Sci. Rep.*, **5**, 8228, https://doi.org/10.1038/srep08228.

South African Weather Service, 2024: Cape Town's record-breaking July 2024 rainfall. Document Reference: CS-CMS-LETT-003, accessed 12 August 2024, https://www.suidkaapforum.com/News/Article/National-News/cape-town-s-record-breaking-july-2024-rainfall-202408120436.

SPARC/IO3C/GAW, 2019: SPARC/IO3C/GAW report on long-term ozone trends and uncertainties in the stratosphere. I. Petropavlovskikh et al., Eds., SPARC Rep. 9, WCRP-17/2018, GAW Rep. 241, 102 pp., https://doi.org/10.17874/f899e57a20b.

Spencer, R. W., J. R. Christy, and W. D. Braswell, 2017: UAH version 6 global satellite temperature products: Methodology and results. *Asia-Pac. J. Atmos. Sci.*, **53**, 121–130, https://doi.org/10.1007/s13143-017-0010-y.

Stackhouse, P. W., T. Wong, D. P. Kratz, P. Sawaengphokhai, A. C. Wiber, S. K. Gupta, and N. G. Loeb, 2016: Earth radiation budget at top-of-atmosphere [in "State of the Climate in 2015"]. *Bull. Amer. Meteor. Soc.*, **97** (8), S41–S43, https://doi.org/10.1175/2017BAMSStateoftheClimate.1.

Staub, B., C. Lambiel, and R. Delaloye, 2016: Rock glacier creep as a thermally-driven phenomenon: A decade of inter-annual observation from the Swiss Alps. *XI Int. Conf. on Permafrost*, Potsdam, Germany, Alfred Wegener Institute Helmholtz Center for Polar and Marine Research, 96–97, https://doi.org/10.2312/GFZ.LIS.2016.001.

Stein, A. F., R. R. Draxler, G. D. Rolph, B. J. B. Stunder, M. D. Cohen, and F. Ngan, 2015: NOAA's HYSPLIT atmospheric transport and dispersion modeling system. *Bull. Amer. Meteor. Soc.*, **96**, 2059–2077, https://doi.org/10.1175/BAMS-D-14-00110.1.

Steinbrecht, W., and Coauthors, 2017: An update on ozone profile trends for the period 2000 to 2016. *Atmos. Chem. Phys.*, **17**, 10 675–10 690, https://doi.org/10.5194/acp-17-10675-2017.

Steiner, A. K., and Coauthors, 2020: Observed temperature changes in the troposphere and stratosphere from 1979 to 2018. *J. Climate*, **33**, 8165–8194, https://doi.org/10.1175/JCLI-D-19-0998.1.

Stocker, M., F. Ladstädter, and A. K. Steiner, 2021: Observing the climate impact of large wildfires on stratospheric temperature. *Sci. Rep.*, **11**, 22994, https://doi.org/10.1038/s41598-021-02335-7.

—— , A. K. Steiner, F. Ladstädter, U. Foelsche, and W. J. Randel, 2024: Observed impacts of the Hunga Tonga eruption on stratospheric temperature. *EGU General Assembly 2024*, Vienna, Austria, EGU, EGU24-11683, https://doi.org/10.5194/egusphere-egu24-11683.

Stoy, P. C., J. Roh, and G. T. Bromley, 2022: It's the heat and the humidity: The complementary roles of temperature and specific humidity to recent changes in the energy content of the near-surface atmosphere. *Geophys. Res. Lett.*, **49**, e2021GL096628, https://doi.org/10.1029/2021GL096628.

Streletskiy, D. A., and Coauthors, 2025: Thawing permafrost is subsiding in the Northern Hemisphere—Review and perspectives. *Environ. Res. Lett.*, **20**, 013006, https://doi.org/10.1088/1748-9326/ada2ff.

Susskind, J., G. Molnar, L. Iredell, and N. G. Loeb, 2012: Interannual variability of outgoing longwave radiation as observed by AIRS and CERES. *J. Geophys. Res.*, **117**, D23107, https://doi.org/10.1029/2012JD017997.

Szopa, S., and Coauthors, 2021: Short-lived climate forcers. *Climate Change 2021: The Physical Science Basis*, V. Masson-Delmotte et al., Eds., Cambridge University Press, 817–922, https://doi.org/10.1017/9781009157896.008.

Taha, G., R. Loughman, P. R. Colarco, T. Zhu, L. W. Thomason, and G. Jaross, 2022: Tracking the 2022 Hunga Tonga-Hunga Ha'apai aerosol cloud in the upper and Middle stratosphere using space-based observations. *Geophys. Res. Lett.*, **49**, e2022GL100091, https://doi.org/10.1029/2022GL100091.

Tandon, A., 2024: Record-breaking Philippines typhoon season was 'supercharged' by climate change. Carbon Brief, https://www.carbonbrief.org/record-breaking-philippines-typhoon-season-was-supercharged-by-climate-change/.

Tapley, B. D., S. Bettadpur, J. C. Ries, P. F. Thompson, and M. M. Watkins, 2004: GRACE measurements of mass variability in the Earth system. *Science*, **305**, 503–505, https://doi.org/10.1126/science.1099192.

Tarasick, D. W., and Coauthors, 2019: Tropospheric ozone assessment report: Tropospheric ozone from 1877 to 2016, observed levels, trends and uncertainties. *Elementa*, **7**, 39, https://doi.org/10.1525/elementa.376.

The GlaMBIE Team, 2025: Community estimate of global glacier mass changes from 2000 to 2023. *Nature*, **639**, 382–388, https://doi.org/10.1038/s41586-024-08545-z.

Thibert, E., and X. Bodin, 2022: Changes in surface velocities over four decades on the Laurichard rock glacier (French Alps). Permafrost Periglacial Processes, **33**, 323–335, https://doi.org/10.1002/ppp.2159.

Thiery, W., E. Davin, S. Seneviratne, K. Bedka, S. Lhermitte, and N. van Lipzig, 2016: Hazardous thunderstorm intensification over Lake Victoria. *Nat. Commun.*, **7**, 12786, https://doi.org/10.1038/ncomms12786.

Thomason, L. W., and Coauthors, 2018: A global space-based stratospheric aerosol climatology: 1979–2016. *Earth Syst. Sci. Data*, **10**, 469–492, https://doi.org/10.5194/essd-10-469-2018.

Tian, H., and Coauthors, 2024: Global nitrous oxide budget 1980–2020. *Earth Syst. Sci. Data*, **16**, 2543–2604, https://doi.org/10.5194/essd-16-2543-2024.

Todt, M. A., E. Asher, E. Hall, P. Cullis, A. Jordan, K. Xiong, D. F. Hurst, and T. Thornberry, 2023: Baseline balloon stratospheric aerosol profiles (B2SAP)—Systematic measurements of aerosol number density and size. *J. Geophys. Res. Atmos.*, **128**, e2022JD038041, https://doi.org/10.1029/2022JD038041.

Toreti, A., and Coauthors, 2024a: Global drought overview September 2024 – GDO analytical report. Publications Office of the European Union Rep. JRC139423, 36 pp., https://data.europa.eu/doi/10.2760/7511271.

—— , and Coauthors, 2024b: Drought in Europe - July 2024: GDO analytical report. 24 pp., https://doi.org/10.2760/420832.

—— , and Coauthors, 2024c: Drought in the Amazon and the La Plata basins - December 2024: GDO analytical report. 30 pp., https://doi.org/10.2760/9524487.

Torralba, V., F. J. Doblas-Reyes, and N. Gonzalez-Reviriegol, 2017: Uncertainty in recent near-surface wind speed trends: A global reanalysis intercomparison. *Environ. Res. Lett.*, **12**, 114019, https://doi.org/10.1088/1748-9326/aa8a58.

Trenberth, K. E., 1997: The definition of El Niño. *Bull. Amer. Meteor. Soc.*, **78**, 2771–2777, https://doi.org/10.1175/1520-0477(1997)078<2771:TDOENO>2.0.CO;2.

—— , and J. T. Fasullo, 2013: Regional energy and water cycles: Transports from ocean to land. *J. Climate*, **26**, 7837–7851, https://doi.org/10.1175/JCLI-D-13-00008.1.

UNEP, 2024: Report of the Scientific Assessment Panel in response to Decision XXXV/7: Emissions of HFC-23. 35 pp., https://ozone.unep.org/system/files/documents/SAP_Report_on_HFC23_September2024.pdf.

United Nations, 2016: Paris Agreement to the United Nations Framework Convention on Climate Change, Dec. *12*, **2015**, T.I.A.S. No. 16-1104. 54 pp., https://unfccc.int/sites/default/files/resource/parisagreement_publication.pdf.

UNOCHA, 2024: Southern Africa: El Niño regional humanitarian overview. OCHA, https://www.unocha.org/publications/report/mozambique/southern-africa-el-nino-regional-humanitarian-overview-september-2024.

USDA and USDC, 2024: *Weekly Weather and Crop Bulletin*. Vol. 111, No. 11, 28 pp., https://downloads.usda.library.cornell.edu/usda-esmis/files/cj82k728n/m326np628/pk02f026h/wwcb1124.pdf.

van der Schalie, R., and Coauthors, 2017: The merging of radiative transfer based surface soil moisture data from SMOS and AMSR-E. Remote Sens. *Environ.*, **189**, 180–193, https://doi.org/10.1016/j.rse.2016.11.026.

van der Schrier, G., J. Barichivich, K. R. Briffa, and P. D. Jones, 2013: A scPDSI-based global dataset of dry and wet spells for 1901–2009. *J. Geophys. Res. Atmos.*, **118**, 4025–4048, https://doi.org/10.1002/jgrd.50355.

van der Werf, G. R., and Coauthors, 2017: Global fire emissions estimates during 1997–2016. *Earth Syst. Sci. Data*, **9**, 697–720, https://doi.org/10.5194/essd-9-697-2017.

Van Dijk, A. I. J. M., and Coauthors, 2025: Global Water Monitor 2024, Summary Report. Global Water Monitor Consortium, 58 pp., https://www.globalwater.online/globalwater/report/.

Virts, K. S., and S. J. Goodman, 2020: Prolific lightning and thunderstorm initiation over the Lake Victoria basin in East Africa. *Mon. Wea. Rev.*, **148**, 1971–1985, https://doi.org/10.1175/MWR-D-19-0260.1.

——, J. M. Wallace, M. L. Hutchins, and R. H. Holzworth, 2015: Diurnal and seasonal lightning variability over the Gulf Stream and the Gulf of Mexico. *J. Atmos. Sci.*, **72**, 2657–2665, https://doi.org/10.1175/JAS-D-14-0233.1.

Vivero, S., X. Bodin, D. Farías-Barahona, S. MacDonell, N. Schaffer, B. A. Robson, and C. Lambiel, 2021: Combination of aerial, satellite, and UAV photogrammetry for quantifying rock glacier kinematics in the Dry Andes of Chile (30°S) since the 1950s. *Front. Remote Sens.*, **2**, 784015, https://doi.org/10.3389/frsen.2021.784015.

Vömel, H., S. Evan, and M. Tully, 2022: Water vapor injection into the stratosphere by Hunga Tonga-Hunga Ha'apai. *Science*, **377**, 1444–1447, https://doi.org/10.1126/science.abq2299.

von Schuckmann, K., and Coauthors, 2023: Heat stored in the earth system 1960–2020: Where does the energy go? *Earth Syst. Sci. Data*, **15**, 1675–1709, https://doi.org/10.5194/essd-15-1675-2023.

Vose, R. S., and Coauthors, 2021: Implementing full spatial coverage in NOAA's global temperature analysis. *Geophys. Res. Lett.*, **48**, e2020GL090873, https://doi.org/10.1029/2020GL090873.

Vreugdenhil, M., and Coauthors, 2022: Microwave remote sensing for agricultural drought monitoring: Recent developments and challenges. *Front. Water*, **4**, 1045451, https://doi.org/10.3389/frwa.2022.1045451.

Wang, L., and Coauthors, 2023: Quantification of water released by thawing permafrost in the source region of the Yangtze River on the Tibetan Plateau by InSAR monitoring. *Water Resour. Res.*, **59**, e2023WR034451, https://doi.org/10.1029/2023WR034451.

Weatherhead, E. C., and Coauthors, 1998: Factors affecting the detection of trends: Statistical considerations and applications to environmental data. *J. Geophys. Res.*, **103**, 17 149–17 161, https://doi.org/10.1029/98JD00995.

Wells, N., S. Goddard, and M. J. Hayes, 2004: A self-calibrating palmer drought severity index. *J. Climate*, **17**, 2335–2351, https://doi.org/10.1175/1520-0442(2004)017<2335:ASPDSI>2.0.CO;2.

Wentz, F. J., 1997: A well-calibrated ocean algorithm for special sensor microwave/imager. *J. Geophys. Res.*, **102**, 8703–8718, https://doi.org/10.1029/96JC01751.

——, 2015: A 17-yr climate record of environmental parameters derived from the Tropical Rainfall Measuring Mission (TRMM) microwave imager. *J. Climate*, **28**, 6882–6902, https://doi.org/10.1175/JCLI-D-15-0155.1.

——, L. Ricciardulli, K. Hilburn, and C. Mears, 2007: How much more rain will global warming bring? *Science*, **317**, 233–235, https://doi.org/10.1126/science.1140746.

Wentz, K., T. Meissner, F. Wentz, and A. Manaster, 2024: Absolute intercalibration of spaceborne microwave radiometers. *J. Atmos. Oceanic Technol.*, **41**, 1121–1138, https://doi.org/10.1175/JTECH-D-24-0024.1.

Western, L. M., and Coauthors, 2023: Author correction: Global increase of ozone-depleting chlorofluorocarbons from 2010 to 2020. *Nat. Geosci.*, **16**, 546, https://doi.org/10.1038/s41561-023-01205-3.

——, and Coauthors, 2024: A decrease in radiative forcing and equivalent effective chlorine from hydrochlorofluorocarbons. *Nat. Climate Change*, **14**, 805–807, https://doi.org/10.1038/s41558-024-02038-7.

Weyhenmeyer, G. A., and Coauthors, 2024: Global lake health in the anthropocene: Societal implications and treatment strategies. *Earth's Future*, **12**, e2023EF004387, https://doi.org/10.1029/2023EF004387.

WFP, 2024: Eastern Africa Seasonal Monitor: Severe flooding across equatorial areas, April–May 2024. ReliefWeb, 15 pp., https://reliefweb.int/report/kenya/eastern-africa-seasonal-monitor-severe-flooding-across-equatorial-areas-april-may-2024.

WGMS, 2023: Global Glacier Change Bulletin. No. 5 (2020–2021), ISC(WDS)/IUGG(IACS)/UNEP/UNESCO/WMO, World Glacier Monitoring Service, 148 pp., https://doi.org/10.5904/wgms-fog-2023-09.

Wielicki, B. A., B. R. Barkstrom, E. F. Harrison, R. B. Lee, I. I. I. G. L. Smith, and J. E. Cooper, 1996: Clouds and the Earth's Radiant Energy System (CERES): An Earth observing system experiment. *Bull. Amer. Meteor. Soc.*, **77**, 853–868, https://doi.org/10.1175/1520-0477(1996)077<0853:CATERE>2.0.CO;2.

——, and Coauthors, 1998: Clouds and the Earth's Radiant Energy System (CERES): Algorithm overview. *IEEE Trans. Geosci. Remote Sens.*, **36**, 1127–1141, https://doi.org/10.1109/36.701020.

Wiese, D. N., F. W. Landerer, and M. M. Watkins, 2016: Quantifying and reducing leakage errors in the JPL RL05M GRACE Mascon solution. *Water Resour. Res.*, **52**, 7490–7502, https://doi.org/10.1002/2016WR019344.

Willett, K. M., 2023a: HadISDH.extremes Part I: A gridded wet bulb temperature extremes index product for climate monitoring. *Adv. Atmos. Sci.*, **40**, 1952–1967, https://doi.org/10.1007/s00376-023-2347-8.

——, 2023b: HadISDH.extremes Part II: Exploring humid heat extremes using wet bulb temperature indices. *Adv. Atmos. Sci.*, **40**, 1968–1985, https://doi.org/10.1007/s00376-023-2348-7.

——, 2023c: Sidebar 2.1: Assessing humid heat extremes over land [in "State of the Climate in 2022"]. *Bull. Amer. Meteor. Soc.*, **104** (9), S51–S53, https://doi.org/10.1175/BAMS-D-23-0090.1.

——, C. N. Williams Jr., R. J. H. Dunn, P. W. Thorne, S. Bell, M. de Podesta, P. D. Jones, and D. E. Parker, 2013: HadISDH: An updateable land surface specific humidity product for climate monitoring. *Climate Past*, **9**, 657–677, https://doi.org/10.5194/cp-9-657-2013.

——, R. J. H. Dunn, P. W. Thorne, S. Bell, M. de Podesta, D. E. Parker, P. D. Jones, and C. N. Williams Jr., 2014: HadISDH land surface multi-variable humidity and temperature record for climate monitoring. *Climate Past*, **10**, 1983–2006, https://doi.org/10.5194/cp-10-1983-2014.

—— , —— , J. Kennedy, and D. Berry, 2020: Development of the HadISDH.marine humidity climate monitoring dataset. *Earth Syst. Sci. Data*, **12**, 2853–2880, https://doi.org/10.5194/essd-12-2853-2020.

—— , R. M. Horton, Y. T. E. Lo, C. Raymond, and C. D. W. Rogers, 2024: Humid-heat extremes over land [in "State of the Climate in 2023"]. *Bull. Amer. Meteor. Soc.*, **105** (8), S55–S56, https://doi.org/10.1175/2024BAMSStateoftheClimate.1.

WMO, 2022: Scientific Assessment of Ozone Depletion: 2022. WMO Ozone Research and Monitoring GAW Rep. 278, 520 pp., https://ozone.unep.org/sites/default/files/2023-02/Scientific-Assessment-of-Ozone-Depletion-2022.pdf.

—— , 2024: State of the Climate 2024. Update for COP29. WMO, 12 pp., https://library.wmo.int/idurl/4/69075.

—— , 2025a: State of the Global Climate 2024. WMO-1368, 42 pp., https://library.wmo.int/records/item/69455-state-of-the-global-climate-2024.

—— , 2025b: State of the Climate 2024. Significant Weather & Climate Events. https://wmo.int/sites/default/files/2025-03/State%20of%20the%20Global%20Climate%202024_Extremes%20Supplement.pdf

Wohland, J., N.-E. Omrani, D. Witthaut, and N.-S. Keenlyside, 2019: Inconsistent wind speed trends in current twentieth century reanalyses. *J. Geophys. Res. Atmos.*, **124**, 1931–1940, https://doi.org/10.1029/2018JD030083.

Woolway, R. I., and C. J. Merchant, 2018: Intralake heterogeneity of thermal responses to climate change: A study of large Northern Hemisphere lakes. *J. Geophys. Res. Atmos.*, **123**, 3087–3098, https://doi.org/10.1002/2017JD027661.

—— , and Coauthors, 2017: Lake surface temperature [in "State of the Climate in 2016"]. *Bull. Amer. Meteor. Soc.*, **98** (8), S13–S14, https://doi.org/10.1175/2017BAMSStateoftheClimate.1.

—— , and Coauthors, 2018: Lake surface temperature [in "State of the Climate in 2017"]. *Bull. Amer. Meteor. Soc.*, **99** (8), S13–S15, https://doi.org/10.1175/2018BAMSStateoftheClimate.1.

WWA, 2024a: Climate change increased Typhoon Gaemi's wind speeds and rainfall, with devastating impacts across the western Pacific region. WWA, 58 pp., https://www.worldweatherattribution.org/climate-change-increased-typhoon-gaemis-wind-speeds-and-rainfall/.

—— , 2024b: Rapid urbanisation and climate change key drivers of dramatic flood impacts in Nepal. WWA, 30 pp., https://www.worldweatherattribution.org/rapid-urbanisation-and-climate-change-key-drivers-of-dramatic-flood-impacts-in-nepal/.

Xing, J. W., and M. M. Wang, 2023: Trend and drivers of satellite-detected burned area changes across Arctic region since the 21st century. J. Geophys. Res. Atmos., 128, https://doi.org/10.1029/2023JD038946.

Xu, H., L. Zhang, Z. Jin, A. Wang, Z. Liu, and F. Wang, 2025: Physiological strain under different wet bulb temperatures during daylong humid heat exposure in young men. *Build. Environ.*, **274**, 112783, https://doi.org/10.1016/j.buildenv.2025.112783.

Xu, N., H. Lu, W. Li, and P. Gong, 2024: Natural Lakes dominate global water storage variability. *Sci. Bull.*, **69**, 1016–1019, https://doi.org/10.1016/j.scib.2024.02.023.

Yang, Y., and Coauthors, 2023: Evapotranspiration on a greening earth. *Nat. Rev. Earth Environ.*, **4**, 626–641, https://doi.org/10.1038/s43017-023-00464-3.

Yao, F., B. Livneh, B. Rajagopalan, J. Wang, J.-F. Crétaux, Y. Wada, and M. Berge-Nguyen, 2023: Satellites reveal widespread decline in global lake water storage. *Science*, **380**, 743–749, https://doi.org/10.1126/science.abo2812.

Yeh, S., and Coauthors, 2018: ENSO atmospheric teleconnections and their response to greenhouse gas forcing. *Rev. Geophys.*, **56**, 185–206, https://doi.org/10.1002/2017RG000568.

Yoon, J., and S.-W. Yeh, 2010: Influence of the Pacific decadal oscillation on the relationship between El Niño and the northeast Asian summer monsoon. *J. Climate*, **23**, 4525–4537, https://doi.org/10.1175/2010JCLI3352.1.

Yosef, Y., E. Aguilar, and P. Alpert, 2021: Is it possible to fit extreme climate change indices together seamlessly in the era of accelerated warming? *Int. J. Climatol.*, **41**, E952–E963, https://doi.org/10.1002/joc.6740.

Young, S. S., 2023: Global and regional snow cover decline: 2000–2022. *Climate*, **11**, 162, https://doi.org/10.3390/cli11080162.

Yu, P., and Coauthors, 2021: Persistent stratospheric warming due to 2019–2020 Australian wildfire smoke. *Geophys. Res. Lett.*, **48**, e2021GL092609, https://doi.org/10.1029/2021GL092609.

Zeng, Z., and Coauthors, 2019: A reversal in global terrestrial stilling and its implications for wind energy production. *Nat. Climate Change*, **9**, 979–985, https://doi.org/10.1038/s41558-019-0622-6.

Zha, J., and Coauthors, 2021: Projected changes in global terrestrial near-surface wind speed in 1.5°C–4.0°C global warming levels. *Environ. Res. Lett.*, **16**, 114016, https://doi.org/10.1088/1748-9326/ac2fdd.

Zhang, G. F., and Coauthors, 2021: Uneven warming likely contributed to declining near-surface wind speeds in northern China between 1961 and 2016. *J. Geophys. Res. Atmos.*, **126**, e2020JD033637, https://doi.org/10.1029/2020JD033637.

Zhang, S., S. Solomon, C. D. Boone, and G. Taha,2024: Investigating the vertical extent of the 2023 summer Canadian wildfire impacts with satellite observations. *Atmos. Chem. Phys.*, **24**, 11 727–11 736, https://doi.org/10.5194/acp-24-11727-2024.

Zhang, W., and Coauthors, 2025: A year marked by extreme precipitation and floods: Weather and climate extremes in 2024. *Adv. Atmos. Sci.*, **42**, 1045–1063, https://doi.org/10.1007/s00376-025-4540-4.

Zhang, X., L. Alexander, G. C. Hegerl, P. Jones, A. K. Tank, T. C. Peterson, B. Trewin, and F. W. Zwiers, 2011: Indices for monitoring changes in extremes based on daily temperature and precipitation data. *Wiley Interdiscip. Rev.: Climate Change*, **2**, 851–870, https://doi.org/10.1002/wcc.147.

Zhang, Z., B. Poulter, A. F. Feldman, Q. Ying, P. Ciais, S. Peng, and X. Li, 2023: Recent intensification of wetland methane feedback. *Nat. Climate Change*, **13**, 430–433, https://doi.org/10.1038/s41558-023-01629-0.

Zhao, L., and Coauthors, 2024: Investigation, monitoring, and simulation of permafrost on the Qinghai–Tibet Plateau: A review. *Permafrost Periglacial Processes*, **35**, 412–422, https://doi.org/10.1002/ppp.2227.

Zhao, Y., and Coauthors, 2019: Inter-model comparison of global hydroxyl radical (OH) distributions and their impact on atmospheric methane over the 2000–2016 period. *Atmos. Chem. Phys.*, **19**, 13 701–13 723, https://doi.org/10.5194/acp-19-13701-2019.

Zhao, Y., H. Norouzi, M. Azarderakhsh, and A. AghaKouchak, 2021: Global patterns of hottest, coldest, and extreme diurnal variability on earth. *Bull. Amer. Meteor. Soc.*, **102**, E1672–E1681, https://doi.org/10.1175/BAMS-D-20-0325.1.

Zheng, B., and Coauthors, 2023: Record-high CO_2 emissions from boreal fires in 2021. *Science*, **379**, 912–917, https://doi.org/10.1126/science.ade0805.

Zhou, X., and Coauthors, 2024: Antarctic vortex dehydration in 2023 as a substantial removal pathway for Hunga Tonga-Hunga Ha'apai water vapor. *Geophys. Res. Lett.*, **51**, e2023GL107630, https://doi.org/10.1029/2023GL107630.

Zhu, Z., and Coauthors, 2016: Greening of the Earth and its drivers. *Nat. Climate Change*, **6**, 791–795, https://doi.org/10.1038/nclimate3004.

Ziemke, J. R., and Coauthors, 2019: Trends in global tropospheric ozone inferred from a composite record of TOMS/OMI/MLS/OMPS satellite measurements and the MERRA-2 GMI simulation. *Atmos. Chem. Phys.*, **19**, 3257–3269, https://doi.org/10.5194/acp-19-3257-2019.

——, and Coauthors, 2022: NASA satellite measurements show global-scale reductions in free tropospheric ozone in 2020 and again in 2021 during COVID-19. *Geophys. Res. Lett.*, **49**, e2022GL098712, https://doi.org/10.1029/2022GL098712.

Ziese, M., A. Rauthe-Schöch, S. Hänsel, P. Finger, E. Rustemeier, and U. Schneider, 2022: GPCC full data daily version 2022 at 1.0°: Daily Land-Surface precipitation from Rain-Gauges built on GTS-based and historic data: Globally gridded daily totals (version 2022, p. approx. 25 MB per gzip file) [NetCDF]. GPCC, https://doi.org/10.5676/DWD_GPCC/FD_D_V2022_100.

Zolghadrshojaee, M., S. Tegtmeier, S. M. Davis, and R. Pilch Kedzierski, 2024: Variability and long-term changes in tropical cold-point temperature and water vapor. *Atmos. Chem. Phys.*, **24**, 7405–7419, https://doi.org/10.5194/acp-24-7405-2024.

Zotta, R. M., R. van der Schalie, W. Preimesberger, R. De Jeu, and W. Dorigo, 2023: Vegetation optical depth [in "State of the Climate in 2023"]. *Bull. Amer. Meteor. Soc.*, **105** (8), S113–S114, https://doi.org/10.1175/BAMS-D-24-0116.1.

——, L. Moesinger, R. van der Schalie, M. Vreugdenhil, W. Preimesberger, T. Frederikse, R. De Jeu, and W. Dorigo, 2024a: VODCA v2: Multi-sensor, multi-frequency vegetation optical depth data for long-term canopy dynamics and biomass monitoring (1.0.0). TU Wien, accessed 16 January 2025, https://doi.org/10.48436/t74ty-tcx62.

——, ——, ——, ——, ——r, ——, ——, and ——, 2024b: VODCA v2: Multi-sensor, multi-frequency vegetation optical depth data for long-term canopy dynamics and biomass monitoring. *Earth Syst. Sci. Data*, **16**, 4573–4617, https://doi.org/10.5194/essd-16-4573-2024.

Zou, C.-Z., H. Xu, X. Hao, and Q. Liu, 2023: Mid-tropospheric layer temperature record derived from satellite microwave observations with backward merging approach. *J. Geophys. Res. Atmos.*, **128**, e2022JD037472, https://doi.org/10.1029/2022JD037472.

Zou, D., and Coauthors, 2024: Estimation of permafrost ground ice to 10-m depth on the Qinghai–Tibet Plateau. *Permafrost Periglacial Processes*, **35**, 423–434, https://doi.org/10.1002/ppp.2226]